ENTROPIC ELASTICITY OF POLYMERS AND THEIR NETWORKS

Tianxiang Su

A DISSERTATION

in

Mechanical Engineering and Applied Mechanics

Presented to the Faculties of the University of Pennsylvania

in

Partial Fulfillment of the Requirements for the

Degree of Doctor of Philosophy

2011

Assistant Professor Prashant K. Purohit
Department of Mechanical Engineering and Applied Mechanics
Supervisor of Dissertation

Associate Professor Jennifer R. Lukes
Department of Mechanical Engineering and Applied Mechanics
Graduate Group Chairperson

Dissertation Committee:

Professor John L. Bassani,
Department of Mechanical Engineering and Applied Mechanics
Professor Pedro Ponte Castañeda,
Department of Mechanical Engineering and Applied Mechanics
Professor Dennis E. Discher,
Chemical and Biomolecular Engineering Department

ACKNOWLEDGEMENT

I would like to express my gratitude to my advisor, Dr. Prashant K. Purohit. I have been fortunate to have an advisor, who has great enthusiasm for science and deep understanding in his research field, who can discuss problems with me almost whenever I need discussions, and who can give me helpful and clever advice on how to tackle the problems. I will never forget the days and nights in these four years working with Prashant. This thesis would not have been possible without his guidance, patience and support.

I would also like to thank all the members in my thesis committee: Dr. John L. Bassani, Dr. Pedro Ponte Castañeda, and Dr. Dennis E. Discher. I am proud of passing all the graduate level solid mechanics classes they offered during these 4 years. Some of the classes were tough, but, with their help, I managed to see the beauty in many of the mechanics problems.

My grateful thanks also go to the friends I met here at Penn, especially to Xin Wang, who helped me a lot in the previous one year when I wrote my thesis and looked for post-doc positions.

Last but not the least, I would like to thank my parents, for their love. They may not be able to help me solve the scientific problems directly, but, they help in another way by always letting me feel their support from the other side of the world.

ABSTRACT

Entropic Elasticity of Polymers and Their Networks

Tianxiang Su

Advisor: Prashant K. Purohit

The elastic energy for many biopolymer systems is comparable to the thermal energy at room temperature. Therefore, biopolymers and their networks are constantly under thermal fluctuations. From the point of view of thermodynamics, this suggests that entropy plays a crucial role in determining the mechanical behaviors of these filamentous biopolymers. One of the main goals of this thesis is to understand how thermal fluctuations affect the mechanical properties and behaviors of filamentous networks, and also how stress affects the thermal fluctuations.

Filaments and filamentous networks are viewed as mechanical structures, whose static equilibrium states under the action of loads or kinematic constraints are determined in the first step of the investigation. Typically, a system is discretized and represented by a finite set of kinematic variables that characterizes the configuration space. In the next step, we apply statistical mechanics to study the thermo-mechanical properties of the system. We approximate the local minimum energy well to quadratic order. Such a quadratic approximation for a discrete system gives rise to a stiffness matrix that characterizes the flexibility of the system around the ground state. Using the multidimensional Gaussian integral technique, the partition function is efficiently evaluated, provided that the energy well around the ground state is steep. In this case, the dominant contribution to the partition function is from the states that are close to the equilibrium state, whose energies are well approximated by the quadratic energy expression. All thermodynamic properties of the system can be further evaluated from the partition function. Fluctuation of the system, in particular, scales linearly with the temperature and inversely with the stiffness matrix. Therefore, the stiffness matrix governs the statistical mechanical behavior of the system near its ground state. We also show that a system with constraints on its kinematic variables can be converted into an effective non-constrained system.

Using the above theoretical framework, we study the thermo-mechanical properties of filaments and filamentous networks under different loadings and confinement conditions. The filaments need not be homogeneous in the mechanical properties, and they can be subjected to non-uniform distributed loads or non-uniform confinements. Under compression, a filament can buckle. Buckling in a filament network can reduce the stiffness of the structure, which leads to significant thermal fluctuations around the buckling point. Properties of a triangular network under pure expansion, simple shear and uniaxial

tension are also investigated in this thesis.

As further applications, we discuss the protein forced unfolding problem. We show that different unfolding behaviors of a protein chain can be understood using a system of three equations. We also discuss the internal fluctuations of DNA under confinement and show a length-dependent transition between the de Gennes and Odijk regimes. We also show that entropy plays a role in driving the motion of a piece of DNA along a non-uniform channel. We derive the entropic force on the DNA in this thesis and discuss the coupled migration and deformation of the polymer under non-uniform confinement.

Contents

1 Introduction **1**

I Heterogeneous Freely-Jointed Chain Model and Its Applications **13**

2 Mechanics of Forced Unfolding of Proteins **14**
2.1 Introduction 14
2.2 Three Equations Governing the Forced Unfolding of Proteins . 16
2.3 Heterogeneous FJC Model and the Equilibrium Force-Extension Relation 16
2.4 Kinetic Equation 20
2.5 Constant Velocity Pulling I – Forced Unfolding of Globular Proteins 22
2.6 Constant Velocity Pulling II – Forced Unfolding of Fibrous Proteins 24
2.7 Pulling with a Force Linearly Increasing with Time 26
2.8 Constant Force Pulling 29
2.9 Discussions 32
2.10 Conclusions 35

II Heterogeneous Wormlike Chain Model and Its Applications **40**

3 Statistical Mechanics of a Discrete System with Quadratic Energy **41**
3.1 General Theory 42
3.2 Statistical Mechanics of a Constrained System: Method 1 . . . 43
3.3 Statistical Mechanics of a Constrained System: Method 2 . . . 45
3.4 An Example 45

4 Heterogeneous Wormlike Chain Under End-to-end Force **49**
4.1 Introduction 49
4.2 Description of the Heterogeneous Wormlike Chain Model . . . 51

4.3 General Theory . . . 53
4.4 Hinged-hinged 2D chain . . . 57
4.5 Partially Clamped 2D Chain . . . 60
4.6 Clamped-clamped 2D Chain . . . 61
4.7 Fluctuation of a 2D Chain . . . 63
4.8 Theory for the 3D Chains . . . 64
4.9 Monte Carlo Simulation . . . 66
4.10 Results and Application . . . 66
4.10.1 Thermo-mechanical properties of the chain . . . 66
4.10.2 Fluctuation and correlation of the angle θ_i . . . 67
4.10.3 Transverse fluctuation of the chains $\langle y^2 \rangle$ . . . 68
4.10.4 Application to the protein unfolding problem . . . 68
4.11 Conclusions . . . 69

5 Statistics of the Heterogeneous Wormlike Chain 78
5.1 Distribution of the End-to-end Extension $P(x)$ . . . 78
5.2 Distribution of the Transverse Displacement . . . 84
5.3 Conclusions . . . 85

6 Fluctuating Elastic Filaments Under Distributed Loads 88
6.1 Introduction . . . 88
6.2 Theory . . . 90
6.2.1 Theory for a continuous elastic filament . . . 90
6.2.2 Energy of a discretized elastic filament or semi-flexible chain . . . 94
6.2.3 Partition function and free energy . . . 96
6.2.4 Force-extension relation . . . 97
6.2.5 Thermal fluctuation around the ground state . . . 97
6.3 Results . . . 98
6.4 Conclusions . . . 100

7 Transition Between Two Regimes Describing Internal Fluctuation of DNA in a Nanochannel 105
7.1 Introduction . . . 106
7.2 Results and Discussion . . . 108
7.3 Materials and Methods . . . 119
7.3.1 Sequence specific labeling and DNA staining . . . 119
7.3.2 Loading DNA into nanochannels . . . 119
7.3.3 Microscopy and image processing . . . 120
7.3.4 Recording and calculations . . . 120
7.3.5 Partition function and angle fluctuation . . . 120

8 Entropically Driven Motion of Polymers in Non-uniform Nanochannels 124
8.1 Introduction . . . 124

8.2 Entropically Driven Diffusion . . . 126
8.3 DNA Confined in Non-uniform Channels – Theory and Computation . . . 129
8.4 DNA Confined in Non-uniform Channels – Results . . . 134
8.4.1 Stationary DNA in nanochannels . . . 134
8.4.2 Migration and deformation of DNA in non-uniform channels . . . 135
8.4.3 Transition to the de Gennes regime under non-zero force 138
8.5 Conclusions . . . 139

III Statistical Mechanics of Filamentous Networks 148

9 Entropic Elasticity of Fluctuating Filament Networks 149
9.1 Introduction . . . 150
9.2 Expansion of a Triangular Network . . . 152
9.3 Entropic Elasticity of a General 2D Network – Theory . . . 155
9.3.1 Stable equilibrium states . . . 156
9.3.2 Thermal fluctuations around the static state . . . 158
9.4 Entropic Elasticity of a Hexagon . . . 163
9.4.1 Hydrostatic edge tension on a hexagon . . . 163
9.4.2 Simple shear on a hexagon . . . 171
9.4.3 Pure tension on a hexagon . . . 181
9.5 A Comparison with Other Networks . . . 186
9.6 Conclusions . . . 186

10 Conclusions and Future Work 191
Appendices . . . 193

A Evaluating the Partition Function 193

B $\det \mathbf{M}$ **for the Hinged-hinged Chain 194**

C Force-extension Relation for a Homogeneous Wormlike Chain 196

D Force-extension Relation for a Special Heterogeneous Wormlike Chain 198

E $\det \mathbf{M}$ **for the Clamped-clamped Chain 200**

F Transverse Fluctuation Scales as T **202**

G Partition Function for a Fixed Extension Ensemble 203

H Theory for the 2D Chains 205

I Relation Between the End-to-end Extension $\langle x \rangle$ and Channel Width D for Wang and Gao's Theory **207**

J Fluctuation for Short Internal Segments **208**

K Heterogeneity on the Backbone of DNA **210**

L Total Extension versus L Relation **212**

M Distribution of Extension in the Deflection Regime **214**

N Results of Entropy-induced Migration Derived from the Sackur-Tetrode Equation **215**

O Transverse Size of a Strongly Confined Polymer **217**

List of Tables

2.1 Eq. 2.39 divides the $F - t$ plane into 4 regions with different signs of dF/dt. 34

List of Figures

1.1 Beam structures made by human beings and by nature. (A) The Akashi-Kaikyō Bridge, located in Japan and spanning 1,991 metres, is the world's longest suspension bridge (Figure comes from http://blogger.sanook.com/confuse/2008/11/23/). (B) In a cell division cycle, the mitotic spindels, composed by microtubules and various other proteins, are used as 'cables' to pull the daughter chromosomes apart. (Figure comes from reference [1].) (C) Man-made tent is usually supported by a frame of poles. (Figure comes from Wikipedia: *Tent*.) (D) A spectrin meshwork under the human red blood cells. Cell membrane is thin and fragile. So most of them are strengthened and supported by a network of protein filamenets. This filamentous network, like the frame in the man-made tent, determines the shape of the membrane. (Figure comes from reference [1].) (E) The 2010 Vancouver Olympic cauldron. (Figure comes from Wikipedia: *Olympic Flame*. (F) Structure of the stereocilia projecting from a hair cell in the inner ear (Figure comes from [2]). 3

1.2 Force-extension relation for a wormlike chain. In the small force limit (red dashed line, Eq. 1.10), the polymer behaves like a spring with a temperature dependent spring constant. In the high force limit (black dashed line, Eq. 1.14), the model predicts that $1 - x/L \sim F^{-1/2}$. These two limits can be combined to construct an approximate formula for all forces (blue line, Eq. 1.15). 5

1.3 Set-ups for measuring the force *vs.* extension behavior of macromolecules (Figure comes from reference [16]). (A) Hinged-hinged condition. Both ends are attached to beads which are held in optical traps that can exert forces but not moments. Hence the curvatures at the ends are constrained but not the slopes. The trap does not allow transverse displacements. (B) Clamped-clamped condition. The slopes and transverse displacements are constrained at both ends. (C) Partially clamped condition. One end of the macromolecule is secured to a cover-slip while the other end is attached to a bead in a magnetic or optical trap which ensures that the slope is held constant, but transverse displacements are allowed. 9

2.1 Illustration of the two-state kinetic model. (a) A chain of mixed folded and unfolded proteins is modeled as a heterogeneous freely-jointed chain. A single folded (unfolded) protein is represented by an N_{fs}-segment (N_{us}-segment) subchain with Kuhn length l_f (l_u). In this illustration, two folded and one unfolded proteins are represented by the two red and one blue subchains respectively. Note that in reality, the actual number of segments in each subchain may be much larger. Also, l_u is expected to be smaller than l_f since an unfolded protein is expected to be floppier than a folded protein. (b) Energy landscape of the two-state model. The ordinate is the Gibbs free energy and the abscissa is the reaction coordinate. The two wells, representing the folded and unfolded states of a protein, are separated by an energy barrier with transition distances Δx_u and Δx_f. At zero force, the folding rate and the unfolding rate are β_0 and α_0 respectively, with $\beta_0 >> \alpha_0$. An applied force can lower the energy barrier and thus change the folding and unfolding rates. 19

2.2 Predictions of the force-extension profiles using the heterogeneous FJC model with only four free parameters. (a) ubiquitin. (b) fibrinogen. Blue curves are the experimental data – ubiquitin data from [7] and fibrinogen data from [9]. We use two of the experimental curves (black dots) to fit the Kuhn length and the contour length of the folded and unfolded proteins (black dashed lines are the fitting results). Then, without any more free parameters, we use the heterogeneous FJC model (Eq. 2.12) to predict all the other curves. The predictions (red curves) match well with the experimental data for both proteins. . . . 21

2.3 Force-extension profiles of six copies of (a) ubiquitin, and (b) fibrinogen (v_c = 1000nm/s) in constant velocity pulling. Blue curves: experimental data (ubiquitin data from [7] and fibrinogen data from [9]); red curves: prediction using our two-state kinetic model. 23

2.4 Force-extension relation (continuous model) of ubiquitin (red) and fibrinogen (blue). In reality, both are globular proteins. Here we plot the force-extension relation using their kinetic parameters, but with N_f, N_u being real numbers instead of integers. 26
2.5 Number of folded proteins as a function of time (continuous model). Red curve for ubiquitin and blue curve for fibrinogen. In reality, both are globular proteins. Here we plot the $N_f(t)$ profile using their kinetic parameters, but with N_f, N_u being real numbers instead of integers. 27
2.6 Constant velocity pulling. (a) Dependence of the average unfolding force on pulling speed. Red: ubiquitin; blue: fibrinogen; solid line: accounting for refolding ($k_f \neq 0$), dashed line: ignoring refolding ($k_f = 0$). For both proteins, the predicted unfolding force using the set of parameters that assume $k_f = 0$ is much smaller, especially at high pulling velocities, than the one that takes the refolding rate into account. (b) Relaxation profiles ($v_c = 0$nm/s). The evolution of the number of refolded proteins is shown as a function of the relaxation extension x_r (normalized by $x_{max} = NL_{us}$). A limit profile (blue) is approached as time approaches infinity. 28
2.7 Extension versus time profiles for pulling using a linearly increasing force ($v_f = 300$pN/s, 9 copies of proteins). (a) ubiquitin and (b) fibrinogen. Red curves: predicted step-wise profile, using integer N_f and N_u in the governing equations (Eq. 2.12 and Eq. 2.13). Each of the steps obeys the equilibrium force-extension relation, which is shown as dashed black curves (Eq. 2.12). Red circles and dashed line: unfolding events and the fitting results. The fitting equation is $x = 680.9t - 52.12$ for ubiquitin and $x = 1419t - 92.01$ for fibrinogen (x is the extension in units of nm. Blue lines: solutions obtained by using continuous N_f and N_u in the governing equations, which match well with the discrete model shown in red. The profiles for ubiquitin obtained here are consistent with those measured in [8]. Insets: if we take the refolding rate into account, some refolding events are observed at small force. (c) Extension versus time profiles for nine copies of ubiquitin assuming $k_f = 0$ shows no refolding events at small force even though it reproduces the overall trend. 28

2.8 The double exponential function $W(F)$ together with the stationary points (blue) and the critical forces (red) for pulling with a force linearly increasing in time. Assume that there are nine copies of ubiquitin in the chain. The double exponential function when $N_f = 8$, $N_u = 1$ is shown as a black solid line (when $N_u = 0$, the function is only a single exponential). As more and more proteins unfold, N_f decreases and the curve $W(F)$ shifts to the right along the F axis (see the arrow). We plot $W(F)$ in black dashed line for $N_f = 5$, $N_u = 4$ and in black dashed-dotted line for $N_f = 1$, $N_u = 8$. The movement of the curve results in the increase of the critical force F_{cl} (red). . . . 29

2.9 Constant force pulling profiles. (a) Extension versus time profile for nine copies of ubiquitin. Blue: $F = 100$pN, red: $F = 120$pN, black: $F = 140$pN. Inset: $F = 80$pN. Step-wise curves: solution when assuming N_f and N_u to be integers in both Eq. 2.12 and Eq. 2.13. Continuous curves: analytic solution obtained by letting N_f and N_u be real numbers in the equations. The dwell time for the step-wise solution, which is obtained analytically in the text, increases as the protein unfolds. The inset shows that when the force is not large enough, not all the proteins can unfold, and refolding/unfolding 'hoppings' occur periodically. (b) $N_{f\infty}/N$ as a function of the dimensionless force Π_F. Red: ubiquitin; Blue: fibrinogen. δF, the range of the dimensionless force over which $N_{f\infty}/N$ changes from 90% to 10%, is a universal constant $\ln 81$ for all proteins. Π_F^* is the dimensionless force for half the proteins to unfold. It is shown in the text that $\Pi_F^* = \ln(\beta_0/\alpha_0)$. (c) Unfolding rate α as a function of the applied force F. Red solid line is the result of taking the refolding rate into account. When the force is large enough, $\log \alpha$ is a linear function of F (red broken line). Blue solid line is the prediction assuming $k_f = 0$. Inset, k_f/k_u as a function of the applied force. 31

3.1 A simple coupled harmonic spring system with two balls attached to three springs. All three springs have the same spring constant k and natural length L. The degrees of freedom for this discrete system are two, characterized by x_1 and x_2, the displacements of the two balls away from their equilibrium positions. 46

4.1 Model of the 2D chain. A thermally fluctuating $N-$segment 2D chain is subjected to an external applied force $\vec{F} = F\hat{X}$. The configuration of the chain is characterized by its N tangent angles θ_i, formed by the segments with respect to the $\hat{X}$ axis. The transverse displacement of the chain, denoted by y_i in the figure, reflects how much the chain fluctuates. (a) Hinged-hinged boundary conditions: both ends of the chain are constrained on the $\hat{X}$ axis, but no moment is acting on them; (b) partially clamped boundary conditions: one end of the chain is clamped on the $\hat{X}$ aixs while the other end, with slope also constrained to be zero, is free to have transverse displacement in the Y direction. (c) clamped-clamped boundary conditions: both ends are clamped on the $\hat{X}$ axis. 51

4.2 The unkown function $W(F)$ can be measured in a single force extension experiment. The shaded area above the force-extension curve is the complementary energy and the area beneath the force-extension curve is $k_BT \cdot W(F)$ by Eq. 4.15. 55

4.3 Thermo-mechanical quantities for a fluctuating chain. Blue: hinged-hinged boundary conditions; red: partially clamped boundary conditions; black: clamped-clamped boundary conditions. (a) Force-extension profile of the chain. Inset: local profile shows that the hinged-hinged chain (blue) has smaller extension and thus is more flexible (to show the figure clearly, we have changed the circles into lines with the same colors); (b) Variance of the extension. Inset: local profile shows that the hinged-hinged chain (blue) fluctuates more than the partially clamped chain (to show the figure clearly, we have changed the circles into lines with the same colors); (c) Average energy of the chain versus the applied force; (d) Variance of the energy; (e) Thermal expansion coefficient α versus the applied force; (f) Isothermal extensibility χ versus the applied force. 70

4.4 Verifying Eq. 4.23. Solid line: theoretical prediciton; circles: MC simulation results. Simulations have been done under 11 different forces varying from 150pN to 1150pN with an increasement of 100pN. Temperature is set to be 300K. Relative extension as well as thermal expansion coefficient are recorded. The result shown is for a homogeneous chain with contour length $L = 25$nm and bending modulus $K = 2.5k_BT \cdot nm$. 71

4.5 Force-extension relation for homogeneous chains (blue curve) and rods (red circle, theory in [17]). (a) Hinged-hinged boundary conditions; (b) partially clamped boundary conditions; (c) clamped-clamped boundary conditions. $K = 2.5k_BT \cdot nm$, $L = 2.5$nm. The figures show that our force-extension relations for the chains reduce to the known formulae for the continuous rods when $N \to +\infty$ with $L = Nl$ fixed. Here $N = 50000$ for the blue curves. 71
4.6 Dependence of the fluctuation of θ angles on the boundary conditions. Blue: hinged-hinged chain, the fluctuation in θ is at maximum and minimum respectively at the two ends and in the middle of the chain; red: partially clamped chain, the fluctuation is at maximum and minimum respectively in the middle and at the two ends; black: clamped-clamped chain, the fluctuation is at minimum at the two ends, but the maximum is not achieved in the middle of the chain. Also, the partially clamped chain (red) fluctuates more than the clamped-clamped chain (black). (a) $\xi_p/L = 5$, the dependence on the boundary conditions is significant througout the chain; (b) $\xi_p/L = 0.2$ the dependence on the boundary conditions is significant only at the two ends of the chain. To make the figures clear, the MC simulation results are not shown in the same figures. 72
4.7 Dependence of the fluctuation of θ angles on the heterogeneity of the chain. Blue: homogeneous chain with $K = 2.5k_BT \cdot nm$; black: corresponding MC simulation results; red: heterogeneous chain with two bending moduli: $K_I = 0.5k_BT \cdot nm$ at the first half of the chain and $K_{II} = 4.5k_BT \cdot nm$ at the second half; black dashed curve: corresponding MC simulation results. (a), (b) and (c) are for hinged-hinged, partially clamped and clamped-clamped boundary conditions respectively. The figures show that jumps in the bending modulus result in jumps in the fluctuation in the $\langle\theta^2\rangle$ profile. The larger the bending modulus, the smaller the fluctuation in θ. 72

4.8 Correlation in the tangent angle θ. (a-f): results for the homogeneous chains. Blue: $\xi_p/L = 5$; red: $\xi_p/L = 1$; black: $\xi_p/L = 0.2$. (a),(c),(e) are the theoretical results for the hinged-hinged, partially clamped and clamped-clamped chains respectively. To make the plots clear, we plot the corresponding MC simulation results separately in (b),(d) and (f) (circles). The figures show that the correlation in θ depends strongly on ξ_p/L. When $\xi_p/L > 1$ (blue), the profile also significantly depends on the boundary conditions. (g-h): results for a heterogeneous chain with $L = 1$nm. The first half and the second half of the chain have bending moduli of $K_I = 0.5k_BT \cdot nm$ and $K_{II} = 4.5k_BT \cdot nm$ respectively. (g) is the theoretical predictions and (h) is the MC simulation results. Blue, red and black colors are for the hinged-hinged, partially clamped and clamped-clamped boundary conditions respectively. The correlation profile loses its symmetry and decreases faster at the first half of the chain where the bending modulus is smaller. 73

4.9 Transverse fluctuation $\langle y^2 \rangle$. (a): blue: hinged-hinged chain; red: partially clamped chain; black: clamped-clamped chain. Solid curve: homogeneous chain with $K = 2.5k_BT \cdot nm$; dashed curve: heterogeneous chain with $K_I = 0.5k_BT \cdot nm$ for the first half of the chain and $K_{II} = 4.5k_BT \cdot nm$ for the second half. In (a), $L = 1nm$ for all the curves. Since the curves are close to each other, to make the theoretical results clear, we do not plot the MC simulation results in (a). (b): transverse fluctuation decreases when the force increases. The results are for a homogeneous hinged-hinged chain with $L = 25$nm and $K = 2.5k_BT \cdot nm$. The corresponding forces are labeled in the figure. Circles: MC simulation results; solid lines: theoretical predictions. 74

4.10 Dependence of the transverse fluctuation on the countour length of the chain. $K = 2.5k_BT \cdot nm$ for all the curves. Black solid curves (theory) and blue circles (MC simulation): $L = 5$nm; black dashed curves (theory) and red circles (MC simulation): $L = 25$nm; (a) hinged-hinged boundary conditions; (b) partially clamped boundary conditions; (c) clamped-clamped boundary conditions. The figures show that for a fixed persistence length, the longer the chain, the more the fluctuation. Also, our theoretical results and the MC simulation results match quite well. Note that here $\xi_p/L \leq 1$ and the results for hinged-hinged chain and clamped-clamped chains are quite similar, which is confirmed by the simulation results. 74

4.11 Unfolding of six copies of ubiquitins under constant velocity pulling condition. Blue dotted curves are the experimental data from [25]. Each peak in the profile represents a unfolding event where the force drops. The first and the last experimental curves are fitted to obtain the contour lengths and the bending moduli of the folded and unfolded proteins (Fig.(a): red circles are the fitted data and the black curves are the fitting results). The intermediate curves are then predicted without any free parameters using the 3D version of Eq. 4.38 (Fig.(b), red curves). Figure.(b) shows that the predictions match well with the experimental data. 75

5.1 End-to-end distance distribution function $P(x)$ using Eq. 5.14 (red circles) and Eq. 5.19 (blue). Here the external force is $F = 0$pN, the segment length is $l = 1$nm and the contour length is $L = 50$nm. The two theories match well with each other. . . 82

5.2 (A): End-to-end distance distribution function $P(x)$ for a freely-jointed chain with different contour lengths $L = 5, 10, 25$nm. Here $F = 10$pN and the Kuhn length is $l = 5$nm. The profile looks symmetric only when the contour length of the chain is long compared to its Kuhn length. (B) Distribution $P(x)$ for a freely-jointed chain under different values of tensile forces: $F = 5, 10, 20$pN. As the force increases, the profile shifts to the right and the peak becomes sharper. For both plots, $T = 300$K. 83

5.3 (A): End-to-end distance distribution function P(x) for a wormlike chain with different contour lengths $L = 1, 5, 25$nm. Here $F = 1000$pN. For short chain, the profile is clearly not symmetric. When the contour length of the chain increases and becomes comparable to its persistence length, the profile looks more symmetric. (B) Distribution P(x) for a wormlike chain under different values of tensile forces: $F = 50, 100, 300$pN. As the force increases, the profile shifts to the right and the peak becomes sharper. For both plots, $T = 300$K, $K_b = 2.5k_BT\cdot$ nm. 83

5.4 Distribution $P(r, x)$ for (A) a freely-jointed chain and (B) a wormlike chain. The chains are subjected to hinged-free boundary conditions. x, r are respectively the extension and transverse displacement of the free end. Here x is fixed for each curve and $P(r)$ versus r is plotted. The parameters are (1) Temperature $T = 300$K; (2) Kuhn length $l = 1$nm (freely-jointed chain) or bending modulus $K_b = 2.0k_BT$ (wormlike chain); (3) Contour length $L = 25$ nm; (4) Fixed force $F = 50$pN. The figures show that as the fixed x increases, the peak in the distribution profile becomes sharper. This makes sense because a chain with large extension has less freedom to fluctuate in the transverse direction. 86

6.1 A fluctuating elastic filament (extensible wormlike chain) under distributed forces. The origin of the $x-y$ coordinate system is set at the head of the filament, which is hinged. The other end of the filament is constrained to move only in the x direction. One possible deformed configuration of the filament is shown in dashed line. 90
6.2 Comparison between the continuous models and the discrete model. (A) Force balance for an infinitesimal segment of a continuous rod. (B) Comparison of the results for a continuous rod (Black curve: Fourier series method and Eq. 6.15; Blue (almost overlaps with the black curve): method using force balance on infinitesimal segment and Eq. 6.20) and a discrete chain (red circles). The filament is under constant τ along the arc length so that Fourier series method can be applied. Here a 100nm chain is discretized into 1000 segments. The results match quite well. 99
6.3 Force-extension relations for a wormlike chain (1: red solid line) under uniform distributed load τ with thermal fluctuations, (2: red dashed line) under uniform distributed load τ without thermal fluctuations, (3: blue solid line) under end-to-end force $F = \tau L_0$ with thermal fluctuations, and (4: blue dashed line) under end-to-end force without thermal fluctuations. The reference contour length of the chain is $L_0 = 50$nm. The persistence length is 5nm. The segment length is 0.5nm with $N = 100$ segments. 100
6.4 Transverse fluctuation of a chain under uniform distributed $\tau = 5pN/nm$ (red), and under end-to-end applied force $F = \tau L_0$ (blue). Under distributed force, the chain has larger thermal fluctuations with an asymmetric fluctuation profile. 101

6.5 DNA in non-uniform microfluidic channels. (A) A piece of DNA confined in a linear channel and a constant-strain rate channel. Both channel types have been fabricated in experiments [15]. (B) The velocity in the non-uniform channel is inversely proportional to the channel width. Therefore, given the velocity v_f at the exit (rightmost) end, the entire velocity profile inside the channel is known, which then leads to the drag force $\tau = d_t v$ along the polymer. Here the end-to-end extension of the polymer is plotted against v_f. As we increase the flow velocity, the strain along polymer increases, resulting in a larger end-to-end extension. Red: DNA in a linear channel. Blue: DNA in a constant-strain-rate channel. Dashed/Solid lines: extension with/without the contribution of thermal fluctuations. (C) Transverse fluctuations along the polymer arc length. Red and blue for DNA in a linear and a constant-strain-rate channel respectively. Solid line is for a DNA with one end hinged and the other end free to fluctuate. Dashed line is for the same DNA with both ends hinged on the x aixs. 102
6.6 Transverse fluctuation of a chain under uniform distributed τ plus a point load F in the middle. The left half of the chain has less fluctuation because the stretching of the point loads reduces the thermal fluctuations. 102

7.1 Measurement of the fluctuations of the internal segments of confined DNA. (A) Image of a dye label (Alexa-546) on a DNA backbone (backbone not shown) with 80ms exposure time. (B) 2D surface plot of the raw image (intensity of the dye vs. the X Y coordinates). (C) Image of one T4 DNA fragment ($\sim$ 36 microns) with backbone (red) and internal labels (green). (D) Time series (8 seconds) of the DNA showing the fluctuations of backbone and internal labels. In (D), the red trace is the backbone and the green traces are the trajectories of internal dye labels. 107
7.2 Internal fluctuation of λ DNA confined in a 80nm$\times$130nm channel. (A) The measured rms fluctuation σ versus mean extension $\langle x \rangle$ for the internal segments of the DNA agrees very well with de Genne's theory with no fitting parameters (red curve, Eq.7.4). (B) A linear $\sigma^2 - \langle x \rangle$ profile confirms the 0.5 power law of $\sigma \sim \langle x \rangle^{1/2}$ of the de Gennes' theory. Note, however, that here we have maximum $\langle x \rangle \lesssim 10\mu$m. As shown in a subsequent figure (Fig.7.4) and in the text, for longer polymer with a maximum $\langle x \rangle \gtrsim 10\mu$m, the data deviates significantly from de Gennes' theory and even the 0.5 power law is lost. 108

7.3 Probability distributions $P(x)$ for 2 internal segments of λ DNA inside a 80nm×130nm channel. The experimental data is fitted to Eq.7.7 (red). The fitting value C (Eq.7.7), when plugged back to Eq.7.6-2, recovers de Gennes's formula Eq.7.4. 109
7.4 Fluctuation of the internal segments of (A) T4 DNA in 80nm×130nm, (B) T4 DNA in 60nm×100nm and (C) λ DNA in 50nm×70nm channels. For all cases, the maximum mean extension $\langle x \rangle > 10\mu$m. For (A) and (B), the data $\langle x \rangle \lesssim 10\mu$m agrees with de Gennes's theory (red, no fitting parameters). Deviation from de Gennes' theory begins at a critical $\langle x \rangle \sim 10\mu$m, above which the data falls into the black curve predicted by the deflection theories of Odijk [6], Wang and Gao [11]. For tighter channels (C), the transition occurs earlier with most data falling in the deflection regime. 111
7.5 Internal fluctuation σ versus mean extension $\langle x \rangle$ for BAC (red squares) and T4 DNA (black circles) in a 80nm×130nm channel. This figure shows that DNAs from two different sources give almost identical results, which suggests that agreement with de Gennes theory for short internal segments, and deviation from de Gennes' theory for long internal segments, are both sequence independent. 111
7.6 (A) Folded structures in the backbone of confined DNA. Each branch of the structure is about $150 - 250$nm, about the width of the channel size. The structures are separated by a distance $\sim 10\mu$m. (B, C) Distribution of extension $P(x)$ for 2 internal segments that contain the folded structures. In disagreement with de Gennes' prediction, the distributions show 2 peaks, from which we infer the existence of the folded structures. However, the structures are not stable as the two peaks in the distributions are comparable in height. The red curves fitted to the left peaks on the histogram are from de Gennes' theory (Eq.7.7) and the ones superimposed on the right peaks are from the deflection theory (Eq.7.10). (D) Extension x versus time for a single internal segment that shows two peaks in the distribution $P(x)$. The extension of this particular internal segment seems to fluctuate around two values shown by the dashed lines. This gives rise to the two peaks seen in the probability distribution. . . . 112

7.7 (A) Phase diagram showing two regimes on the $L - D$ plane, assuming $\xi_p = 50$nm for DNA. Transition from de Gennes' to Odijk's regime can occur when D decreases with L fixed, or when L increases with D fixed. (B) DNA with local folded structures as an intermediate state between de Gennes's and Odijk's regimes. In experiments, we observe heterogeneity in the intensity profile of YOYO-1 dye along the backbone of a confined DNA, which suggests the existence of the local folded structures (see Appendix). 114
7.8 Discrete wormlike chain model for confined DNA in a nanochannel. The confined wormlike chain, subjected to and end-to-end applied force in general, has bending energy represented by a spring of stiffness κ at each node. 115
7.9 Fluctuation versus mean extension of internal segments of the strongly confined DNA in 60nm channels (Eq.7.13 and Eq.7.14). The contour lengths of the DNA are (A) $L = 10\mu$m, (B) 5μm, (C) 1μm and (D) 250nm. For a long DNA (A and B), data from internal segments of various locations of the chain collapse on the a curve with 0.5 power law (light green). The result agrees with Eq.7.9 (blue), which is derived for the end-to-end fluctuation of a confined DNA. For short DNA however (C and D), no power law is found as data from various locations of the chain do not collapse onto a single curve (light green). Therefore, formulae derived for the end-to-end fluctuation of the confined DNA, such as Eq.7.9 (blue), cannot be used for internal fluctuation. The boundary effect is so significant that the rms fluctuation σ not only depends on $\langle x \rangle$, but also on the location of the internal segments. 116
7.10 Fluctuation as a function as the position of an internal segment for a short chain. The contour length of the entire chain is short (250nm), so that the fluctuation not only depends on the length of the internal segment, but also on its position. Here we plot the fluctuation versus position for internal segments with the same size: 50nm (red) and 10nm (blue). For the internal segments close to the boundaries, the fluctuation is larger because they have more freedom compared to the segments inside the chain. 117
7.11 Fluctuation of a 18μm long chain with persistence length $\xi_p = 50$nm confined in a 60nm×60nm channel. From bottom to top: (1) △: no nicks; (2) +: 10 nick in 18μm; (3) ◯: 50 nicks in 18μm; (4) ×: 100 nicks in 18μm; (5) □: 200 nicks in 18μm. This figure shows that when the density of nicks is lower than 50 nicks per 18μm, or 1 nick per kbp of DNA, the fluctuation profile is almost the same as that for a chain without nicks. . . 118

8.1 1D random walk of particles (blue) in the z-direction. In its natural condition, each particle has Ω_{tot} internal states ($\Omega_{\text{tot}} = 6$ in the figure). Some z-dependent spatial constraints reduce the number of accessible states at location z to $\Omega(z) \leq \Omega_{\text{tot}}$ (the blank boxes), creating an entropy varying landscape. Free energy is lower where there are more states to explore. An entropic force arises from this random walk model, driving the system towards regions with lower free energy. 127
8.2 Steady state distribution $P_{\text{steady}}(z)$ (y-axis on the left) on a free energy landscape $G(z) \propto \log(z)$ (y-axis on the right). The random walk domain is $z \in [1, 100]$, with $z = 1$ being a hard wall and $z = 100$ being an absorption wall. Eq. 8.5 predicts a linear steady state distribution (blue line), which is confirmed, without any fitting, by the Kinetic Monte Carlo simulation results (blue circles). The numbers in this figure are in SI units. 129
8.3 A DNA molecule is modelled as a 1D rod confined in a non-uniform channel. Typically, inside a nano-channel the DNA molecule can be subjected to stretching force f_{int}, drag force f_{drag} exerted by the surrounding fluid flow, entropic force f_{ent} due to the non-uniform confinement and also electrical force f_{ele} since the DNA is charged. The figure shows balance of force for an infinitesimal segment on the rod. 130
8.4 Drag coefficient per unit length as a function of the stretching force f_{int} at different channel widths D (calculated using Eq. 8.11, Eq. 8.12 and Eq. 8.14). 132
8.5 Stretch and force distributions along the arc length s of a stationary DNA in a uniform nanofluidic channel. The stretch distribution is non-linear: $(1 - \bar{\lambda}) \sim (-\bar{s})^{-1/2}$ while the force distribution is always linear with slope being $-5\bar{\mathcal{V}}/3$. 134

8.6 Entropically driven DNA crossing a sharp interface where the channel width changes suddenly. The channel shape is shown in (a). No fluid flow or electrical force is applied, so the DNA is driven only by the entropic force. The numbers in the circles represent snapshots of the molecule at different times. The process can be divided into two stages. Stage-(I): DNA moving across the interface at $z = z_*$ (① – ③). In this stage, a large force/strain gradient occurs at $z = z_*$ as is apparent in (b). This force/strain gradient is caused by the migration speed gradient as shown in the enlarged figure in (a) ($v_0 > v_l$, $v_0 > v_r$). The strain gradient travels along the DNA backbone until it completely enters into the wider region. Total extension of the DNA decreases in this stage as is apparent in (c). Stage-(II): DNA leaving the interface (③ – ④). In this stage, the force/strain gradient slowly relaxes as is apparent in (b). The total extension of the DNA stops decreasing, instead, it increases to reach an equilibrium value as is apparent in (c). 135

8.7 Movement of the right end of the DNA ($z(L, t)$ as a function of t) in channels with different η. No fluid flow or electrical force is applied, so the DNA is driven only by the entropic force. For a channel that changes its shape more rapidly (smaller $\eta = 0.01$, blue), the DNA moves faster because of larger entropic force. The initial condition is a stress free state. The boundary conditions are $f_{\text{int}} = 0$ at $s = 0$ and $s = L$. 136

8.8 Migration of a piece of DNA in different types of nanochannels. The polymer is driven purely by entropic forces ($\bar{\mathcal{V}} = 0$). (a) $\bar{z}$ at $\bar{s} = 0$ versus dimensionless time. (b) Total stretch $\Delta z/L = [z(L) - z(0)]/L$ versus dimensionless time. Different lines are for different channel shapes $D(z)$. Blue circles: linear channel with $D(z) = az + b$. Red triangles: $D(z) = (az + b)^{-1/2}$. Black squares: $D(z) = (az + b)^{-2}$. Cyan stars: $D(z) = (az + b)^{-1}$. Here a and b are different constants for different channel types. For comparison, a and b for each channel type are chosen so that the entrance/exit widths of the four channels are the same. 141

8.9 Motion and deformation of a piece of DNA in symmetric non-uniform channels without fluid flow or applied electric fields. (a–c): In the symmetric channel shown in (a), the initially stress-free polymer is pulled by a pair of entropic forces created by the channel. As a result, force and strain build up along the polymer backbone. In particular, large force gradient occurs at locations where the channel changes its shape most rapidly (b). The total extension of the polymer increases initially in response to the entropic pulling and then reaches equilibrium (c). (d–f): The symmetric channel shown in (d) creates a pair of entropic forces, which pushes the DNA inwards. In response, strain is developed along the polymer backbone (e). The total extension of the DNA decreases because of the pushing and then reaches equilibrium (f). 142
8.10 (a) A piece of DNA migrates along a non-uniform nano-channel with fluid flow $\bar{\mathcal{V}} > 0$. The numbers 1,2,3,4,5,6 represent snapshots in time. (b) Total stretch of the DNA increases as the polymer squeezes through the middle narrow region of the channel. (c) Two strain/stress gradients travel through the polymer backbone sequentially because there are two locations where the width of the channel varies rapidly. 143
8.11 Migration of three different pieces of DNA in a periodic channel as shown in (a) (width in the wide/narrow region is $D = 50$nm and $D = 25$nm respectively, only one DNA molecule is shown). No electrical force is applied. Fluid in the channel flows to the right $v_{\text{fluid}} > 0$. (b) z at $s = 0$ versus time. Blue: $L = 8\mu$m, $p = 50$nm. Red: $L = 3\mu$m, $p = 50$nm. Black: $L = 8\mu$m, $p = 100$nm. At $t = 5s$, the long DNA (blue) and the short DNA (red) have been separated by 6.6 microns. 143
8.12 Transition between Odijk's and de Gennes' regimes. The two curves on the $f - D$ plane correspond to errors $e = 3\%$ (black), and 5% (blue) respectively. Region to the left of the curves is with less error. For the region with $e < 3\%$, we claim the polymer is in Odijk's regime. On the other hand, for the region with $e > 5\%$, the polymer is more likely to be in de Gennes' regime. We define 3%–5% as an uncertain zone, where transition between the two regimes occurs. The transition channel width is shown to increase with the increase of force. 144

9.1 Illustration of the primary plant cell wall, which is a network consisting of various filaments with very different mechanical properties. The cellulose microfibrils are thick and provide tensile strength for the cell walls while the polysaccharide pectins, much smaller in the cross section dimensions, fill the spaces between the cellulose microfibrils and provide resistance to compression [18]. 152
9.2 A triangular network made up of 3 wormlike chains. 153
9.3 Expansion of a triangular network made up of 3 wormlike chains. There is a phase transition at $\bar{p} = 3$. 155
9.4 Illustration of a discrete fluctuating filament network. 155
9.5 Configuration of a hinged-hinged buckled rod. The rod is under uniaxial compression. If we start with a perfectly straight rod, the computational scheme always leads to a straight configuration, which is unstable when the compressive force is large. With initial perturbation, however, we obtain the correct post-buckling configurations, as shown in the figure. 158
9.6 Buckling of a hinged-hinged rod. (A) Tangent angle at $s = 0$, (B) Deflection at the middle of the rod, and (C) $\Delta x = L - x(L)$ as a function of the compressive force. Blue: exact solution. Red: Computational results. 158
9.7 Extension a hinged-hinged rod. Blue dashed line: without thermal fluctuation. Blue circles: with thermal fluctuation. Red: analytic solution. 160
9.8 Compression of a hinged-hinged rod. Dashed line: without thermal fluctuation. Solid line: with thermal fluctuation. Small perturbations are applied to the initial configuration of the rod. 160
9.9 Influence of the initial imperfection. When the imperfection is small, the path is closer to the singularity and a large peak shows in the force-extension curve. When there is no imperfection, the curve will go to infinitely. When the imperfection is large, the path is further away from the singularity and the curve transition smoothly to the post-buckling regime. (B) is the enlarged figure of (A) around the peak. Blue: 0.1°. Red: 0.5°. Black: 1.0°. Green: 2.0°. Cyan: 3.0°. 161

9.10 Influence of the material properties on the compression behavior. (A) Force-extension curve for different bending modulus K_b. Increasing the bending modulus shift the peak to the right and decreases the intensity of the peak. Blue: $K_b = 150k_BT \cdot nm$. Red: $K_b = 250k_BT \cdot nm$. Black: $K_b = 350k_BT \cdot nm$. Green: $K_b = 450k_BT \cdot nm$. Cyan: $K_b = 550k_BT \cdot nm$. (B) Force-extension curve for different stretching modulus K_s. Increasing the bending modulus shift the peak to the left. Blue: $K_s = 2.0k_BT/nm$. Red: $K_b = 4.0k_BT/nm$. Black: $K_b = 1000k_BT \cdot nm$. The force-extension behavior of a single filament is more sensitive to a change in the bending modulus than a change in the stretching modulus. 162
9.11 Influence of the boundary conditions on the compression behavior. Rotational springs are added to the two ends of the rod. When the stiffness of the spring becomes infinity, the rod is under clamped-clamped conditions. Black: $K_\theta = 0.0k_BT$. Red: $K_\theta = 10.0k_BT$. Black: $K_\theta = 1000.0k_BT$. The clamped-clamped rod buckles at $F = 4$pN, as expected. 162
9.12 (A) Hydrostatic edge tension on a filament ring with $n = 6$ interior filaments. (B) If we assume linear elasticity and do not consider thermal fluctuations, the network always becomes softer at larger hydrostatic tension. 164
9.13 (A) Plot of Eq. 9.35. The size of the network versus the dimensionless hydrostatic tension $\bar{p} = \beta\pi\xi_p Lp/n$. (B) Plot of Eq. 9.38. The dimensionless bulk modulus is defined as $K_{\text{bulk}} \cdot (8\pi\xi_p L/(k_BTn))$. 166
9.14 Expansion of two hexagons under hydrostatic tension. Each filament is 20nm long. Their persistence length is 10nm. (A) Stretching modulus is $10k_BT/nm$. Black: undeformed configuration. Red: deformed configuration under $p = 0.5$pN/nm. Green: deformed configuration under $p = 1.0$pN/nm. Blue: deformed configuration under $p = 1.5$pN/nm. (B) Stretching modulus is $100.0k_BT/nm$. Black: undeformed configuration. Red: deformed configuration under $p = 0.5$pN/nm. Green: deformed configuration under $p = 2.5$pN/nm. Blue: deformed configuration under $p = 5$pN/nm. 166

9.15 Expansion of a hexagon under hydrostatic tension p. Each filament in the hexagon is 20nm long. Dashed lines are the results without taking thermal fluctuations into account. Solid lines are the results with thermal fluctuations. Circles are the analytic solutions of Eq. 9.32. (A) Persistence length $\xi_p = 10$nm, stretching modulus $K_s = 10k_BT/nm$. The results with thermal fluctuations shows strain stiffening, i.e, the bulk modulus increases during the expansion process. The bulk modulus changes from $K_{\text{bulk}} = 0.07$pN/nm (fitting from $p = 0$ to 0.06pN/nm) to $K_{\text{bulk}} = 1.29$pN/nm (fitting from $p = 0.3$ to 0.6pN/nm). (B) $\xi_p = 5$nm, $K_s = 10k_BT/nm$ (red). Changing the bending modulus does not change the static solution. But, the results with thermal fluctuation changes a lot. In particular, the initial bulk modulus is $K_{\text{bulk}} = 0.02$pN/nm (fitting from $p = 0$ to 0.06pN/nm). For $p = 0.3$ to 0.8pN/nm, the bulk modulus is $K_{\text{bulk}} = 1.18$pN/nm. The results in plot A are superimposed as blue lines and circles. (C) $\xi_p = 10$nm, $K_s = 100k_BT/nm$ (red). Changing the stretching modulus (compared to A) affects both the static and thermo-mechanical solutions. The fittings for K_{bulk} are for the intervals $p = 0$ to 0.06pN/nm and $p = 0.4$ to 0.8pN/nm respectively. The results in plot A are superimposed as blue lines and circles. (D) $\xi_p = 10$nm, $K_s = 100k_BT/nm$ (red). The fittings are for the intervals $p = 0$ to 0.05pN/nm and $p = 0.15$ to 0.3pN/nm respectively. The results in plot A are superimposed as blue lines and circles. 167

9.16 (A)-(C): Three different hexagonal structures. The structures shown in (B) and (C) are obtained by removing and adding filaments from/into (A). (D): Expansion behaviors of the three structures shown in A-C are shown in red, blue and black, respectively. Thermal fluctuation is significantly reduced for network (C). 169

9.17 Scaling law of stretching the thermal fluctuations. An equilateral triangle whose initial length for the sides is $L = 20$nm is under hydrostatic tension p. The persistence length of the filaments is $\xi_p = 10$nm. Δr, as defined in Eq. 9.39, characterizes the size difference between the static solution and the thermal solution. The fitting result suggests $\Delta r \sim p^{-1}$. Thermal fluctuation is stretched out faster than the -0.5 power law. 170

9.18 Principal stretch during an expansion process. Denote the principal stretches as λ_1 and λ_2, then the stretch associate with expansion and with shear are respectively $\lambda_{\text{ex}} = \sqrt{\lambda_1\lambda_2}$, $\lambda_{\text{sh}} = \sqrt{\lambda_1/\lambda_2}$. For the expansion of a hexagon, λ_{ex} versus the the hydrostatic tension is plotted in blue, while λ_{sh} versus p is plotted in red. 171

9.19 Expansion of two hexagons. (A) λ_{ex} (blue) and λ_{sh} (red) versus hydrostatic tension p. (B) Average area versus p. Solid line: hexagon whose filaments have persistence length $\xi_p = 10$nm. Dashed line: hexagon whose filaments have persistence length $\xi_p = 20$nm. The behavior of the two networks is different at low p, because bending dominates at this regime. 172
9.20 Analytic static solutions for simple shear on a hexagon. Two components, F_{12} (blue) and F_{22} (red) of the deformation gradient $\mathbf{F}$ is plotted as a function of the applied shear stress τ. Dashed lines are the asymptotic behavior at small τ. Dimensionless shear stress is defined as $\bar{\tau} = \tau l_0/2K_s$, with l_0 and K_s being the contour length and stretching modulus of the filaments. 173
9.21 (A) Illustration of shear on a single hexagon. Uniform distributed forces in $\pm x$ direction are applied on the top and bottom filaments of hexagon to cause the shear deformation. Some filaments that are under compression will buckle during the shear deformation. Each filament is 20nm long. Their persistence length is 10nm. Stretching modulus is $10k_BT/nm$. (B) Reference configuration with initial perturbation. (C-E) Deformed configurations with buckled filaments. 175
9.22 When buckling occurs, the hexagon undergoes significant deformation for even a small increases in the shear stress (compared to B $\rightarrow$ C in Fig. 9.21). Black: $\tau = 40$fN/nm. Blue: $\tau = 45$fN/nm. Red: $\tau = 50$fN/nm. The deformation shown here is significant compared the the deformation before buckling at $\tau < 40$fN/nm (Fig. 9.21). 176
9.23 Shear on a hexagon with small stretching modulus $K_s = 1k_BT/nm$. Unlike the deformation shown in Fig. 9.21, the hexagon can achieve large shear deformation without buckling when the stretching modulus is small. Filaments in many cellular networks have large stretching modulus. They achieve large deformation by stretching out thermal fluctuations. 176

9.24 X direction separation of the top and bottom filaments. Δx is the distance between node 1 and node 2 shown in Eq. 9.21A. This quantity is plotted as a function of the shear stress τ. Effective stiffness is defined as $k = \tau/\Delta x$ here. Dashed line is the result without thermal fluctuation. The hexagon is much softer after buckling if thermal fluctuation is not taken into account. Solid line is the result with thermal fluctuations. The hexagon becomes stiffer after buckling when thermal fluctuation is taken into account. Circles are the results from the analytic static solutions assuming affine deformation (Eq. 9.50). They match with our computational results at small τ. For large τ, buckling occurs and the deformation of the hexagon is non-affine. (A) and (B) are for different persistence length ξ_p = 10nm and $\xi_p = 5$nm respectively. 177
9.25 Average separation between the top and bottom filaments as a function of the shear stress. (A) and (B) are the results without and with thermal fluctuations respectively. The results show that the hexagon contracts in the direction perpendicular to the shear direction. At small shear stress, the deformation is affine. The static solution (shown in A) roughly agrees with Eq. 9.50 (shown in circles). The difference is caused by the perturbations on the initial configuration. For the result with thermal fluctuations (shown B), a fitting to the solution shows that the separation decreases quadratically. 178
9.26 Shear strain γ as a function of the shear stress τ. Effective shear modulus can be defined as $G = \tau/\gamma$. Dashed line: static solution. Solid line: result including the thermal effects. The strain and stress relation is linear before and after buckling at $\tau \approx 40$fN/nm. For the static solution, the shear modulus decreases significantly after buckling. For the result that includes the thermal fluctuation, shear modulus does not change a lot before and after buckling. The reason is that before buckling, the shear modulus is much less than that of the static solution because of the fluctuations. Figure A and B are for $\xi_p = 10$nm.and 5nm respectively. Contour length of the filaments is $L = 20$nm. Stretching modulus is $K_s = 10k_BT/nm$. 179
9.27 Affine, non-affine deformation during shear on a hexagon. . . . 180
9.28 (A) λ_{ex} and λ_{sh} as a function of the shear stress τ. (B) Eigen-direction (direction of $\vec{e}_1^0$) as a function of the shear stress. The other eigen-direction $\vec{e}_2^0$ is perpendicular to $\vec{e}_1^0$. 180

9.29 Analytic static solutions for uniaxial tension on a hexagon. Two components, F_{11} (blue) and F_{22} (red) of the deformation gradient $\mathbf{F}$ are plotted as functions of the applied tensile stress q. Dashed lines are the asymptotic behavior at small q. Dimensionless tensile stress is defined as $\bar{q} = 3ql_0/K_S$, with l_0 and K_s being the contour length and stretching modulus of the filaments. 182
9.30 (A) Uniaxial tension on a hexagon. Each filament is 20nm long. Their persistence length is 10nm. Stretching modulus is $10k_BT/nm$. (B-E) Deformed configurations with buckling of the diagonal filaments. 183
9.31 Uniaxial tension on a hexagon with smaller stretching modulus $K_s = 1.0k_BT/nm$. Unlike the hexagon shown in Fig. 9.30, where $K_s = 10k_BT/nm$, the hexagon here can undergoes large deformation without buckling. 184
9.32 Width of the hexagon (Δx) is defined as the average x direction separation between the left and right filaments. Height (Δy) is defined as the average y direction separation between the top and bottom filaments. This figure shows Δx (blue) and Δy (red) as functions of the tension q with (solid lines) and without (dashed) thermal fluctuations. Solid lines are always below the dashed lines because of thermal fluctuation. Interestingly, height of the hexagon increases in the initial state of the tensile pulling. 184
9.33 Pure tension on a hexagon. (A) and (B): $\xi_p = 10$nm, $K_s = 10k_BT/nm$. (C) and (D) $\xi_p = 10$nm, $K_s = 1k_BT/nm$. (A) and (C): stretch λ_x (blue) and λ_y (red) during the uniaxial pulling. Initial Young's moduli are $E_{\mathrm{A,static}} = 0.31$pN/nm, $E_{\mathrm{A,thermal}} = 0.07$pN/nm, $E_{\mathrm{C,static}} = 0.14$pN/nm and $E_{\mathrm{C,thermal}} = 0.07$pN/nm. (B) and (D): Poisson's ratio as a function of the tensile stress q. Solid lines are the results with thermal fluctuations. Dashed lines are the results without thermal fluctuations. 185
9.34 λ_{ex} and λ_{sh} as functions of the pulling stress q. At $q = 0$, λ_{ex} is less than 1 because of thermal fluctuations. 185
9.35 (A) Expansion of four networks: two hexagons and two squares, with or without the interior filaments removed. (B) Expansion of the two hexagonal networks. (C) Expansion of two square networks. Red: without the interior filaments. Blue: with the interior filaments. Dashed line: static results. Solid line: with thermal fluctuations. 186

J.1 σ versus $\langle x \rangle$ profile for the $\langle x \rangle \leq 10\mu$m region. Fluctuation of short internal DNA segments from different sources matches with de Gennes' theory with NO fitting parameters. 209

K.1 (A) The backbone intensity images of a confined DNA fragment ($\sim$34μm) stained with YOYO-1 iodide in a 80nm$\times$130nm channel. The images are recorded at time interval of 1.6s. From the heterogeneity of the intensity profile, we infer that there exist some local structures on the backbone. (B) Images of the time series (8 seconds) of a T4 DNA fragment ($\sim$32μm). The backbone of the DNA is shown in red and the internal dyes are shown in green. The region with high fluorescence density is the area with local folded structures. The green traces are the trajectories of internal dye labels in the time series. This image shows two internal dyes coming together, which is evidence of formation of local folded structures. 211

L.1 Mean end-to-end extension $\langle x \rangle$ versus contour length L of confined DNA in a 60nm$\times$100nm channel. The fitting result is $x = 0.5L$, which is consistent with the prediction of the Odijk deflection theory: $x = 0.7L$. 213

O.1 Given θ, we find the l that minimizes the energy of the confined chain. 217

Chapter 1

Introduction

Key concepts of this chapter:

1. Cells use filaments and filamentous networks as the basis of their structures. The mechanics and energetics of these one dimensional 'biological beams' and their networks play a role in regulating a cell's activities.

2. In the world of nanoscale mechanics, entropy, or thermal fluctuation, plays a role as important as the elastic energy.

3. The freely-jointed chain model is the simplest model for a biopolymer. The entropic nature of this model leads to the prediction that a polymer behaves like a spring in the limit of small force, with a temperature dependent spring constant.

4. The wormlike chain model is the most widely used model for a biopolymer. It considers both the elastic energy and the entropy of the system and predicts that the shrinking of a chain under tension F scales as $F^{-1/2}$ in the limit of large force.

5. The fact that thermal fluctuation scales linearly with the temperature and inversely with the effective stiffness of the system is a rather universal law.

6. This thesis develops theoretical methods to efficiently evaluate the statistical mechanical properties of rod-like filaments and filamentous networks. In particular, the theory can be applied to study heterogeneous filaments and networks under various boundary and loading conditions.

Beams as structural elements have been used by human beings for thousands of years. But the fact that nature, or our own bodies, has put these one-dimensional elements to similar architectural uses was not appreciated until recent decades. It is now widely acknowledged that cells not only make use of various rod-like filaments as the basis of their structures, but also use them smartly and efficiently. Well-known examples of rod-like macromolecules and structures in our bodies include the three different types of filaments that make up the cytoskeleton networks, such as actin filaments, intermediate filaments and microtubules, the slender protrusions of hair cells, known as stereocilia that vibrate in response to sound, and also the DNA molecules, whose backbones are double helices that can be further folded to adopt supercoiled configurations, etc. All being one-dimensional objects though, these macromolecules and structures differ a lot in their sizes and mechanical properties. They are so designed to meet specific needs and perform different functions inside cells. For example, an intermediate filament has a diameter around 10nm while a DNA molecule is about 2.5nm wide. Correspondingly, the former is stiff and has a function of supporting mechanical stress in cells, while the latter is relatively flexible and can be highly coiled up and packed into confined spaces when needed.

The mechanics and energetics of these 'biological beams' have been of great interest to many researchers because to some extent, they determine and regulate the functions of the cells. For example, the activity of a gene regulated by the lac repressor is found to depend periodically on the distance between the operator sites [3]. Here the key element in the modulation of the activity of the gene is the twisting and bending deformations of the DNA that is looped between the operator sites. Similarly, an enhancer's (a binding site for an activator protein) activity depends periodically on its distance away from the promoter [1]. Such periodicity occurs because a nonideal binding site can result in unfavorably large twisting energy in the DNA molecule and finally leads to differences in gene expression. Lately, scientists have even begun to make use of the mechanics of the rod-like filaments to develop new tools for molecule detection. For instance, the change in the bending energy of a molecular beacon caused by binding has been used for mRNA detection [4].

Important as the mechanical aspect is, it does not completely describe the behavior of rod-like filaments inside cells. In the world of molecular biology, the relevant units are piconewtons and nanometers, which combine to give the relevant energy scale as $\sim$ 1pN-nm. This is comparable to the typical value of thermal energy $k_BT \approx 4.1$pN-nm at room temperature. Therefore, unlike beams that statically support loads on a building, the rod-like filaments inside cells are under erratic and constant Brownian motion. Therefore, entropy plays a significant role in their mechanics and can not be neglected compared to the elastic bending and twisting energies.

In fact, the simplest model that captures the relation between force and extension for a single rod-like polymer is based on a purely entropic interpretation of the free energy, neglecting all the elastic energy terms. This is the

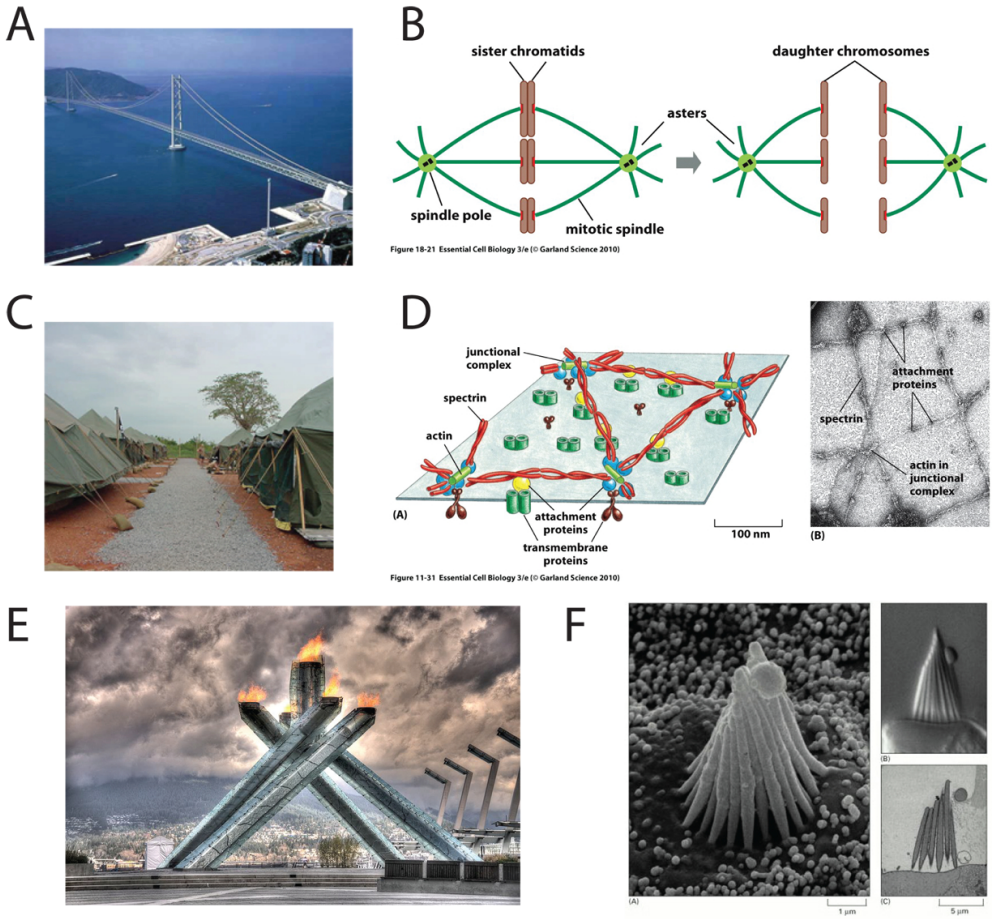

Figure 1.1: Beam structures made by human beings and by nature. (A) The Akashi-Kaikyō Bridge, located in Japan and spanning 1,991 metres, is the world's longest suspension bridge (Figure comes from http://blogger.sanook.com/confuse/2008/11/23/). (B) In a cell division cycle, the mitotic spindels, composed by microtubules and various other proteins, are used as 'cables' to pull the daughter chromosomes apart. (Figure comes from reference [1].) (C) Man-made tent is usually supported by a frame of poles. (Figure comes from Wikipedia: *Tent*.) (D) A spectrin meshwork under the human red blood cells. Cell membrane is thin and fragile. So most of them are strengthened and supported by a network of protein filamenets. This filamentous network, like the frame in the man-made tent, determines the shape of the membrane. (Figure comes from reference [1].) (E) The 2010 Vancouver Olympic cauldron. (Figure comes from Wikipedia: *Olympic Flame*. (F) Structure of the stereocilia projecting from a hair cell in the inner ear (Figure comes from [2]).

so-called freely-jointed chain model, or random walk model because each configuration of a chain in this model is essentially a random walk in the space. In this model, one imagines a polymer as a chain of N inextensible monomeric segments without interactions between each other. Elastic energy E is zero for all the configurations and therefore the free energy $G = E - TS$ is purely determined by the entropy S. Since the number of configurations and thus the entropy decreases with the increase of polymer end-to-end distance, larger extension leads to a higher value of free energy. Hence, the principle of minimum free energy implies that the polymer favors highly convoluted configurations where a large number of conformations are available. In other words, one needs to exert tensile force to extend the polymer even without stretching it beyond its contour length. The force extension relation in this model (in 3D space) is [5, 6]:

$$\frac{\langle x \rangle}{L} = \coth\left(\frac{Fl}{k_B T}\right) - \frac{k_B T}{Fl} = \mathcal{L}\left(\frac{Fl}{k_B T}\right), \tag{1.1}$$

where $\langle x \rangle$ is the average extension of the chain in the direction along which an end-to-end tensile force F is applied, L is the contour length of the chain and l is the length of a single monomeric segment. The function $\mathcal{L}(x) = \coth(x) - 1/x$ is called the Langevin function, named after the prominent French physicist Paul Langevin who developed Langevin dynamics for molecular systems. This function is most commonly known to occur in the expressions for the paramagnetic susceptibility of a collection of classical (non-quantum-mechanical) magnetic dipoles, and for the polarizability of a molecule having a permanent electric dipole moment [7].

In the small-force limit ($Fl << k_B T$), the Langevin function reduces to a linear relation, suggesting an effective spring constant for the polymer $k_{\text{eff}} = 3k_B T/(Ll)$:

$$F = \frac{Dk_B T}{Ll}\langle x \rangle. \tag{1.2}$$

Here $D = 3$ is the dimension of space. The fact that the spring constant is proportional to the temperature reveals the entropic nature of the model: the higher the temperature, the more significant the entropic effect is. Thus one needs a larger force to extend the chain. In the limit of large force, the Langevin function saturates at $\langle x \rangle \to 1$, which makes sense because the model assumes that the chain is inextensible.

The freely-jointed chain model takes the entropy of the system into account and reveals an entropic force that is proportional to the temperature. But it totally neglects the elastic energy of the chain. This simplification will overestimate the stiffness of the polymer because a chain with elastic energies does not like to be highly coiled up, and so it is relatively easier to pull it straight. Elastic energies of a chain usually include the stretching energy, the bending energy, the twisting energy as well as twist-stretch coupling energy [6]:

$$E = E_{\text{stretch}} + E_{\text{bend}} + E_{\text{twist}} + E_{\text{stretch-twist}}. \tag{1.3}$$

In some cases, Eq. 1.3 can be simplified. For example, for polymers that consist of monomers joined by single chemical bonds, the twisting energy is usually negligible because the monomers can rotate freely around the bonds [6]. Also, many polymers cannot sustain large stretching deformation before undergoing phase transitions. In these cases, one can neglect the twisting and stretching terms in Eq. 1.3. This leads to the so-called wormlike chain model, or the Kratky-Porod model, whose elastic energy consists of only the bending term:

$$E = E_{\text{bend}} = \frac{K_b}{2} \int_0^L \left| \frac{d\hat{t}}{ds} \right|^2 ds. \tag{1.4}$$

Here K_b is the bending modulus of the polymer and $\hat{t}(s)$ is the tangent vector along the arc length s.

Using a fixed temperature and fixed force ensemble, the partition function for the wormlike chain model is:

$$Z = \int \exp\left\{ -\frac{E\left[\hat{t}(s)\right] - Fx[\hat{t}(s)]}{k_B T} \right\} \mathcal{D}\hat{t}(s), \tag{1.5}$$

where $\mathcal{D}$ denotes a path integral that sums over all the possible configurations of the chain.

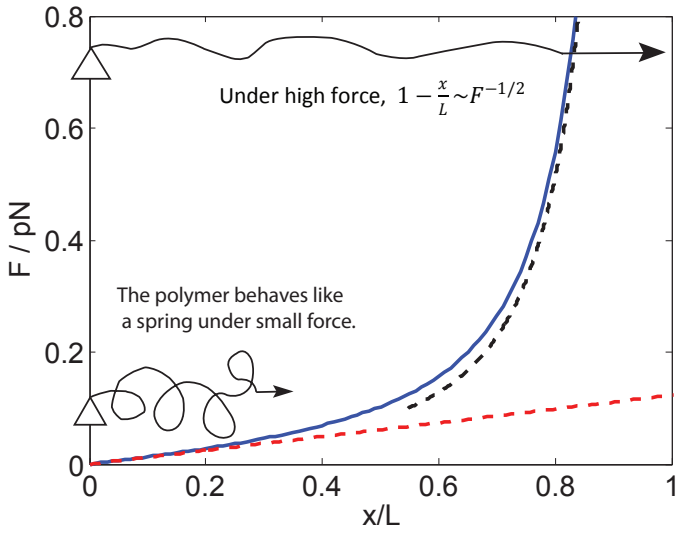

Figure 1.2: Force-extension relation for a wormlike chain. In the small force limit (red dashed line, Eq. 1.10), the polymer behaves like a spring with a temperature dependent spring constant. In the high force limit (black dashed line, Eq. 1.14), the model predicts that $1 - x/L \sim F^{-1/2}$. These two limits can be combined to construct an approximate formula for all forces (blue line, Eq. 1.15).

In the limit of small force, one can expand the $\exp(Fx/k_BT)$ term in Eq. 1.5

and obtain [5]:

$$Z = Z_0 \left[1 + \frac{1}{2} (\beta F)^2 \langle x^2 \rangle_0 + \frac{1}{24} (\beta F)^4 \langle x^4 \rangle_0 + \cdots \right], \tag{1.6}$$

where $\beta = 1/k_B T$, Z_0 is the partition function at zero force, and $\langle \cdots \rangle_0$ denotes the average evaluated in the zero force ensemble. Eq. 1.6 implies that the behavior of a polymer under a finite applied force is closely related to and completely determined by its behavior under zero force. However, the quantities $\langle x^{2n} \rangle_0$ are in general difficult to evaluate except when $n = 1$. Fortunately, this term alone is enough to give us the leading order approximation of the force-extension relation under small force. By using basic statistical mechanics, the partition function Eq. 1.6 leads to:

$$\langle x \rangle = \frac{\langle x^2 \rangle_0}{k_B T} F. \tag{1.7}$$

Hence, at small force, the polymer again behaves like a spring (Fig. 1.2), with the effective spring constant given by:

$$k_{\text{eff}} = \frac{k_B T}{\langle x^2 \rangle_0}. \tag{1.8}$$

It is worth pointing out that to derive Eq. 1.8, we do not need to use any particular form of the elastic energies. In other words, Eq. 1.8 holds for the freely-jointed chain model, the wormlike chain model, and even models that consider more complicated forms of the elastic energies. In fact, for the 3D freely-joined chain model, it is easy to see that $\langle x^2 \rangle_0 = Ll/3$ [5]. Plugging this into Eq. 1.8, we recover exactly the effective spring constant in Eq. 1.2. For the wormlike chain model, $\langle x^2 \rangle_0$ can be shown to depend on the so-called persistence length $\xi_p = \beta K_b$ of the polymer by [5]:

$$\langle x^2 \rangle_0 = \frac{2}{3} \xi_p L. \tag{1.9}$$

This relation is valid in the limit $L >> \xi_p$. The force extension relatioin Eq. 1.7 can now be rewritten as:

$$\langle x \rangle = \frac{2\xi_p L}{3 k_B T} F = \frac{2 K_b L}{3 (k_B T)^2} F. \tag{1.10}$$

It is interesting that unlike the freely-jointed chain model, the effective spring constant scales as $k_{\text{eff}} \sim T^2$ in the wormlike chain model.

The above analysis is for the wormlike chain in the small force limit. Before going to the large force limit, we note that Eq. 1.8 is a rather universal expression for the thermal fluctuation of a spring-like system. In fact, the fluctuation in any quadratic energy well can be expressed as:

$$\langle x^2 \rangle = \frac{\int x^2 \exp\left(-\frac{1}{2} \beta \, k_{\text{eff}} \, x^2\right) dx}{\int \exp\left(-\frac{1}{2} \beta \, k_{\text{eff}} \, x^2\right) dx} = \frac{k_B T}{k_{\text{eff}}}. \tag{1.11}$$

In other words, fluctuation in a quadratic energy well always scales linearly with the temperature and inversely with the effective stiffness of the well. This is true when k_{eff} is independent of T. As we shall show in details in later chapters, for a multidimensional quadratic well characterized by a stiffness matrix $\mathbf{M}$, the fluctuation is:

$$\langle x_i x_j \rangle = k_B T \left(\mathbf{M}^{-1}\right)_{ij}, \tag{1.12}$$

which is a natural generalization of Eq. 1.11. In fact, the idea that thermal fluctuation scales linearly with temperature T and inversely with the susceptibility of the system is believed to be so universal that it not only is used in equilibrium systems, but has been applied to define the effective temperature for systems that are far away from equilibrium [8].

Coming back to the wormlike chain model, in the limit of large force, the chain is approximately straight and the components of the tangent vector in a cartesian coordinate system can be approximated by:

$$\hat{t} = \left[t_x,\ t_y,\ 1 - \frac{1}{2}\left(t_x^2 + t_y^2\right) \right], \tag{1.13}$$

in which the x and y axes are perpendicular to the direction of the applied force. By introducing the Fourier series for $t_x(s)$ and $t_y(s)$ and then using the equipartition theorem, one can obtain the force extension relation for large force [5]:

$$\langle x \rangle = L \left[1 - \frac{1}{2\sqrt{\beta F \xi_p}} \right]. \tag{1.14}$$

Eq. 1.14 implies that in the large force limit, the shrinking of the chain scales as $1 - \langle x \rangle / L \sim F^{-1/2}$, which is an important prediction of the wormlike chain model (Fig. 1.2).

The force extension relation in the two limits analyzed above (Eq. 1.10 and Eq. 1.14) can be combined to construct an approximate formula for all forces [5, 9]:

$$\frac{F\xi_p}{k_B T} \approx \frac{\langle x \rangle}{L} + \frac{1}{4\left(1 - \langle x \rangle / L\right)^2} - \frac{1}{4}, \tag{1.15}$$

which is the famous interpolation formula for a wormlike chain (see Fig. 1.2) and has been used widely for fitting experimental data [10]. However, it has up to 6% error when compared to the exact solution in an intermediate-force regime [9].

Models that consider more elastic energy terms can also be found in the literature and are not discussed here [11]. Instead, we address another simplification made in both the two classical models discussed above – homogeneous mechanical properties of the filaments. In the freely-jointed chain model, the segment lengths of all the monomers are assumed to be the same. But we know that the effective stiffness of the chain depends inversely on the segment

length (Eq. 1.2), so we have implicitly assumed homogeneous mechanical properties along the polymer. Similarly, in the wormlike chain model, the bending modulus K_b is assumed to be independent of the arc length s. For the freely-jointed chain model, the simplification is made for the sake of simplicity. A random walk with variable step sizes is more difficult to analyze but the result is still the same [6]. For the wormlike chain model, however, the simplification is vital for the classical theory that takes advantage of the special properties of the Fourier-transformed functions. In other words, the classical method for analyzing the wormlike chain cannot be generalized for a heterogeneous chain whose bending modulus depends on the arc length s. Such a simplification made the classical models not applicable to many biopolymers of interest to the researchers. Partially unfolded protein oligomers in atomic force microscopy (AFM) experiments, for example, are long polymer chains consisting of both folded and unfolded proteins. Their force-extension curves have been measured by many groups to obtain valuable information about the stability and kinetics of various proteins [12, 13, 14]. However, it is not suitable to use a homogeneous wormlike chain model to describe the entire oligomer because the folded and unfolded proteins are expected to have different mechanical properties – the unfoled proteins should be floppier since their stability is expected to be reduced by the breaking of several internal chemical bonds. Heterogeneity is even more important when one extends the theories to study the biological filamentous networks. For example, the primary plant cell walls are networks of various filaments with very different mechanical properties performing diverse functions: the cellulose microfibrils are thick and provide tensile strength for the cell walls while the polysaccharide pectins, much smaller in the cross section dimensions, fill the spaces between the cellulose microfibrils and provide resistance to compression [1]. To analyze such heterogeneous filaments and networks, one needs more general theories without the assumption of homogeneity.

Moreover, the classical method for analyzing the wormlike chain has other limitations preventing it from being generalized for other situations. For example, it fails if there is a distributed load acting along the chain. But distributed loads are rather common for biological filaments, from charged DNA molecules under electric fields to actin filaments loaded by molecular motors on different locations. Also, the classical method does not tell us anything about the internal fluctuations of the filaments, which, as we shall discuss in later chapters, are important for mapping genomes in nanochannels.

Finally, when the classical force-extension relation is derived, little attention is paid to the boundary condition effects. For the wormlike chain model, we have implicitly assumed that the two ends of the chain are subjected to zero moments and zero forces in the transverse direction. With the rapid development of single-molecule techniques, however, scientists are now able to manipulate the biological filaments by different instruments like the atomic force microscopy, optical tweezers and magnetic tweezers, etc (Fig. 1.3). These instruments apply different boundary conditions on the macromolecules and

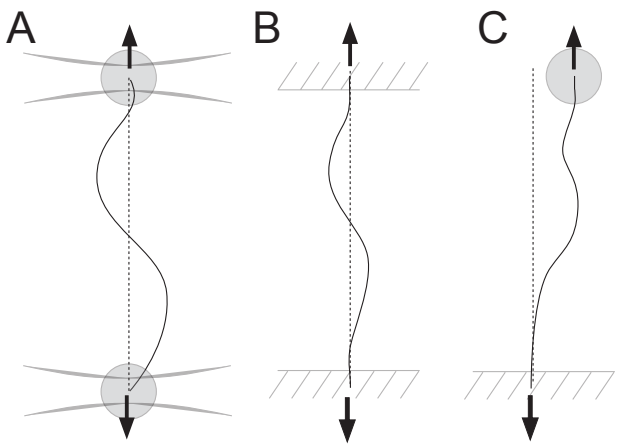

Figure 1.3: Set-ups for measuring the force *vs.* extension behavior of macromolecules (Figure comes from reference [16]). (A) Hinged-hinged condition. Both ends are attached to beads which are held in optical traps that can exert forces but not moments. Hence the curvatures at the ends are constrained but not the slopes. The trap does not allow transverse displacements. (B) Clamped-clamped condition. The slopes and transverse displacements are constrained at both ends. (C) Partially clamped condition. One end of the macromolecule is secured to a cover-slip while the other end is attached to a bead in a magnetic or optical trap which ensures that the slope is held constant, but transverse displacements are allowed.

analysis of the experimental results requires detailed theory that addresses the boundary effects more carefully [16]. In fact, several groups have pointed out that boundary conditions can have significant influence on the thermomechanical behavior of a short filament whose contour length is comparable to or smaller than its persistence length [15, 16, 17].

This thesis proposal is made up of three major parts:

1. In Part I, we generalize the freely-jointed chain model for a heterogeneous chain with various Kuhn lengths along the polymer. The heterogeneous model is then applied to study the forced unfolding of a protein oligomer, which contains both folded and unfolded proteins and hence is expected to be heterogeneous in its mechanical properties. Bell's model [18] is added to analyze the kinetics of the problem and to predict the unfolding events observed in experiments. By considering a third equation which takes into account the loading conditions, we are able to reproduce the force-extension profiles under various loading modes. The advantage of using the freely-jointed chain model is that most of our results are simple and analytic. This enables us to consider some other issues that are hard to tackle when the model becomes complicated. In fact, unlike most of the analyses in the literature, we do not assume the protein refolding rate to vanish. Protein folding rate is much larger than the unfolding

rate when the unfolding force is small. Therefore, to model the behavior of forced unfolding of proteins under general loading modes, one must keep the protein folding rate in the analysis. To support this argument, we shall show the consequences of neglecting the refolding rate in the model.

2. In Part II, we discuss the heterogeneous wormlike chain model. General properties of a wormlike chain that hold for any type of boundary condition and heterogeneity are derived. Distributions of the end-to-end extension and the transverse displacement of the chain are evaluated. Further, we use the multidimensional Gaussian integral to obtain the partition function for a heterogeneous wormlike chain. Fluctuations and other thermo-mechanical properties are also calculated and compared to Monte Carlo simulation results. Boundary conditions are treated carefully and they are shown to have significant effects for short chains. Lastly, the theory is extended to study a wormlike chain under distributed forces and spatial confinement. We analyze the internal fluctuations of a piece of DNA in a nanochannel and show a length-dependent transition between the de Gennes and Odijk regimes. We also investigate the migration and deformation of a piece of DNA in a non-uniform channel. Under non-uniform confinement, the DNA is driven by an entropic force to minimize the free energy of the system.

3. In Part III, we extend the theory for a wormlike chain to study a filamentous network. The challenge for studying filamentous networks is that even under some very common loading conditions, some of the filaments are under compression and buckling will occur when the compressive forces reach some critical values. Buckling of beams is a bifurcation phenomenon where the first order approximation of the energy well ceases to be quadratic. When buckling happens, $\delta E = 0$ is no longer sufficient to determine a stable equilibrium state. In fact, the solution of $\delta E = 0$ can probably lead to an unstable state with $\delta^2 E > 0$. For these reasons, exact post-buckling behavior of filaments in a network is not easy to tackle. We introduce "imperfection" into the filaments and start with curved configurations. In this way, we avoid the singularity at the buckling point and the solutions go into the post-buckling path smoothly. Taking thermal fluctuations into account, we determine the material properties, such as, Young's modulus, shear and bulk moduli, and also Poisson's ratio for a triangular network.

Bibliography

[1] Alberts B, Bray D, Hopkin K, Johnson A, Lewis J, Raff M, Roberts K, Walter P. 2009. **Essential Cell Biology.** 3rd ed. Garland Science, New York and London.

[2] Alberts B, Johnson A, Lewis J, Raff M, Roberts K, Walter P. 2007. **Molecular Biology of the Cell.** 5th ed. Garland Science.

[3] Purohit PK, Nelson PC. 2006. **Effect of supercoiling on formation of protein-mediated DNA loops.** *Physical Review E.* 74:061907.

[4] Santangelo PJ, Nix B, Tsourkas A, Bao G. 2004. **Dual FRET molecular beacons for mRNA detection in living cells.** *Nucleic Acids Res.* 32: e57.

[5] Phillips R, Kondev J, Theriot J. 2009. **Physical Biology of the Cell.** Garland Science, New York.

[6] Nelson P. 2008. **Biological Physics: Energy, Information, Life.** updated first ed. W. H. Freeman and Company, New York.

[7] Kittel C. 2005. **Introduction to Solid State Physics.** 8th ed. Wiley.

[8] Ono IK, OHern CS, Durian OJ, Langer SA, Liu AJ, Nagel SR. 2002. **Effective temperatures of a driven system near jamming.** *Phys. Rev. Lett.* 89:095703.

[9] Marko JF, Siggia ED. 1995. **Stretching DNA.** *Macromolecules* 28:8759-8770.

[10] Bustamante C, Marko JF, Siggia ED, Smith S. 1994. **Entropic elasticity of lambda-phage DNA.** *Science* 265:1599–1600.

[11] Marko JF. 1997. **Stretching must twist DNA.** *Europhys. Lett.* 38:183-188.

[12] Brown AE, Litvinov RI, Discher DE, Weisel JW. 2007. **Forced unfolding of coiled-coils in fibrinogen by single-molecule AFM.** *Biophys. J.* 92:L39–L41.

[13] Chyan CL, Lin FC, Peng H, Yuan JM, Chang CH, Lin SH, Yang G. 2004. **Reversible mechanical unfolding of single ubiquitin molecules.** *Biophys. J.* 87:3995–4006.

[14] Schlierf M, Li H, Fernandez JM. 2004. **The unfolding kinetics of ubiquitin captured with single-molecule force-clamp techniques.** *Proc. Natl. Acad. Sci. USA* 101:7299–7304.

[15] Seol Y, Li J, Nelson PC, Perkins TT, Betterton MD. 2007. **Elasticity of short DNA molecules: theory and experiment for contour lengths of 0.6-7 microm.** *Biophys. J.* 93:4360-4373.

[16] Purohit PK, Arsenault ME, Goldman Y, Bau HH, 2008. **The mechanics of short rod-like molecules in tension.** *Int. J. Non-linear Mech.* 43:1056-1063.

[17] Hori Y, Prasad A, Kondev J. 2007. **Stretching short biopolymers by fields and forces.** *Phys. Rev. E* 75, 041904.

[18] Bell GI. 1978. **Models for specific adhesion of cells to cells.** *Science* 200:618–627.

[19] Bažant ZP, Cedolin Luigi. 2003. **Stability of structures: elastic, inelastic, fracture, and damage theories.** Courier Dover Publications.

Part I

Heterogeneous Freely-Jointed Chain Model and Its Applications

Chapter 2

Mechanics of Forced Unfolding of Proteins

Main results of this chapter:

1. Forced unfolding of proteins under different pulling conditions can be described by a system of three equations.
2. Kuhn length of an unfolded protein is found to be about half of that of a folded protein. This means unfolded proteins are floppier and more flexible.
3. Kinetic parameters such as protein folding and unfolding rates are extracted using the protein unfolding force-extension profiles with the saw-tooth patterns.
4. Unlike previous Monte Carlo simulation methods, we do not assume zero folding rate in this chapter. As a result, refolding events, such as folding-unfolding hoppings, are predicted in both constant force pulling mode and linearly increasing force pulling mode.

2.1 Introduction

Over the last two decades Atomic Force Microscopy (AFM) has established itself as a valuable experimental technique to probe the structure and energetics of proteins [1, 2, 3, 4, 5, 6, 7, 8, 9, 10, 11]. Force-extension measurements performed using the AFM have shown that the mechanics and chemistry of proteins are intimately linked [3, 12]. The data emerging from the AFM experiments are interpreted using Steered Molecular Dynamics (SMD) and Monte

Carlo (MC) simulations [1, 10, 13, 14]. The SMD simulations complement AFM experiments by providing information about short-lived and metastable intermediate states that could not be gleaned from the experiments alone. But, the unfolding forces predicted by SMD simulations are much larger than those obtained in AFM experiments since the rates of pulling in the SMD simulations are constrained (due to limitations on the time step) to be orders of magnitude larger than realistic AFM pulling rates [13]. The MC simulations are based on the two-state model of Rief *et al.* [14] and they reproduce the AFM data quite well [1, 9, 10]. These methods, however, suffer from the limitation that the kinetic parameters have to be determined by trial and error. Often, the refolding rate is set to zero in these simulations and only one persistence length is used for both the folded and unfolded states of the protein. This reduces the dimensionality of the parameter space to be searched [1, 3] but is unrealistic since refolding is dominant at low forces and unfolded proteins are expected to be floppier than their folded counterparts. Furthermore, MC simulations have been used primarily to fit the data from AFM experiments where the protein is pulled at a constant velocity and we are not aware of any attempt to use MC methods to determine the response of proteins under other pulling conditions, such as, a force linearly increasing with time.

Our goals in this chapter are: (a) to unify the description of protein unfolding under different types of pulling conditions within a single model, (b) to account for refolding and explain the consequences of neglecting it, and (c) to predict the response of proteins under different pulling conditions from a knowledge of its kinetic and mechanical properties. We begin with a brief discussion of the heterogeneous freely-jointed chain model which will be used later to describe the protein oligomer. We further show that the protein forced unfolding problem has 3 unknowns and can be solved analytically using the freely-jointed chain model and Bell's kinetic model with an additional equation to specify the loading condition. The force-extension profile obtained can be directly fitted to the experimental data. Unlike many of the MC simulations, we do not set the refolding rate to zero. In fact, we show that there is a critical value of the applied force under which the equilibrium in the folding/unfolding reaction is biased toward folding. We demonstrate the applicability of our model by fitting it to published AFM experimental data on two different proteins – ubiquitin and fibrinogen. For ubiquitin we show that the kinetic and mechanical parameters obtained from fitting our expressions to a constant velocity pulling experiment can be used to predict its response in an experiment where the force is linearly increasing with time. After validating our model with ubiquitin which has been extensively studied under various types of loading conditions, we apply the same procedure to fibrinogen and obtain predictions for its response under a linearly increasing force.

2.2 Three Equations Governing the Forced Unfolding of Proteins

In the problem of sequentially unfolding a protein oligomer, we have three unknown functions of time t: $x(t)$, $F(t)$ and $N_f(t)$, which are, respectively, the extension, force and the number of folded proteins. The total number of proteins N is a constant throughout the experiment, so that, $N_f + N_u \equiv N$. Therefore, $N_u(t)$, the number of unfolded proteins, is not viewed as an unknown function. The three equations that close the system are: (1) the equilibrium force-extension relation, $x = x(F, N_f)$, obtained from either the freely-jointed chain (FJC) model or wormlike chain (WLC) model of polymer elasticity [15, 16]; (2) the kinetic equation, which measures the rates of unfolding and refolding, obtained from either Bell's model [17], or other more sophisticated kinetic models based on Kramer's rate theory [18]; (3) the equation which determines the manner of applying the external constraint, e.g. for constant velocity pulling, it is $dx/dt = v_c$, where v_c is the pulling speed, and for constant force pulling, it is $dF/dt = 0$. This system of equations unifies problems of protein unfolding under different kinds of loading conditions into a single mathematical framework. By merely changing the last equation, one can get the unfolding behavior of proteins under constant velocity pulling, constant force pulling, pulling with a force linearly increasing with time, etc.

2.3 Heterogeneous FJC Model and the Equilibrium Force-Extension Relation

The freely-jointed chain (FJC) is the simplest theory to model a rod-like polymer. This theory describes the polymer as an N-segment chain. It assumes that there is no interaction between individual segments so that the configuration of the polymer is essentially a random walk in 3D space. The length of the segments – also called the Kuhn length – is the only parameter reflecting the stiffness of the chain. Classical FJC theory, for simplicity's sake, assumes all the segment lengths are the same along the chain. In the protein forced unfolding problem, however, the oligomer consists of mixed folded and unfolded proteins with different mechanical properties. Therefore, the classical FJC theory is not applicable. Here, we extend the classical FJC theory to study a heterogeneous chain in which different segments can have different Kuhn lengths. The force-extension relation for this heterogeneous chain can be used as the first equation in the protein unfolding problem described in the previous section.

We study a heterogeneous freely-jointed chain in a fixed temperature and fixed force ensemble (Fig. 2.1a). Since every segment is independent of others, the partition function of the chain is just the product of the sub-partition function of each segment:

$$Z = \prod_{i=1}^{N} z_i, \tag{2.1}$$

where the sub-partition function z_i for segment i is the summation of the Boltzmann weight for all the possible orientations:

$$z_i = \int_0^{\pi} \exp\left(\beta F l_i \cos\theta\right)\ 2\pi \sin\theta\, d\theta = 4\pi\ \frac{\sinh(\beta F l_i)}{\beta F l_i}, \tag{2.2}$$

with $\beta = 1/k_B T$, k_B being the Boltzmann constant, T being the absolute temperature in Kelvin and θ being the angle formed by the segment with repect to the axis along which the external force F is applied. Note that Eq. 2.2 is valid for small forces as well as large forces [1]. In particluar, as the external force approaches zero, z_i approaches 4π.

The ensemble average of the angle orientation can be evaluated analytically using the formula:

$$\langle A_i \rangle = \frac{1}{z_i} \int_0^{\pi} A_i \exp\left(\beta F l_i \cos\theta\right) 2\pi \sin\theta d\theta, \tag{2.3}$$

and the results turn out to be:

$$\langle \cos\theta_i \rangle = \mathcal{L}(\xi_i), \quad \langle \sin\theta_i \rangle = \frac{\pi}{2}\, \frac{I_1(\xi_i) - L_1(\xi_i)}{\sinh(\xi_i)}, \tag{2.4}$$

$$\langle \cos^2\theta_i \rangle = 1 - 2\mathcal{L}(\xi_i)/\xi_i, \quad \langle \sin^2\theta_i \rangle = 2\mathcal{L}(\xi_i)/\xi_i, \tag{2.5}$$

where $\xi_i = \beta F l_i$ is a dimensionless number, $\mathcal{L}(\xi_i) = \coth(\xi_i) - 1/\xi_i$ is the Langevin function, $I_1(\xi_i)$ is the modified Bessel function of the first kind and $L_1(\xi_i)$ is the modified Struve function.

In the limit of small force/high temperature ($\beta F \to 0$), these results, to the first order approximation, reduce to:

$$\langle \cos\theta_i \rangle \to \beta F l_i/3, \quad \langle \sin\theta_i \rangle \to \pi/4, \quad \langle \cos^2\theta_i \rangle \to 1/3, \quad \langle \sin^2\theta_i \rangle \to 2/3. \tag{2.6}$$

The results approach randomly isotropic orientation in this limit. In the opposite limit ($\beta F \to +\infty$), the results are:

$$\langle \cos\theta_i \rangle \to 1, \quad \langle \sin\theta_i \rangle \to 0, \quad \langle \cos^2\theta_i \rangle \to 1, \quad \langle \sin^2\theta_i \rangle \to 0. \tag{2.7}$$

These results make sense because in the large force limit, energy dominates and $\langle \theta_i \rangle \approx 0$. The segments line up in the force direction.

From the results of average angle orientation, we can calculate the average extension of the chain:

$$\langle x \rangle = \sum_{i=1}^{N} l_i \langle \cos\theta_i \rangle = \sum_{i=1}^{N} l_i \left[\coth(\xi_i) - \frac{1}{\xi_i} \right]. \tag{2.8}$$

[1] Here we neglect the excluded volume interactions.

This is a generalization of the force-extension relation for the homogeneous freely-jointed chain model. It can also be derived from $-\partial G/\partial F$, with G being the Gibbs free energy for the system:

$$G = -k_B T \log Z = -k_B T \sum_{i=1}^{N} \log \left[\frac{4\pi \sinh(\beta F l_i)}{\beta F l_i} \right]. \tag{2.9}$$

In the limit of small force, the average extension is linear with respect to the force. In the opposite limit, the extension saturates at $\langle x \rangle \to \sum_{i=1}^{N} l_i = L$, which is the contour length of the entire chain:

$$\langle x \rangle \to \begin{cases} \left(\sum_{i=1}^{N} \beta l_i^2 / 3 \right) F & \text{as } \beta F \to 0 \\ \\ L & \text{as } \beta F \to \infty \end{cases} \tag{2.10}$$

For homogeneous chain with $l_i \equiv l$, this reduces to:

$$\langle x \rangle \to \begin{cases} (\beta l L / 3)\, F & \text{as } \beta F \to 0 \\ \\ L & \text{as } \beta F \to \infty \end{cases} \tag{2.11}$$

As discussed in the *Introduction* part of this thesis proposal, the polymer behaves like a spring at low forces with an effective spring constant $k = 3k_B T/Ll$. As temperature increases, or the Kuhn length decreases, the fluctuation increases and so the entropic effect becomes more significant, making it more difficult to pull the polymer straight. Thus the effective spring constant is larger.

To apply the theory discussed above to the protein forced unfolding problem, we note that the mechanical properties of a protein in the folded and unfolded states are expected to be different – a folded protein is stiff, whereas an unfolded protein is floppy. Hence, we model the protein oligomer as a heterogeneous FJC with two possible values of Kuhn length l_f and l_u for the folded and unfolded states respectively (Fig. 2.1a). Using Eq. 2.8, the equilibrium force-extension relation can be written as:

$$x = N_f L_{fs} \left[\coth\left(\frac{F l_f}{k_B T} \right) - \frac{k_B T}{F l_f} \right] + N_u L_{us} \left[\coth\left(\frac{F l_u}{k_B T} \right) - \frac{k_B T}{F l_u} \right] \tag{2.12}$$

where L_{fs} and L_{us} are the contour lengths of a single folded and unfolded protein respectively, k_B is the Boltzmann constant, T is the absolute temperature and the meanings of the symbols x, F, N_f, N_u, l_f and l_u have been discussed above. Note that in reality, there is only one contour length L_u, that associates with the fully unfolded proteins. The other contour length L_f in Eq. 2.12 is meant to represent the maximum length of the proteins if unfolding is somehow prevented.

This model implies that the equilibrium force-extension behavior of a protein chain is governed only by four parameters: L_{fs}, l_f, L_{us} and l_u, regardless

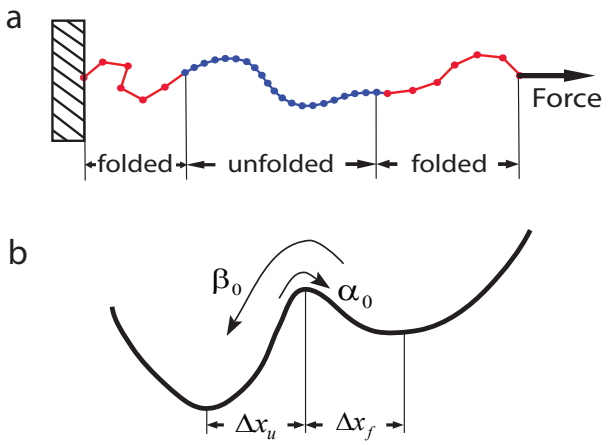

Figure 2.1: Illustration of the two-state kinetic model. (a) A chain of mixed folded and unfolded proteins is modeled as a heterogeneous freely-jointed chain. A single folded (unfolded) protein is represented by an N_{fs}-segment (N_{us}-segment) subchain with Kuhn length l_f (l_u). In this illustration, two folded and one unfolded proteins are represented by the two red and one blue subchains respectively. Note that in reality, the actual number of segments in each subchain may be much larger. Also, l_u is expected to be smaller than l_f since an unfolded protein is expected to be floppier than a folded protein. (b) Energy landscape of the two-state model. The ordinate is the Gibbs free energy and the abscissa is the reaction coordinate. The two wells, representing the folded and unfolded states of a protein, are separated by an energy barrier with transition distances Δx_u and Δx_f. At zero force, the folding rate and the unfolding rate are β_0 and α_0 respectively, with $\beta_0 >> \alpha_0$. An applied force can lower the energy barrier and thus change the folding and unfolding rates.

of the number of copies in the oligomer. However, if the chain is modeled as homogeneous, we need N Kuhn lengths and N contour lengths for fitting the N curves obtained in a constant velocity pulling experiment (see, for instance, [21]).

In order to demonstrate the applicability of our model, we consider force-extension measurements on ubiquitin (N-C linked) and fibrinogen. For ubiquitin (experimental data from [7]), we know that the last curve in the force-extension profile (see Fig. 2.2a) corresponds to six unfolded proteins and zero folded proteins, so we apply the homogeneous FJC model to fit this curve and obtain $L_{us} = 25.37$nm, $l_u = 0.33$nm. The other two parameters can be obtained by fitting one other curve using the heterogeneous FJC model. Here we use the first curve and get $L_{fs} = 6.29$nm and $l_f = 0.60$nm. We similarly determine the parameters for fibrinogen using the first and last curves (Fig. 2.2b, experimental data from [9]) and get $L_{fs} = 11.39$nm, $L_{us} = 44.62$nm, $l_f = 0.57$nm and $l_u = 0.31$nm. These results are not significantly different if we use any other two curves for the fitting. Without any more free parameters, we then predict the intermediate curves for both proteins using Eq. 2.12 and compare the predictions with the experimental data. The results are shown in Fig. 2.2 (red curves) and the predictions of the heterogeneous FJC model match the experimental data quite well for both the proteins.

Our results show that $l_u \approx l_f/2$ for both the proteins, which agrees with our intuition that unfolded proteins should be floppier than the folded ones. Also, our estimates for the contour lengths of the fully unfolded proteins L_{us} agree well with published results (27.4nm for ubiquitin [5, 22] and 40nm for fibrinogen [11]), which shows that our fitted parameters are indeed physically relevant. However, it is worth pointing out that L_{fs} is the maximum length of a single folded protein if unfolding is somehow prevented, therefore, it will be different from the end-to-end distance of the protein in its native state. In fact, the contour length of ubiquitin in its native state is about 3.8nm [5], and simulations have shown that this number increases to 4.7nm under a constant force of 200pN while the protein remains in a native-like state [22].

2.4 Kinetic Equation

It has been shown by both experiments and simulations that, at least for ubiquitin, most ($\sim 95\%$) of the unfolding events follow a two-state pathway [8, 22]. Therefore, following Bell's theory [17], we propose that the change in the number of folded proteins is given by:

$$\frac{dN_f^*}{dt} = -k_u N_f + k_f N_u \tag{2.13}$$

where $k_u = \alpha_0 \exp(F\Delta x_u/k_BT)$, $k_f = \beta_0 \exp(-F\Delta x_f/k_BT)$, α_0 and β_0 are the unfolding and refolding rates when no force is applied, Δx_u and Δx_f are the distances to the transition state (Fig. 2.1b), and N_f^*, set to be a

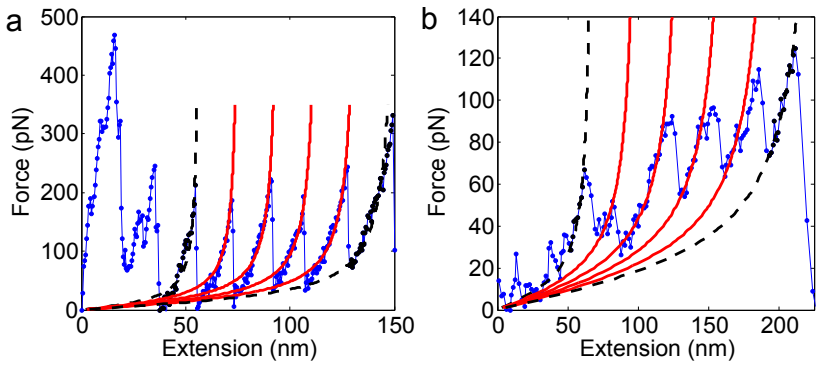

Figure 2.2: Predictions of the force-extension profiles using the heterogeneous FJC model with only four free parameters. (a) ubiquitin. (b) fibrinogen. Blue curves are the experimental data – ubiquitin data from [7] and fibrinogen data from [9]. We use two of the experimental curves (black dots) to fit the Kuhn length and the contour length of the folded and unfolded proteins (black dashed lines are the fitting results). Then, without any more free parameters, we use the heterogeneous FJC model (Eq. 2.12) to predict all the other curves. The predictions (red curves) match well with the experimental data for both proteins.

real number, is a continuous version of the integer N_f. Its initial value is set to be equal to N_f and it evolves according to Eq. 2.13. On the other hand, N_f, the number of folded proteins, evolves in such a way that it jumps by ± 1 whenever N_f^* reaches an integer. Note that for simplicity, here we assume Δx_f and Δx_u are unaffected by the external force. This assumption is valid when the local curvatures of the potential wells are large [23, 24]. More sophisticated kinetic models (see [18] for example) can be easily incorporated into our description. We stick with Bell's model here because the goal of this chapter is to apply the three-equation mathematical framework to understand the unfolding behavior of proteins under different pulling conditions and Bell's model is simple enough to give analytic or semi-analytic solutions for all the conditions discussed below, and at the same time captures most of the physics reported in the experiments. The condition for the unfolding or refolding events to happen is:

$$\int dN_f^* = \int (-k_u N_f + k_f N_u)\, dt = \pm 1 \tag{2.14}$$

where $+1$ represents refolding and -1 represents unfolding of a protein.

The advantage of the present method over MC simulations is that we can solve exactly for all the four kinetic parameters (α_0, β_0, Δx_u and Δx_f) from the experimental data (discussed below) instead of guessing which parameter values fit the data best. Guessing the best fit kinetic parameters is especially difficult for the MC simulations when taking the refolding rate β_0 into account

since the parameter space is large. In fact, in many cases β_0 is simply set to zero by taking advantage of the fact that refolding is negligible at large forces [1, 3]. A caveat of our deterministic model is that it ignores the randomness of the unfolding/folding events, but it is really meant to represent the average behavior of a large ensemble of experiments. In fact, we show in what follows that the kinetic parameters obtained by the deterministic model assuming $k_f = 0$ are close to the ones obtained previously by MC simulations. Furthermore, the kinetic parameters obtained from the deterministic model can be used in the MC simulations to obtain particular instances of the unfolding pathway, thus providing information about higher moments, for instance, the variance of the unfolding force in a constant velocity pulling experiment.

2.5 Constant Velocity Pulling I – Forced Unfolding of Globular Proteins

For the case of constant velocity pulling, the external constraint equation is $dx/dt = v_c$. Using this relation, the unfolding and refolding condition (Eq. 2.14) can be rewritten as:

$$\int_{x_1}^{x_2} (k_u N_f - k_f N_u) dx \pm v_c = 0 \tag{2.15}$$

where the positive (negative) sign represents refolding (unfolding) of one protein, x_1 is the initial extension of a particular continuous force-extension curve, x_2 is the extension when unfolding/refolding is imminent, $k_u(F(x))$ and $k_f(F(x))$ are functions of the extension, and N_f and N_u are the number of folded and unfolded proteins which remain constants for each curve.

Each of the unfolding events in the force-extension profile should satisfy Eq. 2.15 and we can use any four of them to solve for the four free kinetic parameters. This results in four algebraic equations with four unknowns α_0, β_0, Δx_f and Δx_u:

$$\alpha_0 N_{fi} \int_{x_{1i}}^{x_{2i}} \exp\left(\frac{F\Delta x_u}{k_B T}\right) dx - \beta_0 N_{ui} \int_{x_{1i}}^{x_{2i}} \exp\left(\frac{-F\Delta x_f}{k_B T}\right) dx = v_c, \tag{2.16}$$

where $i = 1, 2, 3, 4$ denotes the four curves we choose, N_{fi} and N_{ui} are respectively the number of folded and unfolded proteins along the force-extension curve i, x_{1i} is the initial extension of the curve and x_{2i} is the extension where the curve breaks. We solved these four equations numerically using Newton's method for both ubiquitin and fibrinogen (pulling velocity for both the proteins is $v_c = 1000$nm/s [7, 9]). The result for ubiquitin is: $\alpha_0 = 3.75\text{s}^{-1}$, $\beta_0 = 1293.65\text{s}^{-1}$, $\Delta x_u = 0.08$nm and $\Delta x_f = 0.31$nm. The refolding rate β_0 found here is comparable to the one obtained previously from MD simulations [25]. The result for fibrinogen is: $\alpha_0 = 3.19\text{s}^{-1}$, $\beta_0 = 7691.16\text{s}^{-1}$, $\Delta x_u = 0.10$nm and $\Delta x_f = 0.67$nm. Similar transition distances have been

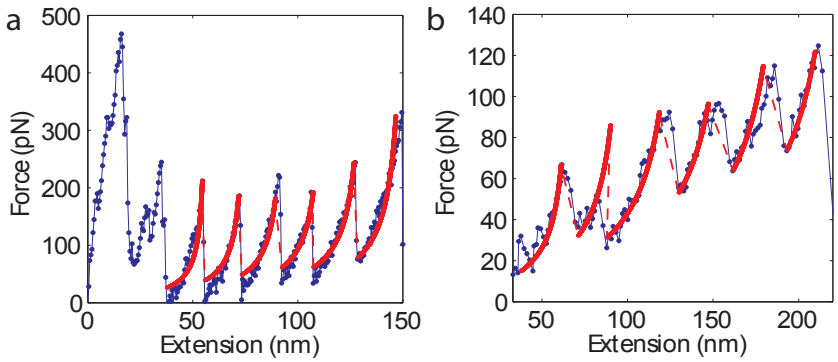

Figure 2.3: Force-extension profiles of six copies of (a) ubiquitin, and (b) fibrinogen ($v_c = 1000$nm/s) in constant velocity pulling. Blue curves: experimental data (ubiquitin data from [7] and fibrinogen data from [9]); red curves: prediction using our two-state kinetic model.

reported for many other protein domains and they are suggested to reflect the critical breaking of hydrogen bonds or hydrophobic interactions in the process of protein unfolding [26]. Using the solved kinetic parameters, we can predict other breaking points and thus the whole force-extension profile using Eq. 2.12, Eq. 2.15 and $dx/dt = v_c$. The predictions match well with the experimental data and are shown in Fig. 2.3. Our solutions for both the proteins imply that β_0 is several orders larger than α_0. Intuitively, this is expected because when no external force is applied, the proteins tend to rapidly fold into their native state. The fact that $\beta_0 >> \alpha_0$ suggests that the refolding rate cannot be ignored, at least when the force is small.

If we assume that the refolding rate β_0 is zero as is commonly done in MC simulations, the solution for the kinetic paramters for ubiquitin is: $\alpha_0 = 0.05\text{s}^{-1}$, $\Delta x_u = 0.17$nm. These results are quite close to those obtained previously by other experiments that also assume $k_f = 0$ [8, 27, 28], and suggest that our model is consistent with the MC simulations used before. In fact, the authors in [8] assumed $k_f = 0$ and found $\alpha_0 = 0.015\text{s}^{-1}$, $\Delta x_u = 0.17$nm using the constant force pulling data and $\alpha_0 = 0.0375\text{s}^{-1}$, $\Delta x_u = 0.14$nm using the linearly increasing force pulling data on ubiquitin. Our results show that the unfolding rate α_0 obtained by ignoring the refolding rate is significantly lower than the one obtained by taking the refolding rate into account. In fact, setting $\beta_0 = 0$ should always lead to an under-prediction of α_0. The reason for the under-prediction is that when the refolding rate is ignored in the kinetic equation, the unfolding rate predicted is in fact a 'net rate' for the proteins to change from the folded state to the unfolded state. This calculated 'net rate' should be smaller than the true unfolding rate because it includes the contribution of the refolding rate which is high at low forces.

It has been shown that the average breaking force is approximately linear with respect to the logarithm of pulling velocity [5, 7]. We use the parame-

ters calculated above and predict the force-extension profiles under different pulling speeds ranging from $v_c = 10^3$nm/s to $v_c = 10^{11}$nm/s for both the proteins (six copies, force-extension profiles not shown). The linear relation between the average breaking force and the logarithm of pulling velocity is found using either set ($k_f = 0$ and $k_f \neq 0$) of the kinetic parameters obtained previously (Fig. 2.6a). For ubiquitin, our calculations show that the slope is 63.1 (piconewton per tenfold change of the velocity in nm/s) if we use the set of parameters that assumes $k_f = 0$, and 135.3 if we use another set of parameters that takes refolding into account. Recent MD results on fibrinogen, with pulling velocity 2.5×10^9nm/s, show that the unfolding events happen at force $\sim 10^3$pN [11]. This result is close to our predicted average breaking force for fibringen at similar pulling velocity (see Fig. 2.6a blue solid line). However, Fig. 2.6a shows that if we set $k_f = 0$, the predicted unfolding force is much smaller than the one that takes the refolding rate into account The reason the unfolding force is higher with non-zero k_f is as follows. Recall that for given k_u and k_f, the breaking extension x_2 (and hence the breaking force) is calculated from the integral over the entire force-extension curve (see Eq. 2.15) including the low force regime where refolding is dominant. The integral in Eq.2.15 is initially negative because the force is low and $k_f >> k_u$, so for the case $k_f \neq 0$, the force-extension curve should go higher in order that the integral reaches the positive value v_c. This suggests that a poor prediction of the unfolding rate at low pulling velocities leads to large errors in the predictions for the breaking events at high pulling velocities.

2.6 Constant Velocity Pulling II – Forced Unfolding of Fibrous Proteins

If we set N_f and N_u in both Eq. 2.12 and Eq. 2.13 to be real numbers that change continuously, then together with the constraint equation $dx/dt = v_c$, we can analytically reproduce the continuous force-extension profile for the coiled-coil proteins with a shallow force-plateau as observed in the experiments [4, 11].

To do this, we first write Eq. 2.12 as:

$$\begin{aligned} x &= N_f L_f(F) + N_u L_u(F) && (2.17) \\ &= N_f(L_f - L_u) + N L_u && (2.18) \end{aligned}$$

where $N = N_f + N_u$ is the total number of proteins, $L_f(F)$ and $L_u(F)$ is the length of a single folded and unfoled protein under force F respectively:

$$L_f(F) = L_{fs}\left[\coth(\frac{Fl_f}{k_BT}) - \frac{k_BT}{Fl_f}\right], \tag{2.19}$$

$$L_u(F) = L_{us}\left[\coth(\frac{Fl_u}{k_BT}) - \frac{k_BT}{Fl_u}\right]. \tag{2.20}$$

Then we rearrange Eq. 2.18 and get:

$$N_f = \frac{NL_u(F) - x}{L_u(F) - L_f(F)}, \tag{2.21}$$

Using $x = v_c t$, Eq. 2.21 becomes:

$$N_f(t, F) = \frac{NL_u(F) - v_c t}{L_u(F) - L_f(F)}. \tag{2.22}$$

Here N_f is a function of F and t.

Next, we differentiate Eq. 2.18 with respect to t once to get the relation between dN_f/dt and dF/dt:

$$\frac{dN_f}{dt} = \frac{v_c - \frac{dF}{dt}[N_f L'_f(F) + (N - N_f)Lu'(F)]}{L_f - L_u}. \tag{2.23}$$

Then by substituting Eq. 2.13 into the right-hand-side of Eq. 2.23 and rearranging the expression to get dF/dt, we obtain:

$$\frac{dF}{dt} = \frac{v_c - (L_f(F) - L_u(F))[Nk_f - (k_f + k_u)N_f(t, F)]}{N_f L'_f(F) + (N - N_f)L'_u(F)}. \tag{2.24}$$

Plugging Eq.2.22 into this expression, we get the decoupled governing equation for $F(t)$. We solve this single-variable ODE numerically, and then use Eq. 2.22 to obtain $N_f(t)$. The following parameters are used in the calculation: the Kuhn length, contour length, and kinetic parameters are those for ubiquitins and fibrinogens. Total number of proteins in the chain is set to be $N_f + N_u = 20$. With initial values $N_f = N$ and $N_u = 0$. Also, the pulling velocity is set to be $v_c = 300$nm/s.

The force-extension profile is shown in Fig. 2.4. Similar profiles have been observed for many fibrous proteins in experiments [4]. Also, number of the folded proteins as a function of time (the $N_f(t)$ profile) is shown in Fig. 2.5 (red for ubiquitin and blue for fibrinogen).

Finally, we note that the model described here can be applied to study the relaxation behavior of the protein chain after all the proteins are fully stretched as has been done in experiments [29]. We keep the relaxation extension x_r fixed by setting $v_c = 0$, let the initial N_f be 0 (i.e., all the proteins are unfolded initially), and get the solution for $N_f(t, x_r)$. Fig. 2.6b shows how the number of refolded proteins evolves as a function of time and also its dependence on x_r. The trend in the solution agrees with recent experimental observations on a different protein [29]. We further note that the correct limit profile as $t \to \infty$ (Fig. 2.6b blue line) can be obtained only by taking both the unfolding and refolding rates into account.

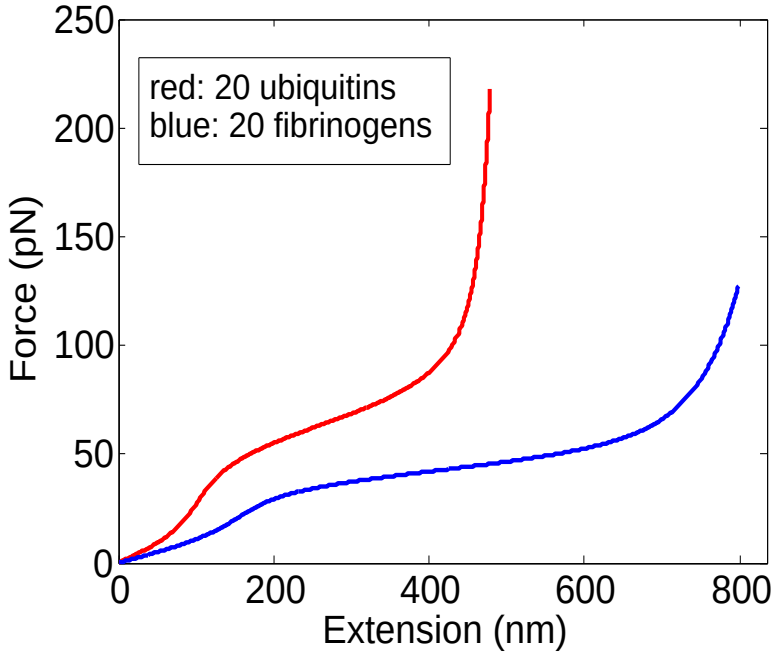

Figure 2.4: Force-extension relation (continuous model) of ubiquitin (red) and fibrinogen (blue). In reality, both are globular proteins. Here we plot the force-extension relation using their kinetic parameters, but with N_f, N_u being real numbers instead of integers.

2.7 Pulling with a Force Linearly Increasing with Time

For a protein oligomer stretched under a linearly increasing force, we have $dF/dt = v_f$, and the unfolding/refolding condition (Eq. 2.14) becomes:

$$W(F_2) = \pm v_f + W(F_1), \quad (F_2 > F_1) \tag{2.25}$$

Eq. 2.25 can be used to determine the unfolding force F_2. The double exponential function $W(F)$ is given by $W(F) = k_B T \left[N_f k_u(F)/\Delta x_u + N_u k_f(F)/\Delta x_f\right]$, and F_1 is the initial force at each step (note that the force-extension profile is step-wise). Depending on the sign (positive/negative) of v_f, one protein unfolds/refolds when F linearly increases to reach F_2.

We use Eq. 2.12, Eq. 2.25 together with $dF/dt = v_f$ ($v_f = 300$pN/s) to generate the step-wise extension-time profile for both ubiquitin and fibrinogen (all the kinetic parameters have been obtained in the constant velocity pulling section). The results are shown in Fig. 2.7a and b (red). For ubiquitin, the unfolding events occur around ~ 100pN and the breaking extension is nearly linear in time, with a slope predicted as 680.9nm/s. Both these results are consistent with experimental obervations [8]. For fibrinogen, the result shown here constitutes a falsifiable prediction from our model and can be easily tested

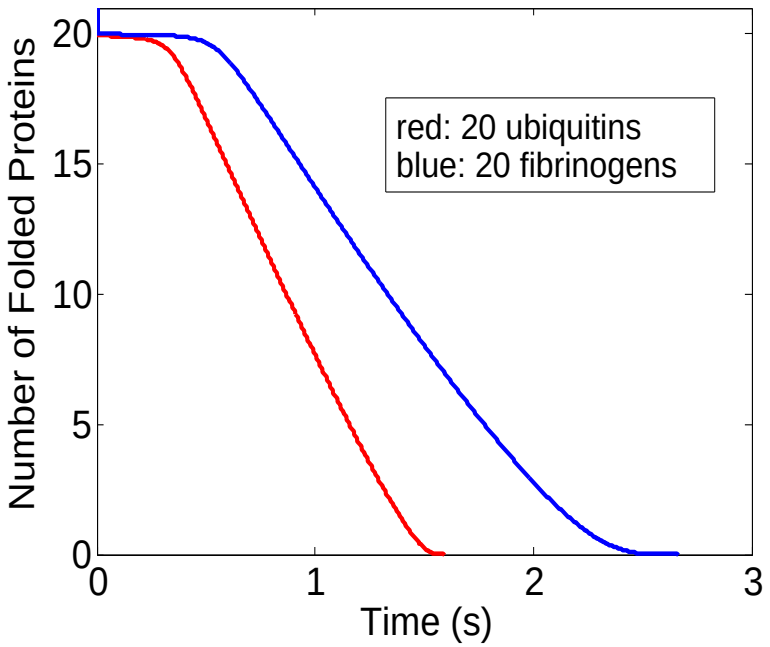

Figure 2.5: Number of folded proteins as a function of time (continuous model). Red curve for ubiquitin and blue curve for fibrinogen. In reality, both are globular proteins. Here we plot the $N_f(t)$ profile using their kinetic parameters, but with N_f, N_u being real numbers instead of integers.

using current AFM techniques. For both proteins, some refolding events are observed at small force (inset of Fig. 2.7a and b), which would not be predicted if the refolding rate is ignored (Fig. 2.7c).

Further analysis of Eq. 2.25 shows that the initial force F_1 at each step should be larger than a critical force in order that one protein unfolds at the end of the step (otherwise one protein will refold at the end of the step). This critical force F_{cl} is determined by:

$$W(F_{cl}) = v_f + W(F_s), \quad (F_{cl} < F_s) \tag{2.26}$$

where F_s is the unique stationary point of the function $W(F)$: $F_s = [k_B T/(\Delta x_u + \Delta x_f)] \ln[\beta_0 N_u/(\alpha_0 N_f)]$. In general, since $W(F)$ depends on N_f, the critical force increases as more and more proteins unfold (Fig. 2.8). For example, consider the unfolding of a chain of nine ubiquitins; the critical force computed using Eq. 2.26 increases from $\sim$ 30pN to $\sim$ 80pN during the unfolding process.

If we let N_f and N_u in both Eq. 2.12 and Eq. 2.13 to be continuous real numbers, then the solution for $N_f(t)$ satisfying $N_f(0) = N$ and $F = v_f t$ is:

$$\frac{N_f(t)}{N} = Q^{-1}(t) \left[\int_0^t \beta_0 Q(t) e^{C_2 t} dt + Q(0) \right] \tag{2.27}$$

where the function $Q(t)$ and the two constants C_1 (appearing in $Q(t)$) and C_2

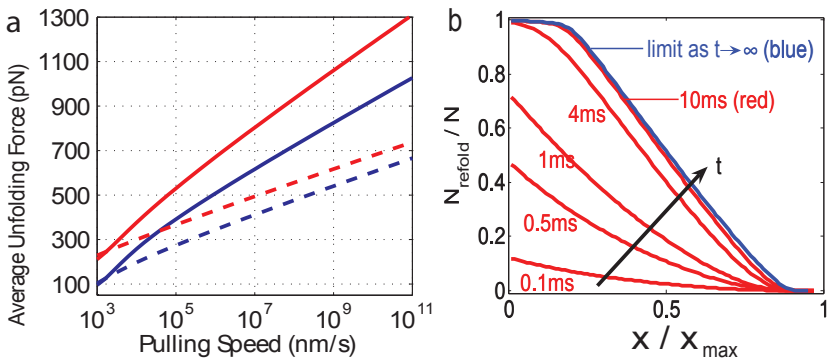

Figure 2.6: Constant velocity pulling. (a) Dependence of the average unfolding force on pulling speed. Red: ubiquitin; blue: fibrinogen; solid line: accounting for refolding ($k_f \neq 0$), dashed line: ignoring refolding ($k_f = 0$). For both proteins, the predicted unfolding force using the set of parameters that assume $k_f = 0$ is much smaller, especially at high pulling velocities, than the one that takes the refolding rate into account. (b) Relaxation profiles ($v_c = 0$nm/s). The evolution of the number of refolded proteins is shown as a function of the relaxation extension x_r (normalized by $x_{max} = NL_{us}$). A limit profile (blue) is approached as time approaches infinity.

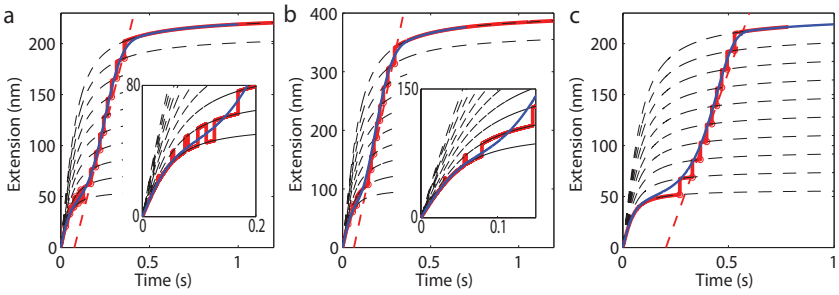

Figure 2.7: Extension versus time profiles for pulling using a linearly increasing force ($v_f = 300$pN/s, 9 copies of proteins). (a) ubiquitin and (b) fibrinogen. Red curves: predicted step-wise profile, using integer N_f and N_u in the governing equations (Eq. 2.12 and Eq. 2.13). Each of the steps obeys the equilibrium force-extension relation, which is shown as dashed black curves (Eq. 2.12). Red circles and dashed line: unfolding events and the fitting results. The fitting equation is $x = 680.9t - 52.12$ for ubiquitin and $x = 1419t - 92.01$ for fibrinogen (x is the extension in units of nm. Blue lines: solutions obtained by using continuous N_f and N_u in the governing equations, which match well with the discrete model shown in red. The profiles for ubiquitin obtained here are consistent with those measured in [8]. Insets: if we take the refolding rate into account, some refolding events are observed at small force. (c) Extension versus time profiles for nine copies of ubiquitin assuming $k_f = 0$ shows no refolding events at small force even though it reproduces the overall trend.

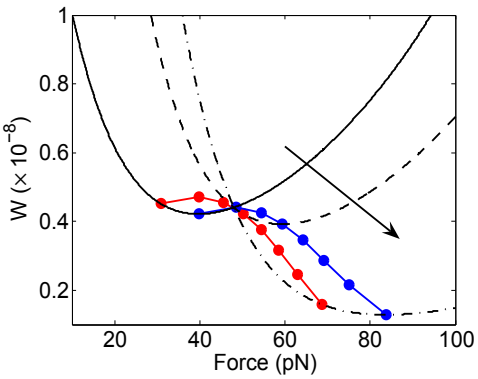

Figure 2.8: The double exponential function $W(F)$ together with the stationary points (blue) and the critical forces (red) for pulling with a force linearly increasing in time. Assume that there are nine copies of ubiquitin in the chain. The double exponential function when $N_f = 8$, $N_u = 1$ is shown as a black solid line (when $N_u = 0$, the function is only a single exponential). As more and more proteins unfold, N_f decreases and the curve $W(F)$ shifts to the right along the F axis (see the arrow). We plot $W(F)$ in black dashed line for $N_f = 5$, $N_u = 4$ and in black dashed-dotted line for $N_f = 1$, $N_u = 8$. The movement of the curve results in the increase of the critical force F_{cl} (red).

are given by:

$$Q(t) = \exp\left[\,\alpha_0 \exp(C_1 t)/C_1 + \beta_0 \exp(C_2 t)/C_2\,\right] \tag{2.28}$$

$$C_1 = \frac{v_f \Delta x_u}{k_B T}, \quad C_2 = \frac{-v_f \Delta x_f}{k_B T} \tag{2.29}$$

An analytic expression of $x(t)$ can be obtained by plugging Eq. 2.27 into $x = x(N_f(t), F(t))$ (Eq. 2.12). The results for both the proteins are shown in Fig. 2.7a and b (blue). The curves agree quite well with the predictions of the discrete model, implying that whether we take N_f and N_u as integers or real numbers does not greatly affect the results for this kind of experiments. The advantage of assuming continuous N_f and N_u is that we have an analytical expression for $x = x(N_f(t), F(t))$. This can be directly fitted to the experimental data for linearly increasing force.

2.8 Constant Force Pulling

Stretching proteins under a constant force produces a staircase-like extension-time profile, in which the extension remains piece-wise constant over each step. Since the force is a constant, the unfolding/refolding condition Eq. 2.14 leads to the dwell time Δt for one unfolding (N_f decreases by 1) or refolding (N_f increases by 1) event:

$$\Delta t = \frac{1}{|k_u N_f - k_f N_u|}. \tag{2.30}$$

If $k_u N_f - k_f N_u > 0$, then $dN_f^*/dt < 0$ (Eq. 2.13), so one protein unfolds after the dwell time Δt, otherwise, one protein refolds after Δt. Note that usually N_u is small or zero at the beginning of the experiment, so that $k_u N_f - k_f N_u > 0$ results in sequential unfolding of the proteins. As more and more proteins unfold, $(k_u N_f - k_f N_u)$ decreases and thus the unfolding time increases, which is indeed observed in experiments [8]. If the force is large enough that the term $(k_u N_f - k_f N_u)$ remains positive before N_f decreases to 0, then all the proteins can unfold (Fig. 2.9a). On the other hand, if the force is small (for example, $\sim$ 80pN for ubiquitin), $(k_u N_f - k_f N_u)$ becomes negative at some time before N_f reaches 0, then unfolding events cease, and periodic refolding and unfolding events ensue with $(k_u N_f - k_f N_u)$ switching sign each time an event occurs (inset of Fig. 2.9a). Although it is difficult to do the constant force experiment on copies of proteins at low force ($<$ 70pN for ubiquitin) using AFM [8], the unfolding and refolding 'hopping' was indeed found in a simulation on an α-helix with a similar force (78.2pN) [23] as well as in experiments on RNA hairpin using optical tweezers [24].

By setting $k_u N_f - k_f N_u = 0$, we can get the critical force below which the refolding/unfolding 'hopping' will happen:

$$F_{cc} = \frac{k_B T}{\Delta x_u + \Delta x_f} \ln\left(\frac{\beta_0 N_u}{\alpha_0 N_f}\right) \tag{2.31}$$

This critical force F_{cc} keeps increasing as more and more proteins unfold. Using the parameters obtained from constant velocity pulling, we find that an applied force larger than 84pN is required for all the ubiquitins to unfold if there are nine copies of the protein in the chain. Note that the critical force is different for constant force pulling and pulling with a linearly increasing force unless $v_f = 0$ (Eq. 2.31 and Eq. 2.26). Also note that there is no such critical force if we assume $k_f = 0$ and therefore a model ignoring refolding unrealistically predicts that all the proteins in the chain should unfold and no 'hopping' events should happen no matter how small the force is.

If we assume that N_f and N_u are continuous real numbers in the model, then the analytic solution for $N_f(t)$ is:

$$N_f(t) = N_{f\infty} + (N_{f0} - N_{f\infty}) e^{-t/\tau} \tag{2.32}$$

where $N_{f\infty} = N k_f/(k_f + k_u)$ is the number of folded proteins that remain in the chain as $t \to \infty$, N_{f0} is the number of folded proteins at $t = 0$ and $\tau = 1/(k_f + k_u)$ is the time constant.

We plot $N_{f\infty}/N$ versus a dimensionless force $\Pi_F = \frac{F(\Delta x_u + \Delta x_f)}{k_B T}$ in Fig. 2.9b and find that the transition of $N_{f\infty}/N$ from 90% to 10% occurs over a narrow range of Π_F, a result also reported in an earlier simulation work on an α-helix and suggested to have some relation to mechanotransduction [23]. From our expression for $N_{f\infty}$, we further show that this transition range δF (Fig. 2.9b) can be calculated analytically and the value turns out to be a universal constant $\ln 81 \approx 4.4$, independent of all the kinetic parameters. In other words,

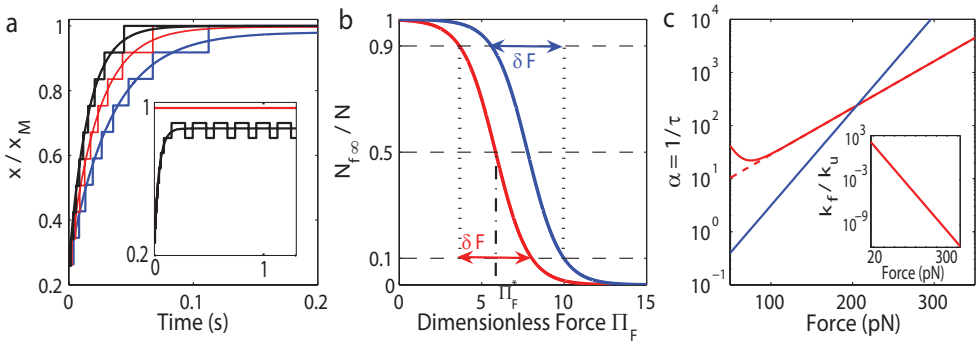

Figure 2.9: Constant force pulling profiles. (a) Extension versus time profile for nine copies of ubiquitin. Blue: $F = 100$pN, red: $F = 120$pN, black: $F = 140$pN. Inset: $F = 80$pN. Step-wise curves: solution when assuming N_f and N_u to be integers in both Eq. 2.12 and Eq. 2.13. Continuous curves: analytic solution obtained by letting N_f and N_u be real numbers in the equations. The dwell time for the step-wise solution, which is obtained analytically in the text, increases as the protein unfolds. The inset shows that when the force is not large enough, not all the proteins can unfold, and refolding/unfolding 'hoppings' occur periodically. (b) $N_{f\infty}/N$ as a function of the dimensionless force Π_F. Red: ubiquitin; Blue: fibrinogen. δF, the range of the dimensionless force over which $N_{f\infty}/N$ changes from 90% to 10%, is a universal constant $\ln 81$ for all proteins. Π_F^* is the dimensionless force for half the proteins to unfold. It is shown in the text that $\Pi_F^* = \ln(\beta_0/\alpha_0)$. (c) Unfolding rate α as a function of the applied force F. Red solid line is the result of taking the refolding rate into account. When the force is large enough, $\log \alpha$ is a linear function of F (red broken line). Blue solid line is the prediction assuming $k_f = 0$. Inset, k_f/k_u as a function of the applied force.

for any protein that obeys the two-state model, the transition always occurs over 4.4 units of the dimensionless force. Also, it can be shown that the dimensionless force Π_F^* that unfolds half the proteins relates to the kinetic paramters by $\Pi_F^* = \ln(\beta_0/\alpha_0)$. This suggests a new way to determine β_0 experimentally. Note that all the discussions here for $N_{f\infty}$ and δF are results of taking the refolding rate into account, otherwise $N_{f\infty}/N \equiv 0$ and is not a function of F.

Eq. 2.32 combined with Eq. 2.12 further leads to an analytic expression for the relative extension as a function of time:

$$\frac{x}{x_M} = (1 - \frac{\Delta x N_{f\infty}}{x_M}) - \frac{\Delta x (N_{f0} - N_{f\infty})}{x_M} e^{-\frac{t}{\tau}} \tag{2.33}$$

where $x_M = NL_{us}[\coth(Fl_u/(k_BT)) - k_BT/(Fl_u)]$ is the extension of the chain when all proteins are unfolded, $\Delta x = L_{us}[\coth(Fl_u/(k_BT)) - k_BT/(Fl_u)] - L_{fs}[\coth(Fl_f/(k_BT)) - k_BT/(Fl_f)]$ is the difference in length between a single unfolded and folded protein. We plot the analytic solution from the continuous model (Eq. 2.33) together with the step-wise solution from the discrete model in Fig. 2.9a. The two results agree quite well.

Moreover, Eq. 2.33 leads to the conclusion that the unfolding rate $\alpha = 1/\tau$ is a double exponential of the force F (Fig. 2.9c):

$$\alpha = \frac{1}{\tau} = \alpha_0 \exp\left(\frac{F\Delta x_u}{k_BT}\right) + \beta_0 \exp\left(-\frac{F\Delta x_f}{k_BT}\right) \tag{2.34}$$

When the applied force is large enough so that $k_f << k_u$ (inset of Fig. 2.9c), then $\ln\alpha \approx (\Delta x_u F/k_BT) + \ln\alpha_0$ is linear with respect to the force F, as has been shown in experiments [8]. For small forces, the unfolding rate decreases with increasing force, which is consistent with earlier works [23, 27]. Note that the decreasing of the unfolding rate at small force is due to the decreasing k_f, which again suggests that k_f cannot be ignored, especially at small forces. Eq. 2.34 further gives a way to fit all the four kinetic parameters using the constant force pulling experimental data.

2.9 Discussions

Any stable system should have a positive definite susceptibility because of the minimum free energy principle $\delta^2 G \geq 0$. Here in the force-extension type problem, stability implies $dF/dx \geq 0$. Violation of this inequality will lead to more complicated phenomena such as phase transitions of the system. When these occur, the force extension relation needs to be modified according to the loading history. In this section, we study the sign of dF/dx in our model. In particular, we focus on the case of constant velocity pulling condition. Other loading modes can be studied in a similar way.

For the constant velocity pulling condition, the three governing equations

are:

$$\begin{aligned} x &= N_f L_f + N_u L_u && (2.35)\\ dN_u/dt &= k_u N_f - k_f N_u && (2.36)\\ dx/dt &= v_c && (2.37) \end{aligned}$$

Here $L_f(F)$ and $L_u(F)$ are the extension of a single folded and unfolded protein under an extension force F.

We first take the derivative with respect to time t for Eq. 2.35 and get:

$$v_c = \frac{dN_u}{dt}(L_u - L_f) + \left(\frac{dL_f}{dF}N_f + \frac{dL_f}{dF}N_u\right)\frac{dF}{dt}. \quad (2.38)$$

This equation can be rearranged to obtain a formula for dF/dt:

$$\frac{dF}{dt} = \frac{v_c - \frac{dN_u}{dt}(L_u - L_f)}{N_f L_f' + N_u L_u'} \quad (2.39)$$

here $L_f' = dL_f/dF$ and $L_u' = dL_u/dF$.

Note that Eq. 2.39 is a decoupled ODE for $F(t)$ because all the quantities on the right-hand-side of the equation are only functions of F and t:

$$N_u = \frac{x - NL_f}{L_u - L_f} = \frac{x_0 + v_c t - NL_f(F)}{L_u(F) - L_f(F)}, \quad (2.40)$$

$$N_f = \frac{NL_u - x}{L_u - L_f} = \frac{NL_u(F) - x_0 - v_c t}{L_u(F) - L_f(F)}, \quad (2.41)$$

$$\frac{dN_u}{dt} = k_u(F)N_f(t,F) - k_f(F)N_u(t,F). \quad (2.42)$$

Also note that L_f and L_u are the length of a single folded/unfolded protein and they are functions of only F (true for both FJC (Eq. 2.12) and WLC).

Since $dx/dt = v_c > 0$, to determine the sign of dF/dx, we only need to study the sign of $\dot{F} = dF/dt$. Hence, we now focus on the $F-t$ plane. Eq. 2.39 tells us that the whole $F - t$ plane can be divided into 4 regions, depending on the signs of the numerator and denominator on the right hand side (see Table. 2.1).

The actual solution to the 3-equation system always satisfies $N_f \geq 0$ and $N_u \geq 0$. Also, it is generally true that $L_f' \geq 0$ and $L_u' \geq 0$, i.e, the length of a single folded/unfolded protein should increase with an increasing pulling force. Therefore the denominator term is always non-negative. Hence the actual solution for $F(t)$ always lies in region I or region II of Table. 2.1. In other words, region III and IV are forbidden.

Now we should study more carefully the numerator $(v_c - \dot{N}_u(L_u - L_f))$ in order to see whether the $F(t)$ curve is in region I (stable with $dF/dx > 0$) or

Region	Numerator	Denominator	dF/dt
I	$v_c - \dot{N}_u(L_u - L_f) > 0$	$N_f L'_f + N_u L'_u > 0$	$dF/dt > 0$
II	$v_c - \dot{N}_u(L_u - L_f) < 0$	$N_f L'_f + N_u L'_u > 0$	$dF/dt < 0$
III	$v_c - \dot{N}_u(L_u - L_f) > 0$	$N_f L'_f + N_u L'_u < 0$	$dF/dt < 0$
IV	$v_c - \dot{N}_u(L_u - L_f) < 0$	$N_f L'_f + N_u L'_u < 0$	$dF/dt > 0$

Table 2.1: Eq. 2.39 divides the $F - t$ plane into 4 regions with different signs of dF/dt.

region II (unstable with $dF/dx < 0$). To do this, we rewrite the numerator as:

$$\begin{aligned} v_c - \dot{N}_u(L_u - L_f) &= v_c - [k_u N_f - k_f N_u](L_u - L_f) && (2.43)\\ &= v_c - [N k_u - (k_u + k_f) N_u](L_u - L_f) && (2.44)\\ &= v_c - N k_u (L_u - L_f) - (k_u + k_f)(x - N L_f) && (2.45)\\ &= v_c - N k_u L_f - N k_f L_f + (k_u + k_f)(x_0 + v_c t) && (2.46) \end{aligned}$$

Based on Eq. 2.46, we define $T(F)$ as:

$$T(F) = \frac{N k_u L_u + N k_f L_f - (k_u + k_f) x_0 - v_c}{v_c (k_u + k_f)}, \tag{2.47}$$

then Eq. 2.46 implies:

$$v_c - \dot{N}_u(L_u - L_f) > 0 \quad \Leftrightarrow \quad t > T(F) \quad \Leftrightarrow \quad dF/dt > 0 \tag{2.48}$$

$$v_c - \dot{N}_u(L_u - L_f) < 0 \quad \Leftrightarrow \quad t < T(F) \quad \Leftrightarrow \quad dF/dt < 0 \tag{2.49}$$

Using this information, we could make some conclusions for the behavior of the $F(t)$ profile. Suppose we have one solution $F(t)$ which behaves as follows:

- For $t \in [t_0, t_1]$, $F(t)$ is a monotonically increasing function. Denote the inverse of this function as $t_I(F)$.
- For $t \in [t_1, t_2]$, $F(t)$ is a monotonically decreasing function, whose inverse is $t_{II}(F)$.

We argue that this is not possible in our model. The reason is: the curve $F(t)$ between $[t_1, t_2]$ is monotonically decreasing, so it is in region II. Therefore $t_{II} \leq T(F)$. But then we have $t_I(F) \leq t_{II}(F) \leq T(F)$ [2], this means $F(t)$ in $\in [t_0, t_1]$ is also monotonically decreasing. This violates our assumption that during $t \in [t_0, t_1]$, $F(t)$ is an increasing function. Therefore, we arrive at the conclusion that no negative slope is possible after a positive slope in the $F - t$ or $F - x$ profile.

[2]Since $F(t)$ first increases and then decreases, so the two regions share the same range of F

On the other hand, our model also has the property that $dF/dt > 0$ as $t \to +\infty$. To see this, note that at sufficiently large time t:

$$\begin{aligned} & v_c - Nk_uL_u - Nk_fL_f + (k_u + k_f)(x_0 + v_ct) && (2.50)\\ = \; & v_c + k_u(v_ct + x_0 - NL_u) + k_f(v_ct + x_0 - NL_f) && (2.51)\\ > \; & 0, && (2.52) \end{aligned}$$

because v_c, k_u and k_f are always positive and NL_f and NL_u are bounded for an inextensible chain. So at sufficiently large time, $t > T(F)$ and the $F(t)$ curve is always in region I.

The conclusions above suggest that there are only two kinds of $F(t)$ behaviors depending on its initial condition: If initially $dF/dt > 0$, then the force will monotonically increase for any $t > 0$. Otherwise, if initially $dF/dt < 0$, the $F(t)$ profile will first decrease, and then increase after some critical time t_r. Once it begins to increase, it can never decrease again.

Finally, we note that generally, we begin with a small force that is close to 0. If we assume $L_f(0)$ and $L_u(0)$ is very small such that:

$$v_c - Nk_u(0)L_u(0) - Nk_fL_f(0) + (k_u + k_f)x_0 \approx v_c > 0, \tag{2.53}$$

then the sign of dF/dt is always positive for all time t. In other words, generally, the force-extension profile should be monotonically increasing.

To summarize, under the following three assumptions, a negative slope plateau in the force-extension relation will never appear in our 3-equation model:

1. The system can be characterized by our 3 equations: Eq. 2.35 to Eq. 2.37. Note that in this section, no assumption of FJC or WLC is made, but the total extension is assumed to be the sum of the extensions of the sub-chains.

2. For a single folded or unfolded protein, if we increase the force, its length should increase: $L_f' > 0$, $L_u' > 0$. This is obviously true for both FJC and WLC.

3. k_f, k_u, L_f and L_u are smooth continuous functions with $(k_f + k_u)v_c > 0$.

2.10 Conclusions

We have obtained solutions to a kinetic two-state model for protein unfolding based on a heterogeneous FJC model and Bell's model. This model describes the forced unfolding of a chain of proteins under various kinds of loading conditions. Using this model we have obtained analytic solutions that can predict the response of a chain of proteins under a linearly increasing force or a constant force. The model can also be used to fit the experimental data from constant velocity pulling experiments, as we have demonstrated for ubiquitin

and fibrinogen. In particular, we have used the experimental data to solve directly for all the four kinetic parameters and predict the response of the proteins under a linearly increasing or constant force. Our solutions show that the refolding rate is much larger than the unfolding rate at zero force and that interesting physics is revealed if we account for the refolding rate at low forces. We argue that in general, the $F(t)$ or $F(x)$ profile is monotonically increasing under the assumptions listed in the main text. We also note that unfolding is a first order phase transition since some energy is required to go to the unfolded state and there is discontinuous change in the entropy per unit length.

Bibliography

[1] Rief M, Gautel M, Oesterhelt F, Fernandez JM, Gaub HE. **Reversible unfolding of individual titin immunoglobulin domains by AFM.** *Science* 1997;276:1109–1112.

[2] Oberhauser AF, Marszalek PE, Erickson HP, Fernandez JM. **The molecular elasticity of the extracellular matrix protein tenascin.** *Nature* 1998;393:181–185.

[3] Carrion-Vazquez M, Oberhauser AF, Fowler SB, Marszalek PE, Broedel SE, Clarke J, Fernandez JM. **Mechanical and chemical unfolding of a single protein: A comparison.** *Proc Natl Acad Sci USA* 1999;96:3694–3699.

[4] Schwaiger I, Sattler C, Hostetter DR, Rief M. **The myosin coiled-coil is a truly elastic protein structure.** *Nat Mater* 2002;1:232–235.

[5] Carrion-Vazquez M, Li H, Lu H, Marszalek PE, Oberhauser AF, Fernandez JM. **The mechanical stability of ubiquitin is linkage dependent.** *Nat Struct Biol* 2003;10:738–743.

[6] Fernandez JM, Li H. **Force-clamp spectroscopy monitors the folding trajectory of a single protein.** *Science* 2004;303:1674–1678.

[7] Chyan CL, Lin FC, Peng H, Yuan JM, Chang CH, Lin SH, Yang G. **Reversible mechanical unfolding of single ubiquitin molecules.** *Biophys J* 2004;87:3995–4006.

[8] Schlierf M, Li H, Fernandez JM. **The unfolding kinetics of ubiquitin captured with single-molecule force-clamp techniques.** *Proc Natl Acad Sci USA* 2004;101:7299–7304.

[9] Brown AE, Litvinov RI, Discher DE, Weisel JW. **Forced unfolding of coiled-coils in fibrinogen by single-molecule AFM.** *Biophys J* 2007;92:L39–L41.

[10] Bornschlog T, Rief M. **Single-molecule dynamics of mechanical coiled-coil unzipping.** *Langmuir* 2008;24:1338–1342.

[11] Lim BBC, Lee EH, Sotomayor M, Schulten K. **Molecular basis of fibrin clot elasticity.** *Structure* 2008;16:449–459.

[12] Bhasin N, Carl P, Harper S, Feng G, Lu H, Speicher DW, Discher DE. **Chemistry on a single protein, VCAM-1, during forced unfolding.** *J Biol Chem* 2004;279:45865–45874.

[13] Sotomayor M, Schulten K. **Single-molecule experiments in vitro and in silico.** *Science* 2007;316:1144–1148.

[14] Rief M, Fernandez JM, Gaub HE. **Elastically coupled two-level systems as a model for biopolymer extensibility.** *Phys Rev Lett* 1998;81:4764–4767.

[15] Bustamante C, Marko JF, Siggia ED, Smith S. **Entropic elasticity of lambda-phage DNA.** *Science* 1994;265:1599–1600.

[16] Marko JF, Siggia ED. **Stretching DNA.** *Macromolecules* 1995;28:8759–8770.

[17] Bell GI. **Models for specific adhesion of cells to cells.** *Science* 1978;200:618–627.

[18] Dudko OK, Hummer G, Szabo A. **Intrinsic Rates and Activation Free Energies From Single-Molecule Pulling Experiments.** *Phys Rev Lett* 2006;96:108101 (1-4).

[19] Nelson P. **Biological physics: energy, information, life.** New York: W.H. Freeman and Co., c2008.

[20] Su T. **A model for forced unfolding of proteins.** Tech. Report, Department of Mechanical Engineering and Applied Mechanics, University of Pennsylvania 2008;1–30.

[21] Fisher TE, Oberhauser AF, Carrion-Vazquez M, Marszalek PE, Fernandez JM. **The study of protein mechanics with the atomic force microscope.** *Trends Biochem Sci* 1999;24:379–384.

[22] Irback A, Mitternacht S, Mohanty S. **Dissecting the mechanical unfolding of ubiquitin.** *Proc Natl Acad Sci USA* 2005;102:13427–13432.

[23] Karcher H, Lee SE, Kaazempur-Mofrad MR, Kamm RD. **A coarse-grained model for force-induced protein deformation and kinetics.** *Biophys. J* 2006;90:2686–2697.

[24] Bustamante C, Chemla YR, Forde NR, Izhaky D. **Mechanical processes in biochemistry.** *Annu. Rev. Biochem* 2004;73:705–748.

[25] Best RB, Hummer G. **Protein folding kinetics under force from molecular simulation.** *J Am Chem Soc* 2008;130:3706–3707.

[26] Schlierf M, Rief M. **Temperature softening of a protein in single-molecule experiments.** *J Mol Biol* 2005;354: 407–503.

[27] Best RB, Paci E, Hummer G, Dudko OK. **Pulling direction as a reaction coordinate for the mechanical unfolding of single molecules.** *J Phys Chem B* 2008;112(19):5968–76.

[28] Imparato A, Pelizzola A, **Mechanical unfolding and refolding pathways of ubiquitin.** *Phys Rev Lett* 2008;100:158104.

[29] Cao Y, Li H. **Polyprotein of GB1 is an ideal artificial elastomeric protein.** *Nat Mater* 2007;6:109–114.

Part II

Heterogeneous Wormlike Chain Model and Its Applications

Chapter 3

Statistical Mechanics of a Discrete System with Quadratic Energy

Main results of this chapter:

1. Partition function of a discrete system with quadratic energy can be evaluated analytically. The free energy is determined by $\det \mathbf{M}$, where $\mathbf{M}$ is the system's stiffness matrix. The thermal fluctuation scales linearly with the temperature and inversely with $\mathbf{M}$.

2. There are two methods to analyze a statistical mechanical system with constraints. The first is to replace each constraint by an infinitely stiff spring. This corresponds to the penalty method in classical mechanics, especially in the finite element setting. The other method makes use of the Fourier transform of the Dirac delta function, which corresponds to the Lagrange multiplier method in classical mechanics.

The partition function of a continuous system is in general difficult to evaluate. However, by discretizing a continuous system into elements and reducing the degrees of freedom to a finite number, it is sometimes possible to obtain an analytic expression for the partition function and all other thermodynamic properties. In this chapter, we will first study a discrete system under no constraints and then discuss the consequences of adding constraints into the system. In specific problems, as we shall see in the chapters that follow, constraints are usually introduced into the system by posing different boundary

conditions.

3.1 General Theory

Consider a discrete system having D degrees of freedom characterized by a finite set of independent variables:

$$\vec{\theta}^{\,T} = [\,\theta_1, \theta_2, \cdots, \theta_D\,]. \tag{3.1}$$

Assume the Hamiltonian of the system takes the quadratic form:

$$\mathcal{H} = \frac{1}{2}\vec{\theta}^{\,T}\mathbf{M}\cdot\vec{\theta} + \mathcal{H}_0, \tag{3.2}$$

where $\mathbf{M}$ and $\mathcal{H}_0$ are the symmetric stiffness matrix and the ground state energy of the system respectively.

The partition function of the system is the sum of all the allowed states weighted by the Boltzmann factor:

$$Z = \int \exp\left[-\frac{1}{2}\,\vec{\theta}^{\,T}\,(\beta\mathbf{M})\cdot\vec{\theta} - \beta\mathcal{H}_0\right]\,d\vec{\theta}, \tag{3.3}$$

with $\beta = 1/k_BT$, k_B being the Boltzmann constant and T being the temperature in Kelvin.

Using the multidimensional Gaussian integral, Eq. 3.3 can be evaluated analytically (see reference [1, 2] and Appendix A):

$$Z = \exp\left(-\beta\mathcal{H}_0\right)\,\sqrt{\frac{(2\pi k_BT)^D}{\det\mathbf{M}}}. \tag{3.4}$$

Here we assume the limits of the integral in Eq. 3.3 are $\pm\infty$. If the range of $\vec{\theta}$ is finite, like an angle typically lies only in the interval of $[-\pi, \pi]$, we can first extend the integral to $\pm\infty$, then Eq. 3.4 is an asymptotic approximation for the partition function. Such an approximation is good when the eigenvalues of $\mathbf{M}$ are large, in which case the energy well is steep and states that are far away from $\vec{\theta} = \vec{0}$ have high energies and extremely small contributions to the partition function [1]

The free energy of the system is $G = -k_BT\log Z$:

$$2\beta G = \log(\det\mathbf{M}) - D\log(2\pi k_BT) + 2\beta\mathcal{H}_0. \tag{3.5}$$

All thermodynamic properties of the system can be derived from the free energy and their expressions depend on the ensemble we use.

[1] If the energy well is not steep, the quadratic approximation may break down. In this case, we need to consider higher order approximation for the energy well. For example, in 1D case, if the energy takes the form $E(x) = ax^2 + bx^4$, then the partition function is $Z = \int_{-\infty}^{+\infty}\exp\left(-\beta ax^2 - \beta bx^4\right)dx = \sqrt{a/4b}\,\exp(\beta a^2/8b)\,K_{1/4}(\beta a^2/8b)$, where a, b are constants and $K_{1/4}(z)$ is the modified Bessel function of the second kind of order 1/4.

Fluctuation of the system can also be evaluated analytically and it is governed by the inverse of the stiffness matrix $\mathbf{M}$ [1, 2]. This makes sense because the stiffer the system is, the less thermal fluctuations it experiences:

$$\langle \theta_i \cdot \theta_j \rangle = \frac{1}{Z} \int (\theta_i \theta_j) \exp\left[-\frac{1}{2} \vec{\theta}^T (\beta \mathbf{M}) \cdot \vec{\theta} - \beta \mathcal{H}_0 \right] d\vec{\theta} = k_B T \left(\mathbf{M}^{-1} \right)_{ij}. \quad (3.6)$$

From Eq. 3.6, we see that $\langle \theta_i \cdot \theta_j \rangle \sim T$ because the stiffness matrix $\mathbf{M}$ is independent of temperature. This relation is a natural generalization of the fluctuation in a 1D system discussed in the *Introduction* of this proposal (Eq. 1.11).

Finally, the Equipartition theorem can be derived directly from Eq. 3.6:

$$\langle \mathcal{H} \rangle - \mathcal{H}_0 = \frac{1}{2} \sum M_{ij} \langle \theta_i \theta_j \rangle = \frac{k_B T}{2} \sum M_{ij} \left(M^{-1} \right)_{ij} = D k_B T / 2. \quad (3.7)$$

Here we have used the fact that $\mathbf{M}$ is a symmetric matrix with dimension $D \times D$.

If the system is decoupled such that the stiffness matrix $\mathbf{M}$ is diagonal:

$$\mathcal{H} = \frac{1}{2} \sum_{i=1}^{D} M_i \theta_i^2 + \mathcal{H}_0, \quad (3.8)$$

then the fluctuation reduces to:

$$\langle \theta_i \theta_j \rangle = \delta_{ij} \frac{k_B T}{M_{ij}}, \quad (3.9)$$

where δ_{ij} is the Kronecker delta function.

The theory described above assumes that the Hamiltonian is a quadratic function of the independent variables θ_i. In general, the Hamiltonian can take various complicated forms. But as long as it has a well-defined ground state $\vec{\theta}^0$, we can always expand the Hamiltonian around $\vec{\theta}^0$ and approximate the ground state energy up to the 2nd order. In this case, the results we obtained above are the asymptotic solutions based on the Laplace method in complex variable theory [3]. Such asymptotic solutions reflect the fluctuation of the system around its ground state and they are good approximations when the energy well is steep, in which case the states far away from the ground state are not important because they have high energies and extremely small Boltzmann factors.

3.2 Statistical Mechanics of a Constrained System: Method 1

Consider the same discrete system characterized by $[\, \theta_1, \theta_2, \cdots, \theta_D \,]$ with a quadratic Hamiltonian shown in Eq. 3.2. Now suppose not all the θ_i are independent, instead, they are constrained by:

$$g_i(\vec{\theta}) = 0 \quad (i = 1, 2, \cdots, p), \quad (3.10)$$

where p is the number of constraints on the system.

The partition function is the sum of Boltzmann weights for all the allowed configurations. Therefore, only those configurations satisfying the constraints g_i can be taken into account:

$$Z = \int \exp\left(-\beta\mathcal{H}\right)\ \delta(g_1)\,\delta(g_2)\cdots\delta(g_p)\,d\vec{\theta}, \tag{3.11}$$

To evaluate Eq. 3.11, we make use the definition of the Dirac δ function:

$$\delta(x) = \lim_{k\to+\infty}\left\{\frac{k}{\sqrt{\pi}}\exp\left[-(kx)^2\right]\right\}. \tag{3.12}$$

Plugging Eq. 3.12 into Eq. 3.11, we get [2]:

$$Z = \lim_{k_i\to+\infty}\left[\frac{\prod_{i=1}^{p}k_i}{(k_BT\pi)^{p/2}}\ \int\exp\left(-\beta\mathcal{H}_{\text{eff}}\right)\ d\vec{\theta}\right], \tag{3.13}$$

where the effective Hamiltonian for the constrained system is:

$$\mathcal{H}_{\text{eff}} = \mathcal{H} + \sum_{i=1}^{p}(k_ig_i)^2. \tag{3.14}$$

Hence, by using the definition of δ function, we have changed the constrained system to an effective unconstrained one. By looking at Eq. 3.14, it is as if we have replaced each constraint with a stiff spring. This is exactly the idea of the penalty method for solving constrained optimization problems in finite element analysis [4]. As we shall see in the following chapters, to compute the fluctuation of a discrete system, the first step is to find the configuration that minimizes the Halmiltonian. For a system with constraints on its kinematic variables, theories of the penalty methods that determine the static configuration of the system can be used for this step.

Further, the free energy of the constrained system is $G = -k_BT\log Z$. Using Eq. 3.13, it can be expressed as (from here, we omit writing $\lim_{k_i\to+\infty}$. All the results below hold as k_i approach infinity.):

$$G = G_{\text{eff}} + G_0(T), \tag{3.15}$$

where the reference G_0 is:

$$G_0(T) = \frac{p}{2}k_BT\log(k_BT\pi) - k_BT\sum_{i=1}^{N}\log k_i. \tag{3.16}$$

The fluctuation of the system is:

$$\langle\theta_i\theta_j\rangle = \frac{1}{Z}\cdot\lim_{k_i\to+\infty}\left[\frac{\prod_{i=1}^{p}k_i}{(k_BT\pi)^{p/2}}\ \int\left(\theta_i\theta_j\right)\ \exp\left(-\beta\mathcal{H}_{\text{eff}}\right)\ d\vec{\theta}\right] = \langle\theta_i\theta_j\rangle_{\text{eff}}. \tag{3.17}$$

Therefore, the fluctuation of the effective unconstrained system approaches the fluctuation of the constrained system as $k_i\to+\infty$.

[2] Here, we change the variable from $k_BTk_i \to k_i$.

3.3 Statistical Mechanics of a Constrained System: Method 2

Zhang & Crothers [1] and later Su & Purohit [2] have used another method to evaluate the partition function with constraints and we briefly summarize their method in this section. Instead of using the definition of the δ function shown in Eq. 3.12, they use the Fourier transform of the δ function:

$$\delta(x) = \frac{1}{2\pi} \int_{-\infty}^{+\infty} \exp(Ikx) dk, \tag{3.18}$$

where $I = \sqrt{-1}$ is the imaginary unit.

Plugging Eq. 3.18 into the partition function Eq. 3.11, we get:

$$Z = \frac{1}{(2\pi)^p} \int \exp\left(-\beta \mathcal{H}_{\text{eff}}\right) d\vec{\theta}\, d\vec{k}, \tag{3.19}$$

where $\vec{k} = [k_1, k_2, \cdots k_p]$ and the effective Hamiltonian for the constrained system is:

$$\mathcal{H}_{\text{eff}} = \mathcal{H} - k_B T I \sum_{i=1}^{p} k_i g_i, \tag{3.20}$$

Here again we have changed the constrained system into an unconstrained one with the price of introducing p more independent variables k_i. The free energy and fluctuation of the system can be evaluated in the same way as we discussed before.

3.4 An Example

To illustrate the general theory discussed above, we consider a simple coupled harmonic spring system shown in Fig. 3.1. Two balls are attached to three springs with the same spring constant k. The system has two degrees of freedom: x_1 and x_2 being the displacements of the two balls from their equilibrium positions. The Hamiltonian of the system is:

$$\mathcal{H} = \frac{1}{2} k x_1^2 + \frac{1}{2} k x_2^2 + \frac{1}{2} k (x_1 - x_2)^2. \tag{3.21}$$

The stiffness matrix constructed from Eq. 3.21 is:

$$\mathbf{M} = \begin{bmatrix} 2k & -k \\ -k & 2k \end{bmatrix} \tag{3.22}$$

Hence, using Eq. 3.6, the fluctuation of the system is:

$$\langle x_i x_j \rangle = k_B T \left(\mathbf{M}^{-1}\right)_{ij} = \frac{k_B T}{3k} \begin{bmatrix} 2 & 1 \\ 1 & 2 \end{bmatrix} \tag{3.23}$$

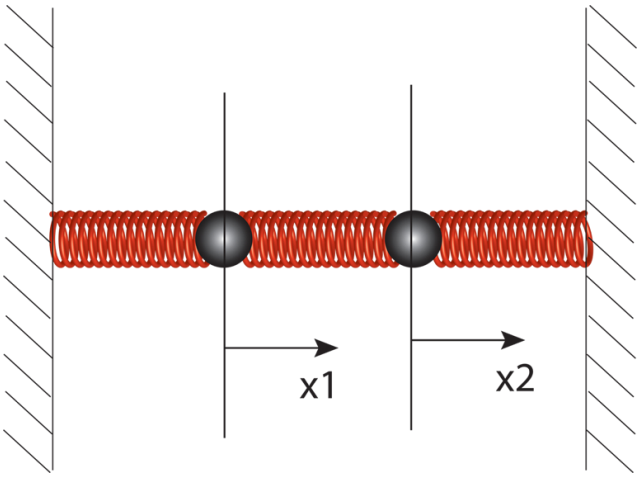

Figure 3.1: A simple coupled harmonic spring system with two balls attached to three springs. All three springs have the same spring constant k and natural length L. The degrees of freedom for this discrete system are two, characterized by x_1 and x_2, the displacements of the two balls away from their equilibrium positions.

Now suppose we have an additional constraint $x_1 = x_2$, i.e, the two balls are further connected by a rigid bar. The first method is to replace the constraint by a stiff spring k_c and the effective Hamiltonian of the system becomes:

$$\mathcal{H} = \frac{1}{2}kx_1^2 + \frac{1}{2}kx_2^2 + \frac{1}{2}(k + k_c)(x_1 - x_2)^2. \tag{3.24}$$

The stiffness matrix constructed from Eq. 3.24 is:

$$\mathbf{M} = \begin{bmatrix} 2k + k_c & -k - k_c \\ -k - k_c & 2k + k_c \end{bmatrix} \tag{3.25}$$

So the fluctuation of the system is:

$$\langle x_i x_j \rangle = k_B T \lim_{k_c \to +\infty} \left(\mathbf{M}^{-1}\right)_{ij} = \frac{k_B T}{2k} \begin{bmatrix} 1 & 1 \\ 1 & 1 \end{bmatrix}. \tag{3.26}$$

This makes sense because the system with constraint $x_1 = x_2$ is just like a rigid bar connected by two springs. The effective spring constant is $2k$.

For the method that uses Fourier transform of the δ-function, the effective Hamiltonian of the system is:

$$\mathcal{H} = \frac{1}{2}kx_1^2 + \frac{1}{2}kx_2^2 + \frac{1}{2}k(x_1 - x_2)^2 - Ik_c k_B T(x_1 - x_2). \tag{3.27}$$

The corresponding stiffness matrix constructed from Eq. 3.27 has three degrees of freedom:

$$\mathbf{M} = \begin{bmatrix} 2k & -k & -k_B TI \\ -k & 2k & k_B TI \\ -k_B TI & k_B TI & 0 \end{bmatrix} \tag{3.28}$$

The inverse of $\mathbf{M}$ multiplied by the thermal energy gives the fluctuation $\langle x_i x_j \rangle = k_B T/2k$, which is exactly the same as the result using the previous method (Eq. 3.26).

Bibliography

[1] Zhang Y, Crothers DM. 2003. **Statistical mechanics of sequence-dependent circular DNA and its application for DNA cyclization.** *Biophys. J.* 84(1), 136-153.

[2] Su T, Purohit PK. 2010, **Thermomechanics of a heterogeneous fluctuating chain.** *J. Mech. Phys. Solids.* 58:164-186.

[3] Carrier GF, Krook M, Pearson CE. 2005. **Functions of a Complex Variable: Theory and Technique**, Society for Industrial and Applied Mathematics, Philadelphia, PA.

[4] Kythe PK, Wei D. 2003. **An introduction to linear and nonlinear finite element analysis: a computational approach.** *Birkhäuser.*

Chapter 4

Heterogeneous Wormlike Chain Under End-to-end Force

Main results of this chapter:

1. Statistical mechanical properties of a general heterogeneous chain under various boundary conditions are evaluated using the multidimensional Gaussian integral technique.
2. All thermodynamic properties of a chain can be expressed in terms of an energy function which is measurable in a single force-extension experiment. Formulae in terms of this energy function hold for any heterogeneous chain under any boundary condition.
3. Folded and unfolded proteins are expected to have different mechanical properties. Here the theory for a heterogeneous chain with two bending moduli is applied to predict the force-extension profile for the forced unfolding of a protein oligomer.

4.1 Introduction

Single molecule mechanical experiments on rod-like biomolecules, such as, DNA and actin have for long been interpreted using a model of a homogeneous fluctuating elastic rod [1, 2, 3, 4]. However, advanced single molecule techniques are now capable of probing the structure and properties of macromolecules at length scales of a few nanometers. At these length scales it is no longer sufficient to think of the molecules as having homogeneous mechanical

properties. In fact, several recent studies have revealed the remarkable effects of the heterogeneous properties of some biopolymers on their conformations as well as their mechanical behavior [5, 6]. For example, heterogeneous mechanical properties are encountered in partially unfolded protein oligomers in atomic force microscopy [7]. Sequence specific mechanical properties of DNA are already well known and it has been suggested that DNA binding proteins can sense these heterogeneities, making them biologically significant [8, 9, 10]. Also, it has been noted that localized softening in DNA can have significant influence on looping probabilities which ultimately affect genetic activity [11, 12]. These examples show that heterogeneous mechanical properties have been observed in experiments on biomolecules and that even at relatively large length scale, they can have significant biological consequences which the homogeneous models cannot caputre. They motivate us to examine the consequences of heterogeneity through detailed mathematical models.

A simple way of introducing heterogeneity in polymer models is to group monomers into hydrophilic and hydrophobic types as has been done in some recent articles [13, 14]. Another model which accounts for heterogeneity is the two-state wormlike chain model of [15], which reduces to the fluctuating rod model in the low force limit, and to the Ising model at high forces [15]. The approach in this chapter is different from these methods in that we allow the bending modulus $K_b(s)$ of our fluctuating rod to vary as an arbitrary function of the arc length s. We first evaluate the partition function of the rod in a constant force and constant temperature ensemble, and then compute the free energy and a host of other thermal and mechanical properties of the rod. The results are verified through Monte Carlo simulations. A special case of our model is one in which there are only two possible values of the bending modulus K_I and K_{II} along the chain. We call this the 'special heterogeneous chain' and use it to interpret the force-extension data from the forced unfolding experiments on protein oligomers.

Our method also allows us to determine the consequences of constraints imposed on the rod. In particular, we can determine the force-extension relation and the magnitude of transverse fluctuations under different types of boundary conditions. Boundary conditions siginificantly affect the fluctuations if the length of the rod is comparable or shorter than its persistence length [16]. The effect of boundary conditions on the fluctuations of homogeneous rods has been analyzed only recently by a few authors [17]. In this chapter we apply three different boundary conditions on the rod and compare our results with those of [17] for homogeneous rods and find excellent agreement. The method used in this chapter is more general than that of [17] which is based on the equipartition theorem and can only be applied to homogeneous rods.

This chapter is organized as follows. We first use the equipartition theorem to derive some general results for heterogeneous chains with arbitrary boundary conditions. We then demonstrate a method for calculating the thermomechanical properties of chains and rods under three different boundary conditions. We use Monte Carlo simulations and comparisons with earlier work

to show that our method gives accurate results. Finally, we apply our method to interpret data from force-extension experiments on the protein ubiquitin.

4.2 Description of the Heterogeneous Worm-like Chain Model

Below we study the thermo-mechanical properties of a fluctuating heterogeneous elastic chain. A theory for a 2D chain is presented first and then the results are generalized to 3D.

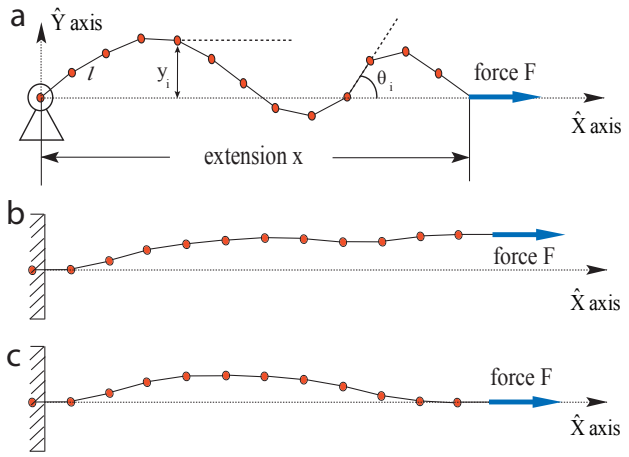

Figure 4.1: Model of the 2D chain. A thermally fluctuating $N-$segment 2D chain is subjected to an external applied force $\vec{F} = F\hat{X}$. The configuration of the chain is characterized by its N tangent angles θ_i, formed by the segments with respect to the $\hat{X}$ axis. The transverse displacement of the chain, denoted by y_i in the figure, reflects how much the chain fluctuates. (a) Hinged-hinged boundary conditions: both ends of the chain are constrained on the $\hat{X}$ axis, but no moment is acting on them; (b) partially clamped boundary conditions: one end of the chain is clamped on the $\hat{X}$ aixs while the other end, with slope also constrained to be zero, is free to have transverse displacement in the Y direction. (c) clamped-clamped boundary conditions: both ends are clamped on the $\hat{X}$ axis.

Let $\{\hat{X}, \hat{Y}\}$ be a standard reference dyad in 2D space, an N-segment chain with one end fixed at the origin and the other end subjected to an external force $\vec{F} = F\hat{X}$ is fluctuating around its equilibrium state. As shown in Fig. 6.1, each configuration of the chain is characterized by N tangent angles θ_i, formed by the segments with respect to the $\hat{X}$ axis. We assume that (1) the length of the segment l is a constant independent of the applied force, and therefore, the chain is inextensible with contour length being $L = Nl$; (2) the chain is untwistable [1]. Therefore, the elastic energy of the chain arises only from

[1] Although twist may be important in some cases, we neglect it here and focus on (1)

bending and it is given by:

$$E = \sum_{i=1}^{N-1} \frac{K_i}{2l}(\theta_{i+1} - \theta_i)^2, \tag{4.1}$$

where K_i is the bending modulus that varies along the heterogeneous chain. A continuum version of this energy is obtained by taking the limit as $l \to 0$ and $N \to \infty$ while $Nl = L$ remains fixed and is given by:

$$E_{\text{rod}} = \int_0^L \frac{K(s)}{2}\dot{\theta}(s)^2 ds, \tag{4.2}$$

where s is the arc length along the rod and $\dot{\theta}$ is the derivative of θ with respect to s.

Up to a quadratic approximation, the Hamiltonian of the chain (or rod in the continuum limit) in a fixed T (temperature in Kelvin) and F (force) ensemble is:

$$\begin{aligned} \beta(E - Fx) &= \int_0^L \frac{\beta K(s)}{2}\dot{\theta}(s)^2 ds - \beta F \int_0^L \cos\theta ds & (4.3)\\ &\approx \beta \sum_{i=1}^{N-1} \kappa_i(\theta_{i+1} - \theta_i)^2 + \beta f \sum_{i=1}^{N} \theta_i^2 - \beta FL, & (4.4) \end{aligned}$$

where $\beta = (k_B T)^{-1}$ and k_B is the Boltzmann constant, x is the extension (end-to-end distance projected onto the $\hat{X}$ axis) of the chain and κ_i, f are respectively the bending modulus and the force in energy units:

$$\kappa_i = \frac{K_i}{2l}, \quad f = \frac{Fl}{2}. \tag{4.5}$$

For a short chain whose contour length L is comparable to its persistence length $\xi_p \sim K/k_B T$ [2], we expect the thermomechanics and the fluctuation of the chain to depend on the boundary conditions. We consider three different boundary conditions in this chapter (Fig. 6.1): (1) hinged-hinged chain: both ends of the chain are hinged on the $\hat{X}$ axis with no moments acting on them; (2) partially clamped chain: one end of the chain is clamped at the origin while the other end, with slope constrained to be zero, is free to have transverse displacement in the Y direction. (3) clamped-clamped chain: both ends of the chain are clamped on the $\hat{X}$ axis. All these three boundary conditions have been realized in experiments using different types of apparatuses [17]. Note that for a long chain with $L >> \xi_p$, we expect the thermomechanics of the chain to be insensitive to the boundary conditions.

---

the effects of heterogeneity and (2) different boundary conditions. Reference [4] gives some explanation on the simplification of the twisting energy.

[2]Here we define the persistence length ξ_p as $\langle \hat{t}(s_0) \cdot \hat{t}(s_0 + s)\rangle = e^{-s/\xi_p}$, where $\hat{t}$ is the unit tangent vector of the chain. This definition leads to $\xi_p = 2K/k_B T$ for a 2D chain and $\xi_p = K/k_B T$ for a 3D chain [19]

4.3 General Theory

For a chain in a fixed temperature T and F ensemble, the partition function is:

$$Z = \sum_{\nu} \exp\left[\, -\beta \left(E_\nu - F x_\nu\right) \right], \tag{4.6}$$

where the summation is over all the allowed configurations ν, with E_ν and x_ν respectively being the energy and the extension of the chain. From the definition of the partition function (Eq. 4.6), we get:

$$\langle E - Fx \rangle = \frac{1}{Z} \sum_{\nu} (E_\nu - F x_\nu) \exp\left[\, -\beta \left(E_\nu - F x_\nu\right) \right] = -\left(\frac{\partial \log Z}{\partial \beta} \right)_F, \tag{4.7}$$

where $\langle A \rangle$ denotes the ensemble average of a quantity A and 'log' denotes the natural logarithm in this chapter.

On the other hand, since the Hamiltonian is quadratic in the configuration angles θ_i (Eq. 4.4), we have the equipartition theorem for a fixed T, F ensemble:

$$\langle E - Fx + FL \rangle = \frac{D}{2} k_B T, \tag{4.8}$$

where D is the number of degrees of freedom of the system.

Eq. 4.7 together with Eq. 4.8 leads to a partial differential equation for the partition function Z:

$$\left(\frac{\partial \log Z}{\partial \beta} \right)_F = -\frac{D}{2\beta} + FL, \tag{4.9}$$

integrating which we get:

$$\log Z = -\frac{D}{2} \log \beta + FL\beta - W(F), \tag{4.10}$$

where $W(F)$ is an unknown function of F. Note that Eq. 4.10 holds for any heterogeneous chain with any boundary condition, and all this information is included in $W(F)$, which is independent of the temperature T. Also, regarding to the units in Eq. 4.10, we shall see in the later sections (Eq. 4.34, Eq. 4.49 and Eq. 4.60) that $W(F)$ includes D terms of the logarithm of quantities in energy units, which combine with the term $-\frac{D}{2} \log \beta$ in Eq. 4.10 to make the argument of the 'log' dimensionless.

Using the relation between the partition function Z and the free energy G, we obtain $G(T, F)$ expressed in terms of $W(F)$:

$$G(T, F) = -k_B T \log Z = \frac{D}{2\beta} \log \beta - FL + \frac{W(F)}{\beta}. \tag{4.11}$$

Eq. 4.11 shows how the free energy $G(T, F)$ depends on T and F up to an unkown function $W(F)$. Note that $G(T, F)$ is the fundamental quantity for a

fixed T, F ensemble because all thermo-mechanical quantities can be derived from it [18]. Here, by using the equipartition theorem, we have been able to deduce a form for $G(T, F)$ in which the dependences on T and F are conveniently decoupled. All thermo-mechanical quantities can now be expressed in terms of $W(F)$. More importantly, we will see that $W(F)$ and its derivative, which we denote as $\Delta(F) = W'(F)$, have clear physical meanings and unlike $G(T, F)$, can be measured directly in a single force-extension experiment.

We derive the thermo-mechanical quantities in terms of $W(F)$ and its derivatives $\Delta(F)$, $\Delta'(F)$ below. The entropy of the chain is given by:

$$S = -\left(\frac{\partial G}{\partial T}\right)_F = \frac{1}{2} D k_B \left[\, 1 + \log(k_B T) \,\right] - k_B W(F). \tag{4.12}$$

Eq. 4.12 shows that the contributions of T and F to the entropy are decoupled.

The extension of the chain is given by a simple formula:

$$\langle x \rangle = -\left(\frac{\partial G}{\partial F}\right)_T = L - k_B T \cdot \Delta(F). \tag{4.13}$$

where again $\Delta(F)$ is the derivative of $W(F)$: $\Delta(F) = W'(F)$. Note that as a special case, the well-known formula for the 2D hinged-hinged homogeneous wormlike chain has exactly the form of Eq. 4.13, with $\Delta(F)$ given by [17]:

$$\Delta_{\text{homo}}(F) = \frac{1}{4}\left[\frac{L}{\sqrt{KF}} \coth\left(\frac{FL}{\sqrt{KF}}\right) - \frac{1}{F}\right]. \tag{4.14}$$

It is interesting that the simple expression Eq. 4.13 holds for any general chain, with all the complexity of the heterogeneity and boundary information appearing only in the function $\Delta(F)$. Also note that the dependence on T of $\langle x \rangle$ is the same for all chains with any heterogeneity and boundary conditions (Eq. 4.13). In fact, this conclusion is true for all the thermo-mechanical quantities shown below.

More importantly, Eq. 4.13 implies that the unknown function $\Delta(F)$ is actually the 'shrinking' of the chain $(L - \langle x \rangle)$ scaled by the inverse of the thermal energy $\beta = (k_B T)^{-1}$. Therefore, this unkown function of F can be measured in a single force-extension experiment and its independence of T can also be tested. Further, to reveal the physical meaning of $W(F)$, we integrate Eq. 4.13 with respect to F once to get:

$$k_B T \cdot W(F) = LF - \int \langle x \rangle dF. \tag{4.15}$$

The integral on the right-hand-side of Eq. 4.15 is the complementary energy of the chain (Fig. 4.2), therefore, $k_B T \cdot W(F)$ is the difference between LF and the complementary energy, which corresponds to the shaded area beneath the force-extension curve shown in Fig. 4.2 and can be measured in a single force-extension experiment. Once $W(F)$ and $\Delta(F)$ are measured, all the other

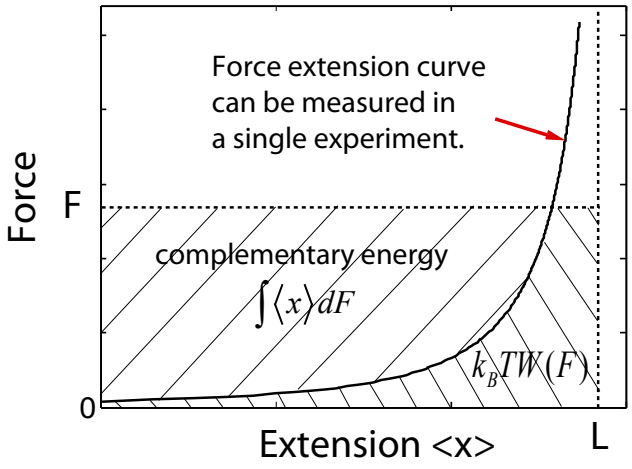

Figure 4.2: The unkown function $W(F)$ can be measured in a single force extension experiment. The shaded area above the force-extension curve is the complementary energy and the area beneath the force-extension curve is $k_BT \cdot W(F)$ by Eq. 4.15.

thermo-mechanical properties of the chain are known, as we will show below. We note that $k_BT \cdot W(F)$ is not exactly the energy stored in the chain, which is $\int F dx = Fx - \int x dF$. We also note that $W(F)$ can only be measured up to a constant because of the indefinite integral in Eq. 4.15. However, this constant will not appear in $\Delta(F)$, which is the derivative of $W(F)$.

The variance of extension is related to the derivative of $\langle x \rangle$ with respect to F [18] and it is given by:

$$\langle (\Delta x)^2 \rangle = k_B T \left(\frac{\partial \langle x \rangle}{\partial F} \right)_T = -(k_B T)^2 \cdot \Delta'(F), \tag{4.16}$$

where Eq. 4.13 has been used. Eq. 4.16 implies that the variance of extension always scales as T^2. Note that $\langle (\Delta x)^2 \rangle$ is non-negative, so $\Delta'(F) \leq 0$ and therefore $\Delta(F)$ is a decreasing function, as it should be, because it is the 'shrinking' of a chain under a force F.

Using basic thermodynamic relations [18], the average energy of the chain and its variance can also be expressed in term of $\Delta(F)$ and $\Delta'(F)$:

$$\langle E \rangle = \langle E - Fx \rangle + F\langle x \rangle = k_B T \left[\frac{D}{2} - F \cdot \Delta(F) \right], \tag{4.17}$$

$$\langle (\Delta E)^2 \rangle = -\left(\frac{\partial \langle E \rangle}{\partial \beta} \right)_{F/T} = (k_B T)^2 \left[\frac{1}{2} D - 2F\Delta(F) - F^2 \Delta'(F) \right] \tag{4.18}$$

Thermo-mechanical properties, such as heat capacity C_F, coefficient of thermal expansion α as well as the isothermal extensibility χ, are second derivatives of the free energy G [18]. Using Eq. 4.11, Eq. 4.12 and Eq. 4.13,

we get:

$$C_F = T\left(\frac{\partial S}{\partial T}\right)_F = \frac{k_B D}{2}, \tag{4.19}$$

$$\alpha = \frac{1}{\langle x\rangle}\left(\frac{\partial \langle x\rangle}{\partial T}\right)_F = \frac{-k_B \cdot \Delta(F)}{\langle x\rangle} = \frac{1}{T\,[\,1-\beta L/\Delta(F)\,]}, \tag{4.20}$$

$$\chi = \frac{1}{\langle x\rangle}\left(\frac{\partial \langle x\rangle}{\partial F}\right)_T = \frac{-k_B T \cdot \Delta'(F)}{\langle x\rangle} = \frac{\Delta'(F)}{\Delta(F)-\beta L}. \tag{4.21}$$

Note that the heat capacity C_F is a constant independent of both T and F.

From Eq. 4.20, we find that the inverse of the coefficient of thermal expansion is linear with respect to T:

$$\frac{1}{\alpha} = T - \frac{L}{k_B \cdot \Delta(F)}. \tag{4.22}$$

This can be tested in a single thermal expansion experiment with constant force F acting at the end of the chain. We further note that the condition $\langle x\rangle \in [0, L]$ on Eq. 4.13 leads to $\alpha \leq 0$ in Eq. 4.22, which means the chain shrinks in response to an increase in temperature.

Moreover, Eq. 4.13 combined with Eq. 4.20 suggests that if one does a force-extension experiment and a thermal expansion experiment, one should find the results of the two experiments related by:

$$\frac{\langle x\rangle}{L} = \frac{1}{1-\alpha T}, \tag{4.23}$$

with both sides evaluated at the same F and T. Note that this relation (Eq. 4.23) does not invlove the unknown function $W(F)$ and therefore it is not affected by the heterogeneity and boundary condition of the chain. It (Eq. 4.23) implies that a stiffer chain, which has a larger value of $\langle x\rangle$/L, will have a smaller value of $|\alpha|$ and therefore is less sensitive to the change of temperature. In addition, Eq. 4.23 constitutes a falsifiable prediction of our theory and can be tested in experiments.

To sum up, we have been able to express the thermo-mechanical properties for any heterogeneous chain with any boundary conditions in terms of a single-variable unknown function $W(F)$, instead of $G(T, F)$ and $Z(T, F)$. Moreover, unlike $G(T, F)$ and $Z(T, F)$, $W(F)$ and its derivative $\Delta(F)$ have clear physical meanings and are easy to measure in a single force-extension experiment using Eq. 4.13[3]. Therefore, by doing a single experiment, one can get all the thermo-mechanical properties for the chain, without assuming the chain is homogeneous and regardless of the type of boundary condition applied. Finally,

[3]Note that the shrinking $\Delta(F)$ can be measured directly while the energy $W(F)$ can be measured only up to an undetermined constant. But, from Eq. 4.13 to Eq. 4.21, we see that most of the thermo-mechanical quantities are expressed only in terms of $\Delta(F)$, instead of $W(F)$, so they can be determined exactly by measuring $\Delta(F)$.

we note that the results in this section hold for the 2D chains as well as the 3D chains except that the prefactor in Eq. 4.14 should be replaced by 1/2 in 3D case (see [19] and also the discussions on the relation between 2D and 3D chains in the latter section 4.8).

4.4 Hinged-hinged 2D chain

As has been shown in the previous section, all the thermo-mechanical quantities can be expressed in terms of $W(F)$ and its derivatives. In what follows we obtain analytic expressions for this function for a general 2D heterogeneous chain with hinged-hinged boundary conditions.

For a hinged-hinged chain (Fig. 6.1(a)), one end of the chain is fixed at the origin while the other end is constrained on the $\hat{X}$ aixs, in other words, the Y coordinate of the end of the chain is 0. This position constraint expressed in terms of the configuration tangent angles θ_i is:

$$g(\theta_i) = \frac{1}{l} \cdot \int_0^L \sin\theta \, ds \approx \sum_{i=1}^{N} \theta_i = 0. \tag{4.24}$$

g is called the constraint function and it has been nondimensionalized. We will use the Laplace method [20] below to evaluate the partition function, so it is sufficient to expand $\sin\theta$ up to the first order in Eq. 4.24 (see the discussions below and also footnote 4).

The partition function (Eq. 4.6), which sums over all the allowed configurations determined by the constraint function $g(\theta_i)$ (Eq. 4.24), can be written in an integral form:

$$Z = \int_{-\infty}^{+\infty} \cdots \int_{-\infty}^{+\infty} \exp\left[\, -\beta(E - Fx) \,\right] \delta(g) \, d\vec{\theta}, \tag{4.25}$$

where $d\vec{\theta} = [\, d\theta_1 \, d\theta_2 \cdots d\theta_N \,]$ and $\delta(g)$ is the Dirac delta function acting on $g(\theta_i)$.

Note that the exact integral limits should be $\theta_i = \pm\pi$. But, noticing that the term $\beta(E - Fx)$ reaches its minimum value $(-\beta FL)$ at $\theta_i \equiv 0$, we have applied the Laplace method to approximate the integral by extending its limit to $\theta_i = \pm\infty$ [20]. Further, by using the Fourier transform of the Dirac delta function δ [20]:

$$\delta(g) = \frac{1}{2\pi} \int_{-\infty}^{+\infty} \exp(Ikg) dk, \tag{4.26}$$

where I is the imaginary identity that satisfies $I^2 = -1$, we can rewrite the partition function Eq. 4.25 as:

$$Z = \frac{1}{2\pi} \int_{-\infty}^{+\infty} \cdots \int_{-\infty}^{+\infty} \exp\left[-\beta(E - Fx) + Ikg\right] \; d\vec{\theta} \, dk. \tag{4.27}$$

Consider the exponent in the partition function Eq. 4.27: the Hamiltonian $\beta(E - Fx)$ is quadratic in θ_i and independent of k (see Eq. 4.4) and the constraint function g is linear in θ_i (see Eq. 4.24). So the whole exponent $[-\beta(E - Fx) + Ikg]$ is quadratic in θ_i and k and therefore we can write it in a matrix form[4] $-\vec{\Theta}^T\mathbf{M}\vec{\Theta}$ (excluding a constant term βFL, which can be taken out of the integral), where $\vec{\Theta} = [\theta_1, \theta_2, \cdots \theta_N, k]^T$. Then the partition function Eq. 4.27 can be evaluated analytically:

$$Z = \frac{e^{\beta FL}}{2\pi} \int_{-\infty}^{+\infty} \exp\left[-\left(\vec{\Theta}^T\mathbf{M}\vec{\Theta}\right)\right] d\vec{\Theta} \tag{4.28}$$

$$= \frac{e^{\beta FL}}{2\pi} \sqrt{\frac{\pi^{N+1}}{\det \mathbf{M}}}. \tag{4.29}$$

The $(N + 1)$ dimensional matrix $\mathbf{M}$, whose upper $N \times N$ submatrix is a tridiagonal matrix, can be written compactly as[5]:

$$[\mathbf{M}]_{ij} = \begin{cases} \beta(\kappa_{i-1} + \kappa_i + f)\delta_{ij} - \beta\kappa_t \cdot \delta_{(|i-j|,1)} & 1 \le i, j \le N \\ -[1 - \delta_{i,(N+1)}\delta_{j,(N+1)}] \cdot I/2 & \text{otherwise} \end{cases} \tag{4.30}$$

where $t = \min(i, j)$ and δ is the Kronecker delta. A similar mathematical technique for evaluating the partition function has been applied for circular DNA by [10].

Eq. 4.29 is the analytic expression for the partition function that involves a determinant $\det \mathbf{M}$. We calculate this determinant in Appendix B and the result is:

$$\det \mathbf{M} = \frac{N\beta^{N-1}}{4} \times \prod_{i=1}^{N-1} \lambda_i, \tag{4.31}$$

where λ_i is a sequence that contains information about the bending modulus sequence κ_i:

$$\lambda_1 = 2\kappa_1 + f, \quad \lambda_i = (2\kappa_i + f) - \frac{\kappa_i\kappa_{i-1}}{\lambda_{i-1}} \quad (i = 2, 3, \cdots N - 1). \tag{4.32}$$

Plugging the expression for $\det \mathbf{M}$ (Eq. 4.31) into the partition function (Eq. 4.29), we get:

$$\log Z = -\frac{N-1}{2} \log \beta + FL\beta - \frac{1}{2} \log\left(\frac{N \prod_{i=1}^{N-1} \lambda_i}{\pi^{N-1}}\right). \tag{4.33}$$

Comparing Eq.4.33 with Eq. 4.10 and noticing that the number of degrees of freedom is $D = (N-1)$ because we have one position constraint on the end

[4]One of the three steps in the Laplace method is to expand the exponent around its minimum point [20], so it is proper to use the Taylor expansion expressions Eq. 4.4 and Eq. 4.24.

[5]Here to make the expression compact, we introduce $\kappa_0 = \kappa_N = 0$

of the chain, we get the analytic expression for $W(F)$:

$$W(F) = \frac{1}{2}\left[\sum_{i=1}^{N-1} \log \lambda_i + \log\left(\frac{N}{\pi^{N-1}}\right)\right]. \tag{4.34}$$

Therefore,

$$\Delta(F) = \frac{dW(F)}{dF} = \frac{1}{2}\sum_{i=1}^{N-1} \frac{\lambda_i'}{\lambda_i}, \tag{4.35}$$

where $\lambda_i' = d\lambda_i/dF$.

By substituting Eq. 4.34 and Eq. 4.35 into Eq. 4.12 through Eq. 4.21, we get all the thermo-mechanical quantities for the 2D heterogeneous hinged-hinged chain. In particular, the force-extension relation is:

$$\langle x \rangle = L - k_B T \cdot \Delta(F) = L - \frac{k_B T}{2} \cdot \sum_{i=1}^{N-1} \frac{\lambda_i'}{\lambda_i}. \tag{4.36}$$

To verify our result, we apply Eq. 4.36 to a homogeneous chain and compare it with the known theory for the homogeneous hinged-hinged continuous rod. We consider the limit as the segment length $l \to 0$ while the contour length $L = Nl$ is held fixed so that the discrete chain becomes a continuous rod. We show in Appendix C that in this special limit case, Eq. 4.36 exactly reduces to the well-known force-extension relation for a homogeneous fluctuating rod [17]:

$$\langle x_{\text{homo}} \rangle = L - \frac{L k_B T}{4\sqrt{KF}} \coth\left(\frac{FL}{\sqrt{KF}}\right) + \frac{k_B T}{4F}. \tag{4.37}$$

Another special case is a continuous rod with 2 separated regions of bending modulus K_I and K_{II} respectively. This special heterogeneous rod is suitable for studying the forced-unfolding of proteins because the bending moduli of folded and unfolded proteins are expected to be different. Let L_I and L_{II} be the contour length of the 2 homogeneous sub-rods ($L_I + L_{II} = L$). We show in Appendix D that the extension of such a rod is given by:

$$\langle x \rangle = L - \frac{k_B T}{2}\left[\frac{\frac{1}{E_1\sqrt{F}}\cosh\left(\sqrt{\frac{F}{F_1}}\right) + \frac{2\overline{K^{-1/2}}}{F}\sinh\left(\sqrt{\frac{F}{F_1}}\right) + \frac{1}{E_0\sqrt{F}}\cosh\left(\sqrt{\frac{F}{F_0}}\right) + \frac{\Delta K^{-1/2}}{F}\sinh\left(\sqrt{\frac{F}{F_0}}\right)}{4\overline{K^{-1/2}}\sinh\left(\sqrt{\frac{F}{F_1}}\right) + 2\Delta K^{-1/2}\sinh\left(\sqrt{\frac{F}{F_0}}\right)} - \frac{1}{F}\right], \tag{4.38}$$

where

$$\overline{K^{-1/2}} = \frac{1}{2}\left(\frac{1}{\sqrt{K_I}} + \frac{1}{\sqrt{K_{II}}}\right), \quad \Delta K^{-1/2} = \frac{1}{\sqrt{K_I}} - \frac{1}{\sqrt{K_{II}}}, \tag{4.39}$$

$$E_1 = \left(\frac{L}{\sqrt{K_I K_{II}}} + \frac{L_I}{K_I} + \frac{L_{II}}{K_{II}}\right)^{-1}, \quad E_0 = \left(\frac{L}{\sqrt{K_I K_{II}}} - \frac{L_I}{K_I} - \frac{L_{II}}{K_{II}}\right)^{-1}, \tag{4.40}$$

$$F_1 = \left(\frac{L_{II}}{\sqrt{K_{II}}} + \frac{L_I}{\sqrt{K_I}} \right)^{-2}, \quad F_0 = \left(\frac{L_{II}}{\sqrt{K_{II}}} - \frac{L_I}{\sqrt{K_I}} \right)^{-2}. \tag{4.41}$$

Note that in general, the extension of the rod is not the sum of the extensions of the two homogeneous sub-rods (Eq. 4.37) because (1) the two sub-rods do not necessarily satisfy the hinged-hinged boundary conditions, so Eq. 4.37 is not applicable to either of them; (2) there is bending cooperativity at the interface of the two sub-rods.

4.5 Partially Clamped 2D Chain

For the partially clamped conditions, one end of the chain is still fixed at the origin but the other end is free to have transverse displacement instead of being constrained on the $\hat{X}$ axis (Fig. 6.1(b)). However, moments are applied such that both angles at the two ends are zero:

$$\theta_1 = \theta_N = 0. \tag{4.42}$$

With the conditions in Eq. 4.42, the Hamiltonian (Eq. 4.4) can be rewritten in terms of only $(N-2)$ angles from θ_2 to θ_{N-1}:

$$\beta(E - Fx) = \sum_{i=2}^{N-1} \beta(\kappa_{i-1} + \kappa_i + f)\theta_i^2 - 2\sum_{i=2}^{N-2} \beta\kappa_i\theta_i\theta_{i+1} - \beta FL. \tag{4.43}$$

The partition function for a partially clamped chain is:

$$Z = \int_{-\infty}^{+\infty} \cdots \int_{-\infty}^{+\infty} \exp\left[-\beta(E - Fx)\right] d\vec{\theta}, \tag{4.44}$$

where $d\vec{\theta} = [\, d\theta_2 \cdots d\theta_{N-1} \,]$.

We plug in the Hamiltonian (Eq. 4.43) into Eq. 4.44 and again write the exponent in Eq. 4.44 in matrix form $-(\vec{\theta}^T \mathbf{M} \vec{\theta})$ (excluding a constant term βFL, which can be written outside the integral), so that the partition function now becomes:

$$Z = e^{\beta FL} \int_{-\infty}^{+\infty} \exp\left[-\vec{\theta}^T \mathbf{M} \vec{\theta}\right] d\vec{\theta} = e^{\beta FL} \sqrt{\frac{\pi^{N-2}}{\det \mathbf{M}}}, \tag{4.45}$$

where in this case, $\mathbf{M}$ is a $(N-2)$ dimensional tridiagonal matrix and it can be written compactly as:

$$[\mathbf{M}]_{ij} = \beta\left(\kappa_i + \kappa_{i+1} + f\right)\delta_{ij} - \beta\kappa_{t+1}\delta_{|i-j|,1}, \tag{4.46}$$

with $t = \min(i, j)$.

By performing elementary row operations on $\mathbf{M}$ and evaluating its eigenvalues, we find that its determinant is given by:

$$\det \mathbf{M} = \beta^{N-2} \times \prod_{i=1}^{N-2} \lambda_i, \tag{4.47}$$

where the sequence λ_i, different from the one in the hinged-hinged case, is given by:

$$\lambda_1 = \kappa_1 + \kappa_2 + f, \quad \lambda_i = (\kappa_i + \kappa_{i+1} + f) - \frac{\kappa_i^2}{\lambda_{i-1}} \quad (i = 2, 3, \cdots N-2). \tag{4.48}$$

By substituting Eq. 4.47 into Eq. 4.45 and comparing the expression of $\log Z$ with Eq. 4.10, we obtain the analytic expression for $W(F)$ and $\Delta(F)$:

$$W(F) = \frac{1}{2}\left[\sum_{i=1}^{N-2} \log \lambda_i - (N-2)\log \pi\right], \tag{4.49}$$

$$\Delta(F) = \frac{1}{2}\sum_{i=1}^{N-2} \frac{\lambda_i'}{\lambda_i}, \tag{4.50}$$

where again $\lambda_i' = d\lambda_i/dF$.

Suprisingly, $\Delta(F)$ has the same form as in the hinged-hinged case. But, we emphasize that the sequence λ_i here is different from the one in the hinged-hinged case (Eq. 4.32 and Eq. 4.48).

Again, by substituting Eq. 4.49 and Eq. 4.50 into Eq. 4.12 through Eq. 4.21, we obtain all the thermo-mechanical quantities.

4.6 Clamped-clamped 2D Chain

For the clamped-clamped chain, the two tangent angles at the ends are constrained to zero and the ends of the chain are constrained on the $\hat{X}$ axis (Fig. 6.1(c)). The Hamiltonian is the same as the one in the partially clamped case given in Eq. 4.43.

The position constraint function, Eq. 4.24, which states that the end of the chain must lie on the $\hat{X}$ axis, can also be expressed in terms of the $(N-2)$ angles $\theta_2, \theta_3, \cdots \theta_{N-1}$:

$$g \approx \sum_{i=2}^{N-1} \theta_i = 0. \tag{4.51}$$

The partition function for a clamped-clamped chain is:

$$Z = \int_{-\infty}^{+\infty} \cdots \int_{-\infty}^{+\infty} \exp\left[-\beta(E - Fx)\right] \delta(g)\, d\vec{\theta} \tag{4.52}$$

$$= \frac{1}{2\pi}\int_{-\infty}^{+\infty} \cdots \int_{-\infty}^{+\infty} \exp\left[-\beta(E - Fx) + Ikg\right] d\vec{\theta}\, dk, \tag{4.53}$$

where Eq. 4.26 has been used and $d\vec{\theta} = [\, d\theta_2 \cdots d\theta_{N-1} \,]$.

Again, to evaluate the partition function, we plug Eq. 4.43 and Eq. 4.51 into Eq. 4.53 and express the exponent in a quadratic form $-\vec{\Theta}^T \mathbf{M} \vec{\Theta}$ (excluding a constant term $\beta F L$, which can be written outside the integral), where $\vec{\Theta} = [\theta_2, \cdots \theta_{N-1},\, k]^T$, then the partition function can be evaluated analytically as:

$$Z = \frac{e^{\beta F L}}{2\pi} \sqrt{\frac{\pi^{N-1}}{\det \mathbf{M}}}, \tag{4.54}$$

where the $(N-1)$ dimensional matrix $\mathbf{M}$ in this case is:

$$[\mathbf{M}]_{ij} = \begin{cases} \beta\left(\kappa_i + \kappa_{i+1} + f\right)\delta_{ij} - \beta\kappa_{t+1}\delta_{|i-j|,1} & 1 \le i, j \le N-2 \\ -I(1 - \delta_{i,(N-1)}\delta_{j,(N-1)})/2 & \text{otherwise} \end{cases} \tag{4.55}$$

again, $t = \min(i, j)$.

We show in Appendix E that in this case, the determinant $\det \mathbf{M}$ is:

$$\det \mathbf{M} = \left(\frac{\beta^{N-3} R}{4}\right) \prod_{i=1}^{N-2} \lambda_i, \tag{4.56}$$

with the sequence of λ_i being the same as the one in the partially clamped case given in Eq. 4.48 and the quantity R is given by:

$$R = \sum_{i=1}^{N-2} (\kappa_i + \kappa_{i+1} + f) g_i^2 - 2 \sum_{i=1}^{N-3} \kappa_{i+1} g_i g_{i+1}, \tag{4.57}$$

with

$$g_{N-2} = \frac{\rho_{N-2}}{\lambda_{N-2}}, \quad g_i = \frac{\rho_i + \kappa_{i+1} g_{i+1}}{\lambda_i} \quad (i = N-3, N-2, \cdots 1), \tag{4.58}$$

$$\rho_i = 1 + \sum_{j=1}^{i-1} \left(\prod_{s=i-j+1}^{i} \frac{\kappa_s}{\lambda_{s-1}} \right). \tag{4.59}$$

We plug Eq. 4.56 into Eq. 4.54, compare the expression for $\log Z$ with Eq. 4.10 to find the expressions for $W(F)$ and $\Delta(F)$ (note that the number of degrees of freedom in this case is $D = N - 3$):

$$W(F) = \frac{1}{2} \left[\sum_{i=1}^{N-2} \log \lambda_i + \log R - (N-3) \log \pi \right], \tag{4.60}$$

$$\Delta(F) = \frac{1}{2} \left[\sum_{i=1}^{N-2} \frac{\lambda_i'}{\lambda_i} + \frac{R'}{R} \right], \tag{4.61}$$

where $R' = dR/dF$.

With Eq. 4.60 and Eq. 4.61, all the thermo-mechanical quantities can be computed. In particular, the force-extension relation for a clamped-clamped chain is:

$$\langle x \rangle = L - k_B T \cdot \Delta(F) = L - \frac{k_B T}{2} \left[\sum_{i=1}^{N-2} \frac{\lambda_i'}{\lambda_i} + \frac{R'}{R} \right]. \tag{4.62}$$

4.7 Fluctuation of a 2D Chain

In addition to the thermo-mechanical quantities discussed above, we are also interested in the quantity $\langle \theta_i \cdot \theta_j \rangle$, because it reflects how much the chain is fluctuating. Also, by calculating $\langle \theta_i \cdot \theta_j \rangle$, we immediately get the fluctuation of the chain in the Y direction, which has been measured in experiments for some biopolymers [21]:

$$\langle y_i^2 \rangle = \left\langle \left(\sum_{j=1}^{i} l \sin\theta_j \right) \left(\sum_{k=1}^{i} l \sin\theta_k \right) \right\rangle \approx l^2 \sum_{j,k=1}^{i} \langle \theta_j \cdot \theta_k \rangle, \tag{4.63}$$

where y_i is the transverse displacement of the i-th segment in the Y direction (Fig. 6.1).

The quantity $\langle \theta_i \cdot \theta_j \rangle$ by definition is:

$$\langle \theta_i \cdot \theta_j \rangle = \frac{1}{Z} \sum_{\nu} (\theta_i \cdot \theta_j) \exp[-\beta(E_\nu - F x_\nu)]. \tag{4.64}$$

By writing it in integral form, we can evaluate it using the following formula [22, 10]:

$$\begin{aligned} \langle \theta_i \cdot \theta_j \rangle &= \frac{\int_{-\infty}^{+\infty} (\theta_i \cdot \theta_j) \exp[-\vec{\Theta}^T \mathbf{M} \vec{\Theta}] \, d\vec{\Theta}}{\int_{-\infty}^{+\infty} \exp[-\vec{\Theta}^T \mathbf{M} \vec{\Theta}] \, d\vec{\Theta}} && (4.65) \\ &= \frac{1}{2} \left(\mathbf{M}^{-1} \right)_{ij}, && (4.66) \end{aligned}$$

where the detailed expressions and dimensionality of $\mathbf{M}$ and $\vec{\Theta}$ depend on the boundary conditions as has been discussed in the previous sections (Eq. 4.30, Eq. 4.46 and Eq. 4.55). For the analytic formula of the inverse of a tridiagonal matrix, we refer the reader to [23].

Note that for the partially clamped chain, from Eq. 4.46, we know that:

$$\langle \theta_i \cdot \theta_j \rangle = \frac{1}{2} \left(\mathbf{M}^{-1} \right)_{ij} \sim \beta^{-1} \sim T, \tag{4.67}$$

and therefore using Eq. 4.63, we conclude that the transverse fluctuation of the chain scales linearly with respect to T:

$$\langle y_i^2 \rangle \sim T. \tag{4.68}$$

Recall that the variance in the extension x scales as T^2 (Eq. 4.16). So as temperature T increases, the fluctuation in x should be more significant compared to the transverse fluctuation.

We show in Appendix F that Eq. 4.67 also holds for the hinged-hinged chain and the clamped-clamped chain. So the conclusion that the transverse fluctuation scales as T holds for all the boundary conditions discussed in this chapter.

4.8 Theory for the 3D Chains

We will show in this section that by choosing a suitable set of angles that represents the configuration of the chain, the results for a 2D chain can be easily generalized to a 3D one.

Let $\hat{X}$, $\hat{Y}$ and $\hat{Z}$ be the standard reference triad in 3D space. As before, a force $\vec{F} = F\hat{X}$ is acting on one end of the chain while the other end is fixed at the origin. We denote the unit tangent vector of the 3D chain as $\hat{t}(s)$, which forms an angle $\theta(s)$ with respect to the $\hat{X}$ axis. The projection of $\hat{t}$ on the $\hat{Y}$-$\hat{Z}$ plane forms an angle ϕ with respect to the $\hat{Y}$ axis so that $\hat{t}(s)$ can be written as:

$$\hat{t} = [\cos\theta, \sin\theta\cos\phi, \sin\theta\sin\phi]. \tag{4.69}$$

It follows then:

$$\left|\frac{d\hat{t}}{ds}\right|^2 = \dot{\theta}^2 + \sin^2\theta\dot{\phi}^2, \tag{4.70}$$

where $\dot{\theta}$ and $\dot{\phi}$ are the derivative of θ and ϕ with respect to the arc length s.

We will discuss the 3D hinged-hinged chain below in detail. 3D chains under the other two boundary conditions can be studied following the same procedure, though some detailed steps are different, the final results turn out be the same and we will give a summary in the end of this section.

We define:

$$\vartheta_x = \theta\cos\phi, \quad \vartheta_y = \theta\sin\phi, \tag{4.71}$$

so that:

$$\vartheta_x^2 + \vartheta_y^2 = \theta^2, \quad \dot{\vartheta_x}^2 + \dot{\vartheta_y}^2 = \dot{\theta}^2 + \theta^2\dot{\phi}^2. \tag{4.72}$$

Representation of the 3D chains using ϑ_x and ϑ_y has been discussed in [19].

The Hamiltonian of the 3D chain, up to a quadratic approximation, can be written as [6]:

$$\begin{aligned}
\mathscr{H}_{3D} &= \beta(E - Fx) = \int_0^L \frac{\beta K}{2}\left|\frac{d\hat{t}}{ds}\right|^2 ds - \beta F\int_0^L \cos\theta ds && (4.73)\\
&\approx \int_0^L \frac{\beta K}{2}\left(\dot{\theta}^2 + \theta^2\dot{\phi}^2\right) ds - \beta F\int_0^L \left(1 - \frac{\theta^2}{2}\right) ds && (4.74)\\
&= \left[\int_0^L \frac{\beta K}{2}\dot{\vartheta_x}^2 ds - \beta F\int_0^L \left(1 - \frac{\vartheta_x^2}{2}\right) ds\right] && (4.75)\\
&\quad + \left[\int_0^L \frac{\beta K}{2}\dot{\vartheta_y}^2 ds - \beta F\int_0^L \left(1 - \frac{\vartheta_y^2}{2}\right) ds\right] + \beta FL. && (4.76)
\end{aligned}$$

[6] We assume there are no torsional constraints here. Problems with torsional or other constraints can be addressed using the same method as long as the Hamiltonian can be expressed quadratically. Also, see [4] for explanations on the simplification of the twist energy.

Here Eq. 4.70 and Eq. 4.72 have been used. Comparing Eq. 4.76 with Eq. 4.3, we conclude that:

$$\mathscr{H}_{3D} = \mathscr{H}_{2D}(\vartheta_x) + \mathscr{H}_{2D}(\vartheta_y) + \beta FL, \tag{4.77}$$

where $\mathscr{H}_{2D}(\vartheta)$ represents the Hamiltonian of the 2D chain with tangent angle denoted as ϑ.

There are two constraints for the 3D chain: the Y and Z coordinates of the end of the chain should be zero. They relate to the constraint function in the 2D problem in the following ways (see Eq. 4.24 for the 2D constraint function):

$$g_Y = \int_0^L \sin\theta\cos\phi\, ds \approx \int_0^L \vartheta_x ds = g_{2D}(\vartheta_x), \tag{4.78}$$

$$g_Z = \int_0^L \sin\theta\sin\phi\, ds \approx \int_0^L \vartheta_y ds = g_{2D}(\vartheta_y). \tag{4.79}$$

Note that the two constraint functions are decoupled in terms of the angles ϑ_x and ϑ_y up to a linear approximation, which is sufficient for using the Laplace method to evaluate the partition function, as we have shown in the 2D case.

Hence, using Eq. 4.77, Eq. 4.78 as well as Eq. 4.79, the partition function for a 3D chain is:

$$Z_{3D} = \int_{-\infty}^{+\infty}\int_{-\infty}^{+\infty} \exp\left(-\mathscr{H}_{3D}\right)\delta(g_Y)\delta(g_Z)d\vec{\vartheta}_x d\vec{\vartheta}_y \tag{4.80}$$

$$= e^{-\beta FL}\int_{-\infty}^{+\infty} e^{-\mathscr{H}_{2D}(\vartheta_x)}\delta\left[g_{2D}(\vartheta_x)\right]d\vec{\vartheta}_x \cdot \int_{-\infty}^{+\infty} e^{-\mathscr{H}_{2D}(\vartheta_y)}\delta\left[g_{2D}(\vartheta_y)\right]d\vec{\vartheta}_y \tag{4.81}$$

$$= e^{-\beta FL}(Z_{2D})^2. \tag{4.82}$$

Eq. 4.82 relates the 3D partition function with the 2D partition function, from which we further get:

$$\log Z_{3D} = -\beta FL + 2\log Z_{2D} = -\beta FL + 2\left[-\frac{D_{2D}}{2}\log\beta + FL\beta - W_{2D}(F)\right] \tag{4.83}$$

$$= -\frac{D_{3D}}{2}\log\beta + \beta FL - 2W_{2D}(F), \tag{4.84}$$

where Eq. 4.10 has been used. Here the number of degrees of freedom of a 3D chain is twice of that of a 2D chain ($D_{3D} = 2D_{2D}$) because for each segment, we have θ_i and also ϕ_i. Comparing Eq. 4.84 with Eq. 4.10, we get:

$$W_{3D}(F) = 2W_{2D}(F), \tag{4.85}$$

and therefore:

$$\Delta_{3D}(F) = 2\cdot\Delta_{2D}(F), \quad \Delta'_{3D}(F) = 2\cdot\Delta'_{2D}(F). \tag{4.86}$$

With the relations of 2D and 3D $\Delta(F)$, we conclude using Eq. 4.12 through Eq. 4.19 that for a 3D chain, the following quantities are twice of those of the 2D chain: the entropy S, the shrinking of the chain $L - \langle x\rangle$, average energy

$\langle E\rangle$, the heat capacity C_F and the variances of the extension and the energy $\langle(\Delta x)^2\rangle$, $\langle(\Delta E)^2\rangle$.

To relate the fluctuation of a 3D chain with a 2D one, note that the transverse displacement of the 3D chain is:

$$\langle\, y(s)_{3D}^2 + z(s)_{3D}^2 \,\rangle = \left\langle \left(\int_0^s \sin\theta\cos\phi\, ds\right)^2 + \left(\int_0^s \sin\theta\sin\phi\, ds\right)^2 \right\rangle \quad (4.87)$$

$$\approx \left\langle \left(\int_0^s \vartheta_x ds\right)^2 + \left(\int_0^s \vartheta_y ds\right)^2 \right\rangle \quad (4.88)$$

$$= 2\langle\, y(s)_{2D}^2 \,\rangle. \quad (4.89)$$

So the transverse fluctuation is twice larger for the 3D chain.

Finally, we note that for the partially clamped and clamped-clamped 3D chain, the corresponding boundary conditions are that for the first and last segment of the chain:

$$\theta = \vartheta_x = \vartheta_y = 0 \quad (4.90)$$

The derivations are almost the same as the hinged-hinged chain and are not shown here. The results of Eq. 4.85, Eq. 4.86 as well as Eq. 4.89 remain the same as for the hinged-hinged chain.

4.9 Monte Carlo Simulation

To verify our theory, we have done Monte Carlo (MC) simulations for the 2D fluctuating chains under an external applied force for all the three boundary conditions. The chain is represented by the N tangent angles θ_i as in the theoretical model and it is initially straight.

At each MC step, a new conformation is generated from the existing one by randomly varying N of the θ_i. Each valid change of the configuration should satisfy the boundary conditions. A new conformation is accepted with a probability according to the Metropolis criterion [24] and the thermo-mechanical quantities and fluctuations of the chain are recorded. To check if equilibrium has been reached in a given simulation, we ensure that the equipartition theorem (Eq. 4.8) is satisfied. Results are recorded only at equilibrium.

4.10 Results and Application

4.10.1 Thermo-mechanical properties of the chain

Fig. 4.3 shows the thermo-mechanical quantities for a homogeneous fluctuating 500-segment chain under different boundary conditions. The contour length of the chain is $L = 2.5$nm and the bending modulus is $K = 2.5k_BT{\cdot}$nm so that $\xi_p/L = 2$ (2D), where ξ_p is the persistence length of the chain. Several interesting results are shown in this figure: (1) All the results show that the

hinged-hinged chain is the most flexible. It has the smallest extension under an applied force and it has the largest variances in extension and energy. On the other hand, the clamped-clamped chain is the least flexible, which is expected because it has the smallest number of degrees of freedom. (2) The variances of extension and energy are decreasing functions of the applied force F. In other words, force suppresses the fluctuations of the chain. (3) Coefficient of thermal expansion α is negative and it is increasing with F. (4) The hinged-hinged chain and partially clamped chain have similar results for the thermo-mechanical quantities that are determined only by $\Delta(F)$ and $\Delta'(F)$, but not $W(F)$. This can be understood by comparing the expressions of $\Delta(F)$ for these two boundary conditions (Eq. 4.35 and Eq. 4.50).

Eq. 4.23, which relates the response of the chain to the force and to temperature, is verified in MC simulations. Average extension and thermal expansion coefficient are recorded in simulations under forces varying from 150pN to 1150pN. The result is shown in Fig. 4.4.

The force-extension relation for a homogeneous continuous rod has been studied under all the three boundary conditions [17]. To check our results, we plot the force extension relation for a homogeneous chain and compare it with the known theory for the rod in Fig. 4.5. Here we choose a large $N = 50000$ so that $l = L/N << L$ and the chain is approximately a smooth rod. Fig. 4.5 shows that our formulae for all the boundary conditions reduce to the known theory for the homogeneous rods when N is large and l is small.

The computational complexity using the formulae for thermo-mechanical properties shown in this chapter is $O(N)$. This is true not only for homogeneous chains, but for any heterogeneous chain under all the three boundary conditions. Note that we need at least N values of K_i to specify an arbitrary heterogeneous chain, so $O(N)$ is the optimal computational complexity for the problem.

4.10.2 Fluctuation and correlation of the angle θ_i

Fig. 4.6 shows the fluctuation in θ_i (i.e., $\langle\theta_i^2\rangle$) along the chain. The profile depends strongly on the boundary conditions when $\xi_p/L > 1$ (Fig. 4.6(a) shows the case when $\xi_p/L = 5$). In this case, the hinged-hinged chain has maximum fluctuation at the two ends whereas the partially clamped and clamped-clamped chains have minimum fluctuations there, which is expected because $\theta_1 = \theta_N \equiv 0$ for these two chains. In the middle point of the chain, the hinged-hinged chain and the partially clamped chain achieve their smallest and largest fluctuations respectively. It is interesting that the maximum fluctuation for the clamped-clamped chain does not occur in the middle of the chain (Fig. 4.6(a) black). When ξ_p/L becomes small, the boundary conditions only influence the profile near the two ends of the chain (Fig. 4.6(b)). Away from the two ends, the profiles almost coincide for different boundary conditions.

Fig. 4.7 shows the dependence of the $\langle\theta_i^2\rangle$ profile on the heterogeneity of the chain. The theoretical predictions are compared to the MC simulation results

for all the three boundary conditions. For all the cases studied here, a jump in the bending modulus leads to a corresponding jump in the $\langle\theta_i^2\rangle$ profile. The larger the bending modulus, the smaller the value of $\langle\theta_i^2\rangle$. The figures imply that the heterogeneity of the chain has a significant influence on $\langle\theta_i^2\rangle$.

Fig. 4.8 shows the correlation in the θ angles. In particular, we show $\langle\theta(s)\cdot\theta(L/2)\rangle$ here. Clearly, the profiles should have a peak at $s = L/2$ and decrease as s moves away from $L/2$. The smaller the persistence length ξ_p is compared to the contour length L, the faster the profile decreases. Again, the results show that the profiles depend strongly on the boundary conditions when $\xi_p/L \approx 1$. For the partially clamped chain, our theory predicts that the correlation decreases but remains positive along the chain whereas for the hinged-hinged and clamped-clamped chains, the correlations can become negative near the two ends of the chain, although for the clamped-clamped chain, due to the constraints that $\theta_1 = \theta_N \equiv 0$, the correlation is exactly 0 at the ends. The MC simulation results confirm our predictions. In order to show the theoretical prediction clearly, we plot the simulation results separately in (b), (d) and (f). In addition, we show in Fig. 4.8(g) (theory) and (h) (MC simulation) that the correlation profile is not symmetric for a heterogeneous chain. The correlation decreases faster where the bending modulus is smaller.

4.10.3 Transverse fluctuation of the chains $\langle y^2\rangle$

Fig. 4.9(a) shows the transverse fluctuation of the chain in the Y direction. As shown in the figure, the transverse fluctuation depends on the boundary conditions and the heterogeneity of the chain. For chains with the same bending modulus, the partially clamped chain has the largest transverse fluctuation while the clamped-clamped chain has the smallest fluctuation, which is expected because the clamped-clamped chain has the smallest number of degrees of freedom. Fig. 4.9(b) shows that the fluctuation decreases when the force increases. The theoretical predictions and the MC simulation results match quite well.

Fig. 4.10(a)-(c) show that for a fixed persistence length, the chain that has longer contour length has more transverse fluctuation. Our theoretical predictions and the MC simulation results match quite well for all the three boundary conditions.

4.10.4 Application to the protein unfolding problem

The mechanical behavior of proteins is studied in experiments by stretching oligomers in an atomic force microscope. As the protein chain is stretched, the number of unfolded oligomers increases in steps and this gives rise to a characteristic saw-tooth pattern in the force-extension profile as seen in Fig. 4.11 (experimental data from [25]). The loss of structural integrity in the unfolded regions is expected to change the stiffness of the chain. We can study these effects through our heterogeneous fluctuating chain model. To see how this

can be achieved we refer the reader to the force-extension curves in Fig. 4.11. The blue dotted curves in Fig. 4.11 are the experimental data of forced unfolding of a chain of ubiquitins under constant velocity pulling from [25]. Each peak in the profile represents an unfolding event where the force drops precipitously. There are six experimental curves in Fig. 4.11 (see the descriptions in [25]) and the last curve corresponds to the force-extension relation of a chain of purely unfolded ubiquitins. We model the entire protein oligomer as a fluctuating chain with two bending moduli K_f (for folded proteins) and K_u (for unfolded proteins), each part with length $N_f L_{fs}$ and $N_u L_{us}$, where N_f, N_u are the number of folded and unfolded proteins (they are changing from curve to curve) and L_{fs}, L_{us} are the contour lengths of a single folded and unfolded protein respectively. We first fit the last curve, which corresponds to six unfolded ubiquitins, with the homogeneous model (Eq. 4.37) and obtain two parameters K_u and L_{us} for the unfolded protein. Similarly, we fit the first curve to obtain the other two parameters K_f and L_{fs} for the folded protein (Fig. 4.11(a), red circles are the fitted data and black curves are the fitting results). Then without any more free parameters, we apply the force-extension relation for a 'special heterogeneous chain' (Eq. 4.38, 3D version) to predict all the intermediate curves using different values of N_f and N_u (Fig. 4.11(b), red curves). As shown in Fig. 4.11(b), our prediction matches the experimental data quite well.

4.11 Conclusions

In this chapter we have developed a method to determine the thermo-mechanics of heterogeneous fluctuating elastic rods and chains with arbitrary boundary conditions. In particular, we are able to compute the force-extension relation and the variance of transverse fluctuation of the chain. Our results are in excellent agreement with Monte Carlo simulations. We have demonstrated the usefulness of our method by using it to interpret experimental data on the stretching of proteins. Our method assumes that there are no torsional constraints on the rod. But, problems with torsional or other constraints can be addressed using this method as long as the energy can be expressed as a quadratic form in the kinematic variables. The framework developed in this chapter is not restricted to one-dimensional rods or chains alone. In fact, our goal is to extend this technique to two- and three-dimensional problems, such as, those involving the mechanics of networks of filaments.

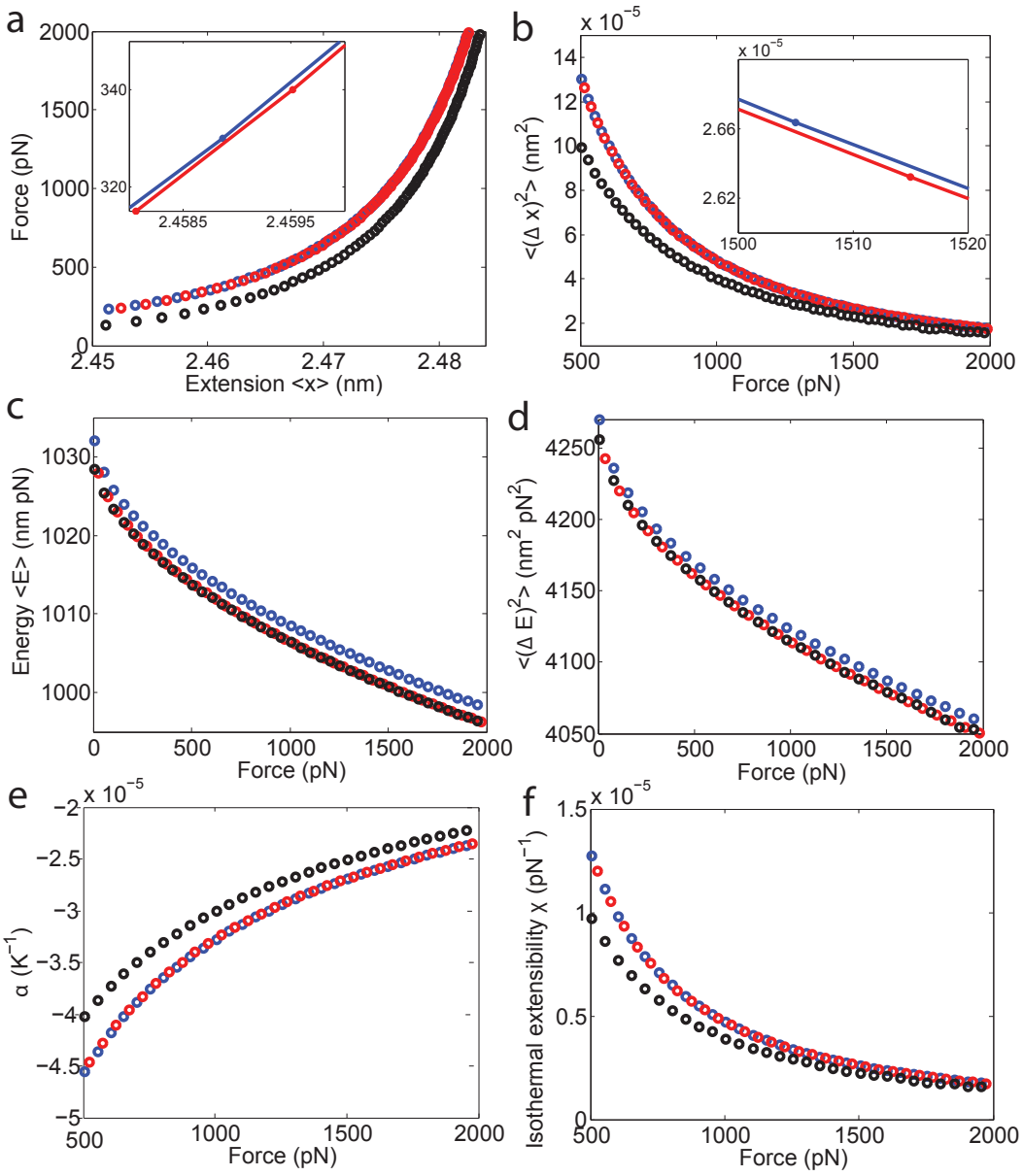

Figure 4.3: Thermo-mechanical quantities for a fluctuating chain. Blue: hinged-hinged boundary conditions; red: partially clamped boundary conditions; black: clamped-clamped boundary conditions. (a) Force-extension profile of the chain. Inset: local profile shows that the hinged-hinged chain (blue) has smaller extension and thus is more flexible (to show the figure clearly, we have changed the circles into lines with the same colors); (b) Variance of the extension. Inset: local profile shows that the hinged-hinged chain (blue) fluctuates more than the partially clamped chain (to show the figure clearly, we have changed the circles into lines with the same colors); (c) Average energy of the chain versus the applied force; (d) Variance of the energy; (e) Thermal expansion coefficient α versus the applied force; (f) Isothermal extensibility χ versus the applied force.

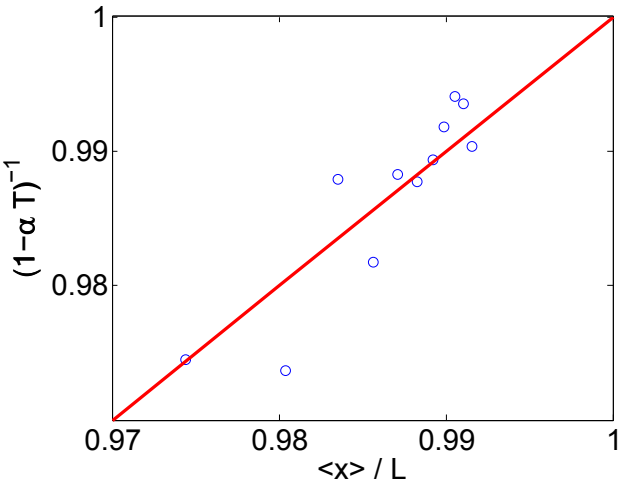

Figure 4.4: Verifying Eq. 4.23. Solid line: theoretical prediciton; circles: MC simulation results. Simulations have been done under 11 different forces varying from 150pN to 1150pN with an increasement of 100pN. Temperature is set to be 300K. Relative extension as well as thermal expansion coefficient are recorded. The result shown is for a homogeneous chain with contour length $L = 25$nm and bending modulus $K = 2.5k_BT \cdot nm$.

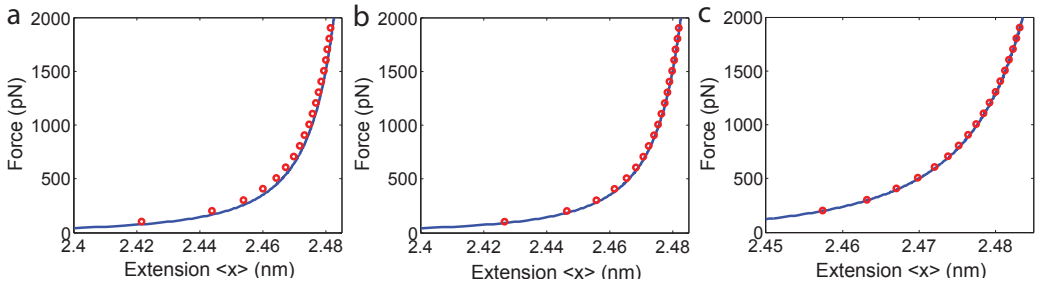

Figure 4.5: Force-extension relation for homogeneous chains (blue curve) and rods (red circle, theory in [17]). (a) Hinged-hinged boundary conditions; (b) partially clamped boundary conditions; (c) clamped-clamped boundary conditions. $K = 2.5k_BT \cdot nm$, $L = 2.5$nm. The figures show that our force-extension relations for the chains reduce to the known formulae for the continuous rods when $N \to +\infty$ with $L = Nl$ fixed. Here $N = 50000$ for the blue curves.

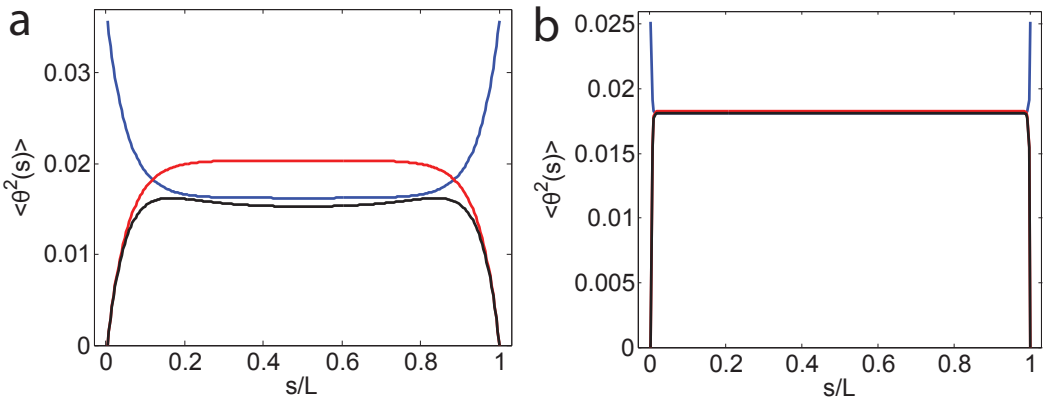

Figure 4.6: Dependence of the fluctuation of θ angles on the boundary conditions. Blue: hinged-hinged chain, the fluctuation in θ is at maximum and minimum respectively at the two ends and in the middle of the chain; red: partially clamped chain, the fluctuation is at maximum and minimum respectively in the middle and at the two ends; black: clamped-clamped chain, the fluctuation is at minimum at the two ends, but the maximum is not achieved in the middle of the chain. Also, the partially clamped chain (red) fluctuates more than the clamped-clamped chain (black). (a) $\xi_p/L = 5$, the dependence on the boundary conditions is significant througout the chain; (b) $\xi_p/L = 0.2$ the dependence on the boundary conditions is significant only at the two ends of the chain. To make the figures clear, the MC simulation results are not shown in the same figures.

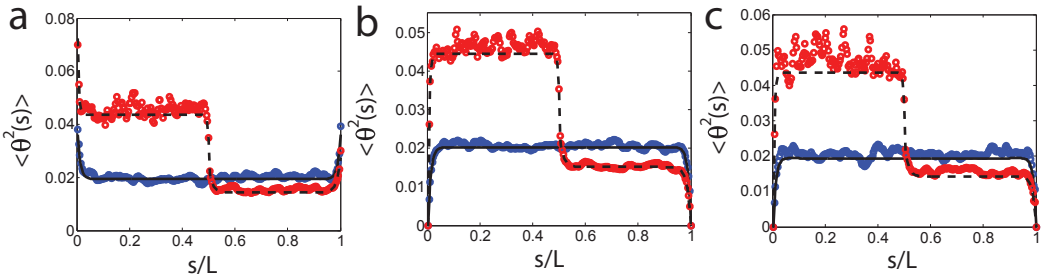

Figure 4.7: Dependence of the fluctuation of θ angles on the heterogeneity of the chain. Blue: homogeneous chain with $K = 2.5k_BT \cdot nm$; black: corresponding MC simulation results; red: heterogeneous chain with two bending moduli: $K_I = 0.5k_BT \cdot nm$ at the first half of the chain and $K_{II} = 4.5k_BT \cdot nm$ at the second half; black dashed curve: corresponding MC simulation results. (a), (b) and (c) are for hinged-hinged, partially clamped and clamped-clamped boundary conditions respectively. The figures show that jumps in the bending modulus result in jumps in the fluctuation in the $\langle\theta^2\rangle$ profile. The larger the bending modulus, the smaller the fluctuation in θ.

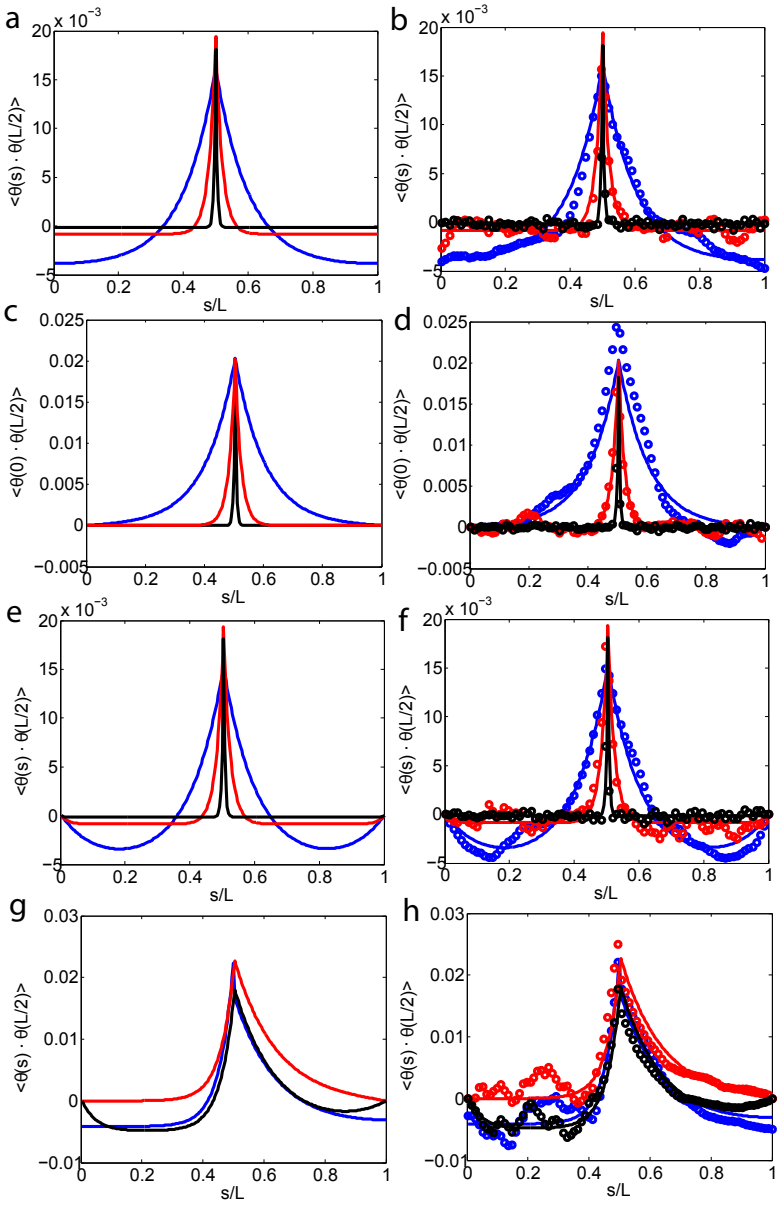

Figure 4.8: Correlation in the tangent angle θ. (a-f): results for the homogeneous chains. Blue: $\xi_p/L = 5$; red: $\xi_p/L = 1$; black: $\xi_p/L = 0.2$. (a),(c),(e) are the theoretical results for the hinged-hinged, partially clamped and clamped-clamped chains respectively. To make the plots clear, we plot the corresponding MC simulation results separately in (b),(d) and (f) (circles). The figures show that the correlation in θ depends strongly on ξ_p/L. When $\xi_p/L > 1$ (blue), the profile also significantly depends on the boundary conditions. (g-h): results for a heterogeneous chain with $L = 1$nm. The first half and the second half of the chain have bending moduli of $K_I = 0.5k_BT \cdot nm$ and $K_{II} = 4.5k_BT \cdot nm$ respectively. (g) is the theoretical predictions and (h) is the MC simulation results. Blue, red and black colors are for the hinged-hinged, partially clamped and clamped-clamped boundary conditions respectively. The correlation profile loses its symmetry and decreases faster at the first half of the chain where the bending modulus is smaller.

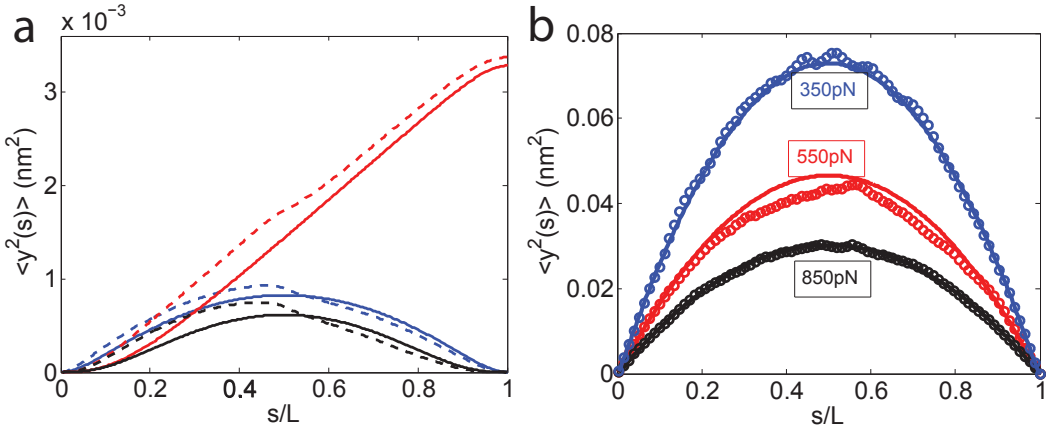

Figure 4.9: Transverse fluctuation $\langle y^2 \rangle$. (a): blue: hinged-hinged chain; red: partially clamped chain; black: clamped-clamped chain. Solid curve: homogeneous chain with $K = 2.5 k_B T \cdot nm$; dashed curve: heterogeneous chain with $K_I = 0.5 k_B T \cdot nm$ for the first half of the chain and $K_{II} = 4.5 k_B T \cdot nm$ for the second half. In (a), $L = 1nm$ for all the curves. Since the curves are close to each other, to make the theoretical results clear, we do not plot the MC simulation results in (a). (b): transverse fluctuation decreases when the force increases. The results are for a homogeneous hinged-hinged chain with $L = 25$nm and $K = 2.5 k_B T \cdot nm$. The corresponding forces are labeled in the figure. Circles: MC simulation results; solid lines: theoretical predictions.

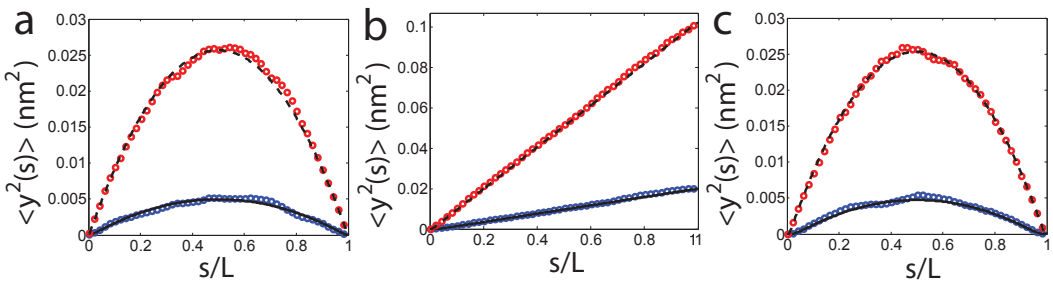

Figure 4.10: Dependence of the transverse fluctuation on the countour length of the chain. $K = 2.5 k_B T \cdot nm$ for all the curves. Black solid curves (theory) and blue circles (MC simulation): $L = 5$nm; black dashed curves (theory) and red circles (MC simulation): $L = 25$nm; (a) hinged-hinged boundary conditions; (b) partially clamped boundary conditions; (c) clamped-clamped boundary conditions. The figures show that for a fixed persistence length, the longer the chain, the more the fluctuation. Also, our theoretical results and the MC simulation results match quite well. Note that here $\xi_p / L \leq 1$ and the results for hinged-hinged chain and clamped-clamped chains are quite similar, which is confirmed by the simulation results.

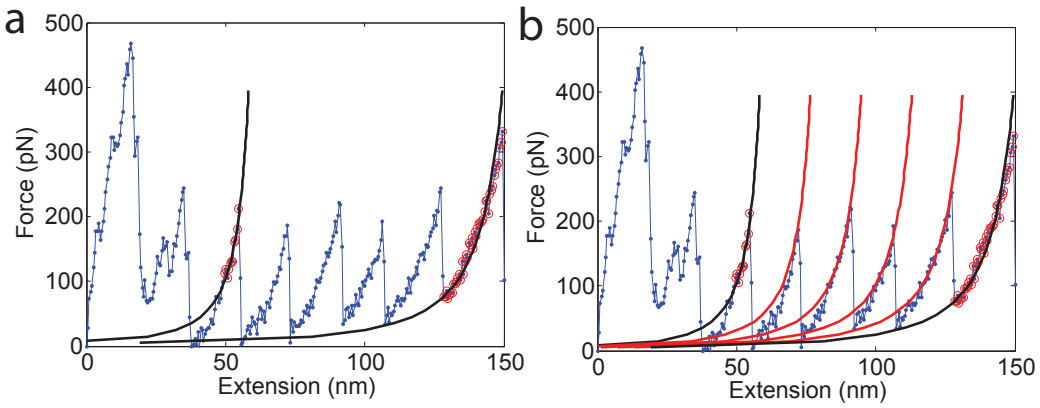

Figure 4.11: Unfolding of six copies of ubiquitins under constant velocity pulling condition. Blue dotted curves are the experimental data from [25]. Each peak in the profile represents a unfolding event where the force drops. The first and the last experimental curves are fitted to obtain the contour lengths and the bending moduli of the folded and unfolded proteins (Fig.(a): red circles are the fitted data and the black curves are the fitting results). The intermediate curves are then predicted without any free parameters using the 3D version of Eq. 4.38 (Fig.(b), red curves). Figure.(b) shows that the predictions match well with the experimental data.

Bibliography

[1] Bustamante, C., Marko, J.F., Siggia, E.D., Smith, S., 1994. **Entropic elasticity of lambda-phage DNA.** *Science* 265(5178), 1599-1600.

[2] Marko, J.F., Siggia, E.D., 1995. **Stretching DNA.** *Macromolecules* 28(26), 8759-8770.

[3] Odijk, T., 1995. **Stiff chains and filaments under tension.** *Macromolecules* 28(20), 7016-7018.

[4] Nelson, P., 2008. **Biological Physics: Energy, Information, Life**, updated first ed. W. H. Freeman and Company, New York.

[5] Popov, Y.O., Tkachenko, A.V., 2007. **Effects of sequence disorder on DNA looping and cyclization.** *Phys. Rev. E* 76(2 Pt 1), 021901.

[6] Moukhtar, J., Fontaine, E., Faivre-Moskalenko, C., Arneodo, A., 2007. **Probing persistence in DNA curvature properties with atomic force microscopy.** *Phys. Rev. Lett.* 98(17), 178101.

[7] Su, T., Purohit, P.K., 2009. **Mechanics of forced unfolding of proteins.** *Acta Biomater.* 5(6):1855-1863.

[8] Hogan, M., Legrange, J., Austin, B., 1983. **Dependence of DNA helix flexibility on base composition.** *Nature* 304(5928), 752-754.

[9] Hagerman, P.J., 1988. **Flexibility of DNA. Annu. Rev. Biophys.** *Biophys. Chem.* 17, 265-286.

[10] Zhang, Y., Crothers, D.M., 2003. **Statistical mechanics of sequence-dependent circular DNA and its application for DNA cyclization.** *Biophys. J.* 84(1), 136-153.

[11] Purohit, P.K., Nelson, P.C., 2006. **Effect of supercoiling on formation of protein-mediated DNA loops.** *Phys. Rev. E* 74(6 Pt 1), 061907.

[12] Wilson, D.P., Lillian, T., Goyal, S., Tkachenko, A.V., Perkins, N.C., Meiners, J., 2007. **Understanding the role of thermal fluctuations in DNA looping.** *Proceeding of the SPIE.* 6602, 660208.

[13] Geissler, P.L., Shakhnovich, E.I., 2002. **Reversible stretching of random heteropolymers.** *Phys. Rev. E* 65(5 Pt 2), 056110.

[14] Jarkova, E., Vlugt, T.J., Lee, N.K., 2005. **Stretching a heteropolymer.** *J. Chem. Phys.* 122(11), 114904.

[15] Ahsan, A., Rudnick, J., Bruinsma, R., 1998. **Elasticity theory of the B-DNA to S-DNA transition.** *Biophys. J.* 74(1), 132-137.

[16] Seol, Y., Li, J., Nelson, P.C., Perkins, T.T., Betterton, M.D., 2007. **Elasticity of short DNA molecules: theory and experiment for contour lengths of 0.6-7 microm.** *Biophys. J.* 93(12), 4360-4373.

[17] Purohit, P.K., Arsenault, M.E., Goldman, Y., Bau, H.H., 2008. **The mechanics of short rod-like molecules in tension.** *Int. J. Non-linear Mech.* 43(10):1056-1063.

[18] Callen, H.B., 1985. **Thermodynamics and an Introduction to Thermostatistics**, second ed. John Wiley and Sons, New York, Chichester, Brisbane, Toronto, Singapore.

[19] Kulić, I., 2004. **Statistical Mechanics of Protein Complexed and Condensed DNA.** Thesis, Max Planck Institute for Polymer Research, Mainz, Germany.

[20] Carrier, G.F., Krook, M., Pearson, C.E., 2005. **Functions of a Complex Variable: Theory and Technique**, Society for Industrial and Applied Mathematics, Philadelphia, PA.

[21] Arsenault, M.E., Zhao, H., Purohit, P.K., Goldman, Y.E., Bau, H.H., 2007. **Confinement and manipulation of actin filaments by electric fields.** *Biophys. J.* 93(8):L42-L44.

[22] Reichl, L.E., 1998. **A Modern Course in Statistical Physics**, second ed. Wiley-Interscience, New York.

[23] da Fonseca, C.M., Petronilho, J., 2001. **Explicit inverse of some tridiagonal matrices.** *Linear Algebra Appl.* 325:7-21.

[24] Allen, M.P., Tildesley, D.J., 1987. **Computer Simulation of Liquids**, Oxford Science, Oxford.

[25] Chyan, C.L., Lin, F.C., Peng. H., Yuan, J.M., Chang, C.H., Lin, S.H., Yang, G., 2004. **Reversible mechanical unfolding of single ubiquitin molecules.** *Biophys. J.* 87(6):3995-4006.

Chapter 5

Statistics of the Heterogeneous Wormlike Chain

Main results of this chapter:

1. Distributions of (1) the end-to-end extension, and (2) the transverse displacement of the free end of a wormlike chain are evaluated analytically. The theory is simple, yet valid for any heterogeneous chain under any boundary condition.
2. Both the distributions are found to be asymmetric in general. Also, the most probable extension is found to coincide with the average extension.
3. The theory can be applied to the freely-jointed chain model as well. The results are verified by comparison to the known theory for the distribution function of a freely-jointed chain.

Since the introduction of the wormlike chain model, many studies have addressed the statistical behavior of a semiflexible polymer as defined by the model and its several variants [1, 2, 3, 4]. Below, we shall show that using the general theory developed in the previous chapter (section 4.3), we can evaluate the distribution functions of several interesting quantities for the wormlike chain, or fluctuating rod.

5.1 Distribution of the End-to-end Extension $P(x)$

In this section, we study the distribution function of the end-to-end extension $P(x)$ for a wormlike chain in a constant force and constant temperature

ensemble.

By definition, the probability $P(x)$ is the sum over the probability for the configurations ν with extension x:

$$P(x) = \sum_{\nu, x_\nu = x} P_\nu = \frac{1}{Z_F} \sum_{\nu, x_\nu = x} \exp\left[-\beta(E_\nu - F x_\nu) \right] \tag{5.1}$$

$$= \frac{\exp(\beta F x)}{Z_F} \sum_{\nu, x_\nu = x} \exp\left(-\beta E_\nu\right), \tag{5.2}$$

Here Z_F is the partition function for a fixed force ensemble. The term $\exp(\beta F x)$ can be pulled out of the summation because all the configurations considered have the same extension $x_\nu = x$. Noticing that the last term in Eq. 5.2 is nothing but the partitioin function Z_x of a fixed extension ensemble, we can write the distribution function as:

$$P(x) = \exp(\beta F x) \times \frac{Z_x}{Z_F}, \tag{5.3}$$

or

$$\log P(x) = \beta F x + \log Z_x - \log Z_F. \tag{5.4}$$

As an aside, here we see that the dependence of $P(x)$ on x comes from the term $\exp(\beta F x)\, Z_x$ (Eq. 5.3). However, recall the relation between Z_x and Z_F:

$$Z_F = \int_{-\infty}^{+\infty} \exp(\beta F x)\, Z_x \, dx, \tag{5.5}$$

which is nothing but a Laplace transform:

$$Z_F(-\beta F) = \mathscr{L}(Z_x). \tag{5.6}$$

Therefore, it is not surprising that many previous works have used the tool of Laplace transform to study the distribution functions [2].

Also, consider the Fourier transform of $(\exp(\beta F x)\, Z_x)$:

$$\mathcal{F}\left[\exp(\beta F x)\, Z_x\right] = \int \exp\left(-\frac{E - Fx}{k_B T}\right) \exp\left(-ikx\right) \mathcal{D}(\hat{t}) \tag{5.7}$$

$$= \int \exp\left(-\frac{E - (F - ik_B T k)x}{k_B T}\right) \mathcal{D}(\hat{t}), \tag{5.8}$$

where $\mathcal{D}$ is the path integral over all the configurations. Eq. 5.8 is nothing but the partition function of a fixed force ensemble with an effective force $F_{\mathrm{e}} = F - ik_B T k$. Therefore, the probability distribution function Eq. 5.3 can also be written as:

$$P(x) = \frac{\mathcal{F}^{-1}\left[Z_F(F - ik_B T k)\right]}{Z_F}. \tag{5.9}$$

It is because of this relation that the tool of Fourier transform has also been widely used to derive $P(x)$ [5, 6, 7, 8].

Coming back to Eq. 5.4, we already know from the previous chapter (section 4.3) that the expression for $\log Z_F$ is:

$$\log Z_F = -\frac{D_F}{2}\log\beta + FL\beta - W(F), \tag{5.10}$$

where D_F is the number of degrees of freedom in the fixed force ensemble, $W(F)$ is the unkown function whose physical meaning is the area below the force-extension curve (up to an undetermined constant) shown in Fig. 4.2.

Using the same method for the fixed extension ensemble (see Appendix G), we get the expression for $\log Z_x$:

$$\log Z_x = -\frac{D_x}{2}\log\beta - \beta A(x) + C_0(T) \tag{5.11}$$

where D_x is the number of degrees of freedom in the fixed extension ensemble, $A(x) = \int F dx$ is the area under the force-extension curve and C_0 is a constant independent of x.

Plugging in Eq. 5.10 and Eq. 5.11 into Eq. 5.4, we get:

$$\log P(x) = \beta Fx - \beta A(x) + C(T, F), \tag{5.12}$$

which is the distribution of the end-to-end extension in terms of an unknown but measurable function $A(x)$. Eq. 5.12 can be also written as:

$$P(x) = P_0 \cdot \exp\left[\,\beta Fx - \beta A(x)\,\right], \tag{5.13}$$

where P_0 is a constant determined by the normalization condition $\int P dx = 1$.

There are three important properties of the distribution function Eq. 5.13:

1. When $F = 0$, the distribution is:

$$\bar{P}(x) = P_0\ \exp\left[-\beta A(x)\right]. \tag{5.14}$$

   Here we use $\bar{P}$ to denote the distribution in a zero force ensemble. This formula has been derived for the classical freely-jointed chain model with $A(x)$ being interpreted as the work done by the external force [5]. Here we show the same result holds for a wormlike chain as well, even if it is heterogeneous. More importantly, Eq. 5.13 implies that to evaluate the distribution function $P(x)$ in a finite force ensemble, we only need to know $\bar{P}$ for a zero force ensemble, since the contribution of F only comes from the term $\exp(\beta Fx)$ in Eq. 5.13:

$$P(x) = P_0\,\bar{P}(x)\ \exp(\beta Fx). \tag{5.15}$$

   Here again, P_0 is a constant determined by the normalization condition $\int P dx = 1$. It may be different from the one in Eq. 5.13. The result that $P(x)$ is closely related to $\bar{P}(x)$ is consistent with the discussion in the *Introduction* of this proposal, where we show that the behavior of a polymer under a finite applied force is closely related to and completely determined by its behavior under zero force (Eq. 1.6).

2. Using Eq. 5.12, the most probable extension x can be evaluated as:

$$\frac{\partial \log P}{\partial x} = 0 \quad \Rightarrow F = \frac{\partial A}{\partial x} = F(x). \tag{5.16}$$

This means that most probable extension is the average extension in this problem.

3. Another universal feature of Eq. 5.13 is that when $Fx >> A(x)$, we have $P \sim \exp(\beta F x)$. The distribution function in this limit is independent of $A(x)$, the energy function that includes all the detailed information of the model. In other words, in the region $Fx >> A(x)$, chains under any boundary condition and with any heterogeneous mechanical property should have roughly the same end-to-end distance distribution.

To plot the distribution function, we need an expression for $A(x)$, which is again the area below the force-extension curve, or the energy stored in the system. For the 3D freely-jointed chain (we assume the equipartition theorem is valid), the force-extension relation is usually expressed as $x = x(F)$ (Eq. 1.1). So it is convenient to calculate the complementary energy $A'(F) = \int x dF$ first and then get $A(x)$ by $A(x) = Fx - A'(F)$:

$$A(x) = Fx - \int_0^F x\, dF = \frac{k_B T}{l}\left[\mathcal{L}^{-1}x - L\, \log \frac{\sinh\left(\mathcal{L}^{-1}\right)}{\mathcal{L}^{-1}}\right]. \tag{5.17}$$

Here $\mathcal{L}^{-1}$ is the inverse of the Langevin function $\mathcal{L}(\xi) = \coth(\xi) - 1/\xi$ evaluated at x/L. It has a series expansion which reads [5, 9]:

$$\mathcal{L}^{-1}(z) = 3z + \frac{9}{5}z^3 + \frac{297}{175}z^5 + \frac{1539}{785}z^7 + \cdots \tag{5.18}$$

On the other hand, the end-to-end distribution function for the freely-jointed chain model under zero force has been solved using the Fourier transform method [5, 6, 7, 8]:

$$\bar{P}(x) = \frac{1}{\pi (k_B T)^N} \int_0^{+\infty} \left[\frac{\sin(kl)}{k}\right]^N \cos(kx)\, dk. \tag{5.19}$$

Eq. 5.19 can be integrated [7], but the result is rather cumbersome and for large N, direct numerical integration is just as convenient [6]. We plot Eq. 5.19 together with our result discussed above (Eq. 5.14) in Fig. 5.1. The two theories match well with each other. But our theory can be easily extended for the wormlike chain model, as we shall discuss below.

For the homogeneous hinged-hinged wormlike chain, the force extension relation is [10]:

$$x = L - \frac{k_B T}{2\sqrt{K_b F}}\left[\coth\left(L\sqrt{\frac{F}{K_b}}\right) - \frac{1}{L}\sqrt{\frac{K_b}{F}}\right]. \tag{5.20}$$

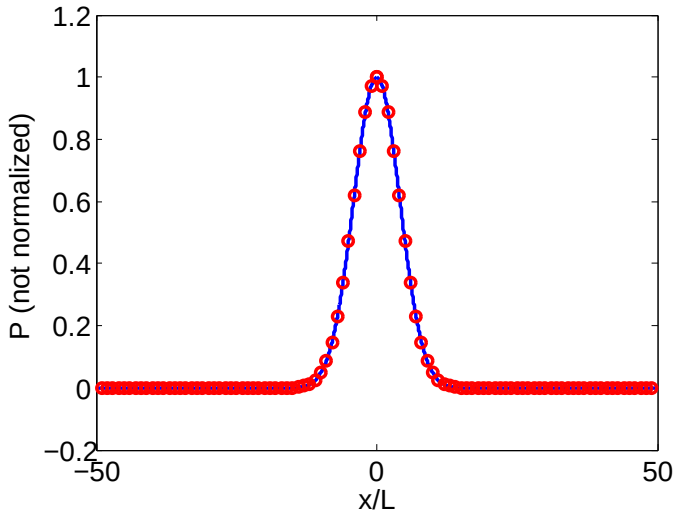

Figure 5.1: End-to-end distance distribution function $P(x)$ using Eq. 5.14 (red circles) and Eq. 5.19 (blue). Here the external force is $F = 0$pN, the segment length is $l = 1$nm and the contour length is $L = 50$nm. The two theories match well with each other.

Again, by integrating the above relation, we get the complementary energy $A'(F)$ and the stored energy $A(x)$ (there will be an unkown funtion of T when we do the integral, but that unkown function will be absorbed into the normalization constant):

$$A'(F) = \int x dF = LF - k_B T \log \left[\sinh \left(L\sqrt{\frac{F}{K_b}} \right) \right] - \frac{k_B T}{2} \log F, \qquad (5.21)$$

$$A(F) = xF - A'(F) = Fx - LF + k_B T \log \left[\sinh \left(L\sqrt{\frac{F}{K_b}} \right) \right] - \frac{k_B T}{2} \log F. \qquad (5.22)$$

With the expressions for $A(x)$, we can now plot the end-to-end distance distribution function (Eq. 5.20).

We plot Eq. 5.13 for different contour lengths and under different forces in Fig. 5.2 (freely-jointed chain) and Fig. 5.3 (wormlike chain). For short chains, the result shows that the distribution is not symmetric. When the contour length of the chain increases and becomes larger than its persistence length, the profile looks more symmetric. Further, increasing the applied force causes the profile to shift to the right and makes the peak sharper, as one can see in Fig. 5.2B and Fig. 5.3B. We note that similar results for the distribution profiles using the Monte Carlo simulation techniques have been reported recently (see Fig. 2 in reference [11]).

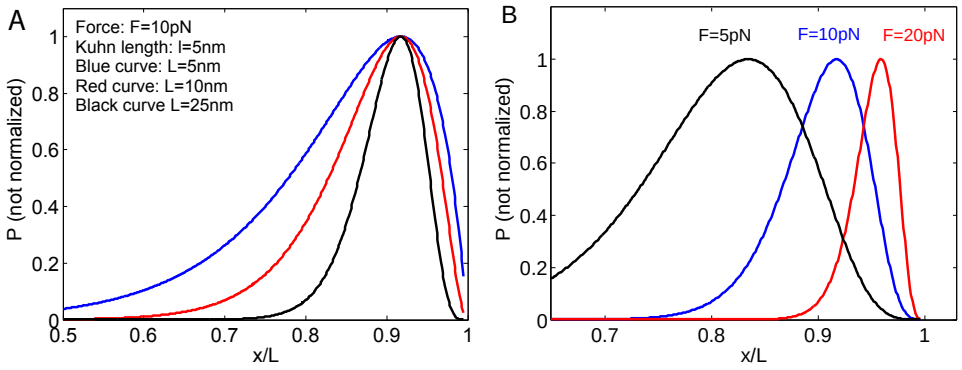

Figure 5.2: (A): End-to-end distance distribution function $P(x)$ for a freely-jointed chain with different contour lengths $L = 5, 10, 25$nm. Here $F = 10$pN and the Kuhn length is $l = 5$nm. The profile looks symmetric only when the contour length of the chain is long compared to its Kuhn length. (B) Distribution $P(x)$ for a freely-jointed chain under different values of tensile forces: $F = 5, 10, 20$pN. As the force increases, the profile shifts to the right and the peak becomes sharper. For both plots, $T = 300$K.

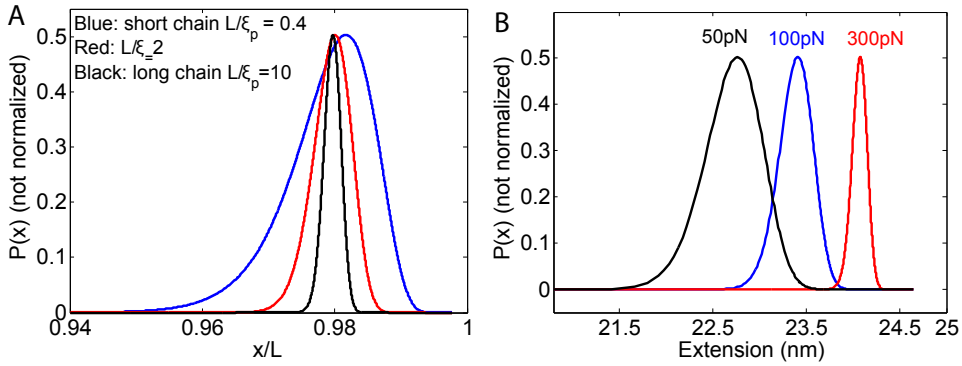

Figure 5.3: (A): End-to-end distance distribution function P(x) for a wormlike chain with different contour lengths $L = 1, 5, 25$nm. Here $F = 1000$pN. For short chain, the profile is clearly not symmetric. When the contour length of the chain increases and becomes comparable to its persistence length, the profile looks more symmetric. (B) Distribution P(x) for a wormlike chain under different values of tensile forces: $F = 50, 100, 300$pN. As the force increases, the profile shifts to the right and the peak becomes sharper. For both plots, $T = 300$K, $K_b = 2.5 k_B T \cdot$ nm.

5.2 Distribution of the Transverse Displacement

In this section, we consider a wormlike chain under hinged-free boundary conditions [1] and try to calculate the probability distribution of the transverse displacement of the free end. This quantity has been calculated previously in reference [4] using a different theory.

Let the position of the end of the chain be (x, r), where x is the end-to-end distance projected on the $\hat{X}$ axis (the direction of the applied force) and r is the transverse displacement. The question we address here is what is the probability $P(r, x)$ that the end of the chain is at (x, r)?

Again, we sum all the Boltzmann factors for the configurations with end of the chain at (x_0, r_0):

$$P(r_0, x_0) = \sum_{\nu, r_\nu = r_0, x_\nu = x_0} P(\nu) = \sum_{\nu, r_\nu = r_0, x_\nu = x_0} \frac{\exp\left[-\beta\left(E_\nu - F x_\nu\right)\right]}{Z_F} \quad (5.23)$$

$$= \frac{\exp(\beta F x_0)}{Z_F} \times \sum_{\nu, r_\nu = r_0, x_\nu = x_0} \exp\left(-\beta E_\nu\right). \quad (5.24)$$

The interesting thing is that although the last term in Eq. 5.24 has two constraints on the summation, it is still a partition function for a hinged-hinged chain in a fixed extension ensemble. But now the fixed extension is $\sqrt{x_0^2 + r_0^2}$ instead of x_0. So the distribution function Eq. 5.24 can be rewritten as:

$$P(r_0, x_0) = \frac{\exp(\beta F x_0)}{Z_F} \cdot Z_x\left(x = \sqrt{x_0^2 + r_0^2}\right). \quad (5.25)$$

We should be careful about the meanings of the two partition functions used in Eq. 5.25: (I) Z_F is the partition function in fixed F ensemble, with boundary conditions of hinged-free ends. (II) Z_x is the partition function in fixed x ensemble, with boundary conditions of hinged-hinged ends.

We can further write the distribution function as:

$$\log P(r_0, x_0) = \beta F_0 x_0 + \log Z_x\left(\sqrt{x_0^2 + r_0^2}\right) - \log Z_F. \quad (5.26)$$

Using Eq. 5.11 again for the expression of $\log Z_x$, we obtain:

$$P(r, x) = P_0 \exp\left[\beta F x - \beta A\left(\sqrt{x^2 + r^2}\right)\right], \quad (5.27)$$

where P_0 is determined by $\int\int P\, dx\, dr = 1$.

Further, note that the $P(r, x)$ calculated above is the probability that the end of the chain is located on a point (r, x). Taking into account the fact that the end of the chain can have different positions for the same r, we get:

$$P(r, x) = P_1 r \exp\left[\beta F x - \beta A\left(\sqrt{x^2 + r^2}\right)\right], \quad (5.28)$$

[1] Although in experiments, filaments are usually under clamped-free boundary conditions, here, for the sake of simplicity, we use the hinged-free boundary conditions.

where $P_1 = 2\pi P_0$.

Plugging Eq. 5.17 or Eq. 5.22 into Eq. 5.28, we obtain the distribution $P(r, x)$ for a freely-jointed chain or a wormlike chain. For simplicity, here for the wormlike chain, we use the formula:

$$F = \frac{(k_B T)^2}{K_b} \left[\frac{1}{4\left(1 - \frac{x}{L}\right)^2} - \frac{1}{4} + \frac{x}{L} \right], \tag{5.29}$$

so that the stored energy is:

$$A(x) = \frac{(k_B T)^2}{4K_b} \left(\frac{L^2}{L - x} - x + \frac{2x^2}{L} \right). \tag{5.30}$$

Then the analytic expression of the distribution function for a wormlike chain is:

$$P(r, x) = P_1 r \exp\left[\beta F x - \frac{k_B T L}{4K_b} \left(\frac{L'}{L' - x} - \frac{x}{L'} + \frac{2x^2}{L'^2} \right) \right], \tag{5.31}$$

where $L' = Lx/\sqrt{x^2 + r^2}$.

The distributions $P(r, x)$ for a freely-jointed chain and a wormlike chain are plotted in Fig. 5.4 for the following parameters: (1) Temperature $T = 300$K; (2) Kuhn length $l = 1$nm (freely-jointed chain) or bending modulus $K_b = 2.0 k_B T$ (wormlike chain); (3) Contour length $L = 25$ nm; (4) Fixed force $F = 50$pN. Here the extension x is fixed and P as a function of r is plotted. The distribution is asymmetric with $P(r = 0) = P(r \to +\infty) = 0$. When the fixed extension x increases, the peak in the distribution profile moves towards $r = 0$ and becomes sharper (Fig. 5.4). This is because a chain with larger extension has less freedom to fluctuate in the transverse direction.

5.3 Conclusions

In this chapter, we have shown one of the applications of the general theory discussed in the previous chapter (section 4.3). This general theory is powerful because it packs all the information about the boundary conditions and heterogeneity into an energy function that is measurable in experiments, as long as the energy is quadratic. Therefore, the theory is valid for any heterogeneous chain under any boundary condition. This is a great advantage when we study a short chain whose contour length is comparable to its persistence length. Moreover, almost all the expressions in this general theory are simple because all the complexity has been packed into the energy function. Using this theory, we have evaluated the end-to-end distance distribution and the also the transverse displacement distribution for a wormlike/freely-jointed chain.

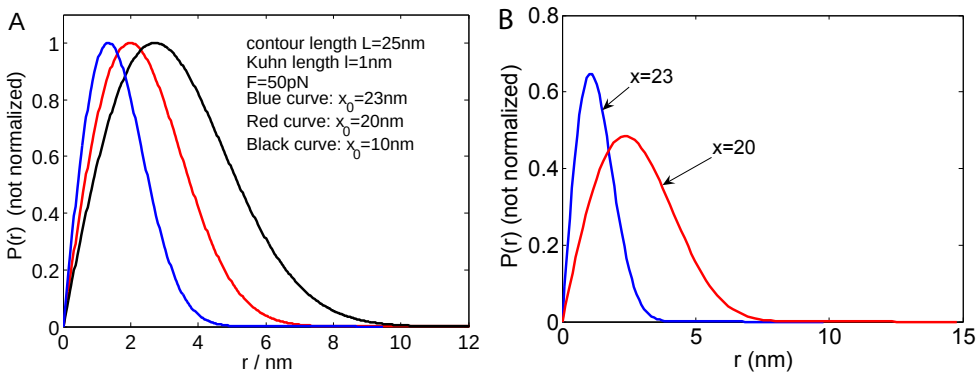

Figure 5.4: Distribution $P(r, x)$ for (A) a freely-jointed chain and (B) a wormlike chain. The chains are subjected to hinged-free boundary conditions. x, r are respectively the extension and transverse displacement of the free end. Here x is fixed for each curve and $P(r)$ versus r is plotted. The parameters are (1) Temperature $T = 300$K; (2) Kuhn length $l = 1$nm (freely-jointed chain) or bending modulus $K_b = 2.0k_BT$ (wormlike chain); (3) Contour length $L = 25$ nm; (4) Fixed force $F = 50$pN. The figures show that as the fixed x increases, the peak in the distribution profile becomes sharper. This makes sense because a chain with large extension has less freedom to fluctuate in the transverse direction.

Bibliography

[1] Yamakawa H, Fujii M. 1973. **Wormlike chains near the rod limit: Path integral in the WKB approximation.** *Chem. Phys.* 59:6641.

[2] Spakowitz AJ, Wang ZG. 2005. **End-to-end distance vector distribution with fixed end orientations for the wormlike chain model.** *Phys. Rev. E* 72:041802.

[3] Mehraeen S, Sudhanshu B, Koslover EF, Spakowitz AJ. 2008. **End-to-end distribution for a wormlike chain in arbitrary dimensions.** *Phys Rev E Stat Nonlin Soft Matter Phys.* 77(6 Pt 1):061803.

[4] Segall DE, Nelson PC, Phillips R. 2006. **Excluded-volume effects in tethered-particle experiments: bead size matters.** *Phys. Rev. Lett.* 96:088306.

[5] Flory PJ. 1989. **Statistical Mechanics of Chain Molecules.** Reprinted ed. Oxford University Press, New York.

[6] Boyd RH, Phillips PJ. 1993. **The Science of Polymer Molecules.** 1st ed. Cambridge University Press.

[7] Yamakawa H. 1971. **Modern Theory of Polymer Solutions.** Harper & Row, Publishers, New York, Evanston, San Francisco, London.

[8] Weiner JH. 1983. **Statistical Mechanics of Elasticity.** John Wiley & Sons. New York.

[9] Johal AS, Dunstan DJ. 2007. **Energy functions for rubber from microscopic potentials.** *J. Appl. Phys.* 101:084917.

[10] Purohit, P.K., Arsenault, M.E., Goldman, Y., Bau, H.H., 2008. **The mechanics of short rod-like molecules in tension.** *Int. J. Non-linear Mech.* 43(10):1056-1063.

[11] Kessler DA, Rabin Y. 2004. **Distribution functions for filaments under tension.** *J. Chem. Phys* 121:1155-1164.

Chapter 6

Fluctuating Elastic Filaments Under Distributed Loads

Main results of this chapter:

1. We study the thermo-mechanical properties of an extensible thermally fluctuating elastic filament under distributed forces in this chapter.

2. For the force-extension relation under uniform tangent distributed loads τ, we show that the filament is equivalent to one under end-to-end applied force $F = \tau L_0/2$ where L_0 is the length of the filament.

3. Applications to the stretching and fluctuation of DNA in non-uniform microfluidic channels are discussed at the end of the chapter.

6.1 Introduction

The wormlike chain model, or the fluctuating elastic filament model, has been extensively used to describe the mechanical behavior of semi-flexible polymers like DNA, actin and other long macromolecules [1, 2, 3, 4]. In particular, its force-extension relation is usually fitted to the experimental data of stretched polymers to extract their mechanical properties like the bending and stretching moduli [2]. Some authors have also used the model to predict the transverse fluctuations of the polymers and compare the results with experiments and simulations [5, 6, 7]. To account for the new and detailed results obtained using sophisticated experimental techniques, the fluctuating rod model is be-

ing continuously improved and generalized. For example, as the length scale at which people probe the mechanics of the polymers becomes shorter and shorter, boundary conditions and heterogeneity of the filament can not be ignored. To account for these effects, we have recently generalized the classical wormlike chain model to study polymers with heterogeneous mechanical properties that are loaded under different boundary conditions [7].

Most of the studies so far consider only the behavior of a polymer under end-to-end applied forces and torques. The reason for this may be that the majority of force-extension measurements on macromolecules are carried out in optical tweezers, magnetic tweezers, or atomic force microscopes (AFM), all of which apply forces at the end of the polymer chains. But, there are many other cases where biological filaments are subjected to distributed loads. For example, DNA in a nanofluidic or microfluidic channel is subjected to distributed drag force applied by the surrounding fluid flow. Molecular motors exert point loads, which are a special case of distributed loads, to the long actin filaments in cells and muscles. Also, a uniformly charged polymer in a constant electric field behaves as if it is stretched by a force that varies along the contour. The behavior of a filament under such distributed loads is not well understood. In fact, if one simply uses an end-to-end force model to fit the extension data for a piece of DNA subjected to uniform flow, the fitted drag coefficient is much lower than the true measured value [8]. A few groups have tried to tackle this problem theoretically in recent years [11, 12, 13]. Some of these works relied on phenomenological arguments [11], while some solved the problem in the limit of a weak force field [12].

In this chapter, we first calculate analytically the force-extension relation for a continuous filament under uniform distributed load. We show using Fourier series that under uniform tangential force per unit reference length τ along the filament, it suffers the same extension as one under end-to-end force of magnitude $F = \tau L_0/2$, where L_0 is the contour length. However, a Fourier analysis of this kind is easy to do only when τ is uniform. To consider more general loadings, we use our theoretical framework [7] developed earlier to investigate the thermo-mechanical properties of a discretized filament. In particular, we first find the ground state, or the minimum energy state, for a filament under distributed loads. Then the thermal fluctuation around this ground state is studied using a statistical mechanical approach. In particular, the partition function is obtained analytically using multi-dimensional Gaussian integrals. Once we get the partition function, the free energy of the system is derived immediately, and the thermo-mechanical properties of the system are calculated by differentiating the free energy. This method is capable of reproducing the classical wormlike chain results [7]. Moreover, because of the discretization, it can easily deal with filaments with heterogeneous mechanical properties. Here, we apply this framework to study the fluctuation of a filament under distributed loads.

6.2 Theory

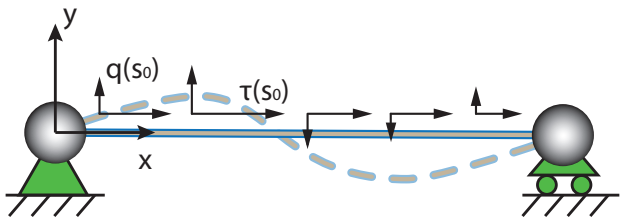

Figure 6.1: A fluctuating elastic filament (extensible wormlike chain) under distributed forces. The origin of the $x-y$ coordinate system is set at the head of the filament, which is hinged. The other end of the filament is constrained to move only in the x direction. One possible deformed configuration of the filament is shown in dashed line.

6.2.1 Theory for a continuous elastic filament

Consider a semi-flexible polymer, or fluctuating elastic filament with stretching modulus K_s and bending modulus K_b. One end of the filament is hinged at the origin of the $x-y$ coordinate system shown in Fig. 6.1, while the other end is constrained to move only in the x-direction. The reference configuration of the filament (the state under zero loads at zero temperature) is straight, lying on the x axis. The coordinate of its center line is $[x, y] = [s_0, 0]$. Here s_0 is the reference arc length with $s_0 \in [0, L_0]$, and L_0 being the undeformed contour length. Under distributed tangential force $\tau(s_0)$ per unit reference length and distributed normal force $q(s_0)$ per unit reference length, the filament deforms into $[x, y] = [s_0 + u, w]$, where $u(s_0)$ and $w(s_0)$ are the tangential and normal displacements respectively. Axial strain develops in the deformed filament and it can be expressed in terms of the displacements $u(s_0)$ and $w(s_0)$ assuming moderate rotations as:

$$\epsilon(s_0) = \frac{ds - ds_0}{ds_0} \approx \frac{\partial u}{\partial s_0} + \frac{1}{2}\left(\frac{\partial w}{\partial s_0}\right)^2. \tag{6.1}$$

Here ds is the infinitesimal deformed arc length, and we keep terms up to the order of $O(u, w^2)$ in the approximation.

The energy of the deformed filament, as a sum of its stretching, bending, and potential energies, is:

$$E = \int_0^{L_0} \frac{K_s}{2}\epsilon^2\, ds_0 + \int_0^{L_0} \frac{K_b}{2}\left(\frac{\partial^2 w}{\partial s_0^2}\right)^2 ds_0 - \int_0^{L_0} \tau u\, ds_0 - \int_0^{L_0} q\, w\, ds_0, \tag{6.2}$$

where K_s and K_b are the stretching and bending moduli of the filament. They are not necessarily constants and can be functions of the arc length s_0 in the reference configuration. As discussed by Odijk [3], rather than express the

energies in terms of the displacements $u(s_0)$ and $w(s_0)$, it is more convenient to use $\epsilon(s_0)$ and $w(s_0)$ as independent variables, because the total energy can be decoupled using these two variables. This is true even when the filament is under distributed loads. Using Eq. 6.1, $u(s_0)$ in Eq. 6.2 can be eliminated and the energy can be grouped into two decoupled terms – one involving $\epsilon(s_0)$ only, and the other involving $w(s_0)$ only:

$$E = E_\epsilon + E_w, \tag{6.3}$$

where the expressions for the two energy terms are:

$$E_\epsilon = \int_0^{L_0} \left[\frac{K_s}{2}\epsilon^2 - \tau \int_0^{s_0} \epsilon \, ds_0 \right] ds_0, \tag{6.4}$$

$$E_w = \int_0^{L_0} \left[\frac{K_b}{2} \left(\frac{\partial^2 w}{\partial s_0^2} \right)^2 + \frac{\tau}{2} \int_0^{s_0} \left(\frac{\partial w}{\partial s_0} \right)^2 ds_0 - qw \right] ds_0. \tag{6.5}$$

The minimum energy configuration can be evaluated by setting the variations $\delta E_\epsilon = 0$ and $\delta E_w = 0$. The former variation gives the strain of the minimum energy configuration:

$$\epsilon_{\min}(s_0) = \frac{1}{K_s} \int_{s_0}^{L_0} \tau(s_0) \, ds_0, \tag{6.6}$$

while the latter variation yields a 4th order ODE for the transverse displacement $w_{\min}(s_0)$ of the minimum energy configuration:

$$(K_b w''_{\min})'' - \left(w'_{\min} \cdot \int_{s_0}^{L_0} \tau \, ds_0 \right)' - q = 0, \tag{6.7}$$

with hinged-hinged boundary conditions $w(0) = w''(0) = w(L_0) = w''(L_0) = 0$. Here we use $'$ to denote the derivative d/ds_0. We note again that in deriving these results, we do not assume the moduli K_s and K_b to be uniform. They can vary along the filament. By specifying the distributed loads $\tau(s_0)$ and $q(s_0)$, we can solve Eq. 6.6 and Eq. 6.7 to get $\epsilon_{\min}$ and $w_{\min}$ respectively. Then by using Eq. 6.1, we can obtain the longitudinal displacement $u_{\min}$. Thus, the deformed configuration of the filament, without taking thermal fluctuations into account, is known. This minimum energy configuration is the ground state of the filament around which the system is fluctuating.

While the partition function and fluctuations of a discrete semi-flexible chain can be evaluated under rather general loading conditions, which we will discuss in the next section, it is difficult to compute the same quantities analytically for a continuous filament unless the distributed load is uniform. Here we briefly discuss how one can evaluate the average end-to-end extension of a continuous filament under constant τ, by using a Taylor expansion of the path integral [9], and the Fourier series method [2, 10] respectively for the

small and large τ limits. For simplicity, we also set the normal distributed force $q = 0$ for now.

In the small τ limit, the potential energy term involving τ in the Boltzmann factor can be expanded using $\exp(x) \approx 1 + x$. After carrying out this exercise the Boltzmann weighted average end-to-end extension reads:

$$\langle \Delta x \rangle = \frac{1}{Z} \int x(L_0) \cdot \exp\left(-\frac{E_b + E_s - \tau \int_0^s x \, ds_0}{k_B T} \right) \mathcal{D}\vec{r} \tag{6.8}$$

$$= \beta\tau \left\langle \int_0^s x(s_0) \cdot x(L_0) \, ds_0 \right\rangle_0 + O(\tau^2), \tag{6.9}$$

where Z is the partition function, $\beta = 1/k_B T$, E_b and E_s are the bending and stretching energies respectively. The key step here is that, after the expansion, the potential energy part in the Boltzmann factor is factored out and so the average $\langle \cdot \rangle_0$ in Eq. 6.9 is evaluated in a $\tau = 0$ ensemble.

Now, the problem in the small τ limit is how to do the average in a $\tau = 0$ ensemble. To solve this problem, we recall that for a wormlike chain in a $\tau = 0$ ensemble, the correlation of its tangent angle θ satisfies: $\langle \theta(s) \cdot \theta(s') \rangle = \exp\left(-|s - s'|/\xi_p\right)$ [9], which can be used to evaluate $\left\langle \int_0^s x(s_0) \cdot x(L_0) \, ds_0 \right\rangle_0$ in Eq. 6.9, given $x(s_0) = \int_0^{s_0} \cos\theta ds_0$. Here ξ_p is the persistence length of the wormlike chain. The calculation is tedious but the final result for $\langle \Delta x \rangle$ turns out to be linear, as expected, in the small τ limit:

$$\langle \Delta x \rangle = \frac{2\xi_p L_0}{D k_B T} \left[1 - \frac{\xi_p}{L_0} \left(1 - e^{-L_0/\xi_p} \right) \right] \cdot \frac{\tau L_0}{2} + \frac{\tau L_0^2}{2K_s}, \tag{6.10}$$

with D being the dimension of space, i.e, $D = 2, 3$ for a 2D and 3D chain respectively. The last term in the above equation is the contribution of the pure stretching term in the energy.

When $L_0 >> \xi_p$, the force-extension relation is simply:

$$\langle \Delta x \rangle = \frac{2\xi_p L_0}{D k_B T} \cdot \frac{\tau L_0}{2} + \frac{\tau L_0^2}{2K_s}. \tag{6.11}$$

One may recognize that the force-extension relation shown here for a filament under small uniform τ is in exactly the same form as the relation for a filament under small end-to-end force F, with F being replaced by $\tau L_0/2$. Therefore, we conclude that, as far as the force-extension relation is concerned, at small loads a uniformly distributed tangential force is equivalent to an end-to-end force $F_{\text{eff}} = \tau L_0/2$.

In the large τ limit, on the other hand, where the approximation of the tangent angle $\theta << 1$ holds, one can use the Fourier series method to tackle the problem. As usual, we expand the tangent angle $\theta = \partial w/\partial s_0$ in a Fourier cosine series:

$$\theta(s_0) = \sum_{n=1}^{+\infty} a_n \cos\left(\frac{2n\pi s_0}{L_0} \right). \tag{6.12}$$

There is no a_0 term here because the hinged-hinged boundary condition requires $\int_0^{L_0} \theta ds_0 = 0$. Plugging the Fourier series into Eq. 6.5, the energy of the filament contributed by w becomes:

$$E_w = \sum_{n=1}^{+\infty} \left(\frac{K_b \pi^2 n^2}{L} + \frac{\tau L^2}{8} \right) a_n^2. \tag{6.13}$$

The equipartition theorem of statistical mechanics states that each quadratic mode should have an average energy equal to $k_B T/2$, which leads to:

$$\langle a_n^2 \rangle = \frac{k_B T}{2\left(\frac{K_b \pi^2 n^2}{L} + \frac{\tau L^2}{8} \right)}, \tag{6.14}$$

Using Parseval's theorem, we obtain the expression for $\int_0^{L_0} \langle \theta^2 \rangle ds_0$ from Eq. 6.14, which finally leads to the force-extension relation of a chain under uniform τ:

$$\langle \Delta x \rangle = L_0 - \frac{k_B T}{4\sqrt{K_b \tau L_0/2}} \left[\coth\left(L_0 \sqrt{\frac{\tau L_0}{2K_b}} \right) - \frac{1}{L_0} \sqrt{\frac{2K_b}{\tau L_0}} \right] + \frac{\tau L_0^2}{2K_s}. \tag{6.15}$$

Here again the last term is the independent contribution from the stretching energy E_ϵ. Once again, we see that the force-extension relation, in the large τ limit, has the same form as a wormlike chain under a large effective end-to-end force $F_{\text{eff}} = \tau L_0/2$. Hence, we have shown that this equivalent relation holds for both small and large τ. Following Marko and Siggia [2], the force-extension relation for a filament under uniform τ can be written as:

$$\frac{\tau L \xi_p}{2k_B T} = \frac{1}{4}\left(1 - \frac{x}{L_0}\right)^{-2} - \frac{1}{4} + \frac{x}{L_0} - \frac{\tau L_0}{2K_s}. \tag{6.16}$$

From here on, we will focus on the large τ limit only because the filament under small loads behaves as a linear entropic spring.

We saw in the above discussion that the Fourier series method works only when τ is a constant. It is possible to deal with non-uniform distributed force if one ignores the boundary conditions and applies the wormlike-chain constitutive law to an infinitesimal segment on the continuous filament, and then integrates to recover the end-to-end extension of the entire filament. In particular, let $f(s_0)$ be the *internal* force along the filament in the tangential direction. Balance of forces on an infinitesimal segment ds_0 reads (Fig. 6.2A):

$$f(s_0 + ds_0) - f(s_0) + \tau ds_0 = 0, \tag{6.17}$$

which leads to $\partial f/\partial s_0 = -\tau$, whose solution with boundary condition $f(L_0) = 0$ is:

$$f(s_0) = \int_{s_0}^{L_0} \tau(s_0)\, ds_0. \tag{6.18}$$

This tells us that, when $\tau > 0$, the internal stress decreases from the fixed end to the other end, which makes sense because τ is positive when pointing away from the fixed end. On the other hand, the stretch $\lambda(s_0) = \epsilon(s_0) + 1$ for a 2D extensible wormlike chain is [3]:

$$\lambda = \frac{\partial x}{\partial s_0} = 1 - \frac{k_B T}{4\sqrt{K_b f}} \left[\coth\left(L\sqrt{\frac{f}{K_b}} \right) - \frac{1}{L}\sqrt{\frac{K_b}{f}} \right] + \frac{f}{K_s}. \tag{6.19}$$

Plugging Eq. 6.18 into Eq. 6.19, eliminating f and solving the ODE for $x(s_0)$, we can obtain $\Delta x = x(L_0) - x(0)$. Note that this procedure works regardless of whether τ is a constant. In particular, if τ is uniform along the length of the filament, the result is:

$$\langle \Delta x \rangle = L_0 - \frac{k_B T}{2\tau L_0} \log\left[\frac{\sinh \omega}{\omega} \right] + \frac{\tau L_0^2}{2K_s}, \tag{6.20}$$

where $\omega = L\sqrt{\tau L_0 / K_b}$. Eq. 6.20 is not exactly the same as Eq. 6.15. This is because to derive Eq. 6.20, we have ignored the boundary condition that leads to the force-extension relation of a wormlike chain, and used it as the constitutive relation for an infinitesimal segment. However, we will show later (Fig. 6.2B) that the force-extension curves from the two equations are close though not exactly the same.

The advantage of analyzing a continuous filament as we have done above is that we get analytic closed form results. However, as we have already seen, the analysis is either limited to special cases or relies on some additional assumptions that are not easy to verify. To get the exact thermal fluctuations of a filament under general distributed loads, it is convenient to first discretize it into segments. The partition function of the system, which is a path integral for a continuous filament, becomes a multi-dimensional Gaussian integral for a discretized filament or chain, and can be evaluated easily [14, 7]. In the limit where the discretized segment length $l_0 \to 0$, the number of discretized segments $N \to +\infty$, while $L_0 = N l_0$ is kept constant, the discrete chain becomes the desired continuous filament. Below, we discuss a discrete fluctuating filament under distributed forces.

6.2.2 Energy of a discretized elastic filament or semi-flexible chain

We use the following notations for a discrete chain. K_{si}, K_{bi} are the stretching and bending moduli of segment i of the chain. They can be different for different i, and $i \in [1, N]$. The reference coordinate of the ith node of the chain is $(x_i,\ y_i) = (il_0, 0)$, so that the chain is straight lying on the x axis. Under distributed loads τ_i and q_i per unit length on the ith segment, the node moves to $(x_i,\ y_i) = (il_0 + u_i,\ w_i)$, with $(u_i,\ w_i)$ being the nodal displacements. The axial strain for each segment is represented by the vector $\vec{\epsilon}^T = [\epsilon_1,\ \epsilon_2, \cdots, \epsilon_N]$. Furthermore, we define the discrete version of the tangent angle $\theta(s_0) = dw/ds_0$

as follows: $\theta_i = (w_i - w_{i-1})/l_0$. We wish to write the energy of the discrete chain in terms of the strains $\vec{\epsilon}$ and the angles $\vec{\theta} = [\theta_1, \cdots \theta_N]$.

The discretized version of the energies (Eq. 6.4 and 6.5) are quadratic expressions which can be written compactly in matrix form. In particular, the discretized version of the energy term involving ϵ is (Eq. 6.4):

$$E_\epsilon = \sum_{i=1}^{N} \left[\frac{K_{si}\, l_0}{2} \epsilon_i^2 - \tau_i l_0^2 \sum_{j=1}^{i} \epsilon_j \right], \tag{6.21}$$

and it can be written compactly as:

$$E_\epsilon = \frac{1}{2} \vec{\epsilon}^T \cdot [\mathbf{K}_\epsilon]\, \vec{\epsilon} + \vec{R}_\epsilon^{\,T} \cdot \vec{\epsilon}, \tag{6.22}$$

with the $N \times N$ stiffness matrix being $[\mathbf{K}_\epsilon]_{ij} = K_{si} l_0 \delta_{ij}$, and the ith component of the vector $\vec{R}_\epsilon$ being $-l_0^2 \sum_{j=i}^{N} \tau_j$. Similarly, the energy term involving only w (Eq. 6.5) can be written in terms of $\vec{\theta}$:

$$\begin{aligned} E_w &= \sum_{i=1}^{N} \left[\frac{K_{bi}}{2l_0} (\theta_i - \theta_{i-1})^2 + \frac{\tau_i l_0^2}{2} \sum_{j=1}^{i} \theta_j^2 - q_i l_0^2 \sum_{j=1}^{i} \theta_j \right] && (6.23) \\ &= \frac{1}{2} \vec{\theta}^T \cdot [\mathbf{K}_\theta]\, \vec{\theta} + \vec{R}_\theta^{\,T} \cdot \vec{\theta}. && (6.24) \end{aligned}$$

We note that the stiffness matrix $[\mathbf{K}_\theta]$ is a sparse tridiagonal matrix.

Finally, to impose the boundary condition and to constrain the end of the chain such that $w(L_0) = 0$, we add a penalty energy:

$$\begin{aligned} E_p &= \frac{K_p}{2} [w(L_0) - 0]^2 = \frac{K_p}{2} \left(\sum_{i=1}^{N} \theta_i l_0 \right)^2 && (6.25) \\ &= \frac{1}{2} \vec{\theta}^T \cdot [\mathbf{K}_p]\, \vec{\theta}. && (6.26) \end{aligned}$$

Eq. 6.24 and Eq. 6.26 can be combined, and therefore, we can write the total energy of the chain $E = E_\epsilon + E_w + E_p$ as:

$$E = \left\{ \frac{1}{2} \vec{\epsilon}^T \cdot [\mathbf{K}_\epsilon]\, \vec{\epsilon} + \vec{R}_\epsilon^{\,T} \cdot \vec{\epsilon} \right\} + \left\{ \frac{1}{2} \vec{\theta}^T \cdot [\mathbf{K}_{\theta p}]\, \vec{\theta} + \vec{R}_\theta^{\,T} \cdot \vec{\theta} \right\}, \tag{6.27}$$

where $[\mathbf{K}_{\theta p}] = [\mathbf{K}_\theta] + [\mathbf{K}_p]$.

As for a continuous filament, the ground state of the discrete chain is computed first by solving $\partial E/\partial \epsilon_i = 0$ and $\partial E/\partial \theta_i = 0$. These result in two linear sets of equations:

$$[\mathbf{K}_\epsilon]\, \vec{\epsilon}_{\min} = -\vec{R}_\epsilon, \quad [\mathbf{K}_{\theta p}]\, \vec{\theta}_{\min} = -\vec{R}_\theta, \tag{6.28}$$

which are solved to determine the ground state around which the chain fluctuates.

We next consider the thermal fluctuation around the ground state. We define the deviations from the ground state as $\Delta\vec{\epsilon} = \vec{\epsilon} - \vec{\epsilon}_{\min}$, $\Delta\vec{\theta} = \vec{\theta} - \vec{\theta}_{\min}$. Then the energy (Eq. 6.27) in terms of these deviation variables is simply:

$$E = E_{\min} + \frac{1}{2}\Delta\vec{\epsilon}^{T} \cdot [\mathbf{K}_{\epsilon}]\, \Delta\vec{\epsilon} + \frac{1}{2}\Delta\vec{\theta}^{T} \cdot [\mathbf{K}_{\theta p}]\, \Delta\vec{\theta}, \tag{6.29}$$

where $E_{\min}$ is the ground state energy. Note that the linear terms disappear when the energy is expressed in terms of the deviation variables.

6.2.3 Partition function and free energy

For a semi-flexible chain, the elastic and potential energies are usually comparable to the thermal energy $k_B T$ at room temperature, where k_B is the Boltzmann constant and T is the temperature in Kelvin, set to be 300K in this study. Therefore, the chain does not stay in the ground state forever. Instead, it fluctuates and samples different configurations, labelled as ν below, around the ground state with Boltzmann statistics: $P_\nu \sim \exp(-E_\nu/k_B T)$. Here P_ν is the probability that a configuration ν with energy E_ν is sampled. The thermo-mechanical behavior of this fluctuating elastic chain can be evaluated using statistical mechanics by computing the partition function Z, which is the sum of Boltzmann factors over all the allowed configurations. In our case, the energy of the system has been written in a quadratic matrix form (Eq. 6.29) and the partition function is:

$$\begin{aligned} Z &= \int_{-\infty}^{+\infty} \cdots \int_{-\infty}^{+\infty} \exp\left(-\frac{E}{k_B T}\right)\; d\left(\Delta\vec{\epsilon}\right)\; d\left(\Delta\vec{\theta}\right) && (6.30)\\ &= e^{-\beta E_{\min}} \cdot \sqrt{\frac{(2\pi k_B T)^N}{\det\left[\mathbf{K}_{\epsilon}\right]}} \cdot \sqrt{\frac{(2\pi k_B T)^N}{\det\left[\mathbf{K}_{\theta p}\right]}}, && (6.31) \end{aligned}$$

where $\beta = 1/k_B T$ and $\mathbf{K}_\epsilon$ and $\mathbf{K}_{\theta p}$ are $N \times N$ matrices. From the partition function Z, we get the free energy G of the system:

$$\begin{aligned} G &= -k_B T \log Z && (6.32)\\ &= E_{\min} + \frac{k_B T}{2}\log\det\left[\mathbf{K}_{\epsilon}\right] + + \frac{k_B T}{2}\log\det\left[\mathbf{K}_{\theta p}\right] - k_B T N \log(2\pi k_B T). && (6.33) \end{aligned}$$

We note that G is the Gibbs free energy because the partition function (Eq. 6.31) is evaluated for a fixed temperature, fixed loads ensemble. Therefore, we have:

$$dG = -S \cdot dT - \sum_{i=1}^{N} u_i \cdot d\left(\tau_i l_0\right) - \sum_{i=1}^{N} w_i \cdot d\left(q_i l_0\right). \tag{6.34}$$

By differentiating the free energy we can get the thermo-mechanical properties, like the force-extension relation, of the chain.

6.2.4 Force-extension relation

Noticing that $\tau_N l_0$ and u_N (distributed force on the last segment and longitudinal displacement of the last node) is a conjugate pair with respect to the energy (Eq. 6.34), we have:

$$\langle u_N \rangle = -\frac{\partial G}{\partial (\tau_N l_0)}. \tag{6.35}$$

In this chapter, $\langle \cdot \rangle$ denotes the usual ensemble average of all sampled configurations weighted by the Boltzmann factor. The average end-to-end extension of the chain is $\langle \Delta x \rangle = \langle x(L_0) - x(0) \rangle = \langle x(L_0) \rangle = L_0 + \langle u_N \rangle$, which turns out to be:

$$\langle \Delta x \rangle = \Delta x_{\min} - \frac{k_B T}{2 l_0} \cdot \frac{\partial}{\partial \tau_N} \left(\log \det \left[\mathbf{K}_{\theta p} \right] \right). \tag{6.36}$$

where $\Delta x_{\min}$ is the extension of the chain in the ground state without thermal fluctuation. Here we have used the facts that $L_0 - \partial E_{\min} / \partial (l_0 \tau_N) = \Delta x_{\min}$, and also that the stiffness matrix $[\mathbf{K}_\epsilon]$ does not depend on the distributed loads τ. We note that the last term in Eq. 6.36, which is proportional to the thermal energy $k_B T$, is the contribution of the average extension from thermal fluctuation. When $T = 0$ and there is no thermal fluctuation, $\langle \Delta x \rangle = \Delta x_{\min}$, as it should be, because the only configuration sampled is the minimum energy state.

6.2.5 Thermal fluctuation around the ground state

For the quantities that do not have clear conjugate pairs, their fluctuations can be evaluated directly from a Boltzmann weighted sum. The key is to use the following multi-dimensional Gaussian integral formula [16]:

$$\langle f(\vec{x}) \rangle = \frac{\int f(\vec{x}) \cdot \exp\left(-\frac{1}{2} \vec{x}^{\,T} \cdot [\mathbf{A}] \, \vec{x} \right) \, d\vec{x}}{\int \exp\left(-\frac{1}{2} \vec{x}^{\,T} \cdot [\mathbf{A}] \, \vec{x} \right) \, d\vec{x}} = \exp\left(\frac{1}{2} \sum_{i,j=1}^{N} [\mathbf{A}]^{-1}_{ij} \, \frac{\partial}{\partial x_i} \frac{\partial}{\partial x_j} \right) f(\vec{x}) \Big|_{\vec{x}=\vec{0}}. \tag{6.37}$$

Here $f(\vec{x})$ can be some general polynomial functions which are weighted by the Boltzmann factor in the numerator. The denominator on the left-hand-side is just the partition function, which serves as the normalization factor to the weighted average. On the right-hand-side, the exponential operating on the differential operator is understood as a power series: $\exp(a) = 1 + a + a^2/2 + \cdots$.

Using Eq. 6.37, the thermal fluctuation in strain can be evaluated. In particular, for the strain ϵ, the mean deviation and mean square deviation from the ground state are respectively:

$$\langle \Delta \epsilon_i \rangle = 0 \tag{6.38}$$

$$\langle \Delta \epsilon_i \cdot \Delta \epsilon_j \rangle = k_B T \left[\mathbf{K}_\epsilon \right]^{-1}_{ij} = \frac{\delta_{ij} k_B T}{K_{si} l_0}. \tag{6.39}$$

Similarly, the fluctuation in the angles $\vec{\theta}$ is:

$$\langle \Delta\theta_i \rangle = 0 \tag{6.40}$$

$$\langle \Delta\theta_i \cdot \Delta\theta_j \rangle = k_B T \left[\mathbf{K}_{\theta p}\right]^{-1}_{ij}. \tag{6.41}$$

We see that the mean square thermal fluctuations around the ground state increase linearly as we increase the temperature, and decrease as the we increase the mechanical stiffness of the system, in agreement with intuition.

In experiments one typically measures the fluctuations in displacements. These can be calculated directly from Eq. 6.37, or alternatively, using Eq. 6.39 and 6.41. In particular, the fluctuation in the transverse displacement is:

$$\langle \Delta w_i \rangle = l_0 \sum_{m=1}^{i} \langle \theta_m \rangle = 0, \tag{6.42}$$

$$\langle \Delta w_i \cdot \Delta w_j \rangle = l_0^2 \sum_{m=1}^{i} \sum_{n=1}^{j} \langle \Delta\theta_m \cdot \Delta\theta_n \rangle. \tag{6.43}$$

Similarly, the fluctuation in displacement u can be obtained by using the fourth moment of the multi-dimensional Gaussian distribution:

$$\langle \Delta u_i \rangle = -\frac{l_0}{2} \sum_{m=1}^{i} \langle \theta_m^2 \rangle, \tag{6.44}$$

$$\langle \Delta u_i^2 \rangle = k_B T l_0 \sum_{m=1}^{i} \frac{1}{K_{sm}} \tag{6.45}$$

$$+ \frac{l_0^2}{4} \sum_{m=1}^{i} \sum_{n=1}^{i} \left(\langle \Delta\theta_m^2 \rangle \langle \Delta\theta_n^2 \rangle + 2\langle \Delta\theta_m \cdot \Delta\theta_n \rangle^2 + 4\bar{\theta}_m \bar{\theta}_n \langle \Delta\theta_m \cdot \Delta\theta_n \rangle \right). \tag{6.46}$$

Here $\bar{\theta}$ is the angle for the ground state configuration. We note that while $\langle \Delta w_i \cdot \Delta w_j \rangle$ is the fluctuation around the ground state, $\langle \Delta u_i \cdot \Delta u_j \rangle$ is not; because $\langle \Delta w_i \rangle = 0$ and $\langle \Delta u_i \rangle$ is not.

6.3 Results

We first show in Fig. 6.2 that the theories for a continuous rod and the theory for a discrete chain yield the same result when τ is a constant along the arc length. For large τ, the thermal fluctuations are already stretched out, so that the force-extension curve is almost linear, due to elastic stretching.

We next focus on the results from the discrete model and compare the behavior of a chain under distributed force and end-to-end force. Average end-to-end extension of the semi-flexible chain $\langle \Delta x \rangle$ versus τ is plotted again in Fig. 6.3 in red solid line. If we turn off the thermal fluctuations, the chain behaves just as a linear elastic rod and the force-extension relation is shown in red dashed line in the same figure. To make a comparison, we apply a point force F at the end of the chain. Under the same net force: $F = \tau L_0$, the

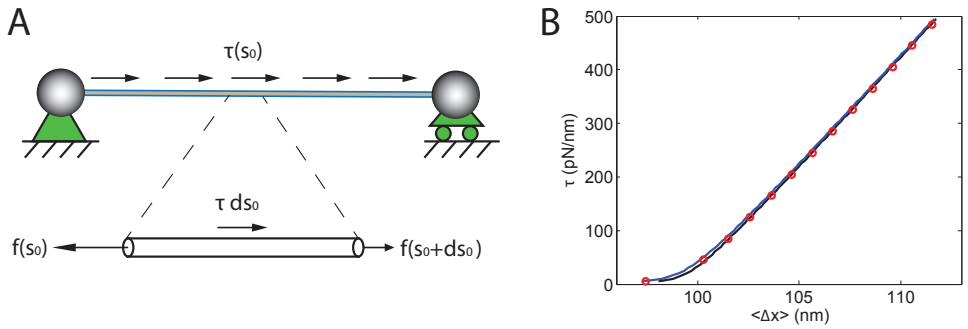

Figure 6.2: Comparison between the continuous models and the discrete model. (A) Force balance for an infinitesimal segment of a continuous rod. (B) Comparison of the results for a continuous rod (Black curve: Fourier series method and Eq. 6.15; Blue (almost overlaps with the black curve): method using force balance on infinitesimal segment and Eq. 6.20) and a discrete chain (red circles). The filament is under constant τ along the arc length so that Fourier series method can be applied. Here a 100nm chain is discretized into 1000 segments. The results match quite well.

chain under end-to-end force suffers larger extension (Fig. 6.3 blue) than the one under distributed load. This is in agreement with result from the Fourier series method for a continuous rod, which tells us the effective end-to-end force for a distributed load is $\tau L_0/2$, instead of τL_0. Another way to understand this result is by doing force balance on the chain. Under end-to-end applied force, the stress along the chain is uniform: $\sigma \equiv F/A = \tau L_0/A$, where A is the cross sectional area of the chain. Under distributed force, on the other hand, the stress along the chain varies linearly $\sigma = \tau(L_0 - s_0)/A$, and it is smaller than the stress in the previous case everywhere except at $s_0 = 0$. Therefore, it is not surprising that a chain under end-to-end force suffers larger extension. The fact that uniform distributed τ causes less internal tension in the chain than the end-to-end force $F = \tau L_0$ is also reflected in the transverse fluctuation profile (Fig. 6.4). Because internal tension stiffens the filament, a chain with less internal tension is expected to have larger thermal fluctuation. Indeed, our result shows that the magnitude of transverse fluctuation is significantly larger for a chain under uniform distributed force. Moreover, unlike the end-to-end force case, internal tension is not a constant along the arc length when the chain is subjected to uniform τ; therefore, the transverse fluctuation profile is not symmetric. The end of the chain with less internal force has more fluctuations, as shown in Fig. 6.4.

Next, as a practical application of our methods, we analyze the stretching and fluctuations of a piece of DNA in a linear microfluidic channel and a constant-strain-rate channel, both of which have been fabricated in experiments [15]. For a linear channel, the channel width varies as $w(x) = ax + b$, where a and b are two constants. On the other hand, a constant-strain-rate channel has a shape $w(x) = a/(1 + x/b)$ (Fig. 6.5A). Since the fluid velocity is

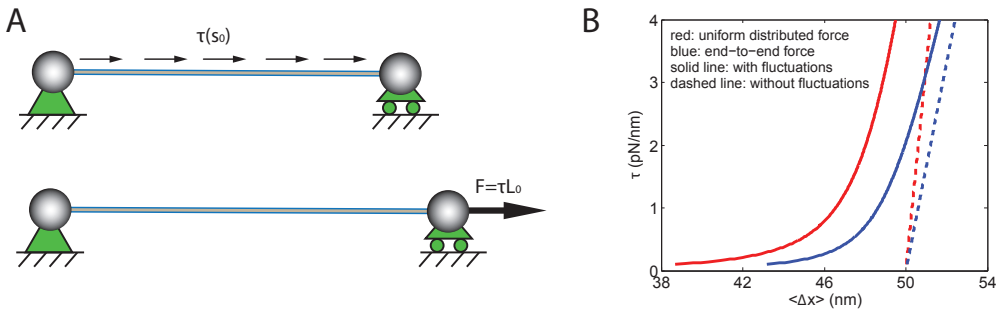

Figure 6.3: Force-extension relations for a wormlike chain (1: red solid line) under uniform distributed load τ with thermal fluctuations, (2: red dashed line) under uniform distributed load τ without thermal fluctuations, (3: blue solid line) under end-to-end force $F = \tau L_0$ with thermal fluctuations, and (4: blue dashed line) under end-to-end force without thermal fluctuations. The reference contour length of the chain is $L_0 = 50$nm. The persistence length is 5nm. The segment length is 0.5nm with $N = 100$ segments.

inversely proportional to the channel width w, a polymer confined in the channel experiences drag force $\tau = d_t v(x)$ that varies along its arc length. Here d_t is the drag coefficient per unit length and it is set to $d_t = 1.2\text{pN} \cdot \text{ms} \cdot \mu\text{m}^{-2}$ [15] in our calculation. Fig. 6.5B and C show respectively the extension and fluctuations of the polymer in fluid flow. With the same entrance width (width on the leftmost side) and exit width (width on the rightmost side), a constant-strain-rate channel is narrower in most of its middle region compared to a linear channel. Therefore, a polymer suffers larger drag force and less transverse fluctuations in a constant-strain-rate channel. This leads to a larger end-to-end extension. In Fig. 6.5C, we also compare the fluctuations of a hinged-hinged polymer (dashed line) and a hinged-free polymer, whose right end is not constrained on the x axis. The fluctuation for the hinged-free polymer is larger than that for the hinged-hinged polymer, as expected. In this study, we neglect the entropic force due to the non-uniform channel width.

Finally, in Fig. 6.6, we show the transverse fluctuation of a chain subjected to uniform τ plus a point load in the middle. The figure shows that the point load stretches the left half of the chain and reduces the fluctuation there.

6.4 Conclusions

We analyze the thermoelastic behavior of a fluctuating elastic filament under distributed loads in this chapter. We obtain, by means of a Fourier analysis on a continuous filament, analytic results when the polymer is under uniform distributed load. We find that a filament under uniform distributed load τ per unit reference length can be viewed as one under an effective end-to-end force of $\tau L_0/2$ if we are only interested in the force-extension relation. However, to get the fluctuations of a filament under general loadings, we need to

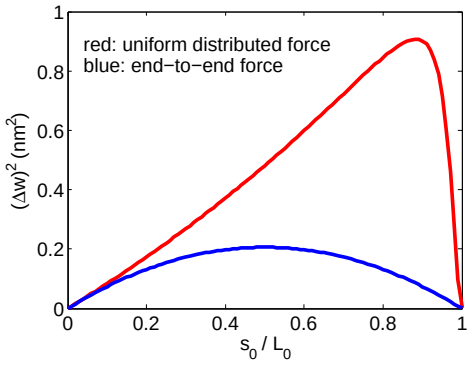

Figure 6.4: Transverse fluctuation of a chain under uniform distributed $\tau = 5pN/nm$ (red), and under end-to-end applied force $F = \tau L_0$ (blue). Under distributed force, the chain has larger thermal fluctuations with an asymmetric fluctuation profile.

first discretize the filament and approximate the path integral for the partition function as a multi-dimensional Gaussian integral. Once the partition function is calculated, all other quantities can be obtained by differentiation using standard thermodynamic techniques. As an illustration, we apply our methods to DNA under non-uniform distributed loads as is the case for DNA stretched by flow fields in microfluidic channels.

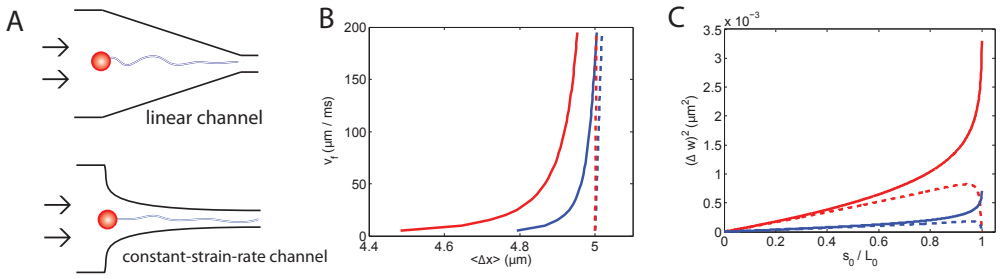

Figure 6.5: DNA in non-uniform microfluidic channels. (A) A piece of DNA confined in a linear channel and a constant-strain rate channel. Both channel types have been fabricated in experiments [15]. (B) The velocity in the non-uniform channel is inversely proportional to the channel width. Therefore, given the velocity v_f at the exit (rightmost) end, the entire velocity profile inside the channel is known, which then leads to the drag force $\tau = d_t v$ along the polymer. Here the end-to-end extension of the polymer is plotted against v_f. As we increase the flow velocity, the strain along polymer increases, resulting in a larger end-to-end extension. Red: DNA in a linear channel. Blue: DNA in a constant-strain-rate channel. Dashed/Solid lines: extension with/without the contribution of thermal fluctuations. (C) Transverse fluctuations along the polymer arc length. Red and blue for DNA in a linear and a constant-strain-rate channel respectively. Solid line is for a DNA with one end hinged and the other end free to fluctuate. Dashed line is for the same DNA with both ends hinged on the x aixs.

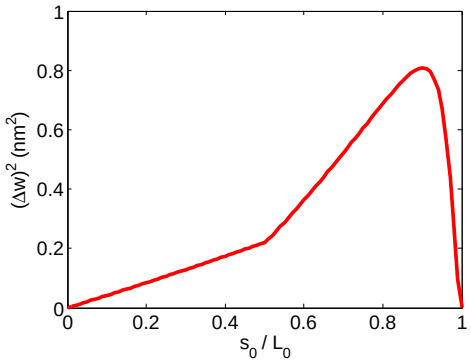

Figure 6.6: Transverse fluctuation of a chain under uniform distributed τ plus a point load F in the middle. The left half of the chain has less fluctuation because the stretching of the point loads reduces the thermal fluctuations.

Bibliography

[1] Bustamante C, Marko JF, Siggia ED, Smith S. 1994. **Entropic elasticity of lambda-phage DNA.** *Science* 265:1599-1600.

[2] Marko JF, Siggia ED. 1995. **Stretching DNA.** *Macromolecules* 28:8759-8770.

[3] Odijk T. 1995. **Stiff chains and filaments under tension.** *Macromolecules.* 28:7016-7018.

[4] Nelson P. 2008. **Biological Physics: Energy, Information, Life.** updated first ed. W. H. Freeman and Company, New York.

[5] Purohit PK, Arsenault ME, Goldman Y, Bau HH. 2008. **The mechanics of short rod-like molecules in tension.** *Int. J. Non-linear Mech.* 43(10):1056-1063.

[6] Arsenault ME, Purohit PK, Goldman YE, Shuman H, Bau HH. 2010. **Comparison of brownian-dynamics-based estimates of polymer tension with direct force measurements.** *Phys. Rev. E* 82:051923.

[7] Su T, Purohit, PK. 2010. **Thermomechanics of a heterogeneous fluctuating chain** *J. Mech. Phys. Solids.* 58:164-186.

[8] Larson RG, Perkins TT, Smith DE, Chu S. 1996. **Hydrodynamics of a DNA molecule in a flow field.** *Phys. Rev. E* 55:1794–1797.

[9] Phillips R. 2008. **Physical Biology of the Cell.** Garland Science.

[10] Wang J, Gao H. 2007. **Stretching a stiff polymer in a tube.** *J. Mater. Sci.* 42:8838-8843.

[11] Maier B, Seifert U, Rädler JO. 2002. **Elastic response of DNA to external electric fields in two dimensions.** *Europhysics Letters* 60:622-628.

[12] Benetatos P, Frey E. 2004. **Linear response of a grafted semiflexible polymer to a uniform force field.** *Phys. Rev. E* 70, 051806.

[13] Hori Y, Prasad A, Kondev J. 2007. **Stretching short biopolymers by fields and forces.** *Phys. Rev. E* 75, 041904.

[14] Zhang YL, Crothers DM. 2003. **Statistical mechanics of sequence-dependent circular DNA and its application for DNA cyclization.** *Biophys. J.* 84:136-153.

[15] Larson JW, Yantz GR, Zhong Q, Charnas R, D'Antoni CM, Gallo MV, Gillis KA, Neely LA, Phillips KM, Wong GG, Gullans SR, Gilmanshin R. 2006. **Single DNA molecule stretching in sudden mixed shear and elongational microflows.** *Lab Chip.* 6:1187-1199.

[16] Chirikjian GS. 2009. **Stochastic models, information theory, and Lie groups.** Birkhauser.

Chapter 7

Transition Between Two Regimes Describing Internal Fluctuation of DNA in a Nanochannel

Main results of this chapter:

1. We measure the thermal fluctuations of the internal segments of a piece of DNA confined in a nanochannel about 50−100nm wide. This local thermodynamic property is key to accurate measurement of distances in genomic analysis.

2. For DNA in ∼100nm channels, we observe a critical length scale ∼10μm for the mean extension of internal segments, below which the de Gennes' theory describes the fluctuations with no fitting parameters, and above which the fluctuation data falls into Odijk's deflection theory regime.

3. By analyzing the probability distributions of the extensions of the internal segments, we infer that folded structures of length 150−250nm, separated by ∼10μm exist in the confined DNA during the transition between the two regimes.

4. We show that existing theories for the end-to-end extension/fluctuation of polymers can be used to study the internal fluctuations only when the contour length of the polymer is many times larger than its persistence length.

5. Our results suggest that introducing nicks in the DNA will not change its fluctuation behavior when the nick density is below 1 nick per kbp DNA.

7.1 Introduction

Stretching DNA in nanochannels has emerged as an important technique for separating DNA, performing genome mapping, and also studying repressor-DNA interactions, *etc* [1, 2, 3]. On the other hand, DNA confined in nanochannels also serves as a simplified model for studying single polymer behavior in concentrated polymeric solutions and melts [4, 5]. For these reasons, mechanical behaviors of DNA inside nanochannels have attracted a long-standing interest. The two most well-known scaling theories in this field are those described by de Gennes [5] and by Odijk [6]. de Gennes' blob theory, which was later generalized by Schaefer and Pincus [7], assumes that the channel width D is much greater than the persistence length ξ_p of the polymer. It models the moderately confined DNA as a chain of spherical blobs inside a cylindrical channel and gives the following expression for the end-to-end extension $\langle x \rangle$ of the polymer [5, 7, 8]:

$$\frac{\langle x \rangle}{L} = A \left(\frac{w\, \xi_p}{D^2} \right)^{1/3}, \tag{7.1}$$

where L, w are the contour length and effective molecule width of the DNA respectively. The prefactor A is found to be close to unity [9]. Odijk's theory, on the other hand, works for DNA under strong confinement in which $D << \xi_p$. In this regime, the polymer is deflected back and forth by the channel walls and the end-to-end extension is predicted to be [6]:

$$\frac{\langle x \rangle}{L} \approx 1 - \alpha_\circ \left(\frac{D}{\xi_p} \right)^{2/3}, \tag{7.2}$$

where $\alpha_\circ = 0.17$ is a constant whose value was determined recently by simulations [10]. Aside from the scaling theories, Wang and Gao [11] showed that the end-to-end extension of a strongly confined polymer in the Odijk regime can be derived analytically by modeling the confinement effect as a quadratic potential $U = 1/2\, \Xi |\vec{r}_\perp|^2$. Here Ξ is the stiffness of the effective quadratic potential, which depends on the channel width D, and $\vec{r}_\perp$ is the transverse displacement of the polymer from the axis of the nanochannel. Wang and Gao considered a confined chain under end-to-end applied force F and obtained an expression for the total extension $\langle x \rangle$ as a function of Ξ and F. We set $F = 0$pN, substitute the relation between Ξ and D (see Appendix) into their expression, and find:

$$\frac{\langle x \rangle}{L} = 1 - \frac{1}{5} \left(\frac{D}{\xi_p} \right)^{2/3}, \tag{7.3}$$

which is the same as Eq.L.1, confirming the scaling theory of Odijk, and at the same time validating the use of quadratic confinement potentials in the strongly confined regime.

Both de Gennes' and Odijk's theories have been tested by experiments as well as simulations over the years [10, 12, 13, 14, 15, 16]. However, most of the

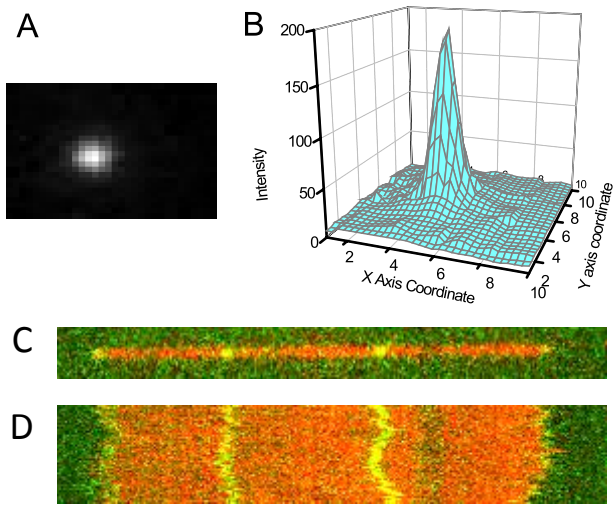

Figure 7.1: Measurement of the fluctuations of the internal segments of confined DNA. (A) Image of a dye label (Alexa-546) on a DNA backbone (backbone not shown) with 80ms exposure time. (B) 2D surface plot of the raw image (intensity of the dye vs. the X Y coordinates). (C) Image of one T4 DNA fragment ($\sim$ 36 microns) with backbone (red) and internal labels (green). (D) Time series (8 seconds) of the DNA showing the fluctuations of backbone and internal labels. In (D), the red trace is the backbone and the green traces are the trajectories of internal dye labels.

studies so far have focused on the properties of the entire DNA, for example, the *end-to-end* extension $\langle x \rangle$, the corresponding *end-to-end* fluctuation σ_x, and also the relaxation time τ of the *entire* DNA *etc.* Local properties of a confined polymer, on the other hand, like the extension and fluctuation of its internal segments, are rarely investigated. In fact, local conformation and alignment of the confined DNA have been probed only recently [17, 18]. It is also not well understood whether the existing theories developed for an entire piece of DNA can be applied locally for its internal segments. These are important issues because, if one considers the case of genome mapping, it is the local fluctuation of the internal segments that determines the resolution of the mapping.

In this chapter, we measure the longitudinal *internal* fluctuation of a piece of DNA confined in rectangular channels about 50$-$100nm wide. We show that neither de Gennes' blob theory nor Odijk's deflection theory can completely describe the measured internal fluctuation versus mean extension profile. A critical length scale of $\sim$10μm for the mean extension is observed, below which the internal DNA segments are more 'blob'-like, and above which Odijk's deflection theory works better. From the histograms of extension of the internal segments, we further infer that there exist folded structures of length 150$-$250nm separated by $\sim$10μm along the backbone of the DNA during the transition between the two regimes. To justify the use of existing theories for studying the internal fluctuation, we focus on the Odijk regime and propose

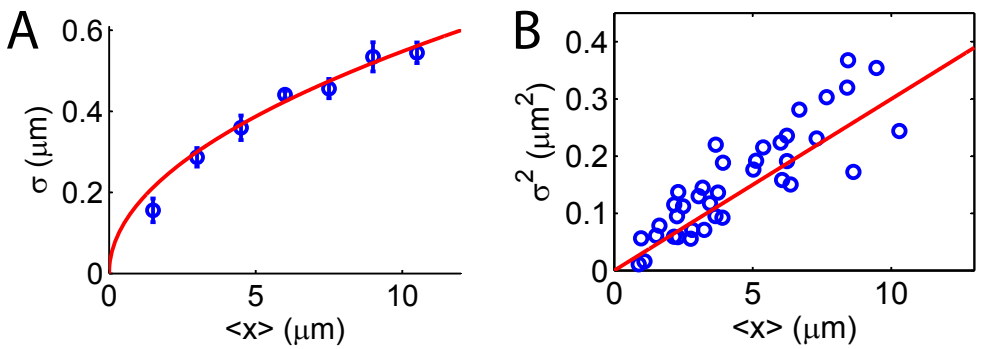

Figure 7.2: Internal fluctuation of λ DNA confined in a 80nm×130nm channel. (A) The measured rms fluctuation σ versus mean extension $\langle x \rangle$ for the internal segments of the DNA agrees very well with de Genne's theory with no fitting parameters (red curve, Eq.7.4). (B) A linear $\sigma^2 - \langle x \rangle$ profile confirms the 0.5 power law of $\sigma \sim \langle x \rangle^{1/2}$ of the de Gennes' theory. Note, however, that here we have maximum $\langle x \rangle \lesssim 10\mu$m. As shown in a subsequent figure (Fig.7.4) and in the text, for longer polymer with a maximum $\langle x \rangle \gtrsim 10\mu$m, the data deviates significantly from de Gennes' theory and even the 0.5 power law is lost.

a method to explicitly calculate the internal fluctuation of a strongly confined DNA. We model the confinement effects by quadratic potentials and show that one can use the existing theories for end-to-end extension/fluctuation to describe the internal segments of the DNA when the contour length of the polymer is many times larger than its persistence length. Our model, which views the confined DNA as a discrete wormlike chain, can describe the fluctuations of heterogeneous polymers confined in non-uniform channels. It is also capable of capturing effects, like the influence of nicking sites on the DNA fluctuation profiles, which we will discuss at the end of the chapter.

7.2 Results and Discussion

To visualize the internal segments, dye-labeled (Alexa-546) nucleotides are introduced into the backbones of the nicked λ DNA (48.5kbp, $L \approx 16.5\mu$m), $T4$ DNA (166kbp, $L \approx 56.4\mu$m) and bacterial artificial chromosome (BAC) human DNA clones (MCF7 BAC clone 9I10, fragmented, full length $\sim$ 180kbp, $L \approx 61.2\mu$m) (Fig.7.1) [19]. The DNA molecules are then driven by electric field into the nanochannels. With the Alexa-546 labels excited by light, extension of each internal segment is recorded frame-by-frame. Average extension $\langle x \rangle$ and the root mean square (rms) fluctuation $\sigma = \sqrt{\langle x^2 \rangle - \langle x \rangle^2}$ for each internal segmenet are calculated and plotted in the $\sigma - \langle x \rangle$ profile.

In Fig.7.2, we first show the result for λ DNA confined in a 80nm×130nm channel. The maximum $\langle x \rangle$, which is roughly the mean extension of the entire DNA, is about 10μm, in agreement with the measurements of Tegenfeldt *et al* [12]. The internal fluctuation σ increases with $\langle x \rangle$ with a 0.5 power law. This

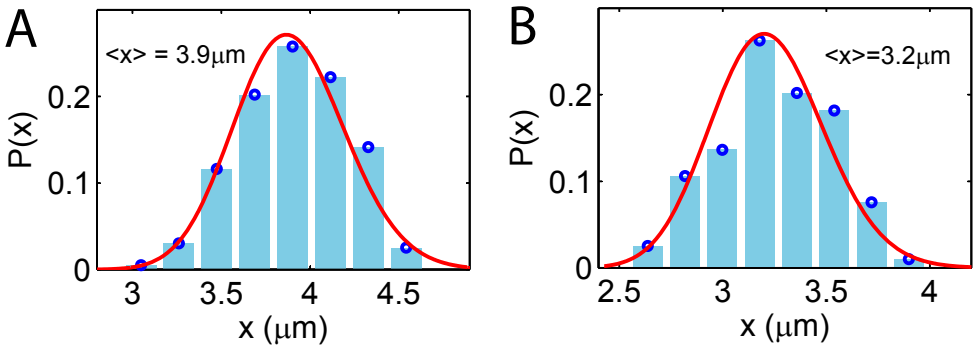

Figure 7.3: Probability distributions $P(x)$ for 2 internal segments of λ DNA inside a 80nm×130nm channel. The experimental data is fitted to Eq.7.7 (red). The fitting value C (Eq.7.7), when plugged back to Eq.7.6-2, recovers de Gennes's formula Eq.7.4.

0.5 power law and even the magnitude of the fluctuation can be well captured by de Gennes' theory (discussed below) with no fitting parameters.

The longitudinal fluctuation of the confined DNA in de Gennes' theory can be evaluated using the effective stiffness k_{eff} of the polymer: $\sigma^2 = k_B T/k_{\text{eff}} \cong (4/15)L(w\xi_p D)^{1/3}$ [12, 20]. Using this expression and Eq.7.1 to eliminate L, we get the relation between σ and $\langle x\rangle$:

$$\sigma \cong \sqrt{\frac{4D}{15}} \cdot \sqrt{\langle x\rangle}. \tag{7.4}$$

Therefore, de Gennes' theory predicts a 0.5 power law for the $\sigma - \langle x\rangle$ profile. It is interesting to note that the prefactor in Eq.7.4 depends only on the channel width D, but not on the effective molecule width w, nor on the persistence length ξ_p. This implies that the $\sigma - \langle x\rangle$ profile is independent of the ionic strength of the experimental buffer. To compare the theory with the measured internal fluctuation, we plot Eq.7.4 together with the experimental data in Fig.7.2. Surprisingly, the data matches with the theory very well without any fitting parameters. Both the 0.5 power law and the magnitude of the fluctuation are correctly predicted by Eq.7.4.

de Gennes' theory also gives the distribution of the extension $P(x)$, which we can compare to our measurement. We consider the recently proposed "renormalized" Flory-type free energy $\mathcal{F}$ for a confined polymer [21] and its corresponding prediction of the longitudinal fluctuation:

$$\beta\mathcal{F} = A\,\frac{x^2}{(N/g)\,D^2} + B\,\frac{D(N/g)^2}{x}, \qquad \sigma^2 = \left(\frac{\partial^2(\beta\mathcal{F})}{\partial x^2}\right)^{-1}, \tag{7.5}$$

where $\beta = 1/k_B T$, A, B are two constants, N, g are the total number of monomers and the number of monomers inside a blob respectively [21]. Both of the relations can be rewritten in terms of $\langle x\rangle$ (which is the solution of

$\partial\mathcal{F}/\partial x = 0$) as:

$$\beta\mathcal{F} = C\left(\frac{x^2}{2D\langle x\rangle} + \frac{\langle x\rangle^2}{Dx}\right), \qquad \sigma = \sqrt{\frac{D}{3C}}\ \sqrt{\langle x\rangle}, \tag{7.6}$$

with $C = (2A)^{2/3}B^{1/3}$ being a constant. The probability distribution $P(x)$ is therefore:

$$P(x) = P_0\ \exp(-\beta\mathcal{F}) = P_0 \exp\left[-C\left(\frac{x^2}{2D\langle x\rangle} + \frac{\langle x\rangle^2}{Dx}\right)\right]. \tag{7.7}$$

Here P_0 is a constant determined by the normalization condition. In our experiments, we record the extension x of each internal segment frame-by-frame and then calculate the distribution $P(x)$ for *each* segment. Fig.7.3 shows the measured $P(x)$ for two internal segments and their fitting results to Eq.7.7 (red). The result again implies that, for λ DNA confined in a 80nm×130nm channel, the behavior of the internal segments can be well captured by de Gennes' theory. Moreover, by fitting the distribution $P(x)$ to Eq.7.7, we obtain the constant C, which, when plugged back into Eq.7.6-2, yields: $\sigma = 0.58\sqrt{D}\sqrt{\langle x\rangle} \approx \sqrt{4D/15}\sqrt{\langle x\rangle}$ (here $D = \sqrt{80\times 130} = 102$nm). Therefore, starting from the "renormalized" Flory-type free energy Eq.7.5, we recover Eq.7.4 with the same prefactor. This indicates that the prefactor in Eq.7.4 is quite accurate although it is derived from a scaling theory. It also explains why Eq.7.4 matches with the measured $\sigma - \langle x\rangle$ profile without any fitting parameters (Fig.7.2). It is important to note that, for λ DNA confined in a 80nm×130nm channel, the maximum $\langle x\rangle$ is less than $\sim 10\mu$m (Fig.7.2). We shall show next that for longer DNA whose maximum $\langle x\rangle$ is greater than $\sim 10\mu$m, the measurement no longer agrees with de Gennes' theory. In particular, the 0.5 power law in the $\sigma - \langle x\rangle$ profile is lost.

Fig.7.4A shows the $\sigma - \langle x\rangle$ profile for the internal segments of T4 DNA in a 80nm×130nm channel. The maximum $\langle x\rangle$, which is roughly the mean extension of the entire DNA, is about 30μm, in agreement with the simulation result of Jung *et al* [14]. Fitting of $\sigma \sim \langle x\rangle^\gamma$ to the experimental data yields $\gamma = 0.19$, which is very different from the prediction of de Gennes' theory (Eq.7.4). Similar results are found for DNA in channels of different sizes: $\gamma = 0.15$ for T4 DNA confined in 60nm×100nm channels (Fig.7.4B) and $\gamma = 0.11$ for λ DNA in 50nm×70nm channels (Fig.7.4C). In all these cases the maximum $\langle x\rangle$ is greater than 10μm. We note, however, that in Fig.7.4, the experimental data for segments with $\langle x\rangle \lesssim 10\mu$m still matches with de Gennes' theory (except for the 50×70nm channel case, which we will explain later). It is the data with $\langle x\rangle \gtrsim 10\mu$m that deviates significantly from de Gennes' prediction. In fact, if we plot the fluctuation results for short segments with $\langle x\rangle \lesssim 10\mu$m for λ and T4 DNA together, the two profiles are almost identical, satisfying de Gennes' theory (see figure in the Appendix).

To rule out the possibility that the observed difference between λ DNA and T4 DNA stems from sequence variations, we perform the same experiments on

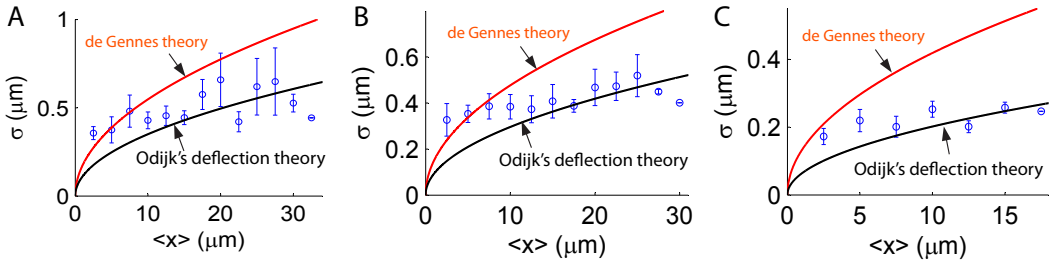

Figure 7.4: Fluctuation of the internal segments of (A) T4 DNA in 80nm×130nm, (B) T4 DNA in 60nm×100nm and (C) λ DNA in 50nm×70nm channels. For all cases, the maximum mean extension $\langle x \rangle > 10\mu$m. For (A) and (B), the data $\langle x \rangle \lesssim 10\mu$m agrees with de Gennes's theory (red, no fitting parameters). Deviation from de Gennes' theory begins at a critical $\langle x \rangle \sim 10\mu$m, above which the data falls into the black curve predicted by the deflection theories of Odijk [6], Wang and Gao [11]. For tighter channels (C), the transition occurs earlier with most data falling in the deflection regime.

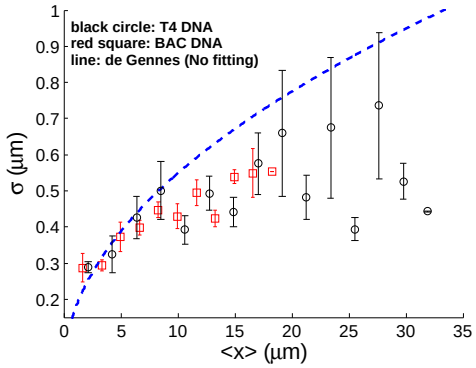

Figure 7.5: Internal fluctuation σ versus mean extension $\langle x \rangle$ for BAC (red squares) and T4 DNA (black circles) in a 80nm×130nm channel. This figure shows that DNAs from two different sources give almost identical results, which suggests that agreement with de Gennes theory for short internal segments, and deviation from de Gennes' theory for long internal segments, are both sequence independent.

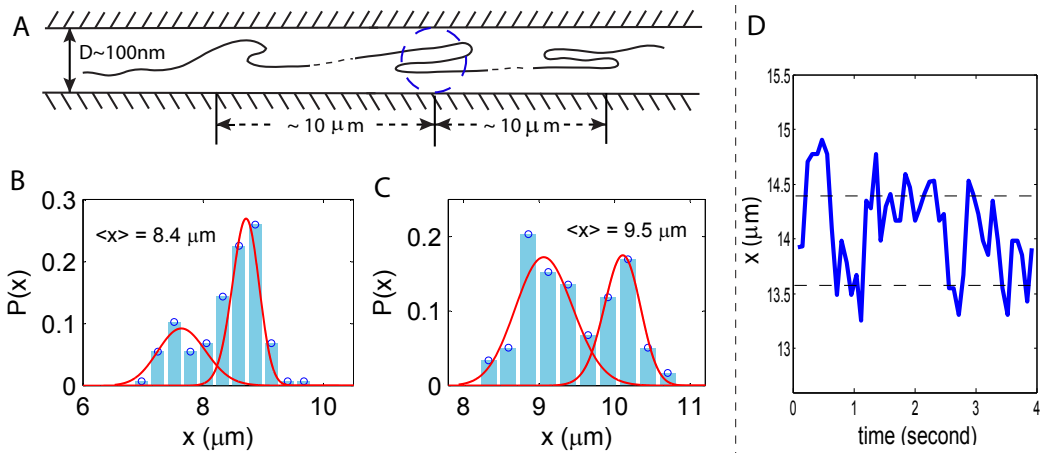

Figure 7.6: (A) Folded structures in the backbone of confined DNA. Each branch of the structure is about $150 - 250$nm, about the width of the channel size. The structures are separated by a distance $\sim 10\mu$m. (B, C) Distribution of extension $P(x)$ for 2 internal segments that contain the folded structures. In disagreement with de Gennes' prediction, the distributions show 2 peaks, from which we infer the existence of the folded structures. However, the structures are not stable as the two peaks in the distributions are comparable in height. The red curves fitted to the left peaks on the histogram are from de Gennes' theory (Eq.7.7) and the ones superimposed on the right peaks are from the deflection theory (Eq.7.10). (D) Extension x versus time for a single internal segment that shows two peaks in the distribution $P(x)$. The extension of this particular internal segment seems to fluctuate around two values shown by the dashed lines. This gives rise to the two peaks seen in the probability distribution.

the bacterial artificial chromosome (BAC) human DNA clones (MCF7 BAC clone 9I10), which also has maximum $\langle x \rangle \gtrsim 10\mu$m. As shown in Fig. 7.5, the results for the BAC DNA are almost identical to those for the T4 DNA. In particular, for small $\langle x \rangle < 10\mu$m, both match with de Gennes' prediction without any fitting parameters, while for $\langle x \rangle > 10\mu$m, both identically deviate from de Gennes' prediction. This suggests that the deviation from de Gennes' theory for long internal segments truly stems from segment size, not from sequence variations.

To better understand the deviation from de Gennes' prediction, we further look into the local structures of the confined DNA. Odijk showed recently that even in a 135nm channel, DNA can fold back on itself, giving rise to a global persist ence length much larger than 50nm, the intrinsic persistence length of the DNA [18, 22]. Because of this, Odjik argued that the transition from Odijk's regime to de Gennes' regime could be delayed with the increase of the channel size [18]. To check whether such local folded structures exist in the DNA in our experiments, we measure the extension distribution $P(x)$ for each single internal segment (see "Materials and Methods" for details).

We find that for most internal segments whose mean extension is longer than 10μm, the distribution $P(x)$ shows two or more peaks (Fig.7.6B-C). From this observation, we infer that there indeed exist some folded structures in those internal segments – one peak in the distribution corresponds to the folded configuration, and the second peak corresponds to the extended configuration (Fig.7.6). The existence of folded structures can be also inferred from the typical extension x versus time plot as shown in Fig. 7.6D, where the steps in x correspond to different states of the internal segments. Furthermore, we find that in the distribution $P(x)$, the measured distances between any two peaks are always integral multiples of $400-500$nm, indicating that the difference in extension of a single folded structure and its extended form is about 500nm, ten times the persistence length of the DNA. This further implies that each branch of the folded structure is about $150-250$nm, if we assume each folded structure has two (loop) or three (hairpin) branches (Fig.7.6). Also, by checking the location of the internal segments that show multiple-peak distributions, we find that the folded structures are separated by $\sim 10\mu$m, which roughly agrees with the value of $\langle x \rangle$ above which de Gennes' theory fails to match with the experimental data (Fig.7.4). In the following we show that for $\langle x \rangle \gtrsim 10\mu$m the fluctuation data is better described by Odijk's deflection theory.

To exactly (rather than in a scaling sense) evaluate the fluctuation of DNA in the Odijk deflection regime, we extend the theory recently developed by Wang and Gao [11]. This theory represents the DNA as a strongly confined wormlike chain (fluctuating elastic rod) subjected to an additional end-to-end force F and produces the relation between the mean extension $\langle x \rangle$ and Ξ, the stiffness of the effective confinement potential (which is a function of the channel width D):

$$\langle x \rangle = L - \frac{k_B T L}{2\sqrt{\kappa}} \frac{1}{\sqrt{F + 2\sqrt{\Xi(D)\kappa}}}, \tag{7.8}$$

where again, $k_B T$ is the thermal energy, κ is the bending modulus of the polymer, and in a rectangular channel the stiffness of the confinement potential can be expressed as $\Xi = 4c^4 \left[k_B T/(\kappa^{1/4} D^2)\right]^{4/3}$, with c being a constant. Using Eq.I.1, we calculate the effective stiffness of the DNA as $k_{\text{eff}} = (\partial \langle x \rangle / \partial F)^{-1}$, and then evaluate the fluctuation as $\sigma^2 = k_B T / k_{\text{eff}}$:

$$\sigma = \frac{D}{2\sqrt{8\xi_p c^3}} \cdot \left[1 - \frac{1}{4c}\left(\frac{D}{\xi_p}\right)^{2/3}\right]^{-1/2} \sqrt{\langle x \rangle}. \tag{7.9}$$

Leaving c as a free parameter, we fit Eq.7.9 to the experimental data with $\langle x \rangle > 10\mu$m in Fig.7.4A-C (black curves) and obtain $c = 1.03$, 0.94 and 0.99 respectively. For the BAC DNA confined in 80nm×130nm channels shown in Fig. 7.5, we obtain $c = 0.9$ from a similar fit. The fact that all the four sets of experimental data for different channel widths yield the same $c \approx 1$ makes sense because c is expected to be a universal constant independent of

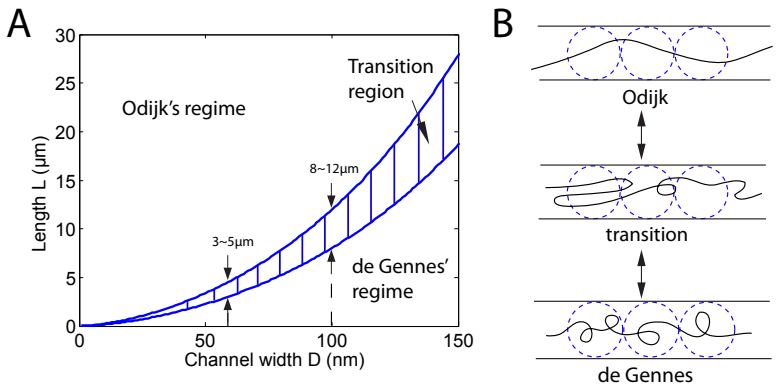

Figure 7.7: (A) Phase diagram showing two regimes on the $L - D$ plane, assuming $\xi_p = 50$nm for DNA. Transition from de Gennes' to Odijk's regime can occur when D decreases with L fixed, or when L increases with D fixed. (B) DNA with local folded structures as an intermediate state between de Gennes's and Odijk's regimes. In experiments, we observe heterogeneity in the intensity profile of YOYO-1 dye along the backbone of a confined DNA, which suggests the existence of the local folded structures (see Appendix).

D. Moreover, the constant c comes from the expression for the free energy of confined chains in the Odijk regime and it has been estimated by Burkhardt to be $c = 1.1$[23], which is very close to our fitting results. This strongly suggests that in the large mean extension regime $\langle x \rangle > 10\mu$m, the DNA segments are better described by the deflection theory.

Furthermore, from Fig.7.4A to C, we observe that the length of the error bars decreases with the decrease of the channel size. The reason for this may be that for moderately confined DNA, the local folded structures can form and unravel with comparable rates, as indicated by the similar height of the two peaks in the distribution in Fig.7.6B-C. Therefore, the behaviors of the confined polymer is a competition between de Gennes' type and Odijk type regimes and the error bar is large. As the channel size becomes smaller, Odijk's theory begins to dominate, resulting in smaller error bars.

By integrating the force-extension relation Eq.I.1, we obtain the free energy expression $G(x)$ in the Odijk (or Wang and Gao) deflection regime (see Appendix), which further leads to the distribution for the extension $P(x)$:

$$P(x) = P_0 \exp\left(Bx - \frac{A}{L-x}\right), \tag{7.10}$$

where $A = L^2/4\xi_p$, $B = 4c^2\xi_p^{1/3}/D^{4/3}$ and P_0 is the normalization factor. We fit this expression to the right peaks in Fig.7.6B-C and find that reasonable parameters ($L \approx 15\mu$m, $\xi_p \approx 50$nm) give excellent matches with the measured probability distributions in experiments. In fact, we can use this free energy expression to understand the transition from a different point of view. We note that the internal segments are expected to stay in the regime with lower

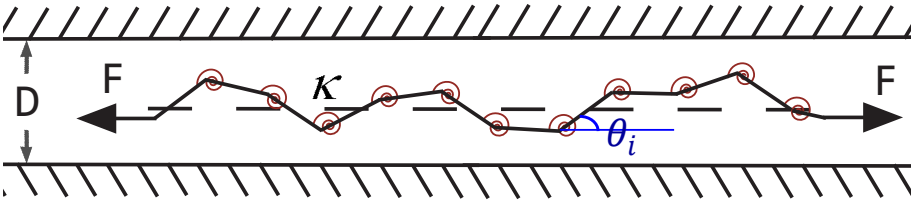

Figure 7.8: Discrete wormlike chain model for confined DNA in a nanochannel. The confined wormlike chain, subjected to and end-to-end applied force in general, has bending energy represented by a spring of stiffness κ at each node.

free energy, and that regime transition occurs when the free energies in the two regimes are equal. By comparing the free energies in the two regimes, we draw a phase diagram on the $L - D$ plane in Fig. 7.7. The result shows that as D decreases, the transition length L decreases. Theoretically, the phase diagram involves an undetermined constant, which we fit such that transition occurs in the range $L \approx 8 - 12\mu$m when $D = 100$nm. Then the result shows that at $D = 60$nm, the transition length is $3 - 5\mu$m, which roughly agrees with our experimental result for λ DNA in a 50nm×70nm channel (Fig. 7.4C). The phase diagram shows that transition from de Gennes' to Odijk's regime can occur when D decreases with L fixed, or when L increases with D fixed.

We also measure the end-to-end extension for DNA with different lengths (longer than 10 microns) in a 60nm×100nm channel and the result agrees with Odijk's theory (Fig. S3).

In the above analysis, we have applied the theories (de Gennes, Odijk, Wang and Gao) for the *end-to-end* extension/fluctuation to evaluate the *internal, or local* extension/fluctuation of a confined DNA. The assumption behind this is that when the internal segments are much longer than the persistence length of the DNA, the behavior of the segments is not very different from that of the entire DNA (with the same length) because the boundary conditions do not play a significant role [24, 25, 26]. To verify such an assumption, we explicitly calculate the internal fluctuation in Odijk's regime by extending a theory we developed earlier [26], and then compare our results to the theories developed for an entire piece of DNA.

Following the procedure in ref.[26], we model the polymer as a confined discrete $N-$segment wormlike chain, or fluctuating elastic rod (Fig.7.8). The Hamiltonian consists of 3 terms (Eq.7.11): (1) bending energy, (2) confinement energy, and (3) potential energy of an end-to-end applied force as shown in Fig.7.8.

$$\mathcal{H} = \int_0^L \frac{\kappa(s)}{2} \left| \frac{d\hat{t}}{ds} \right|^2 ds + \int_0^L \frac{\Xi}{2} y^2 ds - F\Delta x \tag{7.11}$$

$$= \frac{1}{2}\vec{\theta}^T \cdot \mathbf{K}\vec{\theta} - FL. \tag{7.12}$$

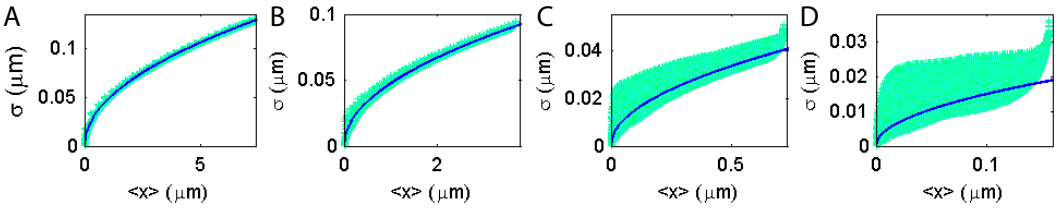

Figure 7.9: Fluctuation versus mean extension of internal segments of the strongly confined DNA in 60nm channels (Eq.7.13 and Eq.7.14). The contour lengths of the DNA are (A) $L = 10\mu$m, (B) 5μm, (C) 1μm and (D) 250nm. For a long DNA (A and B), data from internal segments of various locations of the chain collapse on the a curve with 0.5 power law (light green). The result agrees with Eq.7.9 (blue), which is derived for the end-to-end fluctuation of a confined DNA. For short DNA however (C and D), no power law is found as data from various locations of the chain do not collapse onto a single curve (light green). Therefore, formulae derived for the end-to-end fluctuation of the confined DNA, such as Eq.7.9 (blue), cannot be used for internal fluctuation. The boundary effect is so significant that the rms fluctuation σ not only depends on $\langle x \rangle$, but also on the location of the internal segments.

In the bending energy term, $\kappa(s)$ is the bending modulus of the DNA and it can vary along the arc length s so that the polymer is not necessarily homogeneous in mechanical properties. $\hat{t}$ is the tangent vector along the polymer. For the confinement potential term, we follow Wang and Gao's approach [11] and use an effective quadratic energy characterized by the coefficient Ξ, with y being the transverse displacement. In general, Ξ can be a function of the arc length s in case the confinement is not uniform. Also, for 3D chains in rectangular channels, Ξ can be different in the two transverse directions. For the potential energy term, we consider the chain subjected to an end-to-end force F, which can be set to zero if no force is applied. $\Delta x = x(L) - x(0)$ is the end-to-end extension of the chain. Up to a second order approximation, the Hamiltonian can be written in matrix form as shown in Eq.7.12, with θ_i being the discretized tangent angles and $\mathbf{K}$ being the $N \times N$ stiffness matrix of the chain [26].

It has been shown that when there are no constraints on twist (as is the case here), thermodynamic properties of a 3D chain can be easily generated from those of two 2D chains [26]. Therefore, for simplicity, here we describe the theory for 2D chains and plot the results for the corresponding 3D chains.

To get the internal fluctuation, we first need to calculate (1) the partition function, and (2) the angle fluctuation $\langle \theta_i \theta_j \rangle$. These are evaluated in the "Materials and Methods" section. Finally, for any internal segment between node i and node j of the discrete chain, the mean extension $\langle x_{ij} \rangle$ and the corresponding rms fluctuation can be explicitly calculated as:

$$\frac{\langle x_{ij} \rangle}{l} = (j - i) - \frac{\langle \theta_{i+1}^2 \rangle + \cdots + \langle \theta_j^2 \rangle}{2}, \tag{7.13}$$

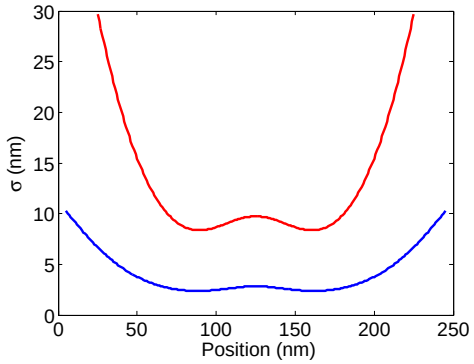

Figure 7.10: Fluctuation as a function as the position of an internal segment for a short chain. The contour length of the entire chain is short (250nm), so that the fluctuation not only depends on the length of the internal segment, but also on its position. Here we plot the fluctuation versus position for internal segments with the same size: 50nm (red) and 10nm (blue). For the internal segments close to the boundaries, the fluctuation is larger because they have more freedom compared to the segments inside the chain.

$$\frac{\sigma_{ij}^2}{l^2} = \frac{\langle (x_j - x_i)^2 \rangle - \langle x_j - x_i \rangle^2}{l^2} = \frac{1}{2} \sum_{m=i+1}^{j} \sum_{n=i+1}^{j} \langle \theta_m \theta_n \rangle^2, \tag{7.14}$$

where l is the segment length of the discrete chain. In Fig.7.9, we consider DNA in 60nm×60nm channels and plot σ_{ij} versus $\langle x_{ij} \rangle$ for all the pairs of internal nodes (i, j) and see if the profiles match with the theories developed for the entire piece of DNA. Fig.7.9(A) shows the result for a chain with contour length $L = 10\mu$m, which is much larger than its persistence length $\xi_p = 50$nm. The internal fluctuation profile agrees exactly with Eq.7.9, which is derived for the end-to-end fluctuations. In particular, all the data collapses into a single curve with 0.5 power law. As the contour length of the polymer decreases, however, (Fig.7.9B-D), the internal fluctuation profile begins to scatter around the curve for the end-to-end fluctuation. This implies that, for short chains, the magnitude of internal fluctuation can be different, even if two internal segments have the same mean extension. The magnitude of the fluctuation depends strongly on where the internal segment is located. In fact, we show in Fig. 7.10 that the internal segments located at the two boundaries have larger fluctuation because they have more freedom to fluctuate compared to the segments inside the chain. The strong boundary effects on short chains (such as, DNA with contour length 0.6-7μm) have been discussed by several groups recently [24, 26, 25]. Our results suggest that the accuracy of DNA sizing depends on the DNA contour length. For a short DNA with contour length $L < 1\mu$m confined in a 60nm×60nm channel, the uncertainty of the measurement will be high. For the experimental results we discussed earlier, the λ DNA, T4 DNA and BAC DNA all have contour lengths of tens of microns, for which boundary effects can be neglected. Therefore, it is safe to

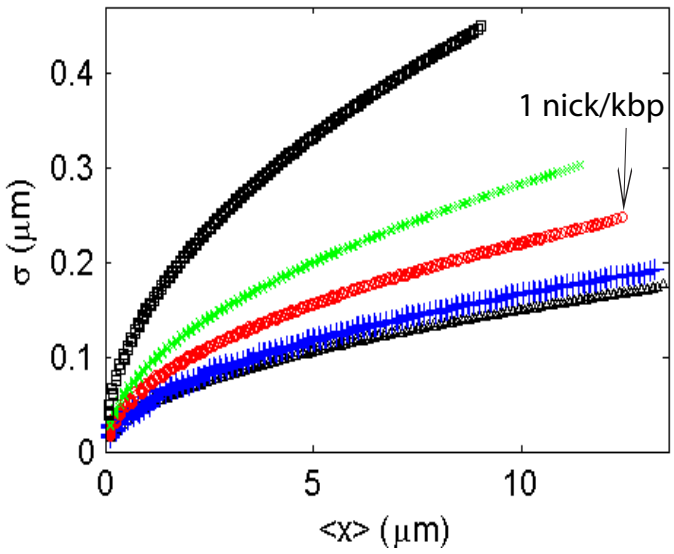

Figure 7.11: Fluctuation of a 18μm long chain with persistence length ξ_p = 50nm confined in a 60nm×60nm channel. From bottom to top: (1) △: no nicks; (2) +: 10 nick in 18μm; (3) ◯: 50 nicks in 18μm; (4) ×: 100 nicks in 18μm; (5) □: 200 nicks in 18μm. This figure shows that when the density of nicks is lower than 50 nicks per 18μm, or 1 nick per kbp of DNA, the fluctuation profile is almost the same as that for a chain without nicks.

use the formulae for end-to-end extension/fluctuation to estimate the internal properties of the confined DNA in our experiments.

To measure the internal fluctuation, we have introduced nicks into the DNA so that internal sites along the DNA can be labeled. Since the theory discussed above allows for arbitrary bending modulus $\kappa(s)$ as a function of the arc length s, we can model the effect of nicking by setting $\kappa = 0$ on some nodes of the discrete chain and see whether the nicks have significant effects on the behavior of the DNA. For simplicity, we assume here that the nicks are equally spaced along the chain. Fig.7.11 shows that the fluctuation profile does not significantly deviate from the homogeneous chain with uniform κ when there are less than 50 nicks along a 18μm chain (∼50kbp DNA in a 60nm×60nm channel). In our experiments, the fluorescent tagging is introduced at the nicking endonuclease recognition sequence sites, which have much lower density than 1 nick/kbp in λ, T4 and BAC DNA. Therefore, the nicks will not significantly affect the DNA internal fluctuation.

To summarize, in this chapter, we have investigated the thermal fluctuations of the internal segments of a piece of confined DNA in a nanochannel. The channel size is on the order of the persistence length of the DNA and we have compared the fluctuation data to several theories in literature. We have found that for channel widths on the order of 100nm there exists a critical length scale ∼10μm for the mean extension of an internal segment below which the de Gennes' theory describes the internal fluctuations and above which the

data agree better with Odijk's deflection theory. For long DNAs confined in nanochannels we have inferred that there are folded structures whose branches are about 3 times the persistence length of DNA which are separated by segments with mean extension $\sim 10\mu$m. We surmise that these folded structures are indicative of a transition from the Odijk regime, in which the DNA is relatively straight, to the deGennes regime, in which the DNA is more blob-like. We have also presented a more detailed theory based on small fluctuations and incorporating the effects of confinement. We have shown that one can use the existing theories for end-to-end extension/fluctuations to study the statistical properties of internal segments only when the contour length of the chain is much larger than the persistence length of the molecule so that boundary effects play no role. Our calculations suggest that introducing nicks into the DNA can change its fluctuation behavior if the density of nicks is greater than about 1 nick per kbp DNA.

7.3 Materials and Methods

7.3.1 Sequence specific labeling and DNA staining

In a 20μl reaction native, duplex DNA samples $50\text{ng}/\mu\text{l}$ (λ, T4 DNA and also MCF7 BAC clone 9I10) are incubated with 0.5U of Nb.BbvCI ($0.5\text{U}/\mu\text{l}$) (NEB, Ipswich, MA) in 1× NEB buffer 2 (NEB) for 1 hr at 37°C and 20 min at 65°C. The nicked DNA samples ($12.5\text{ng}/\mu\text{l}$) are then incubated for 30 min at 50°C in 1×NEB thermopol buffer with DNA polymerase Vent (exo-) (NEB) at $0.5\text{U}/\mu\text{l}$ in presence of a mixture of 75nM dAGC and 75nM Alexa-546 labeled dUTP. Then, the DNA ($4\text{ng}/\mu\text{l}$) samples are stained with intercalating dye YOYO-1 iodide at 1 dye molecule per 10 base pairs of DNA (Invitrogen Inc, Carlsbad, CA) in presence of 0.4M DTT (Promega Inc, Madison, WI).

7.3.2 Loading DNA into nanochannels

Fabrication of silicon based nanochannel chips has been described elsewhere [27, 28]. The DNA sample is diluted by 2 times using the flow buffer consisting of 1×TBE, 3.6% Tween, and 10% Polyvinylpyrrolidone (PVP). Ultrapure distilled water is used for making solutions (Invitrogen Corp., Ultrapure water). The DNA molecules are driven by electric field ($3 - 5$V) at the port of entrance of the chip and allowed to populate there for $2 - 3$ minutes [29]. Under higher voltage ($\sim$10V), the populated molecules are moved to the locos and then through the micro pillar structure of the chip to convert from a compact globular conformation to an open relaxed one. At the 300nm channel area the molecules adopt a more relaxed linear form with some heterogeneity on the backbone. With one end entering the nanochannel under the electric field, the DNA molecules elongate to a linear conformation with almost homogeneous backbone. Most of the structural heterogeneity progressively disappears as it

interacted with the nanochannels, adopting fully confined equilibrium conformation after the field is off (relaxation time $10 - 15$s). A buffer consisting 0.5×TBE, 1.8% Tween 20, 5% PVP has been used to flow the DNA molecules resulting in a stretch of 65%.

7.3.3 Microscopy and image processing

The epi-fluorescence imaging is done in Olympus microscope (Model IX-71, Olympus America Inc, Melville, NY) using a 100×SAPO objective (Olympus SApo 100X/1.4 oil). YOYO-1, the DNA backbone staining dye (∼491nm absorption, ∼509nm emission) is excited using 488nm laser (BCD1, Blue DDD Laser Systems, CVI Melles Griot, Rochester, NY) whereas Alexa-546 (∼550nm absorption, ∼570nm emission) is excited using 543nm green laser (Voltex Inc, Colorado Springs, CO). The same filter cube consisting triple band dichroic and dual band pass emission filters (Z488/532/633rpc, z488/543m respectively) (Custom made, Chroma Technology Corp. Rockingham, VT) is used for detection of YOYO-1 and Alexa-546 emission by alternative laser excitation (using external laser shutters, Thorlabs, Newton, NJ). The emission signal is magnified 1.6× and detected by a back-illuminated, thermoelectric cooled charge coupled device (EMCCD) detector (iXon) (Andor, Ireland). About 200 sequential images of the labeled DNAs confined in nanochannels are recorded at $60 - 80$ms exposure time in blue-green alternative laser excitation.

7.3.4 Recording and calculations

The intensity profile $I(x, y)$ of each Alexa-546 label is fitted by a 2D Gaussian function to determine the position of the label (x_c, y_c) in the channel (Fig.7.1B). The position of each internal label is followed frame-by-frame at a time interval of about 160ms. The probability distribution, the mean value and the corresponding standard deviation of the distance between each pair of internal labels are calculated.

7.3.5 Partition function and angle fluctuation

The partition function for a confined DNA, whose Hamiltonian is expressed in Eq.7.12, is: $Z = \int \exp\left(-\mathcal{H}/k_BT\right) d\vec{\theta} = \exp\left(FL/k_BT\right) \sqrt{(2\pi k_BT)^N / \det \mathbf{K}}$, where N is the number of segments in the discrete chain. The angle fluctuation or correlation is the Boltzmann weighted average of $(\theta_i\theta_j)$ over all the configurations [26, 30]:

$$\langle \theta_i\theta_j \rangle = \frac{1}{Z} \int \theta_i \cdot \theta_j \, \exp\left(-\frac{\mathcal{H}}{k_BT}\right) d\vec{\theta} = k_BT \left(\mathbf{K}^{-1}\right)_{ij} . \tag{7.15}$$

Using Eq.7.15, we can explicitly calculate the mean extension and fluctuation of the internal segments (Eq.7.13-7.14).

Bibliography

[1] Riehn R, Lu M, Wang YM, Lim SF, Cox EC, et al. (2005) Restriction mapping in nanofluidic devices. *P Natl Acad Sci USA* 102:10012-10016.

[2] Douville N, Huh D, Takayama S (2008) DNA linearization through confinement in nanofluidic channels. *Anal Bioanal Chem* 391:2395-2409.

[3] Wang YM, Tegenfeldt JO, Reisner W, Riehn R, Guan XJ, et al. (2005) Single-molecule studies of repressor-DNA interactions show long-range interactions. *P Natl Acad Sci USA* 102:9796-9801.

[4] Doi M, Edwards SF (1986) The Theory of Polymer Dynamics. (Clarendon Press, Oxford).

[5] de Gennes PG (1979) Scaling Concepts in Polymer Physics. (Cornell University Press, Ithaca, NY).

[6] Odijk T (1983) On the statistics and dynamics of confined or entangled stiff polymers *Macromolecules* 16:1340-1344.

[7] Schaefer DW, Joanny JF, Pincus P. (1980) Dynamics of semiflexible polymers in solution. *Macromolecules* 13:1280-1289.

[8] Daoud M, Degennes PG (1977) Statistics of macromolecular solutions trapped in small pores. *J Phys France* 38:85-93

[9] Reisner W, Beech JP, Larsen NB, Flyvbjerg H, Kristensen A, et al. (2007) Nanoconfinement-enhanced conformational response of single DNA molecules to changes in ionic environment. *Phys Rev Lett* 99:058302.

[10] Yang Y, Burkhardt TW, Gompper G (2007) Free energy and extension of a semiflexible polymer in cylindrical confining geometries. *Phys Rev E* 76:011804.

[11] Wang J, Gao H (2007) Stretching a stiff polymer in a tube. *J Mater Sci* 42:8838-8843.

[12] Tegenfeldt JO, Prinz C, Cao H, Chou S, Reisner WW, et al. (2004) The dynamics of genomic-length DNA molecules in 100-nm channels. *P Natl Acad Sci USA* 101:10979-10983.

[13] Reisner W, Morton KJ, Riehn R, Wang YM, Yu Z, et al. (2005) Statics and dynamics of single DNA molecules confined in nanochannels. *Phys Rev Lett* 94:196101.

[14] Jung Y, Jun S, Ha B (2009) Self-avoiding polymer trapped inside a cylindrical pore: flory free energy and unexpected dynamics. *Phys Rev E* 79:061912.

[15] Bonthuis DJ, Meyer C, Stein D, Dekker C (2008) Conformation and dynamics of DNA confined in slitlike nanofluidic channels. *Phys Rev Lett* 101:108303.

[16] Cifra P, Benkova Z, Bleha T (2008) Effect of confinement on properties of stiff biological macromolecules. *Faraday Discuss* 139:377-392.

[17] Persson F, Westerlund F, Tegenfeldt JO, Kristensen A (2009) Local conformation of confined DNA studied using emission polarization anisotropy. *Small* 5:190-193.

[18] Odijk T (2006) DNA confined in nanochannels: hairpin tightening by entropic depletion. *J Chem Phys* 125:204904.

[19] Xiao M, Phong A, Ha C, Chan TF, Cai D, et al. (2007) Rapid DNA mapping by fluorescent single molecule detection. *Nucleic Acids Res* 35:e16.

[20] Persson F, Tegenfeldt JO (2010) DNA in nanochannels-directly visualizing genomic information. *Chem Soc Rev* 39:985-999.

[21] Jun S, Thirumalai D, Ha B (2008) Compression and stretching of a self-avoiding chain in cylindrical nanopores. *Phys Rev Lett* 101:138101.

[22] Odijk T (2008) Scaling theory of DNA confined in nanochannels and nanoslits. *Phys Rev E* 77:060901.

[23] Burkhardt TW (1997) Free energy of a semiflexible polymer in a tube and statistics of a randomly-accelerated particle. *J Phys A-Math Gen* 30:L167-L172.

[24] Seol Y, Li J, Nelson PC, Perkins TT, Betterton MD (2007) Elasticity of short DNA molecules: theory and experiment for contour lengths of 0.6-7 μm. *Biophys J* 93:4360-4373.

[25] Purohit PK, Arsenault ME, Goldman Y, Bau HH (2008) The mechanics of short rod-like molecules in tension. *Int J Nonlin Mech* 43:1056-1063.

[26] Su T, Purohit PK (2010) Thermomechanics of a heterogeneous fluctuating chain. *J Mech Phys Solids* 58:164-186.

[27] Cao H, Yu ZN, Wang J, Tegenfeldt JO, Austin RH, et al. (2002) Fabrication of 10 nm enclosed nanofluidic channels. *Appl Phys Lett* 81:174-176.

[28] Cao H, Tegenfeldt JO, Austin RH, Chou SY (2002) Gradient nanostructures for interfacing microfluidics and nanofluidics. *Appl Phys Lett* 81:3058-3060.

[29] Das SK, Austin MD, Akana MC, Deshpande P, Cao H, et al. (2010) Single molecule linear analysis of DNA in nano-channel labeled with sequence specific fluorescent probes. *Nucleic Acids Res* 38:e177.

[30] Zhang Y, Crothers DM (2003) Statistical mechanics of sequence-dependent circular DNA and its application for DNA cyclization. *Biophys J* 84:136-153.

Chapter 8

Entropically Driven Motion of Polymers in Non-uniform Nanochannels

Main results of this chapter:

1. In nanofluidic devices, non-uniform confinement induces an entropic force that automatically drives biopolymers towards less confined regions to gain entropy.

2. We first analyze the diffusion of an entropy-driven particle system. The derived Fokker-Planck equation reveals an effective driving force as the negative gradient of the free energy. The derivation also shows that both the diffusion constant and drag coefficient are location dependent on an arbitrary free energy landscape.

3. We then investigate DNA motion and deformation in non-uniform channels. Typical solutions reveal large gradients of stress on the polymer where the channel width changes rapidly. Migration and deformation of DNA in several non-uniform channels are discussed.

8.1 Introduction

The development of techniques for confining DNA in nanofluidic channels has pushed genomic studies up to a new level. Researchers are now capable of using nano-channels to stretch a single DNA molecule, to sort DNAs based on their

sizes, and to study repressor-DNA interactions, *etc* [1, 2, 3, 4]. To interpret the experimental data, theorists have been developing models to predict the free energy, the average extension, relaxation time, *etc*, of a confined polymer [5, 6, 7, 8, 9]. Among those theories, the two most well-known in the field are those described by de Gennes [5] and by Odijk [6].

de Gennes' theory is applicable for a moderately confined polymer. The theory requires $D >> p$, where D is the channel width and p is the persistence length of the polymer. In this regime, DNA forms blob-like structures aligned along the channel. Evaluated at the average extension, the free energy G of the confined DNA scales as $G \sim D^{-5/3}$ in this regime [9, 10]. This tells us that, with the increase of the channel size, the free energy of the polymer decreases.

On the other hand, Odijk's theory studies a strongly confined polymer with $D << p$. In this regime, DNA is deflected back and forth by the channel walls, extending its backbone almost linearly inside the channel. Evaluated at the average extension $\langle \Delta z \rangle$, the free energy (per unit length) in this strong confinement regime takes the form [11]:

$$G|_{\Delta z = \langle \Delta z \rangle} = \frac{c k_B T}{p^{1/3}\, D^{2/3}}, \tag{8.1}$$

where k_B is the Boltzmann constant, T is the absolute temperature and $c = 2.5$ is a constant for a cylindrical channel. This expression again suggests that the free energy is a decreasing function of D. The consequences of such a dependence of the free energy on the channel width are rarely investigated because many of the studies so far have focused on confining polymers in a uniform channel. However, in a non-uniform channel the dependence of G on D implies a free energy gradient, and therefore an effective driving force along the channel axis. This effective force can automatically drive the DNA to migrate along the channel without fluid flow or applied electric fields. Understanding this force can therefore help design new nanofluidic channels for better DNA manipulation.

The effective force described here is essentially an entropic force: by moving to a wider region inside a non-uniform channel, DNA experiences less confinement, gains more degrees of freedom and thus increases its entropy. This lowers the free energy of the system. Entropic forces of this kind can be found in problems like translocation of DNA through nanopores, where DNA is driven by an electric field, against an entropic force, to pass through a nanopore that separates two wide compartments [12, 13]. The entropic force acting on the DNA is revealed by the spontaneous retracting motion of the molecule when it is partly inserted into the nano-channel [14]. Such retracting motion was modelled by Mannion et al. [14] by performing a force balance where the drag force on the DNA due to the surrounding fluid counteracts a constant entropic force. For simplicity, evolution of the local deformation of the DNA during its motion was neglected in these studies. Aside from non-uniform confinement, entropic forces on translocating polymers can also arise from reversible binding of particles (proteins, for instance) on one end

of the polymer chain, which creates the so-called entropic Langmuir pressure [15]. Entropic forces have also been reported to play a role in unfolding DNA molecules in channels [16]. In an even broader context, the widely studied diffusiophoresis phenomena on colloidal particles is also created by entropic forces [17, 18, 19].

The goals of this chapter are (1) to understand the channel-shape dependence of the confinement induced entropic force on a polymer, and (2) to study the coupled migration and deformation of a polymer in a non-uniform channel. To understand the entropic force, we first study the diffusion of particles on a free energy landscape with varying entropy. A Fokker-Planck equation is derived, which reveals an effective entropic force $f_{\text{ent}} = -\nabla G$, automatically driving the system to reduce the free energy per particle G. The derivation also reveals that both the diffusion 'constant' and the drag coefficient become location-dependent as long as $\nabla G \neq 0$. Using the derived effective entropic force, we further study the motion and deformation of a polymer in a non-uniform channel. The problem is governed by a second order partial differential equation (PDE), whose solution gives both the migration velocity and the strain distribution along the polymer backbone.

Another issue arising in the context of a polymer confined in a non-uniform channel is the possible transition between the de Gennes' and Odijk's regimes. It is commonly acknowledged that the transition channel width for a stress free DNA is roughly $D \sim 50 - 100$nm, although more complex phenomena have been reported in this transition regime [20, 21]. As the polymer moves and deforms inside a non-uniform channel, stress can develop along its backbone so that the transition width is no longer $D \sim 50 - 100$nm. Even in a uniform channel, when electrical force is applied, the transition width is expected to increase. In this chapter we estimate the transition width D as a function of the applied force so that we know roughly which theory to use based on the current location of the DNA and its local stress state. For simplicity, we will focus on a piece of DNA moving in a narrow non-uniform channel such that it is entirely in Odijk's regime. Then, we will discuss possible generalization of the theory to the de Gennes' regime.

8.2 Entropically Driven Diffusion

Before investigating the migration of DNA in non-uniform channels, we first briefly discuss entropically driven diffusion of particles in this section.

Consider a 1D random walk of an ensemble of particles on a free energy landscape with varying entropy (Fig. 8.1). Unlike in the classical random walk model, the particles considered here have different internal states. In free space where no spatial constraints are imposed, each particle has Ω_{tot} internal states with energy E_i $(i = 1, 2, \cdots \Omega_{\text{tot}})$. Along the z-axis, the 1D random walk domain, some spatially-varying constraints are imposed, reducing the number of accessible states for each particle to $\Omega(z) \leq \Omega_{\text{tot}}$ at location z

(Fig. 8.1). The spatial constraints are non-uniform and therefore $\Omega(z)$ depends on z. The particles are on an entropy-varying landscape. In the context of confined DNA in nano-channels, one can think of the different internal states as different configurations of the DNA. The non-penetration constraint posed by the non-uniform channel wall forbids some of the configurations and reduces the number of accessible states. We define the location dependent partition function as $\Xi(z) = \sum_{i=1}^{\Omega(z)} \exp(-\beta E_i)$, and the z-dependent free energy as $G(z) = -k_B T \log \Xi(z)$. Note that in defining the partition function and the free energy, we have assumed local equilibrium.

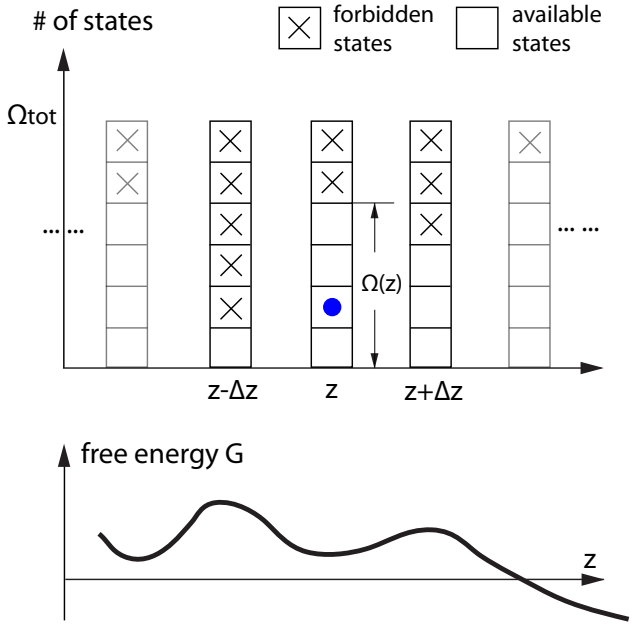

Figure 8.1: 1D random walk of particles (blue) in the z-direction. In its natural condition, each particle has Ω_{tot} internal states ($\Omega_{\text{tot}} = 6$ in the figure). Some z-dependent spatial constraints reduce the number of accessible states at location z to $\Omega(z) \leq \Omega_{\text{tot}}$ (the blank boxes), creating an entropy varying landscape. Free energy is lower where there are more states to explore. An entropic force arises from this random walk model, driving the system towards regions with lower free energy.

One can derive the Fokker-Planck equation rigorously for this problem, which turns out to be:

$$\frac{\partial P}{\partial t} = \frac{\partial}{\partial z}\left[\mathcal{D}\frac{\partial P}{\partial z} - \left(\frac{-dG/dz}{\xi}\right)P\right], \tag{8.2}$$

with $P(z,t)$ being the probability density for a particle being at location z at time t, $\mathcal{D}$ being the diffusion 'constant', and ξ being the drag coefficient.

Compared with the Fokker-Planck equation for a random walk with a 'real' applied force (say, by an optical tweezer or other instruments) [22], Eq. 8.2 reveals that the non-uniform spatial constraint creates an effective force $-dG/dz$,

which drives the system towards regions with higher entropy to reduce the free energy. We note that free energy gradient has been shown to be a good approximation to the Langmuir pressure (an entropic force) in problems where ejection of DNA from bacteriophage is speeded up by the entropic effects of reversible binding of proteins in the host cell [15]. Here in our model, the free energy gradient is exactly, instead of approximately, the entropic force.

It is important to note that in an entropy-varying landscape, the diffusion 'constant' $\mathcal{D}$ is location-dependent:

$$\mathcal{D} \sim \Xi(z). \tag{8.3}$$

This result comes out naturally in deriving the Fokker-Planck equation. It suggests that the particles diffuse faster where there are more states for exploration. This is analogous to the case of diffusion in porous media, where the effective diffusion constant is found to be proportional to the porosity of the media [23]. Furthermore, the Stokes-Einstein relation $\mathcal{D}\xi = k_B T$ implies that the drag coefficient ξ is also location-dependent when there are non-uniform spatial constraints. This is not surprising since it is well-known that the proximity of walls can change the drag coefficient on bodies in low Reynolds number flows [24].

Using conservation of mass: $P_{,t} = -J_{,z}$, we obtain from Eq. 8.2 the particle flux J as:

$$J = -\mathcal{D}\,\frac{\partial P}{\partial z} - \frac{dG/dz}{\xi} P. \tag{8.4}$$

An analytic steady state distribution can be found, even with both $\mathcal{D}$ and ξ being functions of z, by setting J to be a constant:

$$P_{\text{steady}}(z) = P_0\,\Xi(z) \int \frac{dz}{\Xi^2(z)}, \tag{8.5}$$

where we recall that $G(z) = -k_B T \log \Xi(z)$ and P_0 is a normalization constant. This is the steady state probability density of particles on an arbitrary free-energy landscape with a non-uniform diffusion constant. To verify if this solution is correct, we consider a random walk in $z \in [z_0, z_1]$ with $G(z) \propto \log(z)$. The boundary condition at $z = z_0$ is a hard wall, and at $z = z_1$ it is an absorption wall. Without any fitting, Eq. 8.5 agrees almost exactly with the result from a Kinetic Monte Carlo (KMC) simulation (Fig. 8.2). Here the KMC simulation was performed using the algorithms given in Voter [25].

Further, we note that the first term on the right-hand-side of Eq. 8.4 is the diffusive flux, while the second term is the drift flux $(v - v_{\text{fluid}})P$. Therefore, the mean velocity v of the system is:

$$v = v_{\text{fluid}} + \frac{f_{\text{app}} - dG/dz}{\xi}. \tag{8.6}$$

Here v_{fluid} is the fluid velocity and f_{app} is an external applied force. Eq. 8.6 is essentially an equation for force balance if, again, $-dG/dz$ is interpreted as

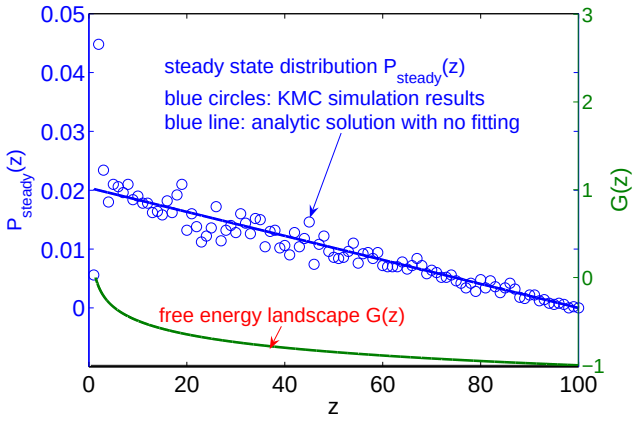

Figure 8.2: Steady state distribution $P_{\text{steady}}(z)$ (y-axis on the left) on a free energy landscape $G(z) \propto \log(z)$ (y-axis on the right). The random walk domain is $z \in [1, 100]$, with $z = 1$ being a hard wall and $z = 100$ being an absorption wall. Eq. 8.5 predicts a linear steady state distribution (blue line), which is confirmed, without any fitting, by the Kinetic Monte Carlo simulation results (blue circles). The numbers in this figure are in SI units.

an effective entropic force:

$$\underbrace{f_{\text{app}}}_{\text{external force}} + \underbrace{\left(-\frac{dG}{dz}\right)}_{\text{entropic force}} + \underbrace{\xi\left(v_{\text{fluid}} - v\right)}_{\text{drag force}} = 0. \tag{8.7}$$

Eq. 8.7 without the entropic force term has been used to model macromolecules stretched in fluid flow [26]. Here we show that a non-uniform spatial constraint gives rise to an effective entropic force term that must be included in the macroscopic force balance equation.

Interestingly, exactly the same results as presented above for particles in an entropy varying landscape can be derived by using another method – starting from the Sackur-Tetrode formula for the entropy of an ideal gas and considering the heat production rate. We show the derivation in Appendix N.

8.3 DNA Confined in Non-uniform Channels – Theory and Computation

We now analyze the migration and deformation of a DNA molecule in a non-uniform channel. Under strong confinement, a DNA molecule (or any semi-flexible polymer) can be modelled as a fluctuating 1D rod (Fig. 8.3) [26]. The rod is parametrized by its arc length $s \in [0, L]$, with L being the contour length of the polymer. We denote the location of the DNA inside the channel at time t as $z(s, t)$, so that $\partial z/\partial t = \dot{z}$ is the local velocity and $\partial z/\partial s = \lambda$ is

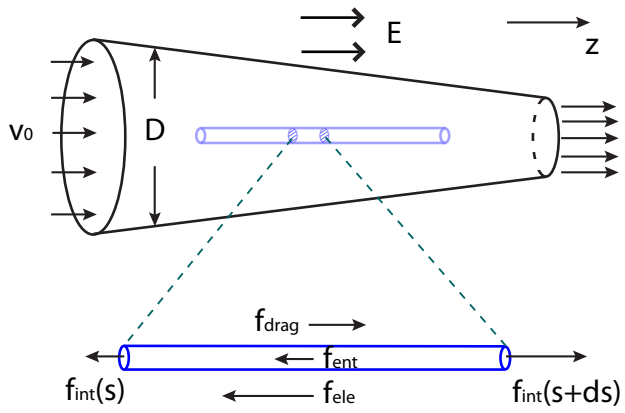

Figure 8.3: A DNA molecule is modelled as a 1D rod confined in a non-uniform channel. Typically, inside a nano-channel the DNA molecule can be subjected to stretching force f_{int}, drag force f_{drag} exerted by the surrounding fluid flow, entropic force f_{ent} due to the non-uniform confinement and also electrical force f_{ele} since the DNA is charged. The figure shows balance of force for an infinitesimal segment on the rod.

the local stretch of the DNA. Note that $\dot{z} > 0$ if the polymer is moving from left to right (Fig. 8.3).

Below, we first analyze different forces that act on the polymer. Of particular interest are the entropic force and the drag force. As pointed out in the previous section, the free energy gradient $-dG/dz$ serves as an effective entropic force *per unit length* f_{ent}. Using Eq. 8.1, we obtain:

$$f_{\text{ent}} = \frac{5}{3} \frac{k_B T}{p^{1/3} D^{5/3}} \frac{dD}{dz}. \tag{8.8}$$

This entropic force is positive when $dD/dz > 0$. Therefore, it drives the system towards regions with higher entropy. Also, like other entropic forces in polymer science, it depends linearly on the thermal energy $k_B T$ [22, 15]. Moreover, its magnitude is governed not only by the gradient of the channel width, but also by the property of the polymer, like the persistence length p. A very stiff polymer with large persistence length p would be extended linearly along the channel without feeling much confinement. Therefore, the entropic force due to non-uniform confinement will be weak on stiff polymers. The total entropic force acting on the entire DNA can be estimated as:

$$\int_0^L (-dG/dz) ds \approx \frac{c \left[D^{-2/3}(0) - D^{-2/3}(L) \right]}{\beta \lambda p^{1/3}}. \tag{8.9}$$

Using Eq. 8.9, a divergent channel with $D(0) = 25$nm and $D(L) = 50$nm will pose a total entropic force of approximately 0.15pN on a strongly confined DNA with $\lambda \approx 0.8$ and $p = 50$nm. This force is significant because the typical thermal force scale on a DNA molecule is $k_B T/p \approx 0.08$pN.

Translating polymers in a nanochannel also experience a fluid drag. When the confinement is strong, hydrodynamic interactions between the polymers and the channel walls become important and cannot be neglected. For example, for a slender body of contour length L and radius a moving between two walls that are separated by a distance $D << L$, the longitudinal drag coefficient per unit length is [27]:

$$d_{t2} = \frac{2\pi\mu}{\log(D/a) - 0.453}, \tag{8.10}$$

with μ being the viscosity of the fluid. The subscript 2 stands for confinement by two walls. d_{t2} is much larger than $d_{t0} = \frac{2\pi\mu}{\log(L/2a)+c}$ with $c \approx \mathcal{O}(1)$, which is the drag cooefficient for the same slender body moving in a fluid with no nearby walls [24]. In our problem, a polymer in a nanochannel can be modelled as a slender body confined by four walls. Using superposition [28] and the fact that $d_{t2} >> d_{t0}$ [24], the drag coefficient for such a slender body is approximately:

$$d_t \approx \frac{4\pi\mu}{\log(D/a) - 0.453}. \tag{8.11}$$

It has been shown, by several independent studies, that the method of superposition for calculating the drag coefficient yields reasonably good agreement with experimental measurements [29, 30, 31], even though it is not exact.

To determine d_t, we still need to know the radius a of the slender body. Marko and Siggia [32] suggested that the effective radius should be taken as the transverse size $R_\perp$ of the elongated polymer. This depends not only on the width D of the channel, but also on the persistence length p of the polymer. Given the stretch λ of the polymer, we estimate $R_\perp$ in Appendix O, and the result is:

$$R_\perp = a_0\lambda + 0.7445\left(pD^2\right)^{1/3}\sqrt{1-\lambda^2}, \tag{8.12}$$

with $a_0 = 1.0$nm being the geometric width (radius) of a DNA molecule [33, 34, 35]. Since $(pD^2)^{1/3} >> a_0$, $R_\perp$ is a decreasing function of λ, which makes sense because for an inextensible rod, the perpendicular deflections should decrease as the stretch increases.

A substitution of $R_\perp$ into a in Eq. 8.11 suggests that a polymer with less transverse fluctuation experiences less drag. In particular, for $D = 50$nm, the drag coefficient per unit length is about 39.6 pN ms μm^{-2} at zero force. In comparison, it has been estimated that when there is no confinement, the drag coefficient is about 0.61 pN ms μm^{-2} for a DNA molecule [36]. In micron scale channels, on the other hand, the drag coefficient is about 1.2 pN ms μm^{-2} [36]. Our estimate shows that when the channel width is on the nanometer scale, the drag coefficient increases significantly. Further, we note that λ and $R_\perp$ depend on the internal stretching force f_{int} (discussed below in Eq. 8.14). Therefore, d_t is also a function of f_{int}. We show their relation in Fig. 8.4. As expected, increasing the stretching force reduces the transverse size of the polymer, which leads to a smaller d_t.

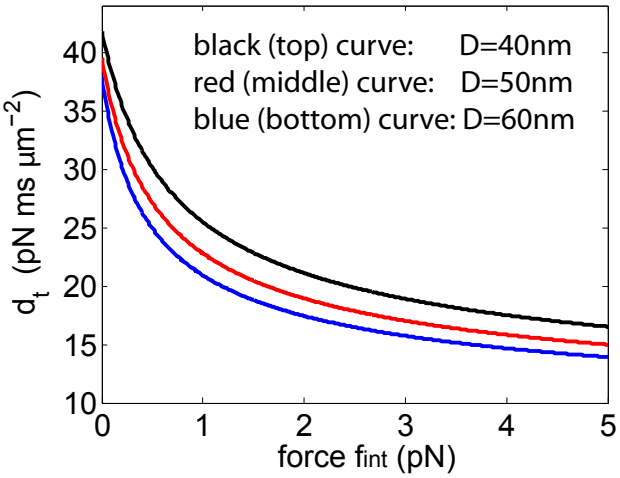

Figure 8.4: Drag coefficient per unit length as a function of the stretching force f_{int} at different channel widths D (calculated using Eq. 8.11, Eq. 8.12 and Eq. 8.14).

Next, we do a force balance on an infinitesimal segment of the rod, which, aside from the above mentioned two forces, also experiences (Fig. 8.3): (1) internal stretching force f_{int} exerted by its neighbouring segments, and (2) electrical force per unit length f_{ele} arising from the applied electric fields. Balance of forces in the longitudinal direction (Eq. 8.7) requires these forces sum to zero:

$$\frac{\partial f_{\text{int}}}{\partial s} - d_t \left(\frac{\partial z}{\partial t} - v_{\text{fluid}} \right) + f_{\text{ele}} + f_{\text{ent}} = 0. \tag{8.13}$$

In this force balance analysis, long-range hydrodynamic interactions between different material points on the DNA are neglected because the polymer is under strong confinement. A random force can be added, but, to study the average behavior, we do not include it in Eq. 8.13. Also, since the Reynolds number is low in a nanofluidic channel, it is legitimate to ignore inertia. We also note that the drag force may also depend on the strain rate $\partial v_{\text{fluid}}/\partial z$ [37], but in this study we neglect this effect. This is consistent with Eq. 8.7.

To solve for the two unknowns $z(s,t)$ and $f_{\text{int}}(s,t)$, we also need a constitutive equation [26]. In particular, following Marko and Siggia [32], we will apply the constitutive relation locally on the polymer. For a strongly confined DNA, Wang and Gao [38] showed that the force-stretch relation is:

$$f_{\text{int}} = \frac{1}{\beta p} \left[\frac{1}{4(1-\lambda)^2} - c^2 \left(\frac{p}{D} \right)^{4/3} \right], \tag{8.14}$$

where again $\lambda = \partial z/\partial s$ is the local stretch of the DNA and $c = 2.5$ is a constant for a cylindrical channel. Eq. 8.13 and Eq. 8.14 form the governing equations for the problem.

To identify the relative order of magnitude of each term in the governing

equations, we scale the problem using the following non-dimensional quantities:

$$\bar{z} = \frac{z}{L}, \quad \bar{s} = \frac{s}{L}, \quad \bar{D} = \frac{D}{p}, \quad \bar{a}_0 = \frac{a_0}{p}, \tag{8.15}$$

$$\bar{f}_{\text{int}} = f_{\text{int}}\beta p, \quad \bar{f}_{\text{ele}} = f_{\text{ele}} \left(\frac{3}{5}\beta p L\right), \tag{8.16}$$

$$\bar{t} = \frac{5t}{3\beta d_{t*} p L^2}, \quad \bar{v}_{\text{fluid}} = v_{\text{fluid}} \left(\frac{3}{5}\beta d_{t*} p L\right). \tag{8.17}$$

Here $d_{t*} = 4\pi\mu$ is the numerator of the drag coefficient d_t (Eq. 8.11). The scaling suggests that the typical time scale for the problem is on the order of $\tau \sim \beta d_{t*} p L^2 \approx 10$s for a DNA molecule about 20μm long in water with viscosity 10^{-3} Nsm^{-2}. For a wider micron scale channel, however, the time scale is expected to be smaller since the drag coefficient is smaller and the molecules move faster. As a comparison, the Rouse bead and spring model predicts the first-mode structural relaxation time τ_1 of a polymer chain as $\tau_1 = \beta\xi L^2$ [39], with ξ being the drag coefficient per bead. Using $\xi = d_t l$ and $l \sim p$, where l is the natural length of each spring, we recover the time scale τ for our governing equations. We note that, more generally, a stretched polymer has two different relaxation times, one in the longitudinal direction $\tau_{\parallel}$ and one in the transverse direction $\tau_{\perp}$ [40]. The time scale $\tau \sim \beta d_{t*} p L^2$ for our governing equations is for the deformation in the longitudinal direction because t appears in our equations as $\partial z/\partial t$.

The two governing equations for $z(s,t)$ and $f_{\text{int}}(s,t)$ (Eq. 8.13 and Eq. 8.14) can be decoupled. By plugging the constitutive law into the equation for force balance, we can eliminate $\bar{f}_{\text{int}}$ and the result is an evolution law for $\bar{z}(s,t)$:

$$H(\lambda)\frac{\partial \bar{z}}{\partial \bar{t}} = \frac{3}{10\left(1-\bar{\lambda}\right)^3}\frac{\partial \bar{\lambda}}{\partial \bar{s}} + \left(\frac{5\bar{\lambda}}{\bar{D}^{7/3}} + \frac{1}{\bar{D}^{5/3}}\right)\frac{d\bar{D}}{d\bar{z}} + \bar{\mathcal{V}}. \tag{8.18}$$

Here, the function $H(\lambda) = \left[\log(\bar{D}/\bar{R}_{\perp}) - 0.453\right]^{-1}$ is the contribution of the polymer-wall hydrodynamic interaction. $\bar{\mathcal{V}} = H(\lambda)\bar{v}_{\text{fluid}} + \bar{f}_{\text{ele}}$ can be viewed as an effective flow that combines the actual drag force with the electrical force. Eq. 8.18 is the central equation for the problem because its solution gives the velocity $\partial z/\partial t$ and also the deformation $\lambda = \partial z/\partial s$ of the DNA inside a non-uniform channel.

It is possible to design a non-uniform channel in which a DNA molecule remains stationary. The key is to use the fluid flow and applied electric field to exactly balance the entropic force. The shape of this special channel can be determined by setting $\partial \bar{z}/\partial \bar{t} = 0$ in Eq. 8.18, so that what remains is an ordinary differential equation (ODE) for the channel shape $D = D(z)$. To see this, we note that all the three terms on the right-hand-side of Eq. 8.18 can be written as functions of D because (1) by setting $f_{\text{int}} = 0$, $\bar{\lambda} = \bar{\lambda}(\bar{D})$ by the constitutive law, and (2) for an incompressible flow, $\bar{v} = \bar{v}(\bar{D})$ because of mass conservation. We do not set up the ODE here for the sake of brevity.

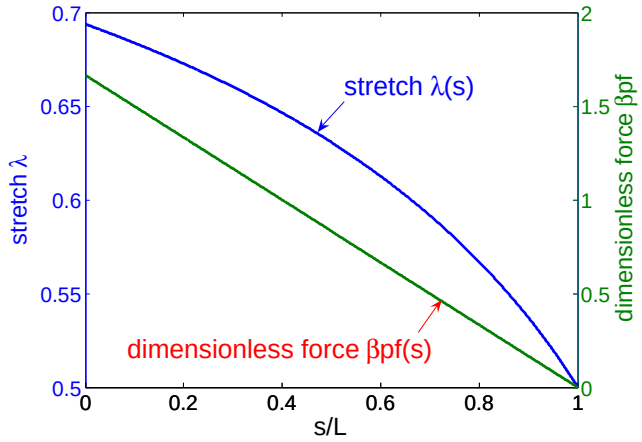

Figure 8.5: Stretch and force distributions along the arc length s of a stationary DNA in a uniform nanofluidic channel. The stretch distribution is non-linear: $(1-\bar{\lambda}) \sim (-\bar{s})^{-1/2}$ while the force distribution is always linear with slope being $-5\bar{\mathcal{V}}/3$.

Eq. 8.18 does not have an analytical solution for most cases. To solve the problem numerically, we discretize the rod into segments and do force balance using the wormlike-chain constitutive relation (with effects of confinement) for each of them. The local velocity and stretch of each segment are determined using the method discussed above. The discrete version of our governing equations essentially constitutes a string of beads connected by wormlike-chain linkers.

8.4 DNA Confined in Non-uniform Channels – Results

8.4.1 Stationary DNA in nanochannels

As the simplest special case, we first briefly discuss the results for a stationary DNA in a uniform channel. In this case, Eq. 8.18 reduces to:

$$\frac{\partial \bar{\lambda}}{\partial \bar{s}} = -\frac{10\bar{\mathcal{V}}}{3}\left(1-\bar{\lambda}\right)^3. \tag{8.19}$$

Assuming uniform flow, i.e, $\bar{\mathcal{V}}$ = constant is independent of $\bar{z}$ (since H depends weakly on λ, we neglect the dependence of H on λ here. When we do numerical simulations in the later discussions, this dependence will be taken into account), we get the analytic solutions:

$$\bar{\lambda}(\bar{s}) = 1 - \frac{1}{2\sqrt{A - \left(5\bar{\mathcal{V}}/3\right)\bar{s}}}, \qquad \bar{f}_{\text{int}}(\bar{s}) = -\frac{5\bar{\mathcal{V}}\bar{s}}{3} - \frac{c^2}{\bar{D}^{4/3}} + A. \tag{8.20}$$

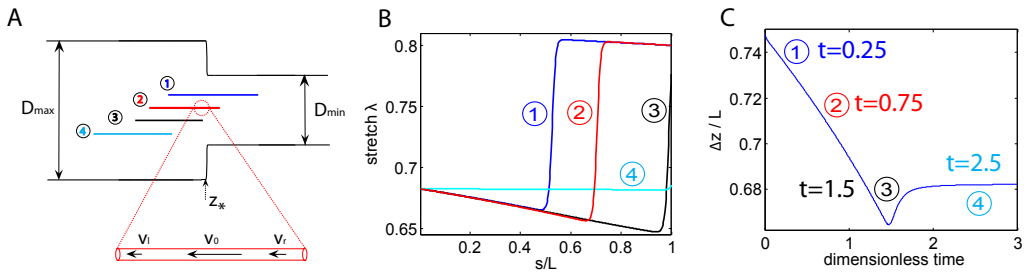

Figure 8.6: Entropically driven DNA crossing a sharp interface where the channel width changes suddenly. The channel shape is shown in (a). No fluid flow or electrical force is applied, so the DNA is driven only by the entropic force. The numbers in the circles represent snapshots of the molecule at different times. The process can be divided into two stages. Stage-(I): DNA moving across the interface at $z = z_*$ (① – ③). In this stage, a large force/strain gradient occurs at $z = z_*$ as is apparent in (b). This force/strain gradient is caused by the migration speed gradient as shown in the enlarged figure in (a) ($v_0 > v_l$, $v_0 > v_r$). The strain gradient travels along the DNA backbone until it completely enters into the wider region. Total extension of the DNA decreases in this stage as is apparent in (c). Stage-(II): DNA leaving the interface (③ – ④). In this stage, the force/strain gradient slowly relaxes as is apparent in (b). The total extension of the DNA stops decreasing, instead, it increases to reach an equilibrium value as is apparent in (c).

Here $c = 2.5$ and A is a constant determined by the boundary condition. For example, $\bar{f}_{\rm int}(1) = 0$ for a free end leads to $A = 5\bar{\mathcal{V}}/3 + c^2\bar{D}^{-4/3}$.

The solution in Eq.8.20 suggests that the force distribution along the arc length is always linear while the stretch varies non-linearly as $(1 - \bar{\lambda}) \sim (-\bar{s})^{-1/2}$ (Fig. 8.5). Moreover, when $\bar{\mathcal{V}} > 0$, both $\bar{f}_{\rm int}$ and $\bar{\lambda}$ are decreasing functions of $\bar{s}$. This implies that the strain along the DNA is highest at its 'upstream' end and lowest at its 'downstream' end, regardless of the boundary conditions posed. This is reasonable because forces applied at the 'upstream' end should balance the drag force along the entire DNA, so that the polymer can stay stationary.

8.4.2 Migration and deformation of DNA in non-uniform channels

We now analyze the entropy-driven migration of DNA in non-uniform channels. Firstly, we consider a channel with a sudden change in its width as shown in Fig. 8.6(a). Similar channels have been used to study the transport of DNA in nanopits [41], although in this section we will focus on channels narrow enough that the polymer is purely in Odijk's regime. The channel shape is modelled as a hyperbolic function $D(z) \sim \tanh(z/\eta)$, where η is a parameter characterizing the length scale over which the channel changes its width. As

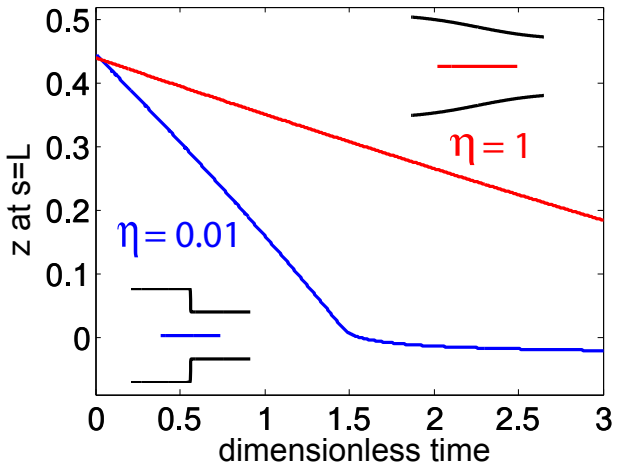

Figure 8.7: Movement of the right end of the DNA ($z(L,t)$ as a function of t) in channels with different η. No fluid flow or electrical force is applied, so the DNA is driven only by the entropic force. For a channel that changes its shape more rapidly (smaller $\eta = 0.01$, blue), the DNA moves faster because of larger entropic force. The initial condition is a stress free state. The boundary conditions are $f_{\text{int}} = 0$ at $s = 0$ and $s = L$.

$\eta \to 0$, $D(z)$ becomes a step function.

To study the entropic effect, fluid flow and electric field are set to zero, so that the DNA is driven purely by the entropic force. We solve Eq. 8.18 numerically to obtain $z(s,t)$, with a stress-free initial condition $f_{\text{int}}(s,0) = 0$ and stress-free boundary conditions $f_{\text{int}}(0,t) = f_{\text{int}}(L,t) = 0$. As expected, the DNA migrates to the wider region. The entire process can be divided into two stages, as explained in detail below.

Stage-(I): DNA moving across the interface $z = z_*$, at which the channel width changes (①–③ in Fig. 8.6). In this stage, the material point at the interface z_* experiences a large entropic force. Therefore, it moves with a larger velocity to the left compared to its neighbouring material points (see the enlarged figure in Fig. 8.6(a)). This stretches the material on the right of the interface and compresses the material on the left. As a result, a large force/strain gradient appears at the interface. This force/strain gradient travels along the DNA backbone as it moves across $z = z_*$, as shown in Fig. 8.6(b). This result implies that, if a polymer were to undergo structural change in a nano-channel, the change is most likely to occur at the interface where the channel shape changes most rapidly. Interestingly, some nanopores in cells, such as those in proteasomes, have indeed been found to cause structural changes in proteins [42, 43].

A second observation in this stage is that both ends of the DNA migrate at constant velocities (Fig. 8.7 shows the migration of the end $s = L$). This can be understood by looking into the central equation (Eq. 8.18). Before completely moving across the interface $z = z_*$, the stretch λ at both ends remains almost

a constant and does not change with time. Therefore, Eq. 8.18 suggests an almost constant $\dot{z}$. This result holds even when there is fluid flow in the channel ($\bar{\mathcal{V}} \neq 0$). Our results also show a decrease in the total extension of the DNA in this stage (Fig. 8.6(c) ①–③). This is expected because during the migration, a larger portion of the DNA moves into the wider region, where it suffers less stretch.

Stage-(II): DNA leaving the interface (③–④ in Fig. 8.6). As the entire DNA molecule enters into the wider part of the channel, the force/strain gradient slowly relaxes and finally disappears (Fig. 8.6(b)). At the same time, the total extension of the polymer stops decreasing, and increases to reach an equilibrium value (Fig. 8.6(c)).

Smoothing the change in width of the channel by increasing η can reduce the entropic force. Therefore, DNA is expected to migrate slower in a channel with a gently varying cross-section. This is confirmed by the solution to the central equation (Eq. 8.18). In Fig. 8.7, $z(L,t)$ is plotted for DNA in two different channels with $\eta = 0.01$ and 1 respectively, to show the velocity difference. No fluid flow is applied and the electrical force is set to zero.

Other more complicated non-uniform channels have also been fabricated in recent years, although most of them are at the micron scale [36]. We show the migration of a piece of DNA in four different types of such channels (in nanoscale so that the polymer is in Odijk's regime) in Fig. 8.8. The channel shape is $D(z) = (az+b)^n$, with $n = 1, -1/2, -2$ and -1 for the four channels. a and b are two constant parameters. No fluid flow or electrical force is applied, so the DNA is driven only by the entropic force. Our results suggest that with the same entrance width and exit width, a linear channel with $n = 1$ drives the polymer to move most slowly and the polymer suffers less stretch in this channel type (Fig. 8.8).

We next consider symmetric channels with two shape-changing regions as shown in Fig. 8.9(a) and (d). Again, the fluid velocity and electrical force are set to zero. These channels can exert entropic pulling and pushing forces on the molecule. In the channel shown in Fig. 8.9(a), the two ends are wider while the middle region is narrower. This creates a pair of pulling entropic forces on the confined polymer. Therefore, even without fluid flow or electrical force, stress/strain along the backbone quickly builds up and reaches a maximum in the middle where the confinement is stronger (Fig. 8.9(b)). The total extension of the polymer increases in response to the opposite entropic stretching and achieves equilibrium after some time as the polymer reaches a stationary state (Fig. 8.9(c)).

Fig. 8.9(d) is another symmetric channel with two narrow ends and a wide middle region. In this case, the entropic forces push the DNA into the middle region. However, as the DNA contracts, negative force builds up along the backbone, pushing against the entropic force until force balance is established (Fig. 8.9(e)). During the process, total extension of the polymer decreases in response to the entropic pushing (Fig. 8.9(f)). Again, we see large stress/strain gradients at the regions where the channel changes its shape.

A fluid flow or an applied electric field in the channel shown in Fig. 8.9(a) can break the symmetry of the problem. The DNA now migrates in response to the flow, or the electric field, through the nano-channel. The results with $v_{\text{fluid}} > 0$ and $f_{\text{ele}} = 0$ are shown in Fig. 8.10(b). The total stretch of the DNA increases as the polymer squeezes through the narrow region (Fig. 8.10(b)). Two force/strain gradients travel along the backbone of the DNA sequentially during the entire process (Fig. 8.10(c)).

Finally, we also investigate the dependence of the migration speed on the polymer contour length L and persistence length p. Three polymers with different contour lengths and persistence lengths ($L = 8$, 3 and 8μm, $p = 50$, 50 and 100nm respectively) are placed in a periodic channel with fluid flow $v_{\text{fluid}} > 0$ (Fig. 8.11(a)). Electrical field is again set to zero. Our results show that longer DNA moves faster in the periodic channel. At $t = 5$s, the long DNA with $L = 8\mu$m has already been separated from the short DNA with $L = 3\mu$m by $6 - 7$ microns (Fig. 8.11(b)). Changing the persistence length of the polymer does not significantly affect the migration velocity, at least in the case we studied. Fig. 8.11(b) shows that a polymer with $p = 50$nm migrates as fast as one with $p = 100$nm. This can be explained in the following way. Increasing the persistence length has two effects. Firstly, it reduces the drag coefficient since the effective radius of the polymer rod is less. This speeds up the migration. Secondly, it also reduces the entropic force (Eq. 8.8), which drives the polymer motion. This lowers the migration velocity. These two effects cancel each other, making the migration velocity not significantly dependent on the persistence length.

8.4.3 Transition to the de Gennes regime under non-zero force

The framework described above can be generalized to the de Gennes' regime by (1) adding proper force terms in the force balance equation (Eq. 8.13) since for a moderately confined DNA, volume exclusion effect and also the hydrodynamic force cannot be neglected any more, (2) changing the constitutive law for a blob-like polymer. To completely solve the problem of DNA in non-uniform channel, we also need to know at which channel width D the transition from the Odijk to de Gennes regime occurs. Although it is well-known that transition for a stress free DNA happens at channel width about $50 - 100$nm, transition width for a DNA under finite stress is unknown. Below we try to estimate the transition width between the two regimes as a function of the force.

We shall find the transition width in the following way. Odijk's theory assumes that under strong confinement, the angle fluctuation of the polymer is small such that second order approximation is proper. We shall find, in the $f - D$ plane, regions where the small angle approximation is valid. The other regions of the $f - D$ plane where small angle approximation is not valid are

assumed to be in de Gennes' regime.

Let $\theta(s)$ be the angle formed by the polymer with respect to the axis of the channel. In the Odijk regime, using the small angle quadratic approximation, the mean angle fluctuation of a confined chain under end-to-end force f is found to be [38]:

$$\langle\theta^2\rangle = \frac{1}{\sqrt{\beta p f + c^2 \left(p/D\right)^{4/3}}}, \tag{8.21}$$

In deriving this result, $\cos\theta \approx 1 - \theta^2/2$ was used. The ratio between the dropped quartic term $\theta^4/24$ and the retained quadratic term $\theta^2/2$ is:

$$e = \frac{\theta^4/24}{\theta^2/2} = \frac{\theta^2}{12}. \tag{8.22}$$

In order for the theory to be self-consistent, we need e to be small. Therefore, we try to find the regions on the $f - D$ plane where e is small and assume the rest of the plane corresponds to the deGennes' regime. The expression for $\langle e\rangle$ as a function of f and D is:

$$\langle e\rangle = \frac{\langle\theta^2\rangle}{12} = \frac{1}{12\sqrt{\beta f p + c^2 \left(p/D\right)^{4/3}}}. \tag{8.23}$$

We plot on the $f-D$ plane curves corresponding to $e = 3\%$ and 5% respectively in Fig. 8.12. For the region with e less than 3%, we claim the polymer is in Odijk's regime, for the zone with error larger than 5%, the polymer is more likely to be in de Gennes' regime. In between, there is uncertainty as to which regime best describes the behavior of the DNA. In fact, complex phenomena have been reported in the transition regions even when $f = 0$ [20, 21]. Fig. 8.12 shows that the transition occurs at wider channel width as the stress in the DNA increases. At $f = 0$, the transition width is around $50 - 100$nm, as expected.

8.5 Conclusions

The configuration and deformation of a confined polymer molecule depends on the channel width. But a non-uniform channel width results in more than a non-uniform deformation along the polymer. It actually drives the polymer to move in a direction perpendicular to the confinement. The driving force is entropic in essence, and it is revealed by a random walk model as $f_{\text{ent}} = -\nabla G$. The negative sign indicates that the force is driving the system to minimize its free energy. Including this force in the force balance analysis, we study the coupled deformation and motion of a piece of DNA in a non-uniform channel. The problem is governed by a second order PDE, whose solutions give the migration velocity and also the strain distribution along the polymer. DNA in different channel shapes are analyzed. A common feature is that large stress

gradient occurs where the channel width changes dramatically. Longer DNA migrates faster through a nanochannel with fluid flow while the persistence length seems to have little effect on the migration velocity. Transition from Odijk's to de Gennes' regimes can occur in a non-uniform channel and is shown to be delayed if the stress along the polymer is high.

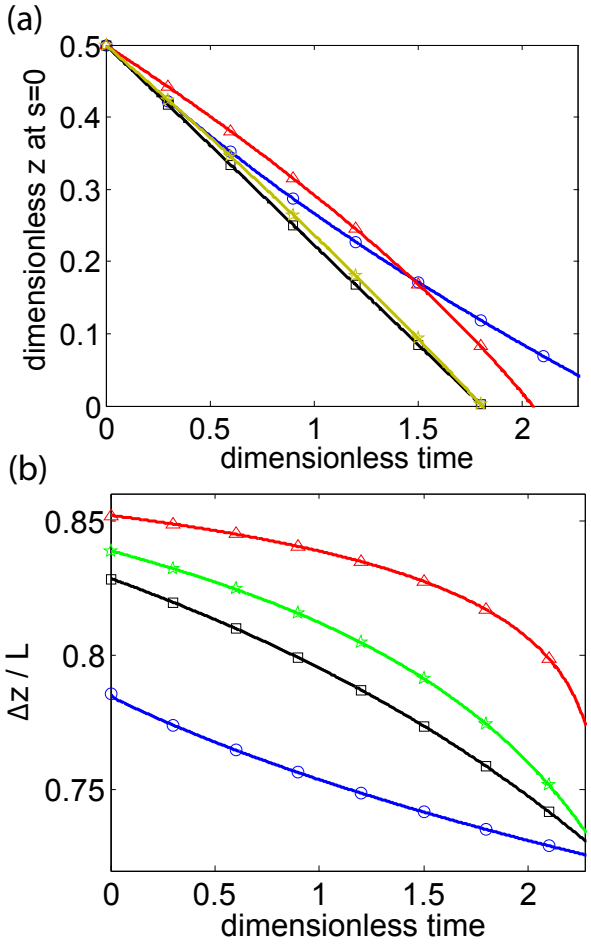

Figure 8.8: Migration of a piece of DNA in different types of nanochannels. The polymer is driven purely by entropic forces ($\bar{\mathcal{V}} = 0$). (a) $\bar{z}$ at $\bar{s} = 0$ versus dimensionless time. (b) Total stretch $\Delta z/L = [z(L) - z(0)]/L$ versus dimensionless time. Different lines are for different channel shapes $D(z)$. Blue circles: linear channel with $D(z) = az + b$. Red triangles: $D(z) = (az + b)^{-1/2}$. Black squares: $D(z) = (az + b)^{-2}$. Cyan stars: $D(z) = (az + b)^{-1}$. Here a and b are different constants for different channel types. For comparison, a and b for each channel type are chosen so that the entrance/exit widths of the four channels are the same.

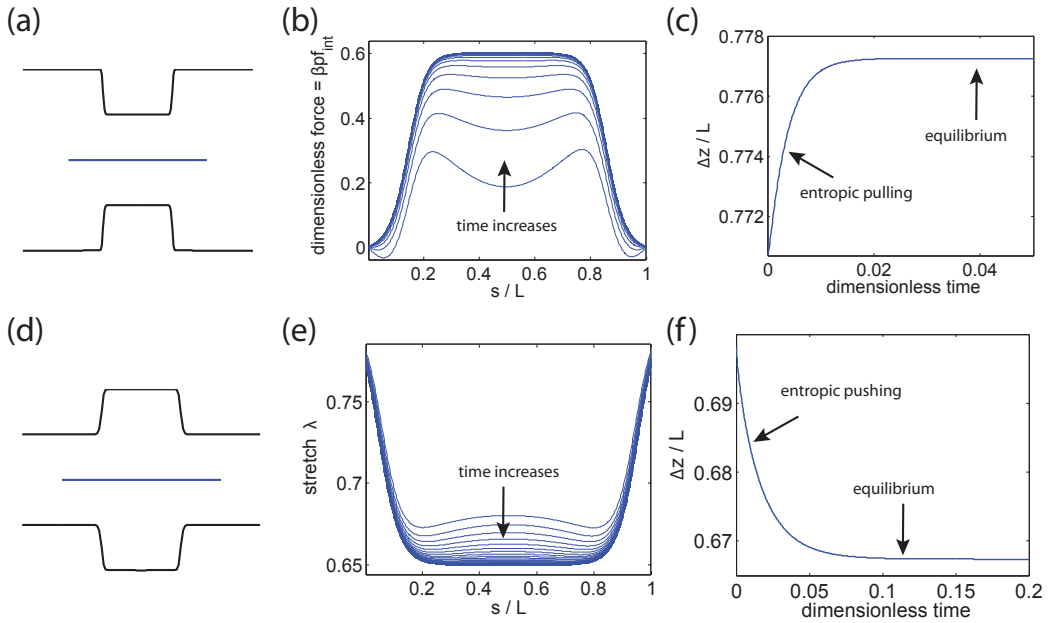

Figure 8.9: Motion and deformation of a piece of DNA in symmetric non-uniform channels without fluid flow or applied electric fields. (a–c): In the symmetric channel shown in (a), the initially stress-free polymer is pulled by a pair of entropic forces created by the channel. As a result, force and strain build up along the polymer backbone. In particular, large force gradient occurs at locations where the channel changes its shape most rapidly (b). The total extension of the polymer increases initially in response to the entropic pulling and then reaches equilibrium (c). (d–f): The symmetric channel shown in (d) creates a pair of entropic forces, which pushes the DNA inwards. In response, strain is developed along the polymer backbone (e). The total extension of the DNA decreases because of the pushing and then reaches equilibrium (f).

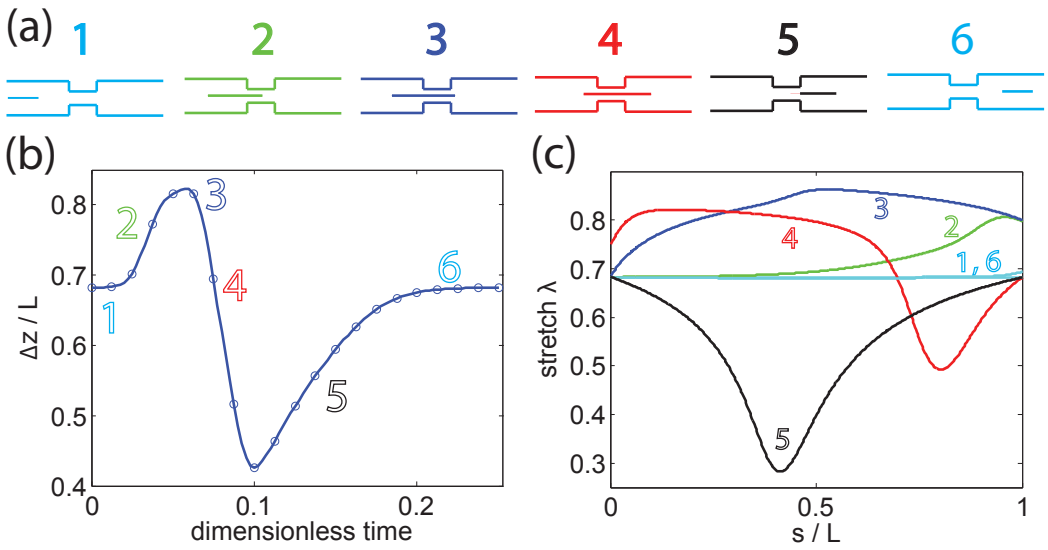

Figure 8.10: (a) A piece of DNA migrates along a non-uniform nano-channel with fluid flow $\bar{\mathcal{V}} > 0$. The numbers 1,2,3,4,5,6 represent snapshots in time. (b) Total stretch of the DNA increases as the polymer squeezes through the middle narrow region of the channel. (c) Two strain/stress gradients travel through the polymer backbone sequentially because there are two locations where the width of the channel varies rapidly.

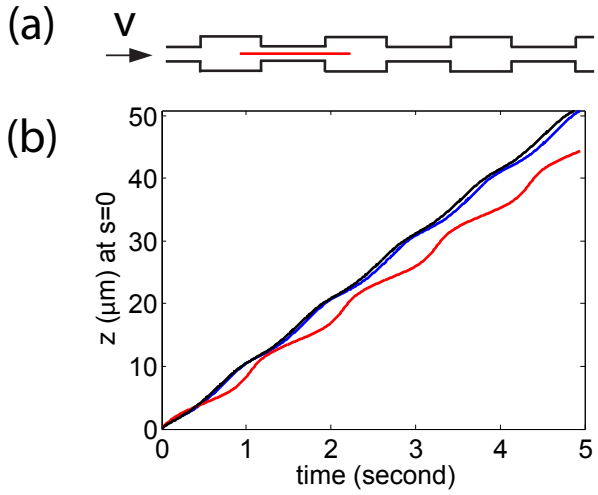

Figure 8.11: Migration of three different pieces of DNA in a periodic channel as shown in (a) (width in the wide/narrow region is $D = 50$nm and $D = 25$nm respectively, only one DNA molecule is shown). No electrical force is applied. Fluid in the channel flows to the right $v_{\text{fluid}} > 0$. (b) z at $s = 0$ versus time. Blue: $L = 8\mu$m, $p = 50$nm. Red: $L = 3\mu$m, $p = 50$nm. Black: $L = 8\mu$m, $p = 100$nm. At $t = 5s$, the long DNA (blue) and the short DNA (red) have been separated by 6.6 microns.

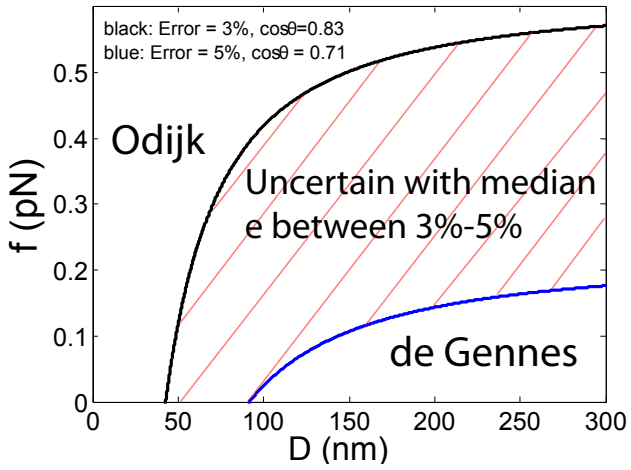

Figure 8.12: Transition between Odijk's and de Gennes' regimes. The two curves on the $f - D$ plane correspond to errors $e = 3\%$ (black), and 5% (blue) respectively. Region to the left of the curves is with less error. For the region with $e < 3\%$, we claim the polymer is in Odijk's regime. On the other hand, for the region with $e > 5\%$, the polymer is more likely to be in de Gennes' regime. We define 3%–5% as an uncertain zone, where transition between the two regimes occurs. The transition channel width is shown to increase with the increase of force.

Bibliography

[1] Q.F. Xia, K.J. Morton, R.H. Austin and S.Y. Chou, Nano. Lett. **8**, 3830 (2008).

[2] R. Riehn, M. Lu, Y. Wang, S.F. Lim, E.C. Cox, and R.H. Austin, P. Natl. Acad. Sci. USA. textbf102, 10012 (2005).

[3] N. Douville, D. Huh and S. Takayama, Anal. Bioanal. Chem. **391**, 2395 (2008).

[4] Y.M. Wang, J.O. Tegenfeldt, W. Reisner, R. Riehn, X. Guan, L. Guo, I. Golding, E.C. Cox, J. Sturm, and R.H. Austin, P. Natl. Acad. Sci. USA. **102**, 9796 (2005).

[5] P.G. de Gennes, *Scaling Concepts in Polymer Physics* (Cornell University Press, Ithaca, NY, 1979).

[6] T. Odijk, Macromolecules **16**, 1340 (1983).

[7] D.W. Schaefer, J.F. Joanny and P. Pincus, Macromolecules **13**, 1280 (1980).

[8] M. Daoud and P.G. Degennes, J. Phys. France **38**, 85 (1977).

[9] S. Jun, D. Thirumalai and B.Y. Ha, Phys. Rev. Lett. **101**, 138101 (2008).

[10] Y. Jung, S. Jun and B.Y. Ha, Phys. Rev. E Stat. Nonlinear Soft Matter Phys. 79, 061912 (2009).

[11] T.W. Burkhardt, J. Phys. A-Math. Gen. **28**, L629 (1995).

[12] J.B. Heng, A. Aksimentiev, C. Ho, P. Marks, Y.V. Grinkova, S. Sligar, K. Schulten and G. Timp, Nano. Lett. **5**, 1883 (2005).

[13] C.A. Merchant, K. Healy, M. Wanunu, V. Ray, N. Peterman, J. Bartel, M.D. Fischbein, K. Venta, Z. Luo, A.T.C Johnson and M. Drndic, Nano. Lett. **10**, 2915 (2010).

[14] J.T. Mannion, C.H. Reccius, J.D. Cross and H.G. Craighead, Biophys. J. **90**, 4538 (2006).

[15] M.M. Inamdar, W.M. Gelbart and R. Phillips, Biophys. J. **91**, 411 (2006).

[16] S.L. Levy, J.T. Mannion, J. Cheng, C.H. Reccius and H.G. Craighead, Nano Lett. **8**, 3839 (2008).

[17] J.P. Ebel, J.L. Anderson and D.C. Prieve, Langmuir. **4**, 396 (1988).

[18] P.O. Staffeld and J.A. Quinn, J. Colloid Interface Sci. **130**, 69 (1989).

[19] P.O. Staffeld and J.A. Quinn, J. Colloid Interface Sci. **130**, 88 (1989).

[20] T. Odijk, J. Chem. Phys. **125**, 204904 (2006).

[21] T. Su, S.K. Das, M. Xiao and P.K. Purohit, PLoS One, **6**, e16890 (2011).

[22] P. Nelson, *Biological physics: energy, information, life* (W. H. Freeman, NY, 2003).

[23] G. Sposito, *The chemistry of solids* (Oxford University Press, Oxford, UK, 1989)

[24] C. Brennen and H. Winet, Ann. Rev. Fluid Mech. **9**, 339 (1977).

[25] A.F. Voter, Introduction to the Kinetic Monte Carlo Simulation Method, in *Radiation effects in solids (NATO science series II: mathematics, physics and chemistry)* (Volume 235, 1-23, 2007).

[26] R. Raj and P.K. Purohit, Europhys. Lett. **91** 28003 (2010).

[27] D.F. Katz, J.R. Blake and S.L. Paveri-Fontana. J. Fluid Mech. **72** 529 (1975).

[28] C.W. Oseen, Neuere Methoden und Ergebnisse in der Hydrodynamik (Akademische Verlagsgesellschaft, Leipzig, 1927).

[29] E.R. Dufresne, D. Altman, and D.G. Grier, Europhys. Lett. **53**, 264 (2001).

[30] L. P. Faucheux and A. J. Libchaber, Phys. Rev. E **49**, 5158 (1994).

[31] B. Lin, J. Yu, and S. A. Rice, Phys. Rev. E **62**, 3909 (2000).

[32] J.F. Marko, E.D. Siggia, Macromolecules, **28**, 8759 (1995).

[33] D. Stigter, Biopolymers, **16**, 1435 (1977).

[34] P.E. Sottas, E. Larquet, A. Stasiak and J. Dubochet, Biophys. J. **77**, 1858 (1999).

[35] V.V. Rybenkov, N.R. Cozzarelli and A.V. Vologodskii, Proc. Natl. Acad. Sci. USA. **90**, 5307 (1993).

[36] J.W. Larson, G.R. Yantz, Q. Zhong, R. Charnas, C.M. D'Antoni, M.V. Gallo, K.A. Gillis, L.A. Neely, K.M. Phillips, G.G. Wong, S.R. Gullans and R. Gilmanshin, Lab Chip. **6**, 1187 (2006).

[37] S. Yip (Ed.), *Handbook of Materials Modeling* (Springer Science and Business Media, 2005).

[38] J. Wang and H. Gao, J. Mater. Sci. **42**, 8838 (2007).

[39] W.C.K. Poon and D. Andelman, *Soft Condensed Matter Physics in Molecular and Cell Biology* (CRC Press, Taylor & Fransic Group, Boca Ration, FL, 2006).

[40] J.W. Hatfield and S.R. Quake, Phys. Rev. Lett. **82**, 3548 (1999).

[41] J.T. Del Bonis-O'Donnell, W. Reisner and D. Stein, New. J. Phys. **11** 075032 (2009).

[42] R. Peters, Biochim. Biophys. Acta. **1793** 1533 (2009).

[43] M. Groll, M. Bochtler, H. Brandstetter, T. Clausen and R. Huber, Chembiochem **6** 222 (2005).

Part III

Statistical Mechanics of Filamentous Networks

Chapter 9

Entropic Elasticity of Fluctuating Filament Networks

Key concepts of this chapter:

1. We analyze the thermo-mechanical properties of a 2D filamentous network in this chapter. The static equilibrium state for the structure is determined first. Potential energy around the static equilibrium state is approximated to quadratic order, so that the network is locally characterized by a stiffness matrix. Using statistical mechanics and multidimensional Gaussian integral, we show that thermal fluctuation around the static equilibrium state is governed by the inverse of the stiffness matrix.

2. Buckling of filaments is common in deformation of filamentous networks. In this chapter, we introduce "imperfections" into the initial configurations of the filaments, so that we can follow the post-buckling path smoothly in our calculations. We show that, near the buckling point, the stiffness of the filamentous network is reduced, which leads to significant thermal fluctuations.

3. A network made up of linear elastic filaments always shows strain softening behavior under isotropic expansion, if no thermal fluctuations are taken into account. On the other hand, when we include thermal fluctuations into the solutions, the network shows strain stiffening behavior. This is because stretching out thermal fluctuations is a strain stiffening process.

4. Pure expansion, simple shear and uniaxial tension are applied on a hexagonal filamentous network. Taking thermal fluctuations into account, material properties of the network, such as, Young's modulus, shear and bulk moduli, and also Poisson's ratio are determined.

9.1 Introduction

In the previous chapters, our focus was on the properties and fluctuations of a single rod-like polymer. However, biofilaments in cells do not function in isolation. With some notable exceptions such as DNA, most filaments in cells are linked together as part of a network, which may extend throughout the interior of the cell [1]. For example, the nuclear lamina is a dense ($\sim$ 30 to 100 nm thick) fibrillar network inside the nucleus [2]. Besides providing mechanical support, this network is involved in most nuclear activities including DNA replication, RNA transcription, nuclear and chromatin organization, cell cycle regulation, cell development and differentiation, nuclear migration, and also apoptosis [3]. Understanding the mechanical response of these filamentous networks is important since many critical cellular processes are known to be mediated by mechanical stimuli. For the nuclear lamina network described above, researchers have shown that changes in the structural and mechanical properties of the lamina can cause diseases including the segmental premature aging disease Hutchinson-Gilford progeria syndrome (HGPS) [4]. Also, it has been found that the mechanical properties of the extracellular matrix, which is also a filamentous network, can determine the differentiation of stem cells [5]. In this chapter, we shall study the statistical mechanics of two-dimensional networks. The elastic behavior of such a network (assuming homogeneity) is a function of the right Cauchy-Green strain tensor $\mathbf{C}$ only. In two dimensions this tensor has three independent components. Hence, we need three independent tests to completely determine the elastic response of the network. For this reason we will study uniaxial tension, shear and pure dilatation of various types of two-dimensional networks.

Different theories have been proposed to study the constitutive relation of a network. Typically, a macroscopic deformation gradient is posed on the network first, displacement fields are determined and the filaments are deformed accordingly. The Helmholtz free energy of the individual filaments is calculated based on their uniaxial strain. The sum of these free energies is the strain energy (density) of the network, whose proper differentiation leads to the macroscopic stress, such as, the Piola-Kirchoff stress. Thus, the stress-strain relation is established [6, 7]. These theories assume that the filaments all deform according to the posed deformation gradient, and therefore the deformation is affine. Also, the Helmholtz free energy is taken from that of a single filament under tension and interactions between filaments are neglected. We will illustrate this method in the next section by applying affine deformations to a simple triangular network.

Filament networks are also widely studied in experiments and in numerical simulations. These studies show that typical networks stiffen at low strain [8]. Also, various studies show that, as one increases the density of the network, or the bending modulus of the filaments, a transition from non-affine deformation to affine deformation occurs [9, 10, 11, 12, 13, 14]. In affine deformation, the elastic energy of the network is mainly stored in form of the stretching

energy, while in non-affine deformation, the elastic energy is stored mostly as bending energy. It has also been shown that heterogeneity in a network, like adding stiff filaments in a soft network, can tune the cross-over between the two regimes [15]. In fact, most biofilament networks are heterogeneous, consisting of elements with very different mechanical properties (Fig. 9.1). Such heterogeneity in the network composition has not been adequately studied in the theoretical models in literature. The model to be proposed here is capable of handling any type of heterogeneity in a network. Some studies have also focused on the dynamic modulus of the network, which show that the mechanical properties of the network depend on the loading frequency [16]. Here we will confine ourselves to the study of equilibrium properties alone.

The thermo-mechanical properties of a network are determined by several factors. One factor is the properties of the individual filaments, which was our focus in the previous chapters. A second important factor is the cross-linking density of the network [17]. For a network with very high concentration of cross-linking proteins, the distance between cross-linked locations on filaments is short, thus the configuration space explored by the thermal fluctuations is small. As a result the entropic contribution to the free energy is small and the response is more enthalpic like a Hooke's law material. On the other hand, for a network with very low concentration of cross-linking proteins, deformations consist of localized bending of filaments rather than affine stretching deformations. Quantitative models that span the entire spectrum from entropic to enthalpic response are still in their infancy. One of the goals of this chapter is to systematically change the density of filaments, determine the mechanical response of the network, and see how it compares with experiments. Since we work in two dimensions we will assume that there is a cross-link at every intersection of filaments.

For a general set of load or displacement boundary conditions, individual filaments in a network can be under tension or compression. For filaments subjected to compression, buckling can occur when the compressive force reaches a critical value. For a hinged-hinged filament the well-known Euler buckling force [19] is:

$$F = \frac{\pi^2 EI}{L^2} = \frac{\pi^2 K_b}{L^2}, \tag{9.1}$$

where E is the Young's modulus of the elastic material, I is the moment of inertia of the cross section of the beam, $K_b = EI$ is the bending modulus and L is the length of the beam. For an F-actin filament, the persistence length is about $\xi_p \sim 12\mu$m [20]. Its contour length *in vivo* varies because the filaments are constantly gaining and losing monomers depending on the amount of free monomers present in cells. Typically, 370 monomers make a filament one micron in length. Using these numbers, the buckling force for the F-actin filament is about $F_b \sim 0.5$pN. In comparison, a single cytoskeletal filament can generate $\sim$ 1pN force as it polymerizes against a load [20, 21]. Also, a single molecule of myosin can contract with a force of $\sim$ 5pN [20, 22, 23]. Both these forces are large enough to trigger buckling if they are acting in compression

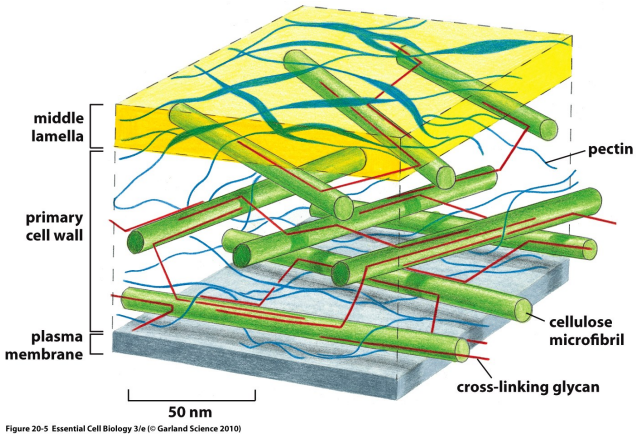

Figure 9.1: Illustration of the primary plant cell wall, which is a network consisting of various filaments with very different mechanical properties. The cellulose microfibrils are thick and provide tensile strength for the cell walls while the polysaccharide pectins, much smaller in the cross section dimensions, fill the spaces between the cellulose microfibrils and provide resistance to compression [18].

mode. Moreover, the contour length of 1μm used above is the typical value *in vivo*. *In vitro*, the length of an actin filament can reach $> 10\mu$m, which makes the critical buckling force even smaller, since $F \sim L^{-2}$. In this case, the individual F-actin filaments cannot carry any compressive load. We note, however, that microtubules are able to bear large compressive loads in living cells because of the lateral reinforcement from the contractile cytoskeleton [24]. This fact reinforces the importance of studying heterogeneous networks. But, first it is necessary to systematically understand what happens to individual filaments under compressive loads when thermal fluctuations are present. To include the buckling and post-buckling behaviors of filaments, one must use nonlinear theories and perform force and moment balances in the current configuration. Since we will use nonlinear theories of filaments, the energy is not quadratic globally and this allows us to follow the post-buckling path. Once we have understood the behavior of a single filament under compression we will extend the method discussed in the previous chapters to study the statistical mechanical properties of a network.

9.2 Expansion of a Triangular Network

We will apply the framework discussed in the previous chapters to investigate the properties of a general network in later sections, i.e, write down the energy of the network, calculate the partition function, free energy, and thermal fluctuation of the filaments, *etc.* Before doing so, we first use a simpler approach (assuming affine deformations) to discuss the expansion of a triangular network. The network is made up of only three inextensible wormlike chains,

as shown in Fig. 9.2. We would like to know its expansion behavior under hydrostatic tension p.

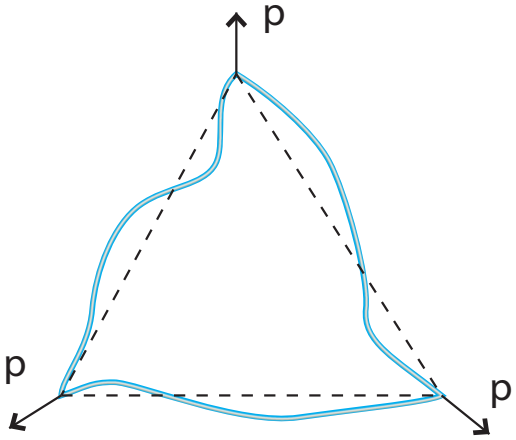

Figure 9.2: A triangular network made up of 3 wormlike chains.

In this section, we denote F, k_B, T, ξ, z, L as the force, Boltzmann constant, absolute temperature, persistence length, extension and contour length of the polymer respectively. The force-extension relation for a wormlike chain is:

$$\frac{F\xi}{k_BT} = \frac{z}{L} + \frac{1}{4\left(1 - z/L\right)^2} - \frac{1}{4}, \tag{9.2}$$

which gives the free energy $w(z) = \int_0^z F dz$ of the polymer as:

$$w(z) = \frac{k_BTL}{4\xi}\left[2\left(\frac{z}{L}\right)^2 - \left(\frac{z}{L}\right) - 1 + \frac{1}{1 - z/L}\right]. \tag{9.3}$$

We note that w is *not* the elastic energy, but instead, the Helmholtz free energy of a single wormlike chain.

The free energy of the triangular network under isotropic expansion pressure p can be written as:

$$W = \frac{k_BTL}{4\xi}\sum_{i=1}^{3}\left[2\left(\frac{z_i}{L}\right)^2 - \left(\frac{z_i}{L}\right) - 1 + \frac{1}{1 - z_i/L}\right] - pA(z_i). \tag{9.4}$$

where z_i is the extension of each polymer and A is the area of the triangle. Eq. 9.4 is an approximation, since it neglects the contribution of the expansion on the entropy of the single filaments. Minimizing W gives the average z_i under temperature T. Since the loading and geometry are both symmetric, we simplify the free energy to:

$$W = \frac{3k_BTL}{4\xi}\left[2\left(\frac{d}{L}\right)^2 - \left(\frac{d}{L}\right) - 1 + \frac{1}{1 - d/L}\right] - pA(d), \tag{9.5}$$

where $d = z_1 = z_2 = z_3$. Now define the dimensionless free energy $\bar{W}$, dimensionless pressure $\bar{p}$ and dimensionless length $\bar{d} = d/L$:

$$\bar{W} = \frac{W}{3k_BTL/4\xi}, \quad \bar{p} = \frac{\sqrt{3}p\xi L}{3k_BT}, \quad \bar{d} = \frac{d}{L}, \tag{9.6}$$

After substituting for $A(d)$ eq. 9.5 can be rewritten as:

$$\bar{W} = (2 - \bar{p})\bar{d}^2 - \bar{d} - 1 + \frac{1}{1 - \bar{d}}. \tag{9.7}$$

Since $\bar{d} < 1$, we can expand the last term rigorously and get:

$$\bar{W} = (3 - \bar{p})\bar{d}^2 + \bar{d}^3 + \bar{d}^4 + \sum_{i=5}^{+\infty} \bar{d}^i. \tag{9.8}$$

When $\bar{p} \leq 3$, the only solution within $\bar{d} \in [0, 1]$ is $\bar{d} = 0$. So the average area $\langle A \rangle = 0$. This tells us that the network cannot be expanded for small pressure. The critical pressure of $\bar{p} = 3$ corresponds to:

$$p = \frac{9k_BT}{\sqrt{3}\xi_p L}. \tag{9.9}$$

When $\bar{p} \geq 3$, the non-zero solution is:

$$\bar{d} = \frac{4\bar{p} - 9 - \sqrt{8\bar{p} - 15}}{4\bar{p} - 8}, \tag{9.10}$$

and the average dimensionless area is $\langle \bar{A} \rangle = \bar{d}^2$. Below, we discuss the expansion of the network at $\bar{p}$ slightly larger than 3, and much larger than 3. In the small pressure limit ($\bar{p} - 3 << 1$), Eq. 9.10 becomes:

$$\bar{d} = \frac{2}{3}(\bar{p} - 3) - \frac{16}{27}(\bar{p} - 3)^2 + O\left((\bar{p} - 3)^3\right). \tag{9.11}$$

The average area of the triangle in this small pressure limit is:

$$\langle \bar{A} \rangle = \frac{4}{9}(\bar{p} - 3)^2 \tag{9.12}$$

In the large pressure limit ($\bar{p} >> 1$), eq. 9.10 becomes:

$$\bar{d} = 1 - \frac{1}{2}\sqrt{\frac{3}{\bar{p}}}. \tag{9.13}$$

The average area of the triangle is:

$$\langle \bar{A} \rangle = \left(1 - \frac{1}{2}\sqrt{\frac{3}{\bar{p}}}\right)^2. \tag{9.14}$$

The full pressure versus average area relation is shown in Fig. 9.3. This approach assumes affine deformations and is good for this special case where we study pure dilatations. In general the deformations do not have to be affine and we have to consider more sophisticated methods.

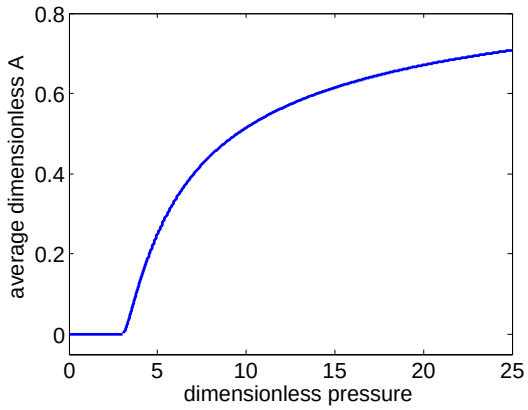

Figure 9.3: Expansion of a triangular network made up of 3 wormlike chains. There is a phase transition at $\bar{p} = 3$.

9.3 Entropic Elasticity of a General 2D Network – Theory

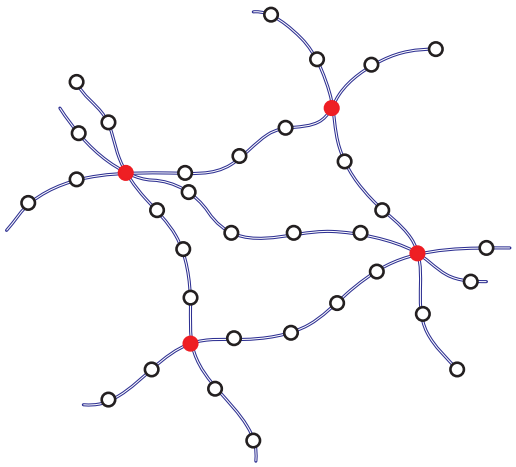

Figure 9.4: Illustration of a discrete fluctuating filament network.

We now apply the framework in the previous chapters to study the thermomechanical properties of a 2D network. We first discretize each filament in the network into segments (Fig. 9.4). The filaments are extensible and can be stretched, bent and rotated, so that the deformed state of each discrete segment is characterized by its axial strain ϵ and its rotation angle θ with respect to its reference orientation. If there are no constraints on the configuration of the network, a system with N discrete segments will have $2N$ degrees of freedom. We denote these as the generalized coordinates q_i, and the generalized force conjugate to q_i as p_i, so that the energy of the network-load system can be written as $E = E(q_i, p_i)$. Here the system is conservative and the energy E

includes both the elastic energy and the potential energy due to generalized forces acting on the network.

The elastic energy of a filament is:

$$E_{\text{elastic}} = \int_0^L \frac{K_s}{2}\epsilon^2 ds + \int_0^L \frac{K_b}{2}\dot{\theta}^2 ds \tag{9.15}$$

$$= \sum_i^N \frac{K_s l_0}{2}\epsilon_i^2 + \sum_i^{N-1} \frac{K_b}{2l_0}\left(\theta_{i+1} - \theta_i\right)^2. \tag{9.16}$$

where K_s, K_b are the stretching and bending moduli respectively. The second expression is a discrete version of the energy and the summation is over the N segments along the filament. On the other hand, the potential energy caused by a point force $\vec{F}$ on a node is:

$$E_{\text{force}} = -\vec{F}\cdot\vec{r}, \tag{9.17}$$

where $\vec{r}$ is the position vector of the node. It is a function of the general coordinates $\vec{r} = \vec{r}(q_i)$. The potential energy caused by live pressure, or hydrostatic tension p is:

$$E_{\text{pressure}} = -pA(q_i), \tag{9.18}$$

where A is the area of the network as a function of q_i. In the end, the energy E is a function of q_i and p_i. This section tries to answer the following two questions: (1) Given the loading p_i, what is the equilibrium static configuration q_i? (2) Given the equilibrium state q_i under loads p_i, what is the fluctuation around this equilibrium state?

9.3.1 Stable equilibrium states

To answer the first question, we note that an equilibrium state is one that satisfies:

$$\frac{\partial E}{\partial q_i} = 0. \tag{9.19}$$

In order that the equilibrium state is stable, the stiffness matrix $[\mathbf{K}]_{ij} = \partial^2 E/\partial q_i \partial q_j$ must be positive definite. In particular, $\det \mathbf{K} > 0$ is a necessary condition. Now, for a problem involving instabilities and buckling, the energy usually involves terms higher than quadratic order. Therefore, Eq. 9.19 are not linear equations. Here we will solve Eq. 9.19 incrementally, as discussed below.

Suppose (q_i, p_i) is a known equilibrium state, we would like to compute a new equilibrium state $(q_i + \delta q_i, p_i + \delta p_i)$, where δp_i are given small quantities and δq_i are desired. Usually, the load-free equilibrium state at $p_i = 0$ is known and can serve as the initial state for the computation. To compute δq_i, we note that since $(q_i + \delta q_i, p_i + \delta p_i)$ is an equilibrium state, we have:

$$\left.\frac{\partial E}{\partial q_i}\right|_{(q_i+\delta q_i, p_i+\delta p_i)} = 0. \tag{9.20}$$

These non-linear equations can be solved using the Newton−Raphson method. We use $(q_i, p_i + \delta p_i)$ as the initial values and repeat the following scheme until the solution converges:

$$\left.\frac{\partial E}{\partial q_i}\right|_{(q_i, p_i+\delta p_i)} + \left.\frac{\partial^2 E}{\partial q_i \partial q_j}\right|_{(q_i, p_i+\delta p_i)} \delta q_j = 0. \tag{9.21}$$

Note that both the derivatives in the above equations are evaluated at the current configuration and $p_i + \delta p_i$.

By increasing the loads step by step from $p_i = 0$, we know the equilibrium state (q_i, p_i). However, the computational scheme discussed above does not guarantee that the obtained equilibrium state is stable. For example, if we start with a straight filament and apply a compressive force on it, the scheme will always lead to straight compressed configurations, no matter how large the compressive force is. The straight configuration is stable at small force, but unstable at a force that is large enough to trigger a buckling. Unstable configurations are not desirable because (1) a real system never goes into the unstable regime, especially when thermal fluctuations and perturbations are significant, and (2) an unstable system has a negative $\det \mathbf{K}$, which will cause the partition function and fluctuation of the system to diverge, as we will see later.

To avoid unstable configurations, we perturb the initial state of the filaments and start with curved configurations. The motivation to do so is that in most biofilament networks, thermal fluctuation causes the filaments to be in curved states. Beginning with the curved configurations, the computed equilibrium state smoothly follows one of the stable bifurcation buckling paths, avoiding both the singularities at the buckling point, and the unstable regime after the buckling point. The effects of initial curved configurations, or so-called "imperfections", are well-known in structural mechanics. The sensitivity of the stability of a structure to the initial imperfection is crucial [19].

As an example, consider a hinged-hinged rod under compression. As has been mentioned above, without initial perturbation, the computational scheme leads to unstable straight configurations. With small perturbation on the initial straight state, we obtain the correct post-buckling configurations as shown in Fig. 9.5. The problem of rod buckling is mathematically identical to the problem of large oscillations of a pendulum and the solutions are well known [19]. To make sure that we obtain the correct post-buckling behavior, we compare our computational results with these known solutions. In Fig. 9.6, we show (1) the tangent angle at the end of the rod $\theta_0 = \theta(s = 0)$, (2) deflection at the middle of the rod, and (3) end-to-end distance of the rod, all as functions of the compressive force. Our computational scheme correctly reproduces the known stable solutions before and after buckling occurs. Note that all the plots show a sharp rise once buckling occurs. This indicates that after buckling, the filament deforms a lot while the compressive force remains almost a constant [19]. We also note that these plots give only the static results without taking

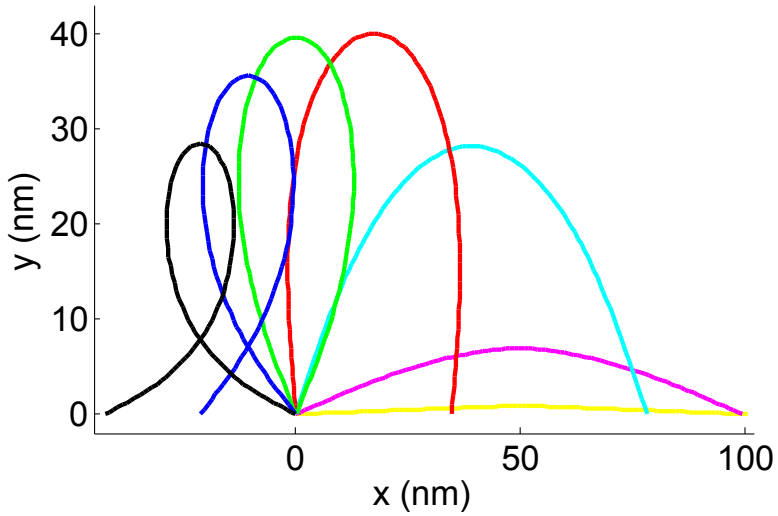

Figure 9.5: Configuration of a hinged-hinged buckled rod. The rod is under uniaxial compression. If we start with a perfectly straight rod, the computational scheme always leads to a straight configuration, which is unstable when the compressive force is large. With initial perturbation, however, we obtain the correct post-buckling configurations, as shown in the figure.

into account the thermal fluctuations. The effects of thermal fluctuations are summarized in the next section.

9.3.2 Thermal fluctuations around the static state

In the previous subsection, we discussed how to obtain the static configuration of a network (or a filament) without going into the unstable regime. Now we investigate the thermal fluctuation around the static stable configurations. In this section, we denote the static configuration using a subscript m, as it corresponds to an energy minimum. Around the static state, the energy can

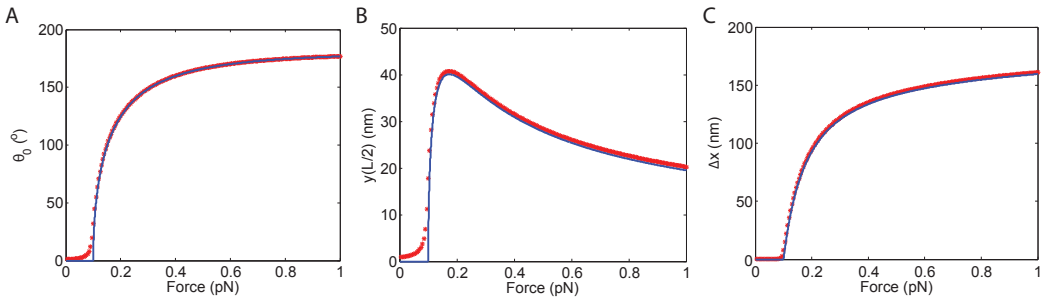

Figure 9.6: Buckling of a hinged-hinged rod. (A) Tangent angle at $s = 0$, (B) Deflection at the middle of the rod, and (C) $\Delta x = L - x(L)$ as a function of the compressive force. Blue: exact solution. Red: Computational results.

be approximated as quadratic:

$$E = E_m + \frac{1}{2}\vec{\Delta q}^{\,T}\mathbf{K}\cdot\vec{\Delta q}, \tag{9.22}$$

where $\Delta q = q - q_m$ is the deviation from the static configuration. Thermal fluctuations and correlations of the generalized coordinates satisfy Boltzmann statistics (muti-dimensional Gaussian distribution). They are given by:

$$\langle \Delta q_i \rangle = 0, \tag{9.23}$$

$$\langle \Delta q_i \Delta q_j \rangle = k_B T \left[\mathbf{K}\right]^{-1}_{ij}. \tag{9.24}$$

Now consider a quantity A that depends on the generalized coordinates: $A = A(q_1, \cdots q_N)$. For example, A can be the area of a network, or the end-to-end extension of a filament, *etc.* Assuming small fluctuations, the thermal average of A is:

$$\begin{aligned}
\langle A \rangle &= \langle A(q_i) \rangle & (9.25)\\
&= \left\langle A(q_i^m) + \frac{\partial A}{\partial q_i}\Delta q_i + \frac{1}{2}\frac{\partial^2 A}{\partial q_i \partial q_j}\Delta q_i \Delta q_j \right\rangle & (9.26)\\
&= A_m + \frac{1}{2}\frac{\partial^2 A}{\partial q_i \partial q_j}\langle \Delta q_i \Delta q_j \rangle. & (9.27)
\end{aligned}$$

We see that thermal average of a quantity $\langle A \rangle$ is in general different from the static value A_m, as long as $\partial^2 A/\partial q_i \partial q_j \neq 0$. This means the fluctuation is not symmetric around the static values for those quantities.

Before investigating the properties of a network, we first apply the framework described above to the extension and compression of a single filament. The thermal average of the end-to-end extension of the filament is computed under different tensile loadings. The result is shown in Fig. 9.7. The result from the computation matches exactly with the analytic solution for an extensible wormlike chain:

$$\langle x \rangle = L + \frac{FL}{K_s} - \frac{k_B T}{4\sqrt{K_b F}}\left[\coth\left(L\sqrt{\frac{F}{K_b}}\right) - \frac{1}{L}\sqrt{\frac{K_b}{F}}\right]. \tag{9.28}$$

Results for compressing a single filament are shown in Fig. 9.8. Small perturbations are applied to the initially straight rod, so that the static configuration transitions smoothly to the post-buckling path. The role of thermal fluctuation is non-trivial – the solid line and the dashed line cross each other on the plot. Around the buckling point the stiffness suddenly decreases, but after transition to the post-buckling path, the rod regains stability. For small forces, the thermal fluctuations cause the end-to-end distance of the rod to be less than that in the purely static configuration, but at larger forces the thermal fluctuations cause the end-to-end distance to be more than that in the purely static configuration. This result agrees with a current study on the role of thermal fluctuation on a buckled rod [27].

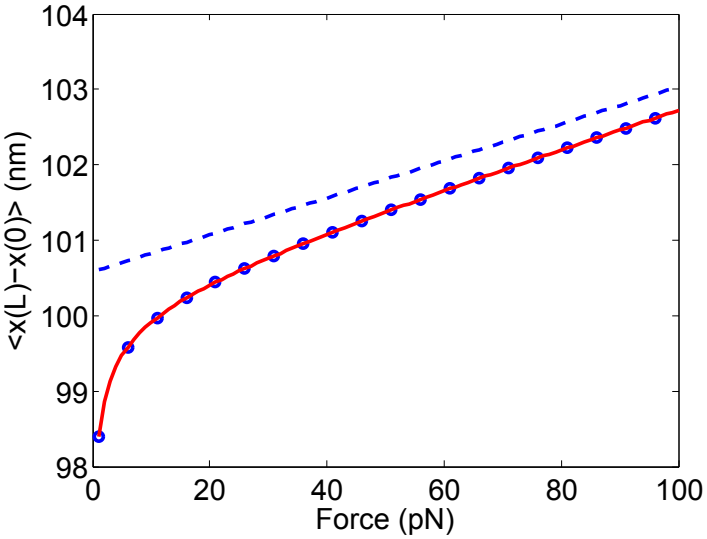

Figure 9.7: Extension a hinged-hinged rod. Blue dashed line: without thermal fluctuation. Blue circles: with thermal fluctuation. Red: analytic solution.

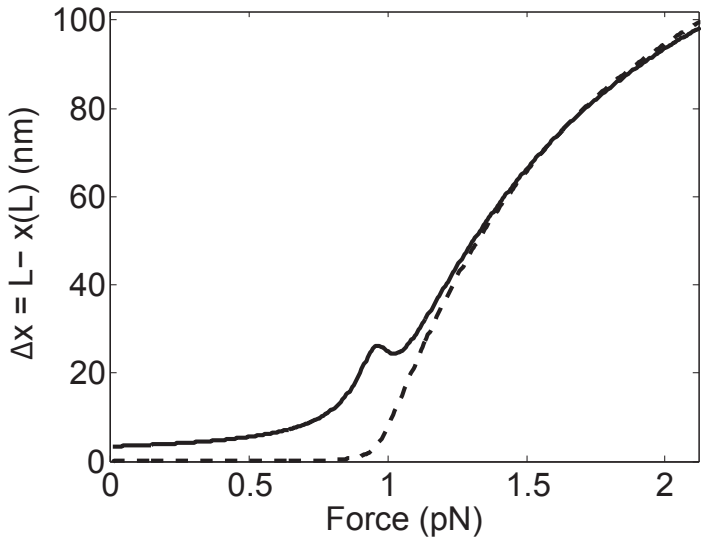

Figure 9.8: Compression of a hinged-hinged rod. Dashed line: without thermal fluctuation. Solid line: with thermal fluctuation. Small perturbations are applied to the initial configuration of the rod.

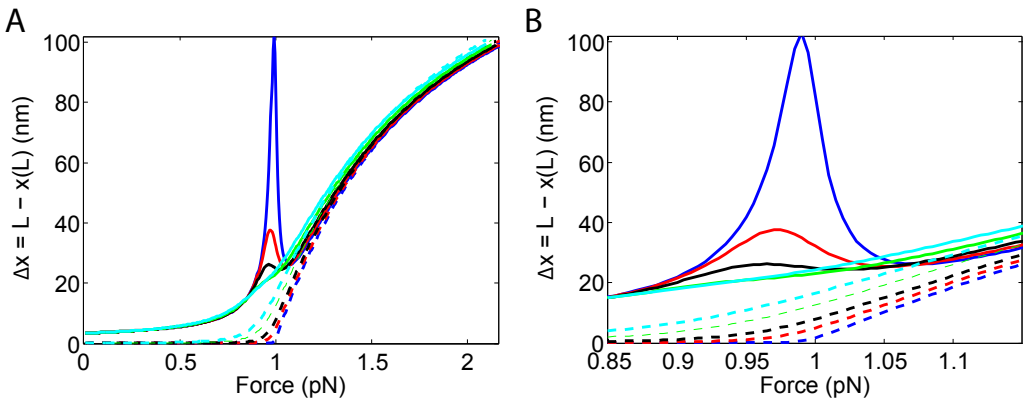

Figure 9.9: Influence of the initial imperfection. When the imperfection is small, the path is closer to the singularity and a large peak shows in the force-extension curve. When there is no imperfection, the curve will go to infinitely. When the imperfection is large, the path is further away from the singularity and the curve transition smoothly to the post-buckling regime. (B) is the enlarged figure of (A) around the peak. Blue: 0.1°. Red: 0.5°. Black: 1.0°. Green: 2.0°. Cyan: 3.0°.

The peak in Fig. 9.8 is caused by the instability around the buckling point. It strongly depends on the amount of imperfection in the initial configuration (see Fig. 9.9). When the imperfection is small, the path is closer to the singularity so the peak is large. When the imperfection is large, the path is further away from the singularity so the transition is smoother. If the filament is fluctuating due to thermal motion we expect the initial configurations to be bent so that the overall response would look smooth.

The force-extension curve for a compressed filament depends on the material properties as shown in Fig. 9.10. Increasing the bending modulus shifts the instability peak to the right and at the same time smoothens the peak. On the other hand, increasing the stretching modulus shifts the instability peak to the left. But, the force-extension curve is much more sensitive to a change in the the bending modulus than a change in the stretching modulus. We had to decrease the stretching modulus by ~ 100 folds to see a different response in the force-extension curve, while changing the bending modulus by 2 fold is enough to change the curve dramatically (see Fig. 9.10).

Lastly, the force-extension curve for a compressed filament depends on the boundary conditions. For example, a clamped-clamped boundary condition leads to a buckling force 4 times that of the hinged-hinged filament. To account for this kind of effects, we put a rotational spring of stiffness k_θ at the two ends of the filament and show the results for different k_θ in Fig. 9.11. As expected, when $k_\theta \to \infty$, the rod buckles at 4pN which is 4 times the load required for buckling a hinged-hinged filament in the earlier plots. Increasing the stiffness of the rotational spring shifts the force-extension curve to the right.

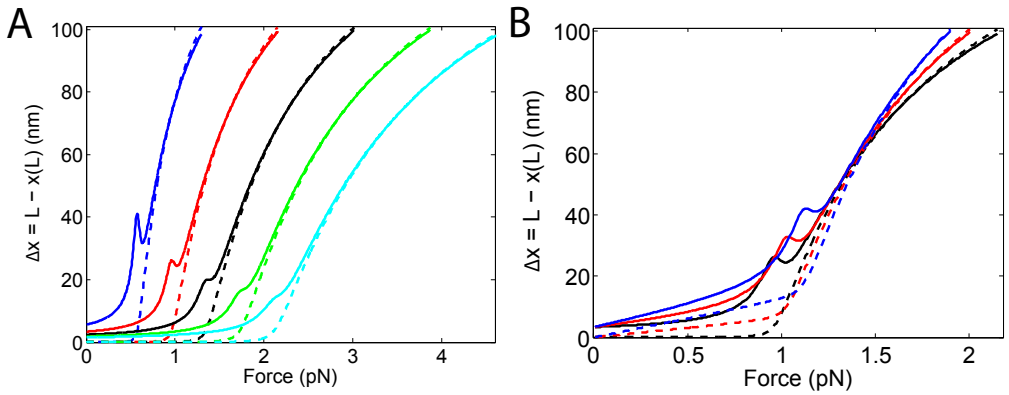

Figure 9.10: Influence of the material properties on the compression behavior. (A) Force-extension curve for different bending modulus K_b. Increasing the bending modulus shift the peak to the right and decreases the intensity of the peak. Blue: $K_b = 150k_BT \cdot nm$. Red: $K_b = 250k_BT \cdot nm$. Black: $K_b = 350k_BT \cdot nm$. Green: $K_b = 450k_BT \cdot nm$. Cyan: $K_b = 550k_BT \cdot nm$. (B) Force-extension curve for different stretching modulus K_s. Increasing the bending modulus shift the peak to the left. Blue: $K_s = 2.0k_BT/nm$. Red: $K_b = 4.0k_BT/nm$. Black: $K_b = 1000k_BT \cdot nm$. The force-extension behavior of a single filament is more sensitive to a change in the bending modulus than a change in the stretching modulus.

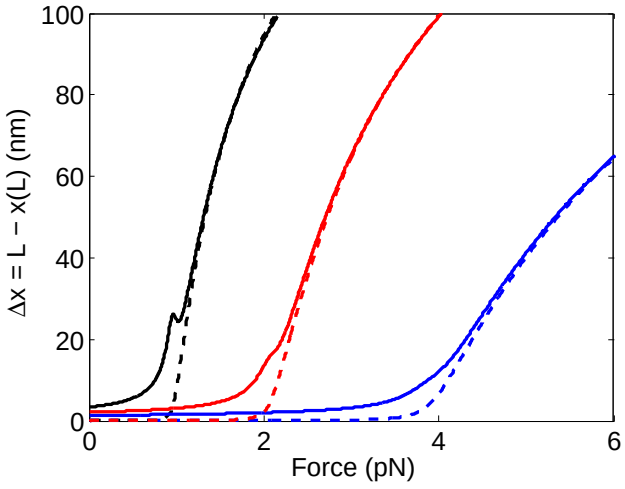

Figure 9.11: Influence of the boundary conditions on the compression behavior. Rotational springs are added to the two ends of the rod. When the stiffness of the spring becomes infinity, the rod is under clamped-clamped conditions. Black: $K_\theta = 0.0k_BT$. Red: $K_\theta = 10.0k_BT$. Black: $K_\theta = 1000.0k_BT$. The clamped-clamped rod buckles at $F = 4$pN, as expected.

9.4 Entropic Elasticity of a Hexagon

Now, that we fully understand the behavior of a single filament, we move on to simple two-dimensional networks. We first consider a single hexagon and apply hydrostatic edge tension (constant in value and normal to the local tangent), simple shear and uniaxial tension on it.

9.4.1 Hydrostatic edge tension on a hexagon

Many soft biopolymer gels, such as, fibrin gels, become stiffer when deformed [28]. This is a mechanism to protect the materials from large deformations [29]. In this subsection, we argue that, for a network *linear elastic* filaments, thermal fluctuations play a crucial role in its strain stiffening behavior. Without thermal fluctuations and under hydrostatic edge tension, the network shows strain softening behavior instead.

First, we analyze the static expansion behavior of a network without thermal fluctuations. Assume the filaments inside a network are uniformly distributed (which is true for a hexagon), so that under hydrostatic edge tension, the boundary of the network deforms almost like a circle (Fig. 9.12A). This boundary circle is characterized by its radius r, with reference value (undeformed configuration) r_0 at zero hydrostatic tension. Bending energy of the boundary circle is:

$$E_b = \int_0^{L_0} \frac{K_b}{2} \left(\frac{\partial^2 \vec{r}}{\partial s_0^2} \right)^2 ds_0 = \frac{K_b \pi}{r_0}. \tag{9.29}$$

Here $L_0 = 2\pi r_0$ is the reference perimeter of the circle, $s_0 \in [0, L_0]$ is the reference arc length, and $\vec{r}$ is the position vector. Note that in Eq. 9.29, the "curvature" is calculated as the second derivative with respect to the reference arc length s_0. Eq. 9.29 shows that isotropic expansion of a circular ring does not change its bending energy, because under such deformation, there is no change in the tangent angles for all material points. This suggests that, during pure dilatation deformation, elastic energy is stored in the form of stretching energy. In particular, it is the sum of the stretching energies of the boundary filaments and the interior filaments:

$$E_s = \int_0^{L_0} \frac{K_s}{2} \epsilon^2 ds_0 + \frac{n K_s}{2} \epsilon^2 (2r_0) = (\pi + n) K_s r_0 \left(\frac{r}{r_0} - 1 \right)^2. \tag{9.30}$$

Here n is the number of interior filaments inside the network (see Fig. 9.12A for an example of $n = 6$). Including the potential energy of the hydrostatic edge tension p, the total potential energy of the network is:

$$E = (\pi + n) K_s r_0 \left(\frac{r}{r_0} - 1 \right)^2 - p\pi r^2, \tag{9.31}$$

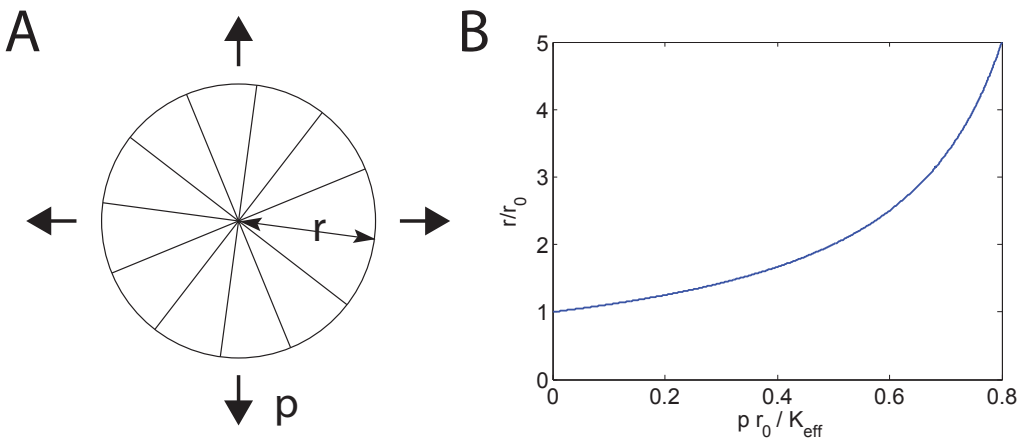

Figure 9.12: (A) Hydrostatic edge tension on a filament ring with $n = 6$ interior filaments. (B) If we assume linear elasticity and do not consider thermal fluctuations, the network always becomes softer at larger hydrostatic tension.

where the constant contribution from the bending energy is neglected. The static configuration of the network can be evaluated by $\partial E/\partial r = 0$, which leads to:

$$\frac{r}{r_0} = \frac{1}{1 - pr_0/K_{\text{eff}}}, \tag{9.32}$$

where the effective stiffness $K_{\text{eff}} = (1+n/\pi)K_s$ depends on both the stretching modulus of the filaments and the number of interior filaments n in the network. A plot of Eq. 9.32 is shown in Fig. 9.12B, the network shows strain softening behavior. Furthermore, from Eq. 9.32, we can compute the static bulk modulus of the hexagon as follows:

$$K_{\text{bulk}} = A\frac{dp}{dA} = \frac{K_{\text{eff}}}{2r}. \tag{9.33}$$

Here $A = \pi r^2$ is the area of the network. The fact that $K_{\text{bulk}} \sim r^{-1}$ again suggests that the network softens as we expand it. Also, since $K_{\text{eff}} = (1 + n/\pi)K_s$, Eq. 9.33 suggests that the bulk modulus depends linearly on the filament density $\rho_0 = n/A_0$, with A_0 being the initial area of the network. The initial static bulk modulus can be computed by setting $r = r_0$ in Eq. 9.33. For a network of filaments with $K_s = 10k_BT/nm$ and $r_0 = 20$nm, we have $K_{\text{bulk, initial}} = 2\text{pN/nm}$.

We note that the strain softening behavior discussed above comes from an analysis that does not take the effects of thermal fluctuations into account. Stretching out fluctuations, on the other hand, is a stiffening process, especially when K_s and n are large. Therefore, if a network (in its linear elastic regime) shows strain stiffening effect during pure dilatation, we argue that it is thermal fluctuations that play a crucial role. Below, we analyze the effects of thermal fluctuation quantitatively.

Suppose the number of interior filaments is large, so that we can neglect the boundary filaments. Then under hydrostatic tension p, each interior filament is subjected to a force $F = p(2\pi r)/n$, where r and n are again the radius of the network and the number of interior filaments respectively (Fig. 9.12A). Then, using the 2D wormlike chain model for each interior filament, we have:

$$\frac{2\pi r \xi_p}{k_B T n} p = \frac{3r}{4L} + \frac{1}{8\left(1 - r/L\right)^2} - \frac{1}{8}, \tag{9.34}$$

which, if we define $\lambda = r/L$, reduces to:

$$\frac{2\pi \xi_p L}{k_B T n} p = \frac{3}{4} + \frac{1}{8\lambda(1-\lambda)^2} - \frac{1}{8\lambda}. \tag{9.35}$$

Interestingly, at the low pressure limit, this relation reduces to:

$$p = \frac{k_B T n}{2\pi \xi_p L}\left(1 + \frac{3}{8}\lambda\right), \tag{9.36}$$

which again suggests that a finite (non-zero) hydrostatic tension $p_{\text{critical}} = k_B T n/(2\pi\xi_p L)$ is needed to expand the network (critical p at $\lambda = 0$). This result is similar to Eq. 9.9. On the other hand, at high p, the result is:

$$\frac{\pi \xi_p L}{k_B T n} p \approx \frac{1}{8\lambda(1-\lambda)^2}. \tag{9.37}$$

The result of Eq. 9.35 is shown in Fig. 9.13A. Note that we have strain stiffening effect in this simple model. In particular, the bulk modulus is:

$$K_{\text{bulk}} = A\frac{dp}{dA} = \frac{k_B T n}{8\pi \xi_p L} \cdot \frac{\lambda(3-\lambda)}{1-\lambda}. \tag{9.38}$$

Fig. 9.13B shows K_{bulk} as an increasing function of the λ.

For a single hexagon, the number of interior filament is $n = 3$. Neglecting the boundary filaments is not a valid assumption. Therefore, we use the theoretical framework described in the previous section to calculate the expansion behavior that includes the thermal fluctuations below. Fig. 9.14A shows the static configurations of a hexagon under pure dilatation. The contour length and persistence length of the filaments are $L = 20$nm and $\xi_p = 10$nm respectively. Stretching modulus of the filaments is $K_s = 10 k_B T/nm$. We observe that the hexagon first deforms into a circular shape, then expands (almost) isotropically. Fig. 9.14B shows the static configurations of a hexagon with larger stretching modulus $K_s = 100 k_B T/nm$.

Fig. 9.15A shows the area versus hydrostatic tension relation for the hexagon with $K_s = 10 k_B T/nm$. Dashed line is the static relation without thermal fluctuations. The solution agrees almost exactly with Eq. 9.32 except at low hydrostatic tension. The reason is that when p is small, the deformation process is not the expansion of a ring, instead, it is a deformation from a hexagon

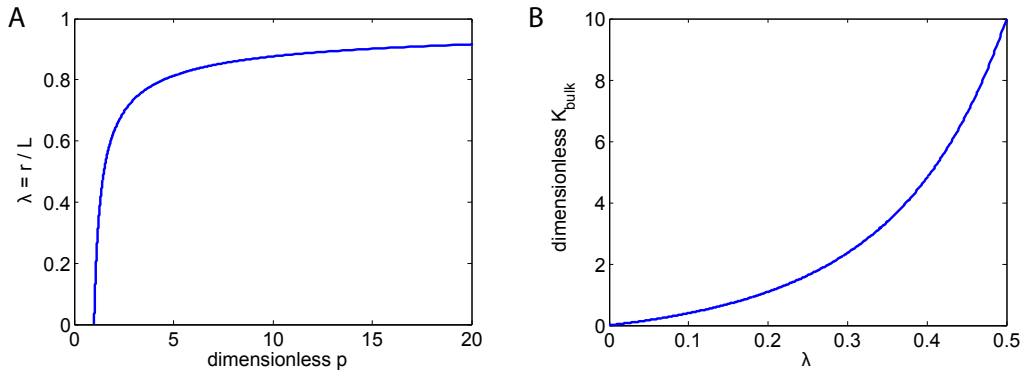

Figure 9.13: (A) Plot of Eq. 9.35. The size of the network versus the dimensionless hydrostatic tension $\bar{p} = \beta\pi\xi_p Lp/n$. (B) Plot of Eq. 9.38. The dimensionless bulk modulus is defined as $K_{\text{bulk}} \cdot (8\pi\xi_p L/(k_B T n))$.

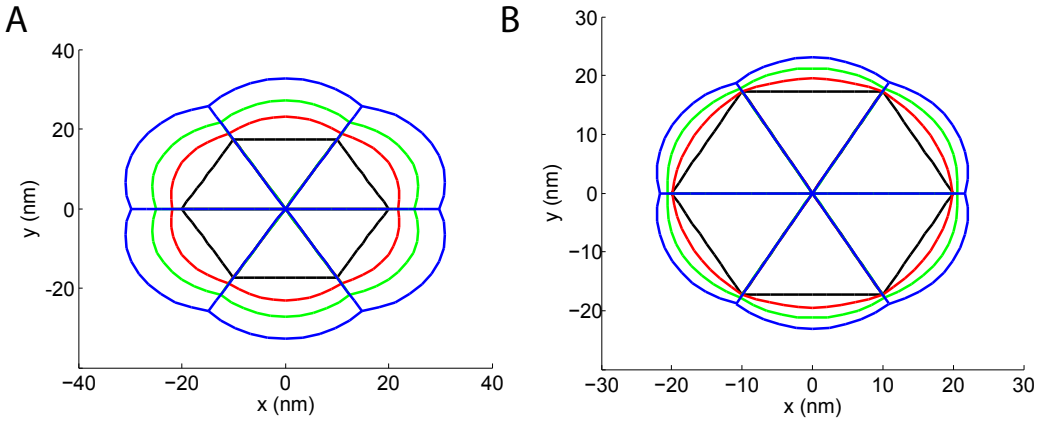

Figure 9.14: Expansion of two hexagons under hydrostatic tension. Each filament is 20nm long. Their persistence length is 10nm. (A) Stretching modulus is $10k_BT/nm$. Black: undeformed configuration. Red: deformed configuration under $p = 0.5$pN/nm. Green: deformed configuration under $p = 1.0$pN/nm. Blue: deformed configuration under $p = 1.5$pN/nm. (B) Stretching modulus is $100.0k_BT/nm$. Black: undeformed configuration. Red: deformed configuration under $p = 0.5$pN/nm. Green: deformed configuration under $p = 2.5$pN/nm. Blue: deformed configuration under $p = 5$pN/nm.

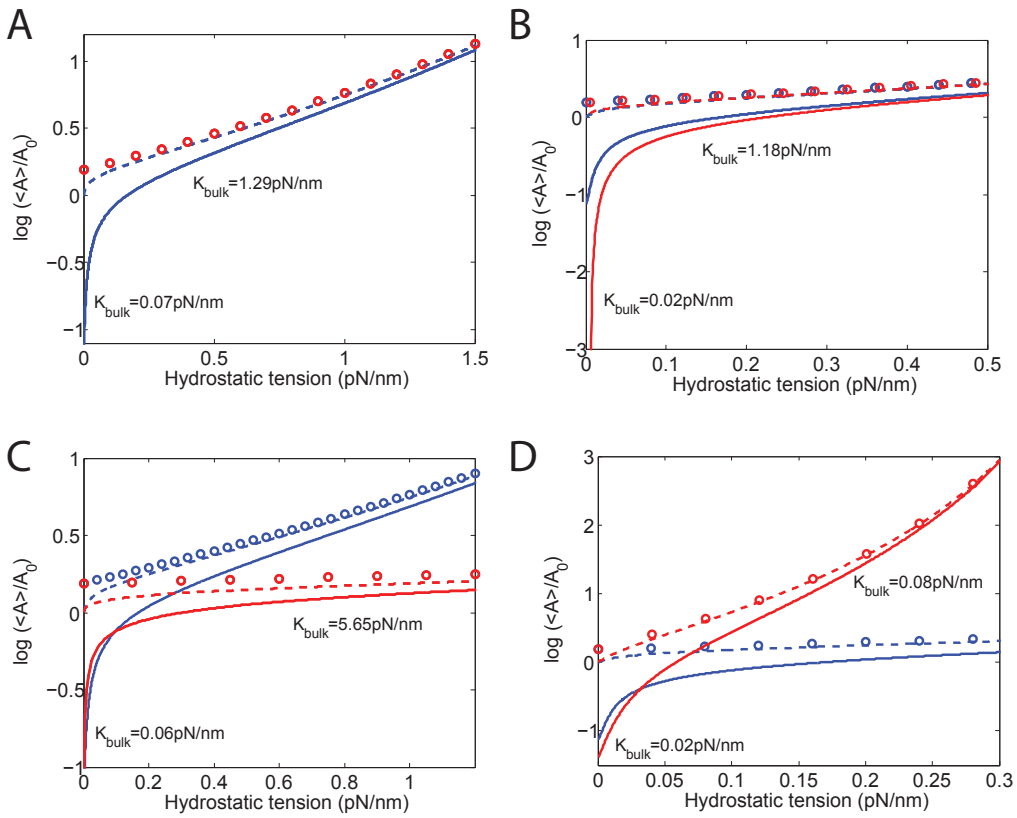

Figure 9.15: Expansion of a hexagon under hydrostatic tension p. Each filament in the hexagon is 20nm long. Dashed lines are the results without taking thermal fluctuations into account. Solid lines are the results with thermal fluctuations. Circles are the analytic solutions of Eq. 9.32. (A) Persistence length $\xi_p = 10$nm, stretching modulus $K_s = 10k_BT/nm$. The results with thermal fluctuations shows strain stiffening, i.e, the bulk modulus increases during the expansion process. The bulk modulus changes from $K_{\text{bulk}} = 0.07$pN/nm (fitting from $p = 0$ to 0.06pN/nm) to $K_{\text{bulk}} = 1.29$pN/nm (fitting from $p = 0.3$ to 0.6pN/nm). (B) $\xi_p = 5$nm, $K_s = 10k_BT/nm$ (red). Changing the bending modulus does not change the static solution. But, the results with thermal fluctuation changes a lot. In particular, the initial bulk modulus is $K_{\text{bulk}} = 0.02$pN/nm (fitting from $p = 0$ to 0.06pN/nm). For $p = 0.3$ to 0.8pN/nm, the bulk modulus is $K_{\text{bulk}} = 1.18$pN/nm. The results in plot A are superimposed as blue lines and circles. (C) $\xi_p = 10$nm, $K_s = 100k_BT/nm$ (red). Changing the stretching modulus (compared to A) affects both the static and thermo-mechanical solutions. The fittings for K_{bulk} are for the intervals $p = 0$ to 0.06pN/nm and $p = 0.4$ to 0.8pN/nm respectively. The results in plot A are superimposed as blue lines and circles. (D) $\xi_p = 10$nm, $K_s = 100k_BT/nm$ (red). The fittings are for the intervals $p = 0$ to 0.05pN/nm and $p = 0.15$ to 0.3pN/nm respectively. The results in plot A are superimposed as blue lines and circles.

to a ring. Solid line in Fig. 9.15A is the result that takes thermal fluctuation into account. A fit to the plot shows that the bulk modulus changes from $K_{\text{bulk}} = 0.07\text{pN/nm}$ to $K_{\text{bulk}} = 1.29\text{pN/nm}$. The hexagon is initially easy to expand because of thermal fluctuations. It is stiffened at large p.

Next, we decrease the bending modulus of the filaments, changing the persistence length from $\xi_p = 10\text{nm}$ to $\xi_p = 5\text{nm}$. The results are shown in Fig. 9.15B (red lines, the results in plot A are superimposed as blue lines). As predicted by Eq. 9.32, changing the bending modulus does not change the static solution at all. However, the results with thermal fluctuations changes a lot by changing ξ_p. The hexagon becomes softer when ξ_p is smaller. The reason is that a network of filaments with less bending modulus have more fluctuations and is easier to expand at small p. This result tells us that, even though the static expansion behavior does not depend on the bending modulus, the behavior with thermal fluctuations is affected by tuning the persistence length.

Fig. 9.15C and D (red lines) show the results with different stretching modulus: $K_s = 100k_BT/nm, 1k_BT/nm$ respectively. Persistence length $\xi_p = 10\text{nm}$ is the same as plot A. The results in plot A are superimposed as blue lines. As expected, changing the stretching modulus changes the static solution as well as the results with thermal fluctuations. The static solutions again agree with Eq. 9.32.

Adding/removing filaments to/from the hexagon can also changes the expansion behavior. In particular, adding filaments stiffens the structure, while removing filaments softens the hexagon. Fig. 9.16D shows the area (with thermal fluctuations) versus hydrostatic tension relation for three different networks (structures shown in plot A-C). The results show that thermal fluctuation is reduced for a network with more interior filaments.

Next, to study the rate at which thermal fluctuations are stretched out, we expand a single triangle with size $L = 20\text{nm}$ and persistence length $\xi_p = 10\text{nm}$. The stretching modulus is set to be $K_s = 300k_BT/nm$. We define the difference between the static size and the "thermal" size of the network as:

$$\Delta r = \sqrt{\frac{A_{\text{static}}}{\pi}} - \sqrt{\frac{A_{\text{thermal}}}{\pi}}, \tag{9.39}$$

where A_{static} and A_{thermal} are the area of the network with and without thermal fluctuations respectively. They are both functions of the hydrostatic tension p. A fitting for the relation between Δr and p reveals $\Delta r \sim p^{-1}$ (Fig. 9.17). The -1 power law suggests that thermal fluctuations are stretched out faster than predicted by the simple model proposed in the previous section (Eq. 9.13 predicts a -0.5 power law). The reason may be that the simple model assumes the triangle always deforms into a triangle. It only considers the entropy loss due to stretching in the filament directions. But, in a real expansion process, entropy loss can also result from bending of the filaments.

We now return to the single hexagon. The deformation of a network can be studied using the deformation gradient $\mathbf{F}_{iJ} = \partial x_i / \partial X_J$, where $\vec{x}(\vec{X})$ is the

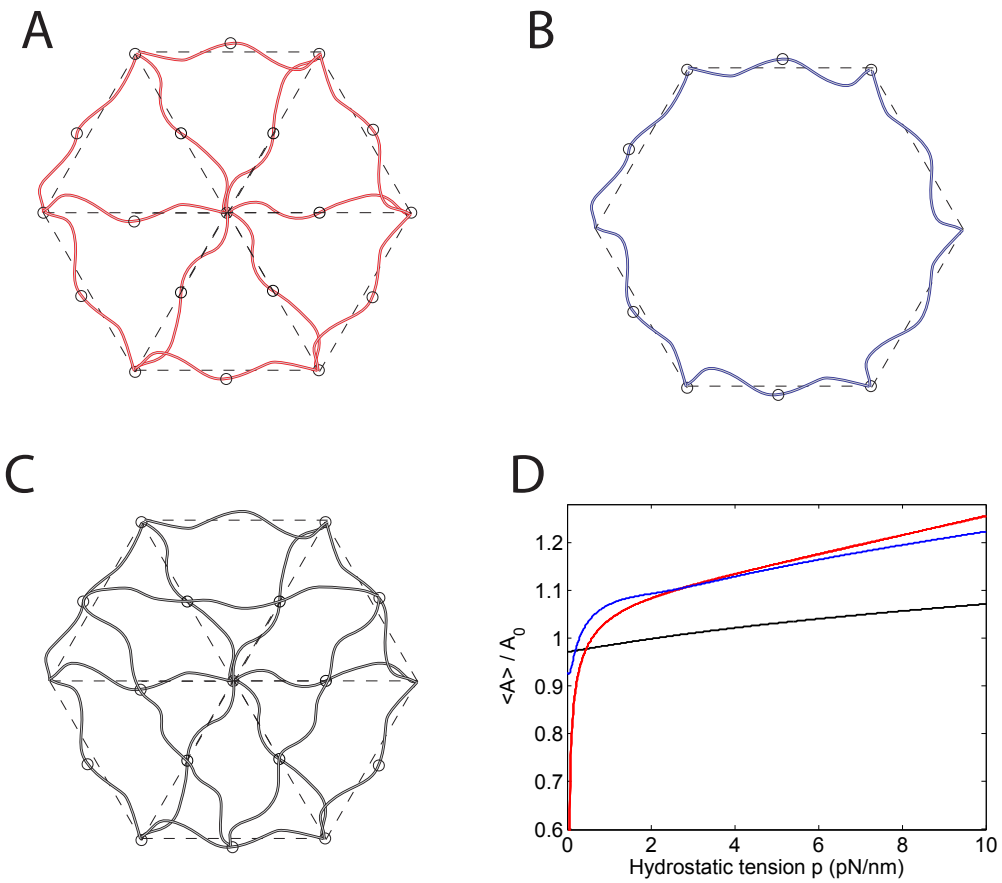

Figure 9.16: (A)-(C): Three different hexagonal structures. The structures shown in (B) and (C) are obtained by removing and adding filaments from/into (A). (D): Expansion behaviors of the three structures shown in A-C are shown in red, blue and black, respectively. Thermal fluctuation is significantly reduced for network (C).

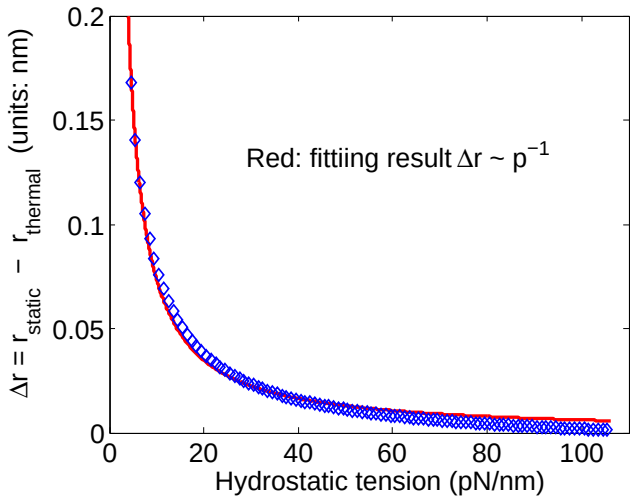

Figure 9.17: Scaling law of stretching the thermal fluctuations. An equilateral triangle whose initial length for the sides is $L = 20$nm is under hydrostatic tension p. The persistence length of the filaments is $\xi_p = 10$nm. Δr, as defined in Eq. 9.39, characterizes the size difference between the static solution and the thermal solution. The fitting result suggests $\Delta r \sim p^{-1}$. Thermal fluctuation is stretched out faster than the -0.5 power law.

deformed position of a material point whose reference position is $\vec{X}$. The material is assumed to deform according to $\vec{x} = \mathbf{F}\vec{X} + \vec{C}$, where $\vec{C}$ is a translation vector. For each triangle inside the hexagon, we compute the deformation gradient using its three vertices ($i = 1, 2, 3$):

$$\begin{pmatrix} X_1 & Y_1 & 1 \\ X_2 & Y_2 & 1 \\ X_3 & Y_3 & 1 \end{pmatrix} \begin{bmatrix} F_{11} \\ F_{12} \\ C_1 \end{bmatrix} = \begin{bmatrix} x_1 \\ x_2 \\ x_3 \end{bmatrix}, \quad \begin{pmatrix} X_1 & Y_1 & 1 \\ X_2 & Y_2 & 1 \\ X_3 & Y_3 & 1 \end{pmatrix} \begin{bmatrix} F_{21} \\ F_{22} \\ C_2 \end{bmatrix} = \begin{bmatrix} y_1 \\ y_2 \\ y_3 \end{bmatrix}. \tag{9.40}$$

The average $\mathbf{F}$ for the six triangles is approximately the deformation gradient of the network. The left and right Cauchy-Green tensors are respectively:

$$\mathbf{C} = \mathbf{F}^T\mathbf{F} = \lambda_i^2 \vec{e}_i^0 \vec{e}_i^0, \tag{9.41}$$

$$\mathbf{B} = \mathbf{F}\mathbf{F}^T = \lambda_i^2 \vec{e}_i \vec{e}_i, \tag{9.42}$$

where λ_i are the principal stretches, $\vec{e}_i = \mathbf{F}\vec{e}_i^0$ are the principal axes in the deformed configuration, and $\vec{e}_i^0$ are the principal axes in the reference configuration. For a 2D problem, we have two principal stretches λ_1 and λ_2. They can be decomposed into a pure dilatation or expansion part and a shear part:

$$\lambda_{\text{ex}} = \sqrt{\lambda_1 \cdot \lambda_2}, \tag{9.43}$$

$$\lambda_{\text{sh}} = \sqrt{\frac{\lambda_1}{\lambda_2}}. \tag{9.44}$$

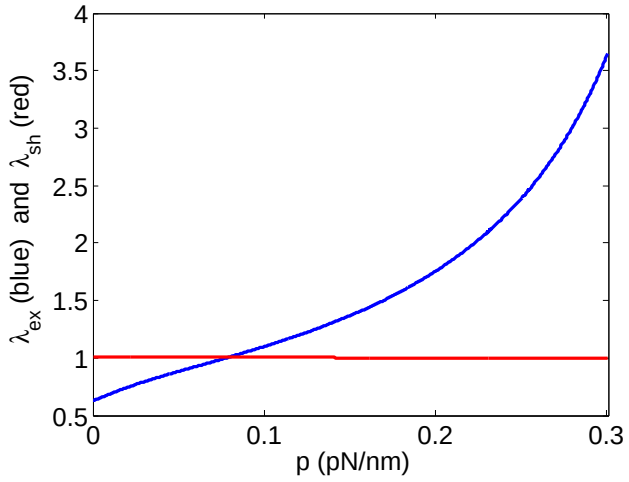

Figure 9.18: Principal stretch during an expansion process. Denote the principal stretches as λ_1 and λ_2, then the stretch associate with expansion and with shear are respectively $\lambda_{\text{ex}} = \sqrt{\lambda_1\lambda_2}$, $\lambda_{\text{sh}} = \sqrt{\lambda_1/\lambda_2}$. For the expansion of a hexagon, λ_{ex} versus the the hydrostatic tension is plotted in blue, while λ_{sh} versus p is plotted in red.

This decomposition can be understood in a slightly different way. One can view the deformation process as a pure expansion process plus a pure shear process:

$$\mathbf{F} = \mathbf{F}_{\text{ex}} \cdot \mathbf{F}_{\text{sh}} \tag{9.45}$$

$$= J\mathbf{I} \cdot \frac{1}{J}\mathbf{F}, \tag{9.46}$$

where $J = \det \mathbf{F} = \lambda_1\lambda_2$. The principal stretch associated with $\mathbf{F}_{\text{ex}}$ is $\sqrt{\lambda_1\lambda_2}$, while the principal stretch associated with $\mathbf{F}_{\text{sh}}$ is $\sqrt{\lambda_1/\lambda_2}$.

In Fig. 9.18, we plot λ_{ex} and λ_{sh} versus the hydrostatic tension p for the expansion of a hexagon. As expected, λ_{sh} remains almost 1 during the process, which means $\lambda_1 = \lambda_2$. Therefore, every direction in the 2D plane is a principal direction. To understand how changing the bending modulus changes the behavior of the network, we expand two hexagons, one with persistence length $\xi_p = 10$nm, the other with $\xi_p = 20$nm. The length of the filament is again 20nm. The results are shown in Fig. 9.19. The difference is significant at low hydrostatic tension p, while at high tension, the two networks have similar behavior. This again suggests that at low p, bending dominates the deformation, while at high tension, stretching plays a more important role.

9.4.2 Simple shear on a hexagon

Next, we study the shear deformation of a single hexagon (Fig. 9.21A). Uniform shear forces, in opposite directions, are applied on the top and bottom filaments of the hexagon to cause shear deformation. Each filament is 20nm

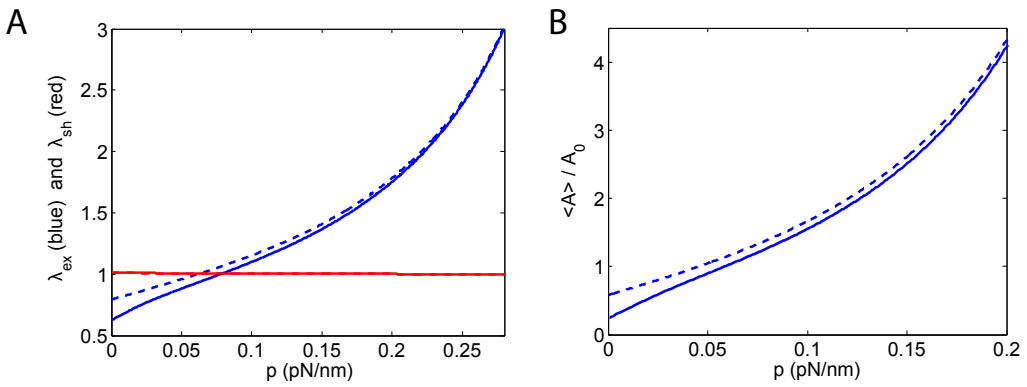

Figure 9.19: Expansion of two hexagons. (A) $\lambda_{\rm ex}$ (blue) and $\lambda_{\rm sh}$ (red) versus hydrostatic tension p. (B) Average area versus p. Solid line: hexagon whose filaments have persistence length $\xi_p = 10$nm. Dashed line: hexagon whose filaments have persistence length $\xi_p = 20$nm. The behavior of the two networks is different at low p, because bending dominates at this regime.

long with persistence length $\xi_p = 10$nm. Stretching modulus of the filament is $K_s = 10 k_B T/nm$.

Suppose that we can neglect the buckling behavior of the filaments, and that the hexagon is under affine shear deformation with a deformation gradient:

$$\mathbf{F} = \begin{bmatrix} 1 & F_{12} \\ 0 & F_{22} \end{bmatrix}. \tag{9.47}$$

Here we leave F_{22} as an unknown. The solution should tell us whether the hexagon, under shear, contracts or expands in the y direction. Now assuming all the filaments in the hexagon deform according to Eq. 9.47, the stretching energy of the network can be computed and the result is:

$$\frac{E_s}{2K_s l_0} = \frac{3}{2}F_{12}^2 + \frac{3}{2}F_{22}^2 - \sqrt{(1-\sqrt{3}F_{12})^2 + 3F_{22}^2} - \sqrt{(1+\sqrt{3}F_{12})^2 + 3F_{22}^2}. \tag{9.48}$$

On the other hand, the potential energy of the shear stress τ can be computed by $E_\tau = -\int \tau x dX$ for the top and bottom filaments. Eventually, the total elastic energy of the network is:

$$\frac{E}{K_s l_0} = \frac{3}{2}F_{12}^2 + \frac{3}{2}F_{22}^2 - \sqrt{(1-\sqrt{3}F_{12})^2 + 3F_{22}^2} - \sqrt{(1+\sqrt{3}F_{12})^2 + 3F_{22}^2} - \frac{\sqrt{3}\tau l_0 F_{12}}{2K_s}. \tag{9.49}$$

The equilibrium configuration for the affine deformation can be computed using $\partial E/\partial \mathbf{F} = 0$. Interestingly, a simple analytic solution exists for these equations, and the final results are:

$$F_{12} = \frac{4}{\sqrt{3}}\frac{\bar{\tau}}{(1-\bar{\tau}^2)^2}, \quad F_{22}^2 = \frac{4}{3(1-\bar{\tau})^2} - \frac{1}{3}\left[1 + \frac{4\bar{\tau}}{(1-\bar{\tau}^2)^2}\right]^2. \tag{9.50}$$

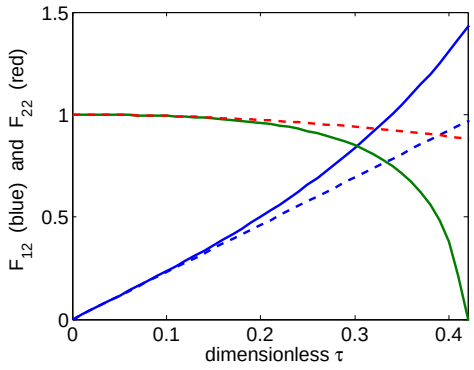

Figure 9.20: Analytic static solutions for simple shear on a hexagon. Two components, F_{12} (blue) and F_{22} (red) of the deformation gradient $\mathbf{F}$ is plotted as a function of the applied shear stress τ. Dashed lines are the asymptotic behavior at small τ. Dimensionless shear stress is defined as $\bar{\tau} = \tau l_0/2K_s$, with l_0 and K_s being the contour length and stretching modulus of the filaments.

Here the dimensionless shear stress is defined as $\bar{\tau} = \tau l_0/2K_s$. When $\bar{\tau} << 1$, the solution is:

$$F_{12} = \frac{4}{\sqrt{3}}\bar{\tau}, \quad F_{22} = 1 - \frac{2}{3}\bar{\tau}^2. \tag{9.51}$$

Eq. 9.50 and 9.51 are plotted as functions of $\bar{\tau}$ in Fig. 9.20 in solid and dashed lines respectively. In particular, Eq. 9.51 tells us that the initial shear modulus of a hexagon is:

$$G = \frac{\sqrt{3}K_s}{2l_0}. \tag{9.52}$$

Note that like the static bulk modulus for the hexagon, G depends only on the stretching modulus. Plugging in the numbers $l_0 = 20\text{nm}$ and $K_s = 10k_BT/nm$, we obtain $G = 1.78\text{pN/nm}$. Eq. 9.51 also tells us that the hexagon will contract in the y direction during shear, because $F_{22} \leq 1$. This is an interesting result, because many materials expand during simple shear. For example, for a Neo-Hookean solid under simple shear γ, the Cauchy stress tensor is:

$$\sigma = \begin{bmatrix} 2\mu\gamma^2/3 & \mu\gamma & 0 \\ \mu\gamma & -\mu\gamma^2/3 & 0 \\ 0 & 0 & -\mu\gamma^2/3 \end{bmatrix}, \tag{9.53}$$

with μ being the shear modulus of the solid. We see that both σ_{yy} and σ_{zz} for the Neo-Hookean material are negative (although the magnitude is small, on the order of γ^2). Therefore, the material tends to expand in the y and z directions during the shear. Filament networks, however, usually show negative normal force under shear, i.e., the network tends to contract in the direction perpendicular to the shear direction. Our result in Eq. 9.51 confirms this unusual behavior for a hexagonal network, even without taking thermal fluctuations into account.

We note that the same analysis can be applied to an empty hexagon without the interior filaments. Interestingly, the results turn out to be exactly the same, except that the dimensionless $\bar{\tau}$ has to be redefined as $\bar{\tau} = \tau l_0/K_s$. The static shear modulus is $G = \sqrt{3}K_s/4l_0$, which is half of that for a regular hexagon with the interior filaments.

This simple model assumes that the filaments are all under affine deformation without bending and buckling. Under shear deformation, however, some of the filaments are under compression and will buckle. Now we use the theoretical framework described in the previous section to study the simple shear of a hexagon. To avoid the singularity, we start with an initial curved configuration.

Static deformed configurations are shown in Fig. 9.21. If we do not take the effects of thermal fluctuations into account, a hexagon is difficult to shear initially. The reason is that a hexagon is made up of triangles. When the filaments are almost inextensible, the triangles are almost undeformable (see Fig. 9.21 B $\rightarrow$ C). When the shear force is large enough, the filaments that are under compression will buckle (see Fig. 9.21D). This reduces the stiffness of the structure, making the hexagon easier to deform under further shear. In fact, after buckling occurs, the hexagon deforms significantly even when the shear stress increases only by a little (see Fig. 9.22). This sudden loss of stiffness is similar to the buckling of a single filament. However, the hexagon as a whole does not lose stability completely. After the buckling events, the hexagon can still sustain shear, although it is much easier to deform (see Fig. 9.21 D $\rightarrow$ E). The above observation suggests that, for a *triangular* network of filaments with high stretching modulus, large *static* deformation is possible only after some buckling events soften the network. Many cellular networks are hexagonal and are made up of triangles. The filaments have large stretching modulus. But, they can easily achieve large deformation. This tells us that some of the deformations must be achieved by stretching out the thermal fluctuations.

To prove that high stretching modulus is the reason for the initial high stiffness of the system, we reduce the stretching modulus to $K_s = 1k_BT/\text{nm}$ and re-do the shear. The result is that the hexagon can achieve large static shear deformation without buckling until the structure completely loses stability (see Fig. 9.23). We emphasize here that the configurations shown in Fig. 9.21, 9.22 and 9.23 are the static configurations without taking thermal fluctuations into account.

To understand the thermo-mechanics of the shear deformation quantitatively, we calculate the displacements and strains during the deformation next. We first investigate the relative displacement, in x direction, between the top and bottom filaments. We calculate the x direction separation Δx between node 1 and node 2 (see Fig. 9.21A) as a function of the shear stress τ. The stiffness in x direction can be characterized by $k = \tau/\Delta x$ (in units of pN/nm^2). The results, with and without thermal fluctuations, are shown in Fig. 9.24A. Dashed line is the result without thermal fluctuations. We observe buckling events at $\tau \approx 0.04\text{pN/nm}$. The relation between Δx and τ is linear before

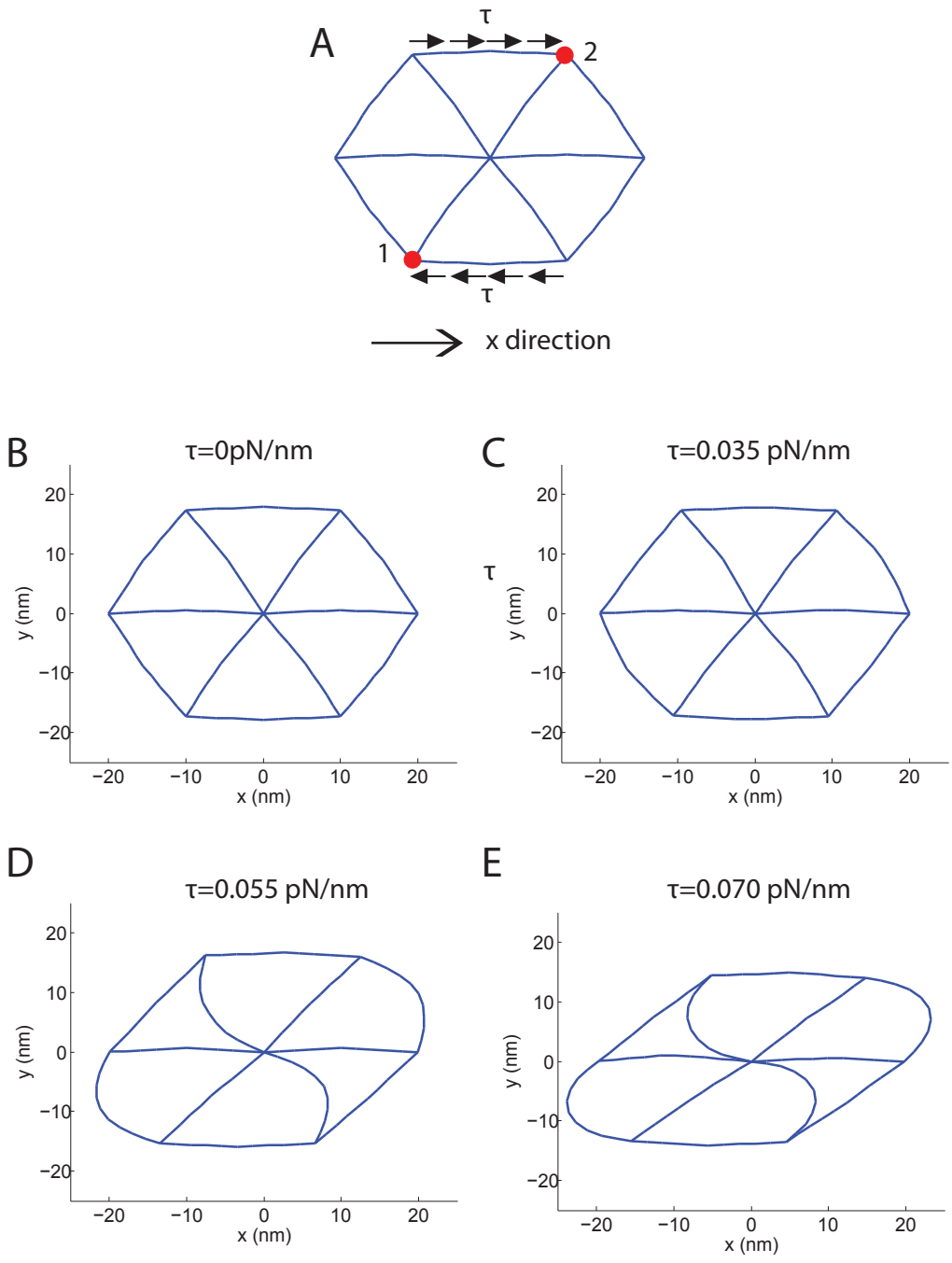

Figure 9.21: (A) Illustration of shear on a single hexagon. Uniform distributed forces in $\pm x$ direction are applied on the top and bottom filaments of hexagon to cause the shear deformation. Some filaments that are under compression will buckle during the shear deformation. Each filament is 20nm long. Their persistence length is 10nm. Stretching modulus is $10 k_B T/nm$. (B) Reference configuration with initial perturbation. (C-E) Deformed configurations with buckled filaments.

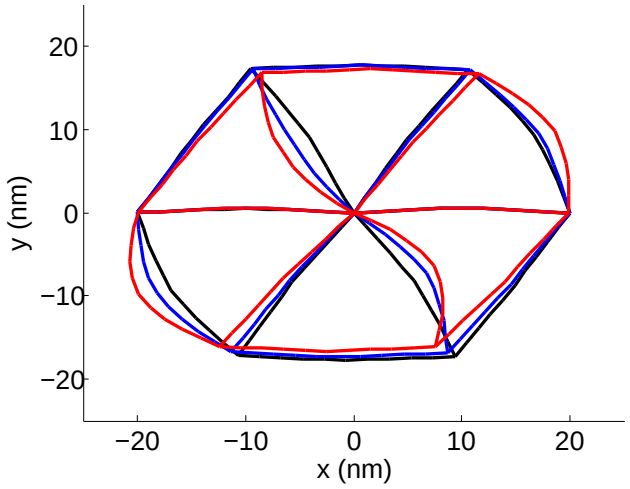

Figure 9.22: When buckling occurs, the hexagon undergoes significant deformation for even a small increases in the shear stress (compared to B $\rightarrow$ C in Fig. 9.21). Black: $\tau = 40$fN/nm. Blue: $\tau = 45$fN/nm. Red: $\tau = 50$fN/nm. The deformation shown here is significant compared the the deformation before buckling at $\tau < 40$fN/nm (Fig. 9.21).

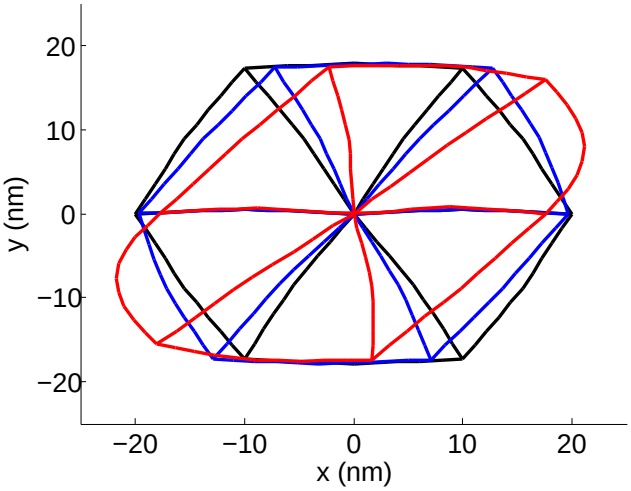

Figure 9.23: Shear on a hexagon with small stretching modulus $K_s = 1k_BT/nm$. Unlike the deformation shown in Fig. 9.21, the hexagon can achieve large shear deformation without buckling when the stretching modulus is small. Filaments in many cellular networks have large stretching modulus. They achieve large deformation by stretching out thermal fluctuations.

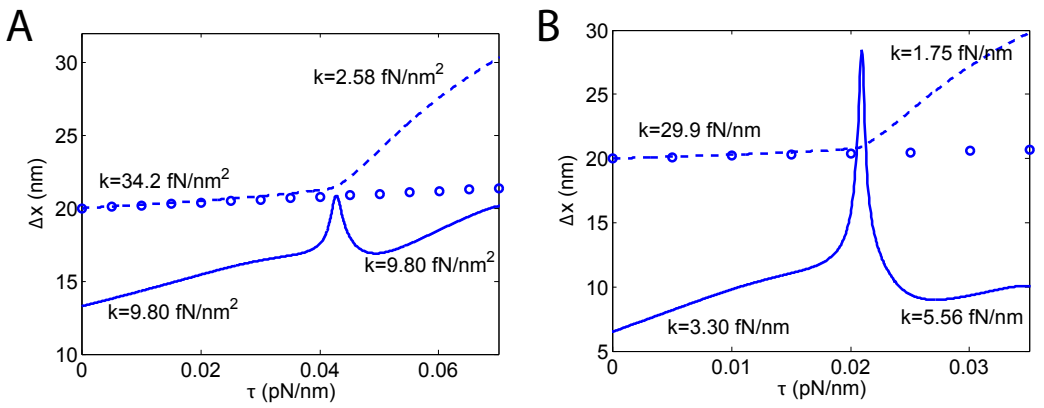

Figure 9.24: X direction separation of the top and bottom filaments. Δx is the distance between node 1 and node 2 shown in Eq. 9.21A. This quantity is plotted as a function of the shear stress τ. Effective stiffness is defined as $k = \tau/\Delta x$ here. Dashed line is the result without thermal fluctuation. The hexagon is much softer after buckling if thermal fluctuation is not taken into account. Solid line is the result with thermal fluctuations. The hexagon becomes stiffer after buckling when thermal fluctuation is taken into account. Circles are the results from the analytic static solutions assuming affine deformation (Eq. 9.50). They match with our computational results at small τ. For large τ, buckling occurs and the deformation of the hexagon is non-affine. (A) and (B) are for different persistence length $\xi_p = 10$nm and $\xi_p = 5$nm respectively.

and after the buckling. The stiffness $k = \tau/\Delta x$ decreases from $34.2 fN/nm^2$ to $3.20 fN/nm^2$ for the static solution. This is again because buckling reduces the stiffness of the network. We also note that the static solution before buckling agrees very well with the simple affine deformation model (Eq. 9.50). After the buckling occurs, however, the deformation is no longer affine and the simple model underestimates the deformation of the structure. Solid line in Fig. 9.24A includes the contribution from thermal fluctuations. We observe that, before buckling, the stiffness ($9.80 fN/nm^2$) is significantly less than the static solution. This suggests that thermal fluctuation makes the hexagon deformable at the beginning of the shear. In particular, shear stress is used to stretch out the thermal fluctuations. After buckling, the stiffness k (with thermal fluctuation) does not change very much. The hexagon is actually stiffer compared to the static solution. This tells us that thermal fluctuation plays different roles before and after buckling. Before buckling occurs, thermal fluctuation makes the hexagon softer and easier to shear. After buckling, thermal fluctuation makes the hexagon stiffer and more difficult to shear. We also observe a peak appearing when the buckling occurs. This is similar to buckling of a single filament discussed in the previous section.

To prove that it is the thermal fluctuation that makes the hexagon deformable at the initial state, we decreases the persistence length of the fil-

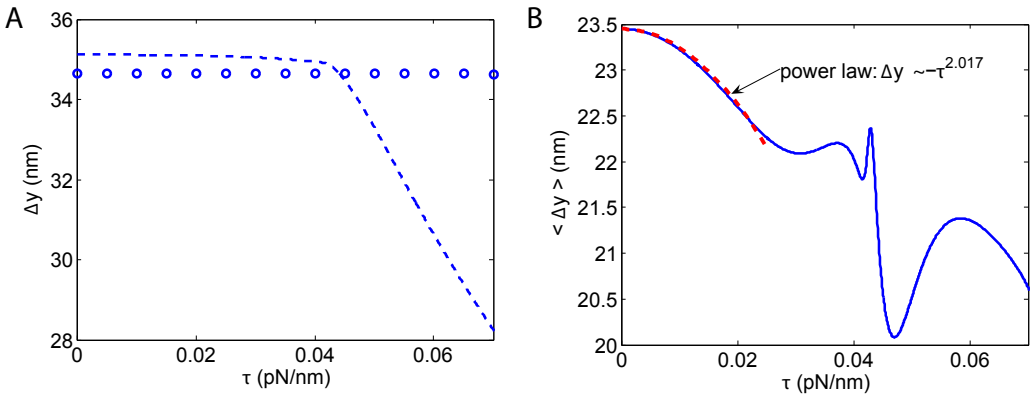

Figure 9.25: Average separation between the top and bottom filaments as a function of the shear stress. (A) and (B) are the results without and with thermal fluctuations respectively. The results show that the hexagon contracts in the direction perpendicular to the shear direction. At small shear stress, the deformation is affine. The static solution (shown in A) roughly agrees with Eq. 9.50 (shown in circles). The difference is caused by the perturbations on the initial configuration. For the result with thermal fluctuations (shown B), a fitting to the solution shows that the separation decreases quadratically.

aments to $\xi_p = 5$nm (note that the contour length of the filaments is $L = 20\text{nm} = 4\xi_p$). The result is shown in Fig. 9.24B. The initial stiffness k reduces to $3.30 fN/nm^2$ before buckling. This is because filaments with smaller persistence length have more thermal fluctuations and therefore are easier to shear. Buckling occurs earlier compared to Fig. 9.24A, as expected, because the bending modulus of the filaments is smaller.

We next discuss the y direction deformation during the shear. We calculate the separation between the top and the bottom filaments as a function of the shear stress. The results with and without thermal fluctuation are shown in Fig. 9.25 A and B respectively. Our results again show that a hexagon indeed contracts during shear. Before buckling, the contraction Δy (including thermal fluctuations) scales as $\Delta y \sim -\tau^{2.017}$, which suggests the separation in the y direction decreases quadratically when the deformation is still affine (no buckling).

Shear strain of the hexagon can be defined as $\gamma = \Delta x/\Delta y$, where Δx and Δy are the relative displacements between the top and bottom filaments, in x and y directions respectively. An effective shear modulus can be introduced as $G = d\tau/d\gamma$. We show the relation between γ and τ in Fig. 9.26A. For the static solution, the shear modulus is significantly reduced (from $G = 1.26$pN/nm to $G = 0.08$pN/nm) after buckling. We note that the initial shear modulus agrees well with the simple affine deformation model, which predicts $G = 1.78$pN/nm (Eq. 9.52).

For the results that include thermal fluctuations, the shear modulus does not change very much. The reason is that before buckling, the shear modulus

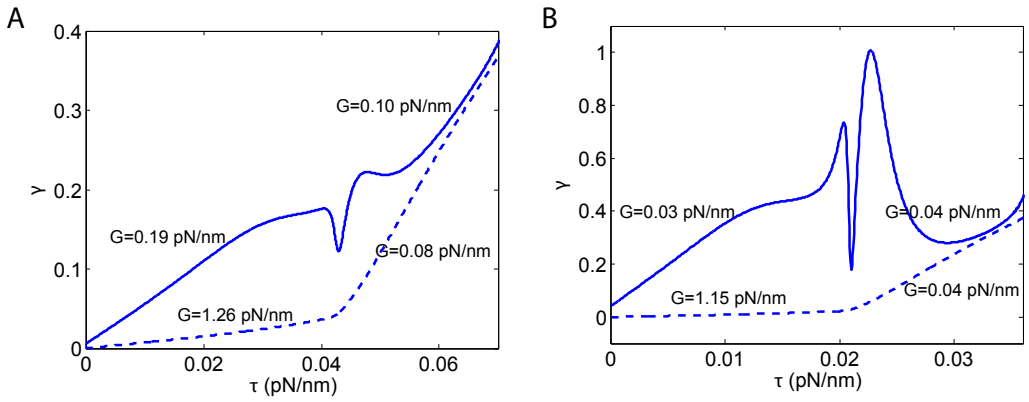

Figure 9.26: Shear strain γ as a function of the shear stress τ. Effective shear modulus can be defined as $G = \tau/\gamma$. Dashed line: static solution. Solid line: result including the thermal effects. The strain and stress relation is linear before and after buckling at $\tau \approx 40$fN/nm. For the static solution, the shear modulus decreases significantly after buckling. For the result that includes the thermal fluctuation, shear modulus does not change a lot before and after buckling. The reason is that before buckling, the shear modulus is much less than that of the static solution because of the fluctuations. Figure A and B are for $\xi_p = 10$nm.and 5nm respectively. Contour length of the filaments is $L = 20$nm. Stretching modulus is $K_s = 10k_BT/nm$.

that takes thermal fluctuations into account is much less that from the static solution. We conclude that the modulus before buckling is due to thermal fluctuations, while the modulus after buckling is due to elastic stretching. Indeed, we change the persistence length of the filaments from $\xi_p = 10$nm to $\xi_p = 5$nm, the initial static shear modulus does not change very much (1.26pN/nm versus 1.15pN/nm), while the initial shear modulus that includes thermal fluctuations changes significantly (0.19pN/nm versus 0.03pN/nm).

We mentioned previously that an affine deformation can be described locally by a linear transformation:

$$\vec{x} = \mathbf{F}\vec{X} + \vec{C}, \tag{9.54}$$

where $\vec{x}$ and $\vec{X}$ are the deformed and reference position of a material point respectively. Filament networks do not always deform in an affine way. To investigate the effect of affine and non-affine deformation, we calculate the difference between the affine displacement field and the actual displacement field. Firstly, the average deformation gradient $\mathbf{F}$ and translation vector C are computed using Eq. 9.40. Then the difference between the affine displacement field and the actual displacement field is characterized by a parameter α:

$$\alpha = \frac{1}{N} \sum_{\text{all nodes}} \frac{|\vec{x}_{\text{affine}} - \vec{x}_{\text{actual}}|}{|\vec{x}_{\text{actual}} - \vec{X}|}, \tag{9.55}$$

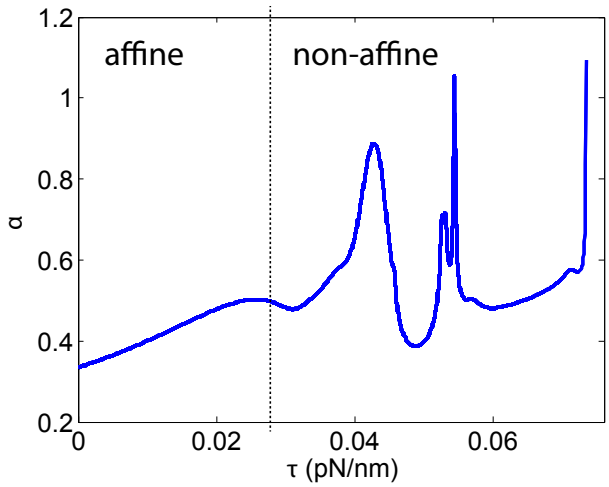

Figure 9.27: Affine, non-affine deformation during shear on a hexagon.

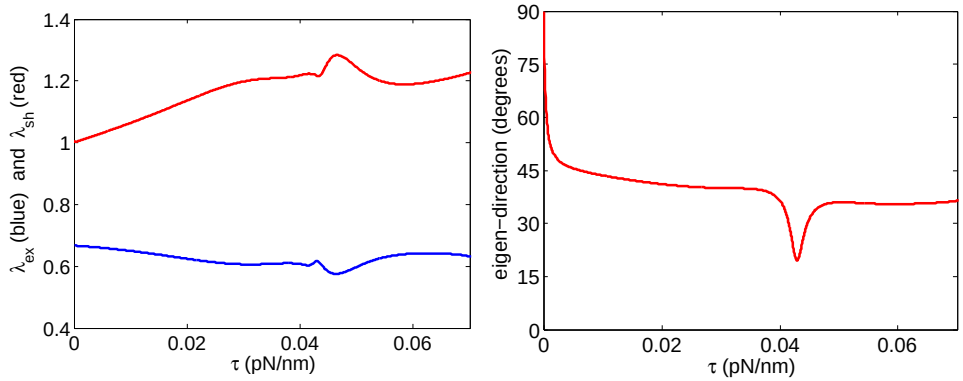

Figure 9.28: (A) λ_{ex} and λ_{sh} as a function of the shear stress τ. (B) Eigen-direction (direction of $\vec{e}_1^0$) as a function of the shear stress. The other eigen-direction $\vec{e}_2^0$ is perpendicular to $\vec{e}_1^0$.

where the summation is over all nodes (not only the vertices, but all the discrete nodes), and N is the number of nodes in the network. If the deformation is affine, α should be small. On the other hand, if the deformation is non-affine, this quantity should be large. The result as a function of the shear force is shown in Fig. 9.27. Our result shows that when the filaments buckle, the deformation becomes less affine.

Further, we plot the shear stretch λ_{sh} and expansion stretch λ_{ex} as a function of the shear stress τ in Fig. 9.28. λ_{ex} is clearly less than 1, even though we do not apply hydrostatic tension on the network. This is caused by the thermal fluctuation. The orientation of the principal axis $\vec{e}_1^0$ is also plotted in Fig. 9.28. $\vec{e}_1^0$ changes from $\pi/2$ to $\pi/4$ (with respect to the x axis) as the shear stress increases. When buckling occurs, the orientation angle drops until the system regains stability.

9.4.3 Pure tension on a hexagon

Lastly, we apply pure tension on the hexagon. The uniaxial tension q is applied as shown in Fig. 9.30A. Each filament has contour length $L = 20$nm and persistence length $\xi_p = 10$nm. The stretching modulus is $K_s = 10k_BT/$nm.

Again, we first assume the deformation is affine, with deformation gradient given by:

$$\mathbf{F} = \begin{bmatrix} F_{11} & 0 \\ 0 & F_{22} \end{bmatrix}. \tag{9.56}$$

Let all the filaments in the hexagon deform according to Eq. 9.56, then the potential energy of the network is:

$$\frac{E}{K_s l_0} = \left(\sqrt{F_{11}^2 + 3F_{22}^2 - 2}\right)^2 + 2(F_{11} - 1)^2 - \frac{3ql_0F_{11}}{K_s}. \tag{9.57}$$

Minimum energy state can be computed using $\partial E/\partial \mathbf{F} = 0$, which leads to:

$$F_{11} = 1 + \frac{3ql_0}{K_s}, \quad F_{22}^2 = \frac{4}{3} - \frac{1}{3}\left(1 + \frac{3ql_0}{K_s}\right)^2. \tag{9.58}$$

The asymptotic solution for $q \to 0$ is:

$$F_{11} = 1 + \frac{3ql_0}{K_s}, \quad F_{22} = 1 - \frac{ql_0}{K_s}. \tag{9.59}$$

From Eq. 9.59, we know that the initial Young's modulus and Poisson's ratio of the hexagon is:

$$E = \frac{K_s}{3l_0}, \quad \nu = \frac{1}{3}. \tag{9.60}$$

Plugging in the number $K_s = 10k_BT/nm$ and $l_0 = 20$nm, we get $E = 0.67$pN/nm. Plots of Eq. 9.59 (solid lines) and 9.60 (dashed lines) are shown in Fig. 9.29.

This simplified model assumes affine deformation and does not consider buckling of the filaments. Below, we use the theoretical framework described in the previous section to study the thermo-mechanical properties of the hexagon under uniaxial tension. Typical deformation is shown in Fig. 9.30 B-E. We again observe buckling of the diagonal filaments during the deformation. The direction of the buckling depends on the initial perturbation we apply on the filaments. If we reduce the stretching modulus of the filaments to $K_s = 1.0k_BT/nm$, the hexagon can deform significantly without buckling (Fig. 9.31).

For the hexagon with $K_s = 10k_BT/nm$ (Fig. 9.30), we calculate its height and the width during the deformation. The height Δy is defined as the average y direction separation between the top and bottom filaments, while the width Δx is defined as the average x direction separation between the left and right filaments. Results with and without thermal fluctuations are shown

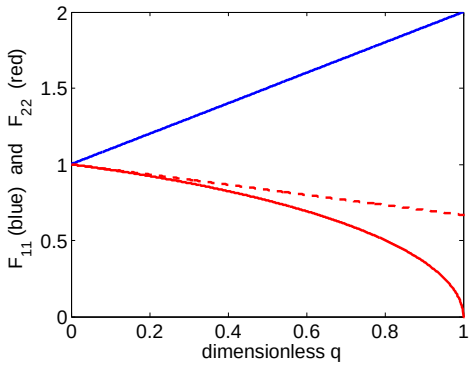

Figure 9.29: Analytic static solutions for uniaxial tension on a hexagon. Two components, F_{11} (blue) and F_{22} (red) of the deformation gradient $\mathbf{F}$ are plotted as functions of the applied tensile stress q. Dashed lines are the asymptotic behavior at small q. Dimensionless tensile stress is defined as $\bar{q} = 3ql_0/K_S$, with l_0 and K_s being the contour length and stretching modulus of the filaments.

in Fig. 9.32. Interestingly, when taking the thermal fluctuations into account, height of the hexagon increases in the initial state of the uniaxial pulling. This would suggests a negative Poisson's ratio, which we will discuss below.

Let Δx_0, Δy_0 be the initial width and height of the hexagon respectively. Then the stretch in these two directions can be defined as: $\lambda_x = \Delta x/\Delta x_0$ and $\lambda_y = \Delta y/\Delta y_0$. We show these stretches as a function of the tensile stress q in Fig. 9.33A. Similar to the results of shear, thermal fluctuations cause larger stretch/strain in the hexagon. This is because the network has smaller size at its initial state when fluctuation is taken into account. Result for a hexagon with smaller stretching modulus $K_s = 1.0k_BT/nm$ is shown in Fig. 9.33C.

Poisson's ratio $\nu = (1 - \lambda_y)/(\lambda_x - 1)$ as a function of q is shown in Fig. 9.33B. For the result including fluctuations, Poisson's ratio is initially negative, because stretching out the thermal fluctuation increases the height of the hexagon. The ratio eventually becomes positive and remains constant for large q. Interestingly, when the thermal fluctuation is not taken into account, Poisson's ratio is close to 1, which is the upper limit of ν for a material in 2D [30, 31]. For a hexagon with smaller stretching modulus $K_s = 1.0k_BT/nm$, Poisson's ratio is smaller (Fig. 9.33D).

Principal stretches (as defined in Eq. 9.43 and Eq. 9.44 in the dilatation section) are also computed during the pulling process. The shear stretch λ_{sh} and expansion stretch λ_{ex} are plotted in Fig. 9.34. Here we show the results for a hexagon with $K_s = 1.0k_BT/nm$. As expected, shear deformation dominates and the eigenvector $\vec{e}_1^0$ and $\vec{e}_2^0$ are in the x and y direction respectively.

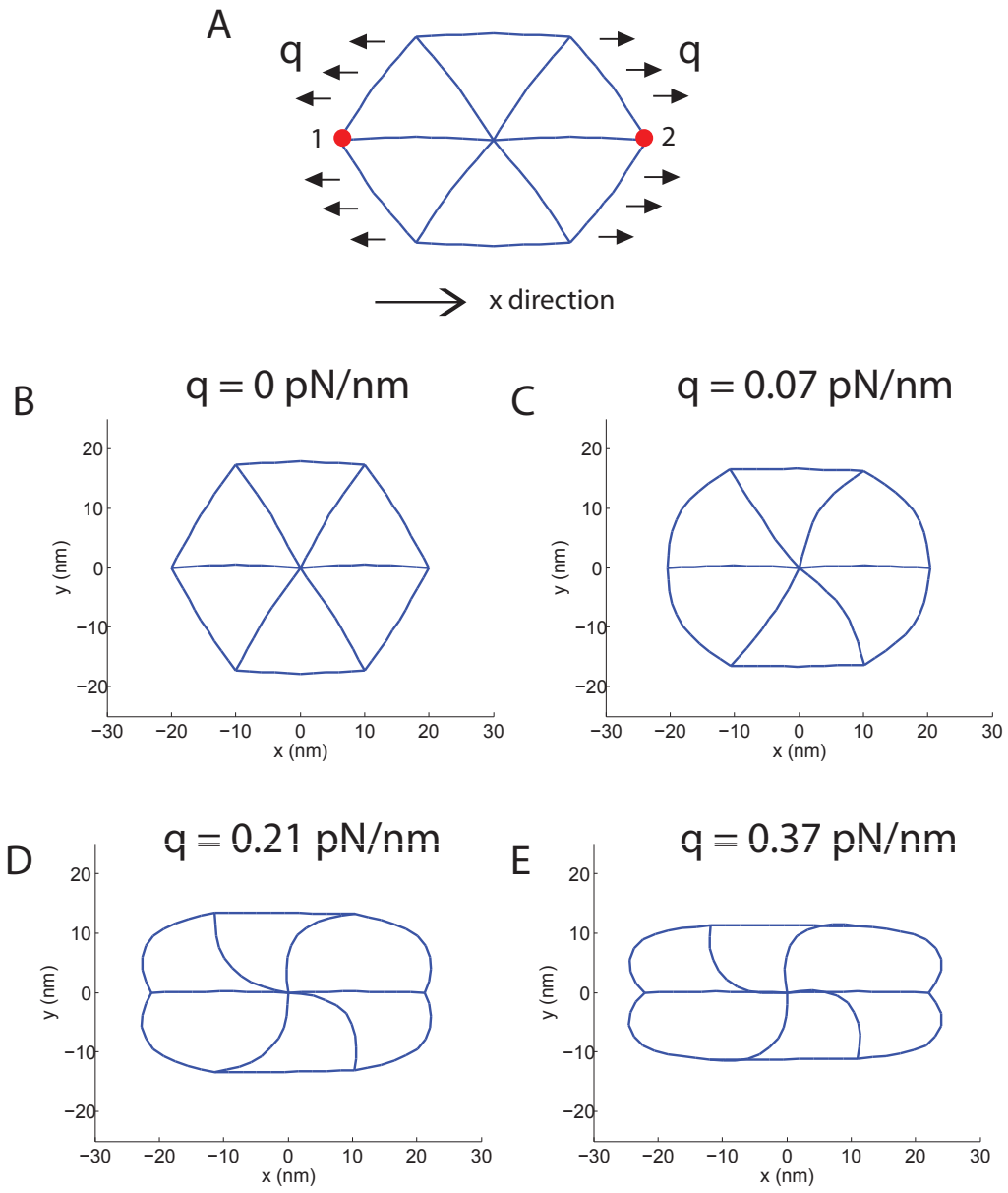

Figure 9.30: (A) Uniaxial tension on a hexagon. Each filament is 20nm long. Their persistence length is 10nm. Stretching modulus is $10k_BT/nm$. (B-E) Deformed configurations with buckling of the diagonal filaments.

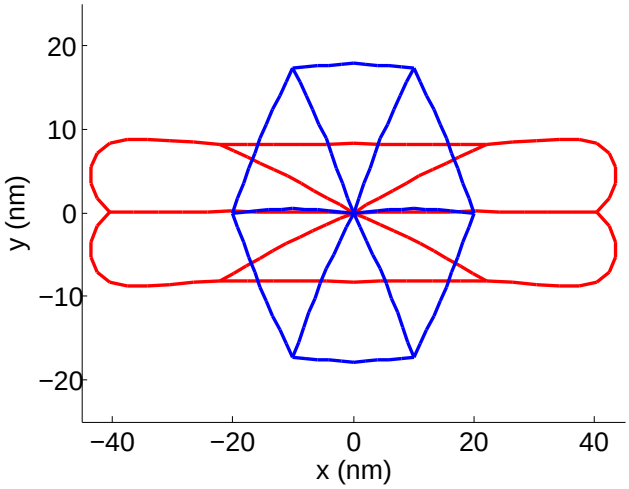

Figure 9.31: Uniaxial tension on a hexagon with smaller stretching modulus $K_s = 1.0 k_B T/nm$. Unlike the hexagon shown in Fig. 9.30, where $K_s = 10 k_B T/nm$, the hexagon here can undergoes large deformation without buckling.

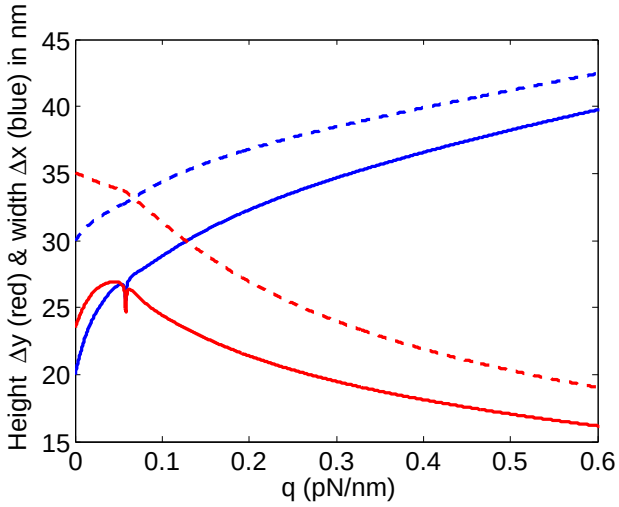

Figure 9.32: Width of the hexagon (Δx) is defined as the average x direction separation between the left and right filaments. Height (Δy) is defined as the average y direction separation between the top and bottom filaments. This figure shows Δx (blue) and Δy (red) as functions of the tension q with (solid lines) and without (dashed) thermal fluctuations. Solid lines are always below the dashed lines because of thermal fluctuation. Interestingly, height of the hexagon increases in the initial state of the tensile pulling.

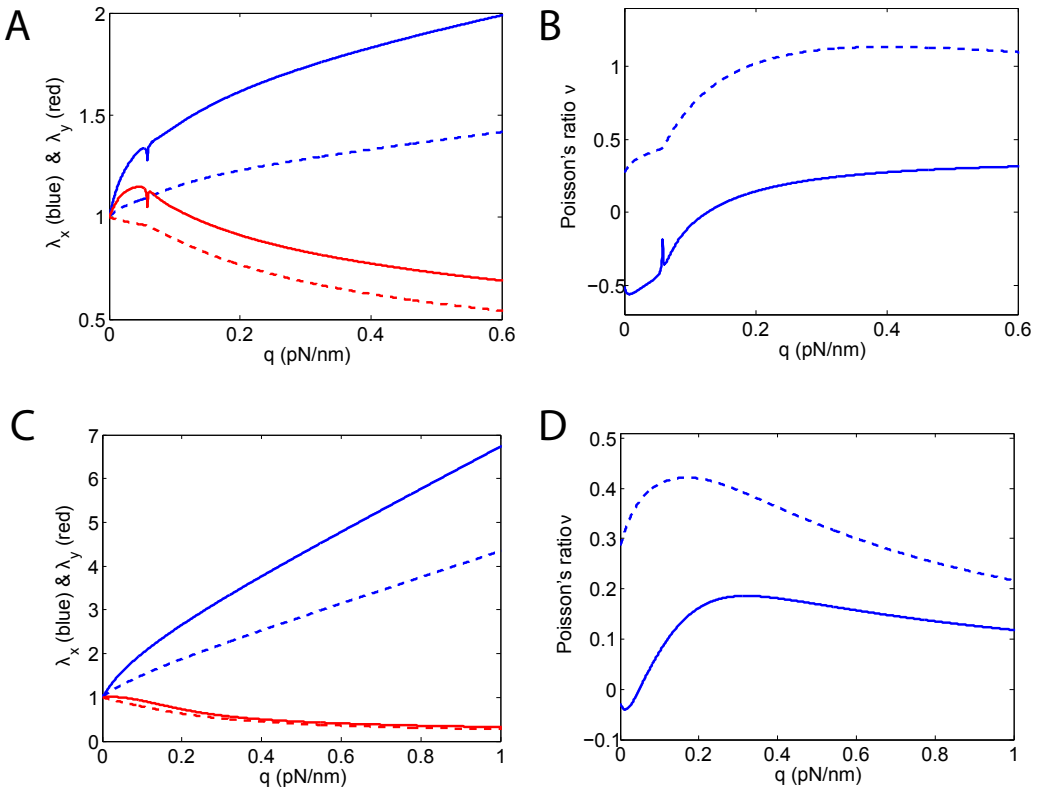

Figure 9.33: Pure tension on a hexagon. (A) and (B): $\xi_p = 10$nm, $K_s = 10k_BT/nm$. (C) and (D) $\xi_p = 10$nm, $K_s = 1k_BT/nm$. (A) and (C): stretch λ_x (blue) and λ_y (red) during the uniaxial pulling. Initial Young's moduli are $E_{\text{A,static}} = 0.31$pN/nm, $E_{\text{A,thermal}} = 0.07$pN/nm, $E_{\text{C,static}} = 0.14$pN/nm and $E_{\text{C,thermal}} = 0.07$pN/nm. (B) and (D): Poisson's ratio as a function of the tensile stress q. Solid lines are the results with thermal fluctuations. Dashed lines are the results without thermal fluctuations.

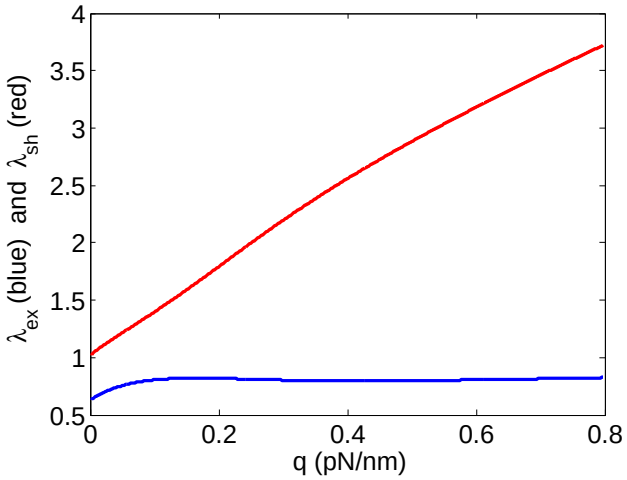

Figure 9.34: λ_{ex} and λ_{sh} as functions of the pulling stress q. At $q = 0$, λ_{ex} is less than 1 because of thermal fluctuations.

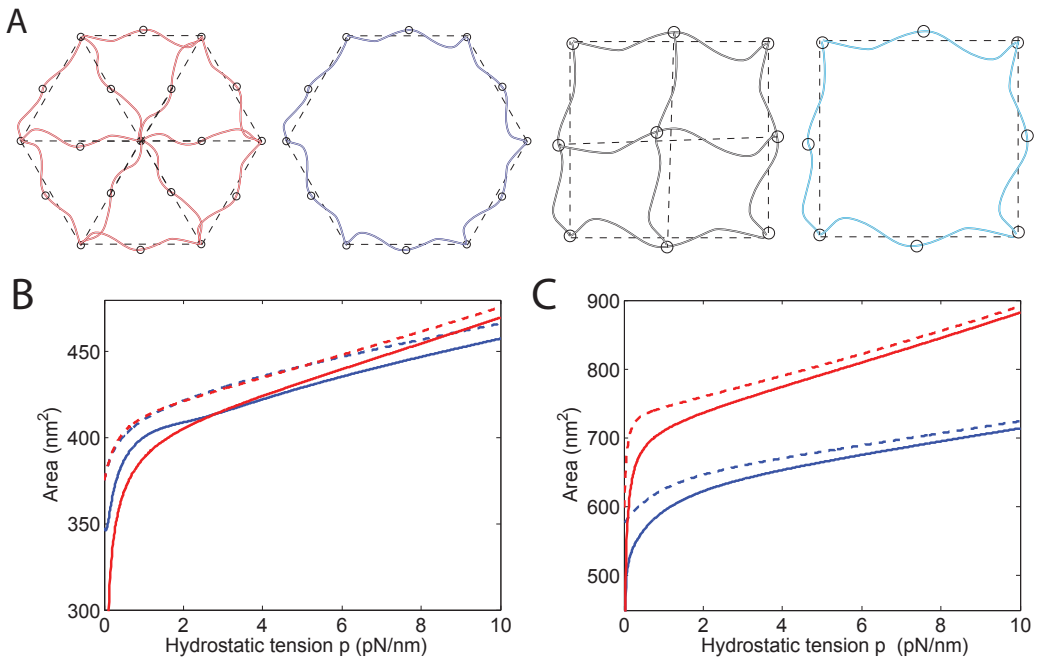

Figure 9.35: (A) Expansion of four networks: two hexagons and two squares, with or without the interior filaments removed. (B) Expansion of the two hexagonal networks. (C) Expansion of two square networks. Red: without the interior filaments. Blue: with the interior filaments. Dashed line: static results. Solid line: with thermal fluctuations.

9.5 A Comparison with Other Networks

We compare pure dilatation of the hexagonal networks and square networks in this section. Again, live hydrostatic tension load $-p$ acts on the boundary of these networks to cause the dilatation. Our results show that the filaments inside the square networks play a key role in stabilizing them, while removing the filaments inside the hexagonal networks does not significantly change the expansion behavior of the network. This may be one of the reasons nature chose hexagonal networks for building cytoskeleton, as defects in the filaments do not significantly weaken the network.

9.6 Conclusions

We investigate the entropic elasticity of network in this section. To extend the theory for a single filament to a theory for a network, one of the main problems is that buckling almost always happens under general deformation in a network. Using the idea of "imperfection" in structural mechanics, we introduce perturbation to the initial configuration of the filament networks to avoid the singularity caused by buckling. This enables us to follow the post-buckling path smoothly to obtain the minimum energy configuration. Thermal

fluctuation is considered for different loadings, including pure expansion, shear and pure tension. It is shown that buckling can soften the network and cause large thermal fluctuations, although typically, soon after entering the post-buckling regime, the network can regain stability.

Bibliography

[1] Boal D. 2002. **Mechanics of the Cell.** *Cambridge University Press.*

[2] Wikipedia contributors. "Nuclear lamina." Wikipedia, The Free Encyclopedia. Wikipedia, The Free Encyclopedia, 24 Jan. 2010. Web. 5 Apr. 2010.

[3] Gruenbaum Y, Goldman RD, Meyuhas R, Mills E, Margalit A, Fridkin A, Dayani Y, Prokocimer M, Enosh A. 2003. **The nuclear lamina and its functions in the nucleus.** *Int. Rev. Cytol.* 226:1-62.

[4] Dahl KN, Scaffidi P, Islam MF, Yodh AG, Wilson KL, Misteli T. 2006. **Distinct structural and mechanical properties of the nuclear lamina in Hutchinson-Gilford progeria syndrome.** *Proc Natl Acad Sci U S A.* 103:10271-10276.

[5] Engler AJ, Sen S, Sweeney HL, Discher DE. 2006. **Matrix elasticity directs stem cell lineage specification.** *Cell* 126:677-89.

[6] Arslan M, Boyce MC. 2006. **Constitutive modeling of the finite deformation behavior of membranes possessing a triangulated network microstructure.** *J. Appl. Mech.* 73: 536-543.

[7] Wu PD, van Der Giessen E. 1993. **On improved network models for rubber elasticity and their applications to orientation hardening in glassy polymers.** *J. Mech. Phys. Solids.* 41, 427456.

[8] Storm C, Pastore JJ, MacKintosh FC, Lubensky TC, Janmey PA. 2005. **Nonlinear elasticity in biological gels.** *Nature* 43: 191-194.

[9] Wilhelm J, Frey E. **Elasticity of stiff polymer networks.** *Phys. Rev. Lett.* 91:108103.

[10] Head D, Levine A, MacKintosh F. 2003. **Deformation of cross-linked semiflexible polymer networks.** *Phys. Rev. Lett.* 91:108102.

[11] Head DA, Levine AJ, MacKintosh FC. 2003. **Distinct regimes of elastic response and deformation modes of cross-linked cytoskeletal and semiflexible polymer networks.** *Phys. Rev. E* 68:061907.

[12] Head DA, Levine AJ, MacKintosh FC. 2005. **Mechanical response of semiflexible networks to localized perturbations.** *Phys. Rev. E* 72:61914.

[13] Heussinger C, Frey E. 2006. **Floppy modes and nonaffine deformations in random fiber networks.** *Phys. Rev. Lett.* 97:105501.

[14] Heussinger C, Schaefer B, Frey E. 2007. **Nonaffine rubber elasticity for stiff polymer networks.** *Phys. Rev. E* 76:31906.

[15] Bai M, Missel AR, Klug WS, Levine AJ. 2011. **The mechanics and affinenonaffine transition in polydisperse semiflexible networks.** *Soft Matter* 7: 907–914.

[16] Gittes F, MacKintosh FC. 1998. **Dynamic Shear Modulus of a Semiflexible Polymer Network.** *Phys. Rev. E* 58: R1241.

[17] Gardel ML, Shin JH, MacKintosh FC, Mahadevan L, Matsudaira P, Weitz DA. 2004. **Elastic behavior of cross-linking and bundled actin networks.** *Science* 304:1301.

[18] Alberts B, Bray D, Hopkin K, Johnson A, Lewis J, Raff M, Roberts K, Walter P. 2009. **Essential Cell Biology.** 3rd ed. Garland Science, New York and London.

[19] Bažant ZP, Cedolin Luigi. 2003. **Stability of structures: elastic, inelastic, fracture, and damage theories.** Courier Dover Publications.

[20] Fletcher DA, Geissler PL. 2009. **Active biological materials.** *Annu. Rev. Phys. Chem.* 60:469-486.

[21] Pollard TD, Kovar DR. 2004. **Insertional assembly of actin filament barbed ends in association with formins produces piconewton forces.** *Proc. Natl. Acad. Sci. USA* 101:14725-14730.

[22] Footer MJ, Kerssemakers JW, Theriot JA, Dogterom M. 2007. **Direct measurement of force generation by actin filament polymerization using an optical trap.** *Proc. Natl. Acad. Sci. USA* 104:2181-2186.

[23] Finer JT, Simmons RM, Spudich JA. 1994. **Single myosin molecule mechanics: piconewton forces and nanometre steps.** *Nature* 368:113-119.

[24] Brangwynne CP, MacKintosh FC, Kumar S, Geisse NA, Talbot J, Mahadevan L, Parker KK, Ingber DE, Weitz DA. 2006. **Microtubules can bear enhanced compressive loads in living cells because of lateral reinforcement.** *J Cell Biol* 173(5):733-41.

[25] Timoshenko SP, Goodier JN. 1985. **Theory of elasticity.** McGraw-Hill.

[26] Kang H, Wen Q, Janmey PA, Tang JX, Conti E, MacKintosh FC. 2009. **Nonlinear elasticity of stiff filament networks: strain stiffening, negative normal stress, and filament alignment in fibrin gels.** *J Phys Chem B* 113(12):3799-805.

[27] Baczynski K, Lipowsky R, Kierfeld J. 2007. **Stretching of buckled filaments by thermal fluctuations.** *Phys. Rev. E* 76:061914.

[28] Erk KA, Henderson KJ, Shull KR. 2010. **Strain stiffening in synthetic and biopolymer networks.** *Biomacromolecules.* 11:1358-1363.

[29] Gardel ML, Shin JH, MacKintosh FC, Mahadevan L, Matsudaira P, Weitz DA. 2004. **Elastic behavior of cross-linked and bundled actin networks.** *Science.* 304:1301-5.

[30] Landau LD, Lifshitz EM. **Theory of Elasticity** (Pergamon Press, London, 1986).

[31] Bhaskar A. 2009. **The effective Poisson's ratio of random cellular matter having bending dominated architecture.** *EPL*, 87:18004.

Chapter 10

Conclusions and Future Work

This thesis develops theoretical methods to efficiently evaluate the statistical mechanical properties of rod-like filaments and filamentous networks. The filament or filamentous network under investigation is viewed as a mechanical structure. The structure is discretized into segments using finite difference or finite element method. Its static equilibrium state under a given loading is determined in the first step. In the second step, we study the thermal fluctuations around the static equilibrium state using statistical mechanics. The energy around the ground state is approximated to quadratic order, so that the system is characterized by a stiffness matrix. Using the multidimensional Gaussian integral technique, partition function of the system is shown to be governed by the determinant of the stiffness matrix, while the thermal fluctuation is governed by the inverse of the stiffness matrix. Connections to penalty methods and spectral methods are also discussed.

Using the theoretical framework discussed above, we investigate the thermomechanical properties of a single filaments under end-to-end pulling force, distributed loads, and also under confinements. We also study the entropic elasticity of a 2D network under hydrostatic edge tension, simple shear and uniaxial tension. Taking the thermal fluctuations into account, material properties like the Young's modulus, shear and bulk moduli, as well as the Poisson's ratio are determined.

In other applications, we study the internal fluctuation of DNA in nanochannels used for genome mapping. The channel is about 100nm wide and we find a length-dependent transition between the de Gennes and Odijk regimes. Such a transition may result from the formation of local folded structures along the extended DNA backbone. For non-uniform channels, an entropic force causes the DNA to migrate to regions of higher entropy. We analyze a random walk model and derive the expression for the entropic force for a strongly confined polymer. Coupled migration and deformation of the polymer in various non-uniform channels are solved.

We also discuss forced unfolding of protein under different loading conditions using a system of three equations. Unlike previous Monte Carlo simulation methods, we do not assume zero folding rate in this thesis. As a result,

refolding events, such as folding-unfolding hoppings, are predicted in both constant force pulling mode and linearly increasing force pulling mode.

Future work in the entropic elasticity of polymer networks should include the study of square networks and also random networks. For the network problem, this thesis mainly focuses on the properties of a single hexagon, which represents a triangular network. But, it is of interest to know the dependence of the properties on the cross-linking density, on the network structure, on the heterogeneity of the filaments, and also on the properties of individual filaments. Using the theoretical framework developed in this thesis, it is also possible to describe the transition between affine and non-affine deformations of a network. Future investigations should also include 3D networks and twisted filaments.

Appendix A

Evaluating the Partition Function

We evaluate the partition function for a general discrete system in this section.

In Eq. 3.3, we have the partition function of the system:

$$Z = \exp\left(-\beta\mathcal{H}_0\right) \int \exp\left(-\vec{\theta}^T \mathbf{K} \cdot \vec{\theta}\right)\, d\vec{\theta}, \tag{A.1}$$

where $\mathbf{K} = \beta\mathbf{M}/2$. Since $\mathbf{K}$ is a real symmetric matrix, it can be diagonalized:

$$\mathbf{K} = \mathbf{R}^T \Lambda \cdot \mathbf{R}. \tag{A.2}$$

Changing the variables in Eq. A.1 from $\vec{\theta}$ to $\vec{\phi}$, we arrive at:

$$Z = \exp\left(-\beta\mathcal{H}_0\right) \prod_{i=1}^{D} \int \exp\left(-\Lambda_i \phi_i^2\right)\, d\phi_i = \exp\left(-\beta\mathcal{H}_0\right) \sqrt{\frac{\pi^D}{\det \Lambda}}. \tag{A.3}$$

Finally, since $\det \mathbf{R} = 1$, the partition function can be expressed as:

$$Z = \exp\left(-\beta\mathcal{H}_0\right) \sqrt{\frac{\pi^D}{\det \mathbf{K}}} = \exp\left(-\beta\mathcal{H}_0\right) \sqrt{\frac{(2\pi k_B T)^D}{\det \mathbf{M}}}. \tag{A.4}$$

Appendix B

$\det \mathbf{M}$ for the Hinged-hinged Chain

The $(N+1)$ dimension matrix $\mathbf{M}$ for the hinged-hinged case is given by (Eq. 4.30), which is:

$$\mathbf{M} = \begin{pmatrix} \beta(\kappa_1+f) & -\beta\kappa_1 & 0 & \cdots & 0 & -I/2 \\ -\beta\kappa_1 & \beta(\kappa_1+\kappa_2+f) & -\beta\kappa_2 & \cdots & 0 & -I/2 \\ 0 & -\beta\kappa_2 & \beta(\kappa_2+\kappa_3+f) & \cdots & 0 & -I/2 \\ & \cdots & \cdots & \cdots & \cdots & \\ 0 & 0 & 0 & \cdots & -\beta\kappa_{N-1} & -I/2 \\ 0 & 0 & 0 & \cdots & \beta(\kappa_{N-1}+f) & -I/2 \\ -I/2 & -I/2 & -I/2 & \cdots & -I/2 & 0 \end{pmatrix} \tag{B.1}$$

To evaluate the determinant of $\mathbf{M}$, we introduce another matrix $\mathbf{M}^*$ as:

$$\mathbf{M}^* = \mathbf{R}^T\mathbf{P}\mathbf{M}\mathbf{Q}\mathbf{R}, \tag{B.2}$$

where the (N+1) dimensional matrices $\mathbf{R}$, $\mathbf{P}$ and $\mathbf{Q}$ are:

$$\mathbf{P} = \operatorname{diag}\left(\beta^{-1}, \beta^{-1}, \cdots, \beta^{-1}, 2I\right), \tag{B.3}$$

$$\mathbf{Q} = \operatorname{diag}\left(1, 1, \cdots, 1, 2I\beta\right), \tag{B.4}$$

$$\mathbf{R} = \begin{pmatrix} 1 & 0 & 0 & \cdots & 0 & 0 & 0 \\ 1 & 1 & 0 & \cdots & 0 & 0 & 0 \\ 1 & 1 & 1 & \cdots & 0 & 0 & 0 \\ & \cdots & \cdots & \cdots & \cdots & & \\ 1 & 1 & 1 & \cdots & 1 & 0 & 0 \\ 1 & 1 & 1 & \cdots & 1 & 1 & 0 \\ 0 & 0 & 0 & \cdots & 0 & 0 & 1 \end{pmatrix} \tag{B.5}$$

From Eq. B.2 and the definitions of the matrics $\mathbf{P}$, $\mathbf{Q}$ and $\mathbf{R}$, we get:

$$\det \mathbf{M} = -\frac{\beta^{N-1}}{4} \det \mathbf{M}^*. \tag{B.6}$$

Now we need to evaluate $\det \mathbf{M}^*$.

Using Eq. B.2, we get the matrix $\mathbf{M}^*$:

$$\mathbf{M}^* = \begin{pmatrix} \mathbf{M}_{\text{in}} & \vec{G} \\ \vec{G}^T & 0 \end{pmatrix}, \tag{B.7}$$

where the N dimensional $\mathbf{M}_{\text{in}}$ is given by:

$$\mathbf{M}_{\text{in}} = \begin{pmatrix} Nf & (N-1)f & (N-2)f & \cdots & 2f & f \\ (N-1)f & \kappa_1+(N-1)f & (N-2)f & \cdots & 2f & f \\ (N-2)f & (N-2)f & \kappa_2+(N-2)f & \cdots & 2f & f \\ & \cdots & \cdots & \cdots & \cdots & \\ 2f & 2f & 2f & \cdots & \kappa_{N-2}+2f & f \\ f & f & f & \cdots & f & \kappa_{N-1}+f \end{pmatrix} \tag{B.8}$$

and N dimensional vector $\vec{G}^T$ is given by:

$$\vec{G}^T = [N, N-1, N-2, \cdots, 2, 1]\,. \tag{B.9}$$

But for the type of matrix in form of Eq. B.7, we have the following formula (see [1]):

$$\det \mathbf{M}^* = -\det \mathbf{M}_{\text{in}} \left(\vec{G}^T \cdot \mathbf{M}_{\text{in}}^{-1} \vec{G}\right). \tag{B.10}$$

So now we need to compute $\det \mathbf{M}_{\text{in}}$ as well as $\vec{G}^T \cdot \mathbf{M}_{\text{in}}^{-1}\vec{G}$.

We first perform elementary row operations on $\mathbf{M}_{\text{in}}$, transform it into a diagonal matrix and find its determinant given by:

$$\det \mathbf{M}_{\text{in}} = f \prod_{i=1}^{N-1} \lambda_i, \tag{B.11}$$

where the sequence λ_i is given by:

$$\lambda_1 = 2\kappa_1 + f, \quad \lambda_i = (2\kappa_i + f) - \frac{\kappa_i \kappa_{i-1}}{\lambda_{i-1}} \quad (i = 2, 3, \cdots N-1). \tag{B.12}$$

Next, to evaluate $\vec{G}^T \cdot \mathbf{M}_{\text{in}}^{-1}\vec{G}$, we define $\vec{g}$ as:

$$\mathbf{M}_{\text{in}}\, \vec{g} = \vec{G}, \tag{B.13}$$

so that

$$\vec{G}^T \cdot \mathbf{M}_{\text{in}}^{-1}\vec{G} = \vec{g}^T \cdot \mathbf{M}_{\text{in}}\, \vec{g}, \tag{B.14}$$

where the symmetry property of $\mathbf{M}_{\text{in}}$ has been used. But Eq. B.13 is easy to solve and one can verify that:

$$\vec{g}^T = \left[f^{-1}, 0, 0, \cdots, 0, 0\right], \tag{B.15}$$

and therefore using Eq. B.8, Eq. B.14 and Eq. B.15, we get:

$$\vec{G}^T \mathbf{M}_{\text{in}}^{-1}\vec{G} = \frac{N}{f}. \tag{B.16}$$

Finally, Eq.B.6, Eq. B.10, Eq. B.11 together with Eq. B.16 leads to:

$$\det \mathbf{M} = \frac{N\beta^{N-1}}{4} \times \prod_{i=1}^{N-1} \lambda_i. \tag{B.17}$$

Appendix C

Force-extension Relation for a Homogeneous Wormlike Chain

For a homogeneous chain, we have $K_i \equiv K$ and $\kappa_i \equiv \kappa$. Using the definition of the sequence λ_i for a hinged-hinged chain (Eq. 4.32), one can verify by mathematical induction that:

$$\prod_{k=i}^{N-1} \lambda_k = \lambda_i \cdot p_{N-i-1} - rd \cdot p_{N-i-2}, \quad (i \leq N-2) \tag{C.1}$$

where r, d are given by:

$$r = \frac{2\kappa + f + \sqrt{4\kappa f + f^2}}{2}, \quad d = \frac{2\kappa + f - \sqrt{4\kappa f + f^2}}{2}, \tag{C.2}$$

and the sequence p_i is given by:

$$p_i = \frac{r^{i+1} - d^{i+1}}{r - d}. \tag{C.3}$$

Using Eq. C.1 to Eq. C.3 and also Eq. 4.32, we get:

$$\prod_{k=1}^{N-1} \lambda_k \;=\; \lambda_1 \cdot p_{N-2} - rd \cdot p_{N-3} = \frac{r^N - d^N}{r - d}. \tag{C.4}$$

Hence,

$$\sum_{k=1}^{N-1} \frac{\lambda_i'}{\lambda_i} \;=\; \frac{d}{dF}\left(\log \prod_{k=1}^{N-1} \lambda_k\right) \tag{C.5}$$

$$\;=\; \frac{Nr'}{r} \cdot \frac{1 - \left(\frac{d}{r}\right)' \cdot \left(\frac{d}{r}\right)^{N-1}}{1 - \left(\frac{d}{r}\right)^N} - \frac{r'}{r} \cdot \frac{1 - \left(\frac{d}{r}\right)'}{1 - \left(\frac{d}{r}\right)}. \tag{C.6}$$

Using the definitions of r, d (Eq. C.2) as well as those for κ, f (Eq. 4.5), we get:

$$r = \frac{K}{2L}N + \frac{\sqrt{KF}}{2} + O(N^{-1}), \tag{C.7}$$

$$r' = \frac{1}{4}\sqrt{\frac{K}{F}} + \frac{L}{4N} + O(N^{-2}), \tag{C.8}$$

$$d = \frac{K}{2L}N - \frac{\sqrt{KF}}{2} + O(N^{-1}), \tag{C.9}$$

$$d' = -\frac{1}{4}\sqrt{\frac{K}{F}} + \frac{L}{4N} + O(N^{-2}). \tag{C.10}$$

Plugging Eq. C.7 to Eq. C.10 into Eq. C.6, taking the limit as $N \to +\infty$, we get:

$$\lim_{N\to\infty} \sum_{k=1}^{N-1} \frac{\lambda_i'}{\lambda_i} \quad = \quad \frac{1}{2}\left[\frac{L}{\sqrt{KF}} \coth\left(L\sqrt{\frac{F}{K}}\right) - \frac{1}{F}\right]. \tag{C.11}$$

Putting Eq. C.11 into Eq. 4.36, we recover the force-extension relation for a homogeneous hinged-hinged continuous rod [2]:

$$\langle x_{\text{homo}} \rangle = L - \frac{Lk_BT}{4\sqrt{KF}} \coth\left(\frac{FL}{\sqrt{KF}}\right) + \frac{k_BT}{4F}. \tag{C.12}$$

Appendix D

Force-extension Relation for a Special Heterogeneous Wormlike Chain

For a special heterogeneous wormlike chain, we have

$$\kappa_i = \begin{cases} \kappa_I & 1 \le i \le s \\ \kappa_{II} & (s+1) \le i \le N \end{cases} \tag{D.1}$$

Here s is an integer indicating the segment that separates the two regions of the chain (s is not the arc length in this section).

Hence, under hinged-hinged conditions, the sequence λ_i is (Eq. 4.32):

$$\lambda_i = \begin{cases} 2\kappa_I + f & i = 1 \\ 2\kappa_I + f - \frac{\kappa_I^2}{\lambda_{i-1}} & 2 \le i \le s \\ 2\kappa_{II} + f - \frac{\kappa_I \kappa_{II}}{\lambda_s} & i = s+1 \\ 2\kappa_{II} + f - \frac{\kappa_{II}^2}{\lambda_{i-1}} & s+2 \le i \le (N-1) \end{cases} \tag{D.2}$$

Using mathematical induction, one can verify that:

$$\prod_{k=i}^{N-1} \lambda_k = \begin{cases} p_{N-i-1}\lambda_i - r_2 d_2 \cdot p_{N-i-2} & (s+1) \le i \le (N-2) \\ p_{N-s-1}\lambda_s - \kappa_I \kappa_{II} \cdot p_{N-s-2} & i = s \\ p_{N-i-1}\lambda_i - r_1 d_1 \cdot p_{N-i-2} & 1 \le i \le (s-1) \end{cases} \tag{D.3}$$

where p_i, r_i and d_i are given by:

$$p_i = \begin{cases} \frac{r_2^{i+1} - d_2^{i+1}}{r_2 - d_2} & 0 \le i \le (N-s-2) \\ (r_2 + d_2) p_{N-s-2} - r_2 d_2 p_{N-s-3} & i = N-s-1 \\ \frac{r_1^{i-N+s+2} - d_1^{i-N+s+2}}{r_1 - d_1} \cdot p_{N-s-1} - \frac{r_1^{i-N+s+1} - d_1^{i-N+s+1}}{r_1 - d_1} \cdot \kappa_I \kappa_{II} \cdot p_{N-s-2} & N-s \le i \le (N-2) \end{cases} \tag{D.4}$$

$$r_1 = \frac{2\kappa_I + f + \sqrt{4\kappa_I f + f^2}}{2}, \quad d_1 = \frac{2\kappa_I + f - \sqrt{4\kappa_I f + f^2}}{2}, \tag{D.5}$$

$$r_2 = \frac{2\kappa_{II} + f + \sqrt{4\kappa_{II} f + f^2}}{2}, \quad d_2 = \frac{2\kappa_{II} + f - \sqrt{4\kappa_{II} f + f^2}}{2}. \tag{D.6}$$

In particular, using Eq. D.3 and setting $i = 1$, we get:

$$\prod_{k=1}^{N-1} \lambda_k = \frac{\left(r_2^{N-s} - d_2^{N-s}\right)\left(r_1^{s+1} - d_1^{s+1}\right) - \kappa_I \kappa_{II}\left(r_2^{N-s-1} - d_2^{N-s-1}\right)\left(r_1^{s} - d_1^{s}\right)}{(r_1 - d_1)(r_2 - d_2)} \tag{D.7}$$

Note that Eq. D.7 reduces to the homogeneous case (Eq. C.4) when we set $s = 0$, or $s = N - 1$, or $r_1 = r_2$, $d_1 = d_2$.

Using Eq. D.5, Eq. D.6 as well as Eq. 4.5, we have:

$$\frac{r_i'}{r_i} = \frac{L}{2K_i}\sqrt{\frac{K_i}{F}}\frac{1}{N} + O(N^{-3}), \tag{D.8}$$

$$\frac{d_i}{r_i} = 1 - \frac{2L\sqrt{K_i F}}{K_i N} + \frac{2FL^2}{K_i N^2} + O(N^{-3}), \tag{D.9}$$

$$\left(\frac{d_i}{r_i}\right)^u = \exp\left(\frac{-2uL\sqrt{K_i F}}{NK_i}\right) + O(N^{-2}) \tag{D.10}$$

where u is a function of N and it satisfies $u(N) \sim N$ as $N \to +\infty$.

$$\frac{d_i'}{r_i'} = -1 + 2L\sqrt{\frac{F}{K_i}}\frac{1}{N} + O(N^{-2}), \tag{D.11}$$

$$\frac{\kappa_i}{r_i} = 1 - \frac{L\sqrt{K_i F}}{K_i N} + O(N^{-2}). \tag{D.12}$$

Here to make the formulae compact, we use κ_1, κ_2, K_1, K_2 to denote κ_I, κ_{II}, K_I and K_{II}. Note that the subscripts 1 and 2 in this section do not mean the 1st and 2nd segments of the chain.

Similarly as in Appendix C, we can use Eq. D.8 to Eq. D.12 to evaluate $\sum \lambda_i'/\lambda_i$ and then the function $\Delta(F)$ (take $N \to +\infty$ while keeping $Nl = L$ fixed), the result is:

$$\Delta(F) = \frac{\frac{1}{E_1\sqrt{F}}\cosh\left(\sqrt{\frac{F}{F_1}}\right) + \frac{2\overline{K^{-1/2}}}{F}\sinh\left(\sqrt{\frac{F}{F_1}}\right) + \frac{1}{E_0\sqrt{F}}\cosh\left(\sqrt{\frac{F}{F_0}}\right) + \frac{\Delta K^{-1/2}}{F}\sinh\left(\sqrt{\frac{F}{F_0}}\right)}{8\overline{K^{-1/2}}\sinh\left(\sqrt{\frac{F}{F_1}}\right) + 4\Delta K^{-1/2}\sinh\left(\sqrt{\frac{F}{F_0}}\right)} - \frac{1}{2F}. \tag{D.13}$$

The meanings of $\overline{K^{-1/2}}$, $\Delta K^{-1/2}$, E_1, E_0, F_1 and F_0 are given in Eq. 4.39 to Eq. 4.41. Using $x = L - k_B T \Delta(F)$ (Eq. 4.13), we get the force-extension relation for a special heterogeneous rod, which is shown in the main text (Eq. 4.38).

Appendix E

$\det \mathbf{M}$ for the Clamped-clamped Chain

The $(N-1)$ dimensional matrix $\mathbf{M}$ for the clamped-clamped chain is given by Eq. 4.55, which is:

$$\mathbf{M} = \begin{pmatrix} \beta(\kappa_1+\kappa_2+f) & -\beta\kappa_2 & 0 & \cdots & 0 & -I/2 \\ -\beta\kappa_2 & \beta(\kappa_2+\kappa_3+f) & -\beta\kappa_3 & \cdots & 0 & -I/2 \\ 0 & -\beta\kappa_3 & \beta(\kappa_3+\kappa_4+f) & \cdots & 0 & -I/2 \\ & \cdots & \cdots & \cdots & \cdots & \\ 0 & 0 & 0 & \cdots & -\beta\kappa_{N-2} & -I/2 \\ 0 & 0 & 0 & \cdots & \beta(\kappa_{N-2}+\kappa_{N-1}+f) & -I/2 \\ -I/2 & -I/2 & -I/2 & \cdots & -I/2 & 0 \end{pmatrix} \tag{E.1}$$

To evaluate the determinant of $\mathbf{M}$, we introduce another matrix $\mathbf{M}^*$ as:

$$\mathbf{M}^* = \mathbf{PMQ}, \tag{E.2}$$

where the $(N-1)$ dimensional matrix $\mathbf{P}$ and $\mathbf{Q}$ are:

$$\mathbf{P} = \operatorname{diag}\left(\beta^{-1}, \beta^{-1}, \cdots, \beta^{-1}, 2I\right), \tag{E.3}$$

$$\mathbf{Q} = \operatorname{diag}\left(1, 1, \cdots, 1, 2I\beta\right). \tag{E.4}$$

Note that the matrics $\mathbf{P}$ and $\mathbf{Q}$ defined here are the same as those defined for the hinged-hinged chain (Eq. B.3 and Eq. B.4) except that their dimensionalities are different.

From Eq. E.2 and the definitions of the matrics $\mathbf{P}$, $\mathbf{Q}$, we get:

$$\det \mathbf{M} = -\frac{\beta^{N-3}}{4} \det \mathbf{M}^*. \tag{E.5}$$

Now we need to evaluate $\det \mathbf{M}^*$.

Using Eq. E.2, we get the matrix $\mathbf{M}^*$:

$$\mathbf{M}^* = \begin{pmatrix} \mathbf{M}_{\text{in}} & \vec{G} \\ \vec{G}^T & 0 \end{pmatrix}, \tag{E.6}$$

where the $(N-2)$ dimensional $\mathbf{M}_{\text{in}}$ in this case is given by:

$$\mathbf{M}_{\text{in}} = \begin{pmatrix} \kappa_1+\kappa_2+f & -\kappa_2 & 0 & \cdots & 0 \\ -\kappa_2 & \kappa_2+\kappa_3+f & -\kappa_3 & \cdots & 0 \\ 0 & -\kappa_3 & \kappa_3+\kappa_4+f & \cdots & 0 \\ & \cdots & \cdots & \cdots & \\ 0 & 0 & 0 & \cdots & -\kappa_{N-2} \\ 0 & 0 & 0 & \cdots & \kappa_{N-2}+\kappa_{N-1}+f \end{pmatrix} \tag{E.7}$$

and $(N-2)$ dimensional vector $\vec{G}^T$ is given by:

$$\vec{G}^T = [1, 1, 1, \cdots, 1, 1]\,. \tag{E.8}$$

Again, for the type of matrix in form of Eq. E.6, we have the formula [1]:

$$\det \mathbf{M}^* = -\det \mathbf{M}_{\text{in}} \left(\vec{G}^T \cdot \mathbf{M}_{\text{in}}^{-1} \vec{G}\right). \tag{E.9}$$

So now we need to compute $\det \mathbf{M}_{\text{in}}$ as well as $\vec{G}^T \cdot \mathbf{M}_{\text{in}}^{-1}\vec{G}$.

We first perform the elementary row operations on $\mathbf{M}_{\text{in}}$ and find that its determinant is given by:

$$\det \mathbf{M}_{\text{in}} = \prod_{i=1}^{N-2} \lambda_i, \tag{E.10}$$

where the sequence λ_i is given by:

$$\lambda_1 = \kappa_1+\kappa_2+f, \quad \lambda_i = (\kappa_i+\kappa_{i+1}+f) - \frac{\kappa_i^2}{\lambda_{i-1}} \quad (i = 2, 3, \cdots N-2). \tag{E.11}$$

Next, to evaluate $\vec{G}^T \cdot \mathbf{M}_{\text{in}}^{-1}\vec{G}$, which we will denote as R below, we again define $\vec{g}$ as:

$$\mathbf{M}_{\text{in}}\, \vec{g} = \vec{G}, \tag{E.12}$$

so that

$$R = \vec{G}^T \cdot \mathbf{M}_{\text{in}}^{-1}\vec{G} = \vec{g}^T \cdot \mathbf{M}_{\text{in}}\, \vec{g}. \tag{E.13}$$

We solve Eq. E.12 and get $\vec{g}$:

$$g_{N-2} = \frac{\rho_{N-2}}{\lambda_{N-2}}, \quad g_i = \frac{\rho_i + \kappa_{i+1} g_{i+1}}{\lambda_i}. \quad (i = N-3, N-4, \cdots 1) \tag{E.14}$$

where the sequence ρ_i is given by:

$$\rho_i = 1 + \sum_{j=1}^{i-1} \left(\prod_{s=i-j+1}^{i} \frac{\kappa_s}{\lambda_{s-1}} \right). \tag{E.15}$$

Therefore using Eq. E.7, Eq. E.13 and Eq. E.14, we get:

$$R = \sum_{i=1}^{N-2} (\kappa_i + \kappa_{i+1} + f) g_i^2 - 2 \sum_{i=1}^{N-3} \kappa_{i+1} g_i g_{i+1}. \tag{E.16}$$

Finally, Eq.E.5, Eq. E.9, Eq. E.10, Eq. E.13 together with Eq. E.16 lead to:

$$\det \mathbf{M} = \left(\frac{\beta^{N-3} R}{4}\right) \prod_{i=1}^{N-2} \lambda_i. \tag{E.17}$$

Appendix F

Transverse Fluctuation Scales as T

We need to show $\langle y_i^2 \rangle \sim T$ for the hinged-hinged and clamped-clamped chain in this section. For chains under both the boundary conditions, the matrix $\mathbf{M}$ have the form (see Eq. B.1 and Eq. E.1):

$$\mathbf{M} = \begin{pmatrix} \beta \mathbf{J} & \vec{v} \\ \vec{v}^T & 0 \end{pmatrix}. \tag{F.1}$$

Using Eq. F.1, one can verify by matrix multiplication (or see [1]) that:

$$\mathbf{M}^{-1} = \begin{pmatrix} \beta^{-1} \left[\mathbf{J}^{-1} - \mathbf{J}^{-1} \vec{v} \left(\vec{v}^T \mathbf{J}^{-1} \vec{v} \right)^{-1} \vec{v}^T \mathbf{J}^{-1} \right] & \mathbf{J}^{-1} \vec{v} \left(\vec{v}^T \mathbf{J}^{-1} \vec{v} \right)^{-1} \\ \left(\vec{v}^T \mathbf{J}^{-1} \vec{v} \right)^{-1} \vec{v}^T \mathbf{J}^{-1} & -\beta \left(\vec{v}^T \mathbf{J}^{-1} \vec{v} \right)^{-1} \end{pmatrix}. \tag{F.2}$$

Note that $\langle \theta_i \cdot \theta_j \rangle$ is determined by the upper corner submatrix of $\mathbf{M}^{-1}$ (Eq. 4.66, the rest of the elements in the matrix $\mathbf{M}^{-1}$ correspond to $\langle \theta_i \cdot k \rangle$, which we are not interested in. Here k is from the Fourier transform of the Dirac delta function in Eq. 4.26). Therefore, noticing that both $\mathbf{J}$ and $\vec{v}$ do not depend on β, we have:

$$\langle \theta_i \cdot \theta_j \rangle = \left(\mathbf{M}^{-1} \right)_{ij} = \beta^{-1} \left[\mathbf{J}^{-1} - \mathbf{J}^{-1} \vec{v} \left(\vec{v}^T \mathbf{J}^{-1} \vec{v} \right)^{-1} \vec{v}^T \mathbf{J}^{-1} \right]_{ij} \sim T. \tag{F.3}$$

Finally, using the relation between $\langle y_i^2 \rangle$ and $\langle \theta_i \cdot \theta_j \rangle$ (Eq. 4.63), we conclude that:

$$\langle y_i^2 \rangle \sim T. \tag{F.4}$$

Appendix G

Partition Function for a Fixed Extension Ensemble

In this section, we shall derive the general expression for the partition function for a wormlike chain in a fixed extension ensemble.

By definition, the partition function is the sum of the Boltzmann weight for all the allowed configurations:

$$Z_x = \sum_\nu \exp(-\beta E_\nu). \tag{G.1}$$

The average energy relates to the partition function by:

$$\langle E \rangle = \frac{1}{Z_x} \sum_\nu E_\nu \exp(-\beta E_\nu) = -\frac{\partial \log Z_x}{\partial \beta}. \tag{G.2}$$

On the other hand, the equipartition theorem reads:

$$\langle E \rangle = E_e(x) + \frac{D_x}{2} k_B T, \tag{G.3}$$

where $E_e(x)$ is the ground state energy for the fixed extension ensemble and D_x is the degrees of freedom of the system.

Eq. G.2 and Eq. G.3 leads to a partial differential equation for Z_x:

$$\frac{\partial \log Z_x}{\partial \beta} = -E_e(x) - \frac{D_x}{2} k_B T, \tag{G.4}$$

the solution of which is:

$$\log Z_x = -\beta E_e(x) - \frac{D_x}{2} \log \beta - U(x), \tag{G.5}$$

where $U(x)$ is an unknown function of x whose physical meaning will be discussed below. The important point here is that $U(x)$ is independent of the temperature T.

The free energy of the fixed extension ensemble can be evaluated from the partitioin function:

$$G = -k_B T \log Z_x = E_e(x) + \frac{D_x}{2} k_B T \log \beta + k_B T U(x). \tag{G.6}$$

Therefore, the force extension relation is:

$$F = \frac{\partial G}{\partial x} = \frac{\partial}{\partial x} \left[E_e(x) + k_B T U(x) \right]. \tag{G.7}$$

This relation tells us that the area $A(x)$ below the force-extension curve, up to a unknown constant is:

$$\beta A(x) = \beta E_e(x) + U(x) + C_0(T). \tag{G.8}$$

Plugging the above equation back to Eq. G.5, we obtain:

$$\log Z_x = -\frac{D_x}{2} \log \beta - \beta A(x) + C_0(T). \tag{G.9}$$

Appendix H

Theory for the 2D Chains

Let $\hat{t}(s)$ be the tangent vector of a 2D chain along the arc length s. In a standard reference diad $\{\hat{e}_1, \hat{e}_2\}$, the tangent vector can be expressed as:

$$\hat{t}(s) = [\cos\theta,\ \sin\theta\,], \tag{H.1}$$

where $\theta(s)$ is the angle formed between $\hat{t}(s)$ and $\hat{e}_1$. Here $\hat{e}_1$ is chosen to be the direction of the axis of the microchannel.

The energy of the 2D chain consists of the bending, confinement and potential energies and can be written as:

$$E = \int_0^L \left[\frac{K(s)}{2} \left| \frac{d\hat{t}}{ds} \right|^2 + \frac{\Xi(s)}{2}\, y^2 \right] ds - Fx(L). \tag{H.2}$$

To use the Gaussian integral method, we discretize the chain into $2N$ segments, and denote the tangent angle with respect to the $\hat{e}_1$ axis for each segment as θ_i $(i = 1, 2, \cdots, 2N)$. The energy of the chain depends not only on these $2N$ configurational angles but also on where the chain is located inside the channel. A chain located close to the channel wall would have higher energy than one with the same $\{\theta_i\}$ but located at the center of the channel. To take this into account, we denote y_N as the y coordinate of the midpoint of the chain, and the energy of the discretized chain can be written as:

The configuration of the chain is characterized by these $2N$ angles and the y coordinate of the midpoint of the chain.

The internal section we are interested in is $i \in [p, q]$. Then Eq. H.2 becomes a quadratic expression in terms of θ_i:

$$E = \sum_{i=1}^{2N} a_i \theta_i^2 - 2 \sum_{i=1}^{2N-1} \kappa_i \theta_i\, \theta_{i+1} + \sum_{m=1}^{N} \sum_{n=1}^{N} \Theta_t \theta_m \theta_n - 2 \sum_{i=1}^{N} \Theta_t \theta_0 \theta_i + 2 \sum_{i=N+1}^{2N} \Theta t \theta_0 \theta_i + \Theta_0 \theta_0^2 - FL, \tag{H.3}$$

where

$$\kappa_i = \begin{cases} 0 & (\text{if } i = 0 \text{ or } 2N) \\ K_i/(2l) & (\text{else}) \end{cases} \qquad a_i = \kappa_{i-1} + \kappa_i + f \tag{H.4}$$

The partition function of the virtual system can be evaluated as:

$$Z = \exp\left(-\frac{E_0}{k_B T}\right) \int \exp\left(-\frac{\vec{\theta}^T \mathbf{M} \cdot \vec{\theta}}{k_B T}\right) d\vec{\theta} = \exp\left(-\frac{E_0}{k_B T}\right) \cdot \frac{(k_B T \pi)^{N/2}}{\sqrt{\det \mathbf{M}}} \tag{H.5}$$

The free energy of the system is therefore:

$$G = E_0 - \frac{N k_B T}{2} \log(k_B T \pi) + \frac{k_B T}{2} \log \det \mathbf{M}. \tag{H.6}$$

The angle fluctuation is:

$$\langle \theta_i \theta_j \rangle = \frac{\int (\theta_i \theta_j) \exp\left(-\frac{\vec{\theta}^T \mathbf{M} \cdot \vec{\theta}}{k_B T}\right) d\vec{\theta}}{\int \exp\left(-\frac{\vec{\theta}^T \mathbf{M} \cdot \vec{\theta}}{k_B T}\right) d\vec{\theta}} = \frac{k_B T}{2} \left(\mathbf{M}^{-1}\right)_{ij} \tag{H.7}$$

Appendix I

Relation Between the End-to-end Extension $\langle x \rangle$ and Channel Width D for Wang and Gao's Theory

For a strongly confined DNA under force F, the total extension $\langle x \rangle$ as a function as F and Ξ (stiffness of the effective confinement potential) is found to be [3]:

$$\langle x \rangle = L - \frac{k_B T L}{2\sqrt{\kappa}} \frac{1}{\sqrt{F + 2\sqrt{\Xi(D)\kappa}}}, \tag{I.1}$$

where κ is the bending modulus of the polymer, Ξ relates to the channel width D in the following way:

$$\Xi = \frac{c^4}{4} \left(\frac{k_B T}{\kappa^{1/4} D^2} \right)^{4/3}., \tag{I.2}$$

and $c = 2.5$ is a constant for a cylindrical channel [3]. Setting $F = 0$ and plugging Eq.I.2 into Eq.I.1, we obtain:

$$\langle x \rangle = L \left[1 - \frac{1}{5} \left(\frac{D}{\xi_p} \right)^{2/3} \right]. \tag{I.3}$$

Appendix J

Fluctuation for Short Internal Segments

The fluctuation for short internal segments is expected to be in the de Gennes' moderately confined regime. In Fig. J.1, we plot the internal fluctuation profiles for short segments with $\langle x \rangle < 10\mu$m for 4 different sets of DNA: (1) λ DNA, (2) T4 DNA, (3) fragmented T4 DNA and (4) BAC DNA. Note that here we not only have short DNA, like λ DNA, but also long DNA like T4 and BAC DNA, but we discuss only the short internal segments on them in this section. The results for all the 4 sets of DNA are almost identical, and they all match with de Gennes' theory with NO fitting parameters. This result suggests that for all internal segments with $\langle x \rangle \leq 10\mu$m, irrespective of the sequence and length, de Gennes' theory works.

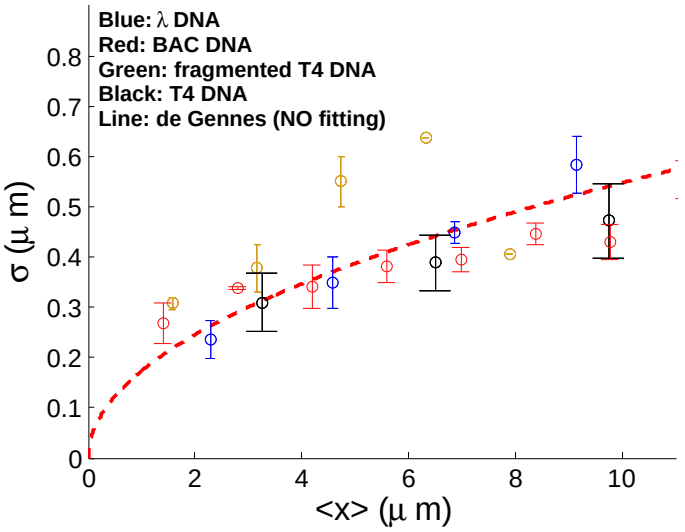

Figure J.1: σ versus $\langle x \rangle$ profile for the $\langle x \rangle \leq 10\mu$m region. Fluctuation of short internal DNA segments from different sources matches with de Gennes' theory with NO fitting parameters.

Appendix K

Heterogeneity on the Backbone of DNA

In experiments, we observe heterogeneity in the intensity profile of the YOYO-1 dye along the backbone of the DNA (Fig. K.1), which can be evidence for the formation of local folded structures. For the left figure of Fig. K.1, in the intensity profiles corresponding to 0s and 1.6s, localized peaks are clearly apparent (Fig. K.1). These localized peaks could represent the deGennes' blobs or local folded structures. On the other hand, regions of uniform intensity could correspond to DNA in the Odijk regime. Heterogeneity in the DNA backbone fluorescence intensity is also shown in the right figure of Fig. K.1. This figure shows two internal labels coming together, which is evidence for formation of local folded structure. Although these images gives us a visual picture of DNA confined to a nanochannel, we believe that the two-peak probability distributions shown in the main text provide much stronger evidence of the transition between the deGennes' and Odijk regimes than the fluorescence intensity profiles.

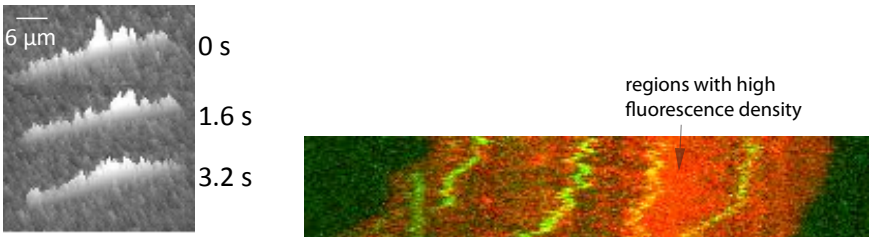

Figure K.1: (A) The backbone intensity images of a confined DNA fragment ($\sim$34μm) stained with YOYO-1 iodide in a 80nm$\times$130nm channel. The images are recorded at time interval of 1.6s. From the heterogeneity of the intensity profile, we infer that there exist some local structures on the backbone. (B) Images of the time series (8 seconds) of a T4 DNA fragment ($\sim$32μm). The backbone of the DNA is shown in red and the internal dyes are shown in green. The region with high fluorescence density is the area with local folded structures. The green traces are the trajectories of internal dye labels in the time series. This image shows two internal dyes coming together, which is evidence of formation of local folded structures.

Appendix L

Total Extension versus L Relation

As another evidence that the deflection theory works for segments with $\langle x \rangle \gtrsim 10\mu$m, we measure the end-to-end extension for DNA with different lengths (but with mean end-to-end extension greater than 10 microns) in a 60nm$\times$100nm channel and plot the result against the contour length (Fig.L.1). A linear relation is found with a fitting result of $\langle x \rangle = 0.5L$. This is consistent with the deflection theories (formulae shown below), which, with numerical values plugged in, gives $\langle x \rangle \approx 0.7L$.

$$\frac{\langle x \rangle}{L} \approx 1 - \alpha_\circ \left(\frac{D}{\xi_p}\right)^{2/3}, \quad \alpha_\circ = 0.17, \quad \text{(Odijk, [4])} \tag{L.1}$$

$$\frac{\langle x \rangle}{L} = 1 - \frac{1}{5}\left(\frac{D}{\xi_p}\right)^{2/3}, \quad \text{(Wang and Gao, [3])} \tag{L.2}$$

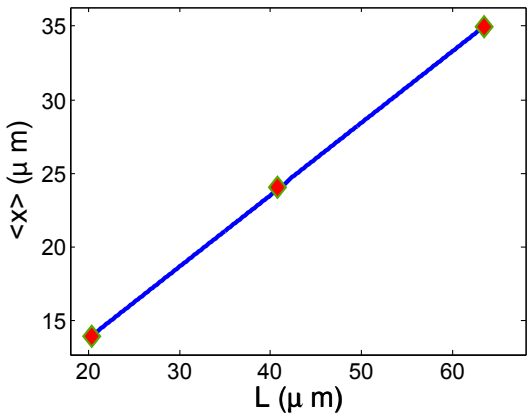

Figure L.1: Mean end-to-end extension $\langle x \rangle$ versus contour length L of confined DNA in a 60nm×100nm channel. The fitting result is $x = 0.5L$, which is consistent with the prediction of the Odijk deflection theory: $x = 0.7L$.

Appendix M

Distribution of Extension in the Deflection Regime

The force-extension relation for a 3D confined chain in Odijk's regime is given in Eq.I.1 [3].

Since $dG = -xdF$, we can integrate Eq.I.1 to obtain the free energy $G = G(F,T)$:

$$\begin{aligned} G &= -\int x dF && \text{(M.1)} \\ &= -\int \left[L - \frac{k_B T L}{2\sqrt{K}} \frac{1}{\sqrt{F + 2\sqrt{\Xi K}}} \right] dF && \text{(M.2)} \\ &= -\frac{(k_B T L)^2}{4K} \frac{2x - L}{(L-x)^2} + \text{const} && \text{(M.3)} \end{aligned}$$

This is the free energy in a fixed force ensemble, i.e $G(F,T) = E - TS - Fx$. We need the free energy in a fixed extension ensemble. Therefore:

$$\begin{aligned} G(x,T) &= G(F,T) + Fx && \text{(M.4)} \\ &= \frac{(k_B T L)^2}{4K} \frac{1}{L-x} - 2\sqrt{\Xi K} x + \text{const} && \text{(M.5)} \end{aligned}$$

Denote $\rho = x/L$, then the free energy is:

$$\frac{G(\rho,T)}{k_B T} = \frac{A}{1-\rho} - B\rho + \text{const}, \qquad \text{(M.6)}$$

where

$$A = \frac{L}{4\xi_p}, \quad B = \frac{4c^2 \xi_p^{1/3} L}{D^{4/3}}, \quad c = 1.1 \qquad \text{(M.7)}$$

Therefore, the probability distribution is:

$$P(\rho) = P_0 \exp\left[B\rho - \frac{A}{1-\rho} \right] \qquad \text{(M.8)}$$

with A, B given in Eq. M.7 and P_0 being the normalization constant.

Appendix N

Results of Entropy-induced Migration Derived from the Sackur-Tetrode Equation

The conclusions drawn from the random walk model in the main text can be understood from a different point of view by considering the heat production rate of the system. In this section, we show that exactly the same results can be re-derived using the Sackur-Tetrode formula for the entropy of ideal gases.

Again, we imagine N particles diffusing on the z axis. In any infinitesimal interval dz, there are $NP(z)dz$ number of particles, where $P(z)$ is the particle density distribution. Using the Sackur-Tetrode formula [5], the entropy at position z can be written as:

$$\begin{aligned} S(z) = NP(z)k_B \log\left[\frac{V(z)}{h^3}\left(2\pi m k_B T\right)^{3/2}\right] \\ - NP(z)k_B \log\left[NP(z)\right] + \frac{5}{2}NP(z)k_B, \end{aligned} \tag{N.1}$$

where h is the Planck constant and m is the mass of an individual particle. Note that the second term on the right-hand-side is the Boltzmann entropy for a probability distribution P, arising from the Gibbs' correction to the entropy of an ideal gas and will eventually lead to pure diffusion, as we shall show later.

Heat production rate of the system can be evaluated using Eq. N.1, conservation of mass: $P_{,t} = -J_{,z}$ and integration by parts with boundary conditions $J(\pm\infty) = 0$. The result turns out to be:

$$\dot{Q} = T\frac{\partial}{\partial t}\int_z S(z)dz \tag{N.2}$$

$$= Nk_BT\int_z \left[\frac{d\ (\log V)}{dz} - \frac{\partial P/\partial z}{P}\right] J\ dz. \tag{N.3}$$

On the other hand, heat generation can be evaluated using the local power

density [6]: $w = P\,(\xi J/P)\,(J/P) = \xi J^2/P$:

$$\dot{Q} = N \int_z \frac{\xi J^2}{P}\, dz. \tag{N.4}$$

A comparison between Eq. N.3 and Eq. N.4 yields:

$$J = -\mathcal{D}\frac{\partial P}{\partial z} + \frac{-dG/dz}{\xi}P, \tag{N.5}$$

where $dG = -k_B T d\,(\log V)$ has been used as the gradient of the free energy for a *single* particle under the condition that temperature is a constant [5]. This result agrees exactly with the one obtained from the microscopic model (Eq. 8.4). Plugged into the mass conservation law, Eq. N.5 gives the evolution law for $P(z,t)$ shown in Eq. 8.2. We note that the first term in Eq. N.5 is pure diffusion and it comes from the Boltzmann entropy for a probability distribution P in Eq. N.1.

Compared to the random walk model, the theory discussed here considers the problem from a different point of view. Here a non-uniform entropy/free energy landscape causes heat production when a particle flux sweeps through. This contributes to the system as a source of heat. The framework for this model has been used to derive equations for thermal diffusion problems where a temperature gradient drives the diffusion of ideal gas [6]. Here we have used it for diffusion in an entropy-varying landscape.

Appendix O

Transverse Size of a Strongly Confined Polymer

Given a polymer under uniform stretch $\lambda = \partial z/\partial s$ inside a nano-channel of width D, we estimate the transverse displacement $R_\perp$ of the polymer in this section.

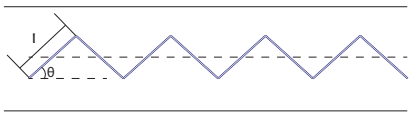

Figure O.1: Given θ, we find the l that minimizes the energy of the confined chain.

Since the stretch λ is uniform, for an inextensible chain, the tangent angle θ (the absolute value) is a constant along the contour. Therefore, the configuration of the polymer, modeled as a chain of links, is piece-wise linear, as shown in Fig. O.1. There is only one free parameter for this configuration: l which is the length of each piece-wise linear segment. Below, we find $l_{\min}$ that minimizes the energy of the chain, from which we can obtain the transverse displacement as a function of the stretch. The energy per unit length of the chain is:

$$E = E_b + E_c + E_p = \frac{2K_b\theta^2}{l^2} + \frac{\Xi\theta^2}{24}l^2 + \frac{1}{2}f\theta^2, \tag{O.1}$$

where K_b is the bending energy, Ξ is the quadratic confinement potential [3], and f is the applied force. The $l_{\min}$ that minimizes this energy is:

$$l_{\min} = \left(\frac{48K_b}{\Xi}\right)^{1/4}. \tag{O.2}$$

Plugging in the relation between Ξ and D [3], we have the scaling relation: $l_{\min} \sim p^{1/3}D^{2/3}$, which agrees exactly with the prediction of Odijk and that of Burkhardt [4, 7, 8].

For the transverse displacement at the nodes (Fig. O.1), we have: $R_\perp = \sin\theta\, l/2 + a_0 \cos\theta$, where a_0 is the effective width of the DNA molecule without fluctuation. Therefore, the transverse displacement $R_\perp$ that minimizes the energy is:

$$R_\perp = a_0 \frac{\partial z}{\partial s} + \left(\frac{3K_b}{\Xi}\right)^{1/4} \sqrt{1 - \left(\frac{\partial z}{\partial s}\right)^2}. \tag{O.3}$$

When $\partial z/\partial s = 1$, there is no thermal fluctuation, so the minimizer $R_\perp = a_0$, as expected. Plugging in the relation between Ξ and D [3], we obtain:

$$R_\perp = a_0\lambda + 0.7445 \left(pD^2\right)^{1/3} \sqrt{1-\lambda^2}. \tag{O.4}$$

Bibliography

[1] Zhang, Y., Crothers, D.M., 2003. **Statistical mechanics of sequence-dependent circular DNA and its application for DNA cyclization.** *Biophys. J.* 84(1), 136-153.

[2] Purohit, P.K., Arsenault, M.E., Goldman, Y., Bau, H.H., 2008. **The mechanics of short rod-like molecules in tension.** *Int. J. Non-linear Mech.* 43(10):1056-1063.

[3] Wang, J., Gao, H., 2007. **Stretching a stiff polymer in a tube.** *J. Mater. Sci.* 42:8838-8843.

[4] Odijk, T., 1983. **On the statistics and dynamics of confined or entangled stiff polymers.** *Macromolecules* 16:1340-1344.

[5] Huang, K., **Statistical Mechanics** (John Wiley & Sons, Inc., New York, London, Sydney, 1963).

[6] Christen, T., 2007. **Modelling diffusion in nonuniform solids using entropy production rate.** *J. Phys. D* 40:5723.

[7] Odijk, T., 1986. **Theory of lyotropic polymer liquid crystals.** *Macromolecules* 19:2313.

[8] Burkhardt, T.W., 1995. **Free energy of a semiflexible polymer confined along an axis.** *J. Phys. A-Math. Gen.* 28:L629.